On the feasibility of using radioactive ion beams in hadrontherapy: dosimetric and imaging studies

Ricardo Manuel dos Santos Augusto

SIGILL. UNIVERSITAT. LUDOVIC. MAXIM.

München 2018

On the feasibility of using radioactive ion beams in hadrontherapy: dosimetric and imaging studies

Ricardo Manuel dos Santos Augusto

Dissertation
an der Fakultät für Physik
der Ludwig–Maximilians–Universität
München

vorgelegt von
Ricardo Manuel dos Santos Augusto
aus Lissabon 1987

München, den Mai 17 2018

Erstgutachter: Prof. Dr. Katia Parodi
Zweitgutachter: Prof. Dr. Otmar Biebel
Tag der mündlichen Prüfung: 11 Juli 2018

Contents

List of Figures

List of Tables

List of Abbreviations

AAPM – *American Association of Physicists in Medicine.*
ART – *Adaptive Radiation Therapy.*
BAMS – *Beam and Application Monitoring System.*
BASTEI – Acronym for *Beta Activity Measurements at the Therapy with Energetic Ions*, a project at GSI.
Bevalac – *A project at Berkeley's Heavy Ion Linear Accelerator (HILAC), combined with the Bevatron synchrotron.*
BGO – *Bismuth germanate* – $Bi_4Ge_3O_{12}$.
BME – FLUKA embedded event generator based on the *Boltzmann Master Equation* theory.
CERN – *European Organization for Nuclear Research* (originally *Conseil Européen pour la Recherche Nucléaire*), Geneva, Switzerland.
CNAO – *Centro Nazionale di Adroterapia Oncologica*, Italian Hadrontherapy Center in Pavia, Italy.
CSDA – *Continuous Slowing Down Approximation.*
CT – *Computerized Tomography.* Using x-ray imaging from different directions for a 3D view inside the human body.
CRT – *Conformal Radiation Therapy.*
DKFZ – *Deutsches Krebsforschungszentrum*, German Cancer Research Center.
DPMJET – *Event generator for high energy nucleus–nucleus interactions based on the Dual Parton Model of particle interactions.*
EOB – *End Of Beam*, time counting after the last beam of an irradiation.
FLUKA – A *Monte Carlo* particle transport and interaction code, named after *FLUktuerende KAskaden*, a legacy german acronym for "fluctuating cascade".
FBP – *Filtered Back Projection*, an image reconstruction method.
FOV – *Field of View*, length parallel to the longitudinal axis in which the PET reconstructs transaxial tomographic images.
FWHM – *Full width at Half Maximum.*
Geant4 – An acronym for Generation of Events ANd Tracks, a *Monte Carlo* particle transport and interaction code.
GSI – *Gesellschaft für Schwerionenforschung*, German National Laboratory for Heavy Ion Research in Darmstadt, Germany.
GSO – *Gadolinium oxyorthosilicate* – Gd_2SiO_5.
HZDR – *Helmholtz-Zentrum Dresden-Rossendorf*, Germany.
HIMAC – *Heavy Ion Medical Accelerator in Chiba*, Japan.
HIRFL – *Heavy Ion Research Facility in Lanzhou*, China.
HIT – *Heidelberger Ionenstrahl Therapiezentrum*, Ion Therapy Center in Heidelberg, Germany.
HU – *Hounsfield Units.*
IAEA – *International Atomic Energy Agency.*
ICRP – *International Commission on Radiological Protection.*
ICRU – *International Commission on Radiological Units and Measurements.*
IMPT – *Intensity Modulated Particle Therapy.*
IMRT – *Intensity Modulated Radiation Therapy.*
INFN – *Instituto Nazionale de Fisica Nucleare*, Italian Institute for Nuclear Physics.
INSIDE – *Innovative Solutions for In-beam Dosimetry in Hadrontherapy* An italian project.
ITEP – *Institute for Theoretical and Experimental Physics in Moscow*, Russia.
LBNL – *Lawrence Berkeley National Laboratory*, Berkeley, US.
LEM – *Local Effect Model.*
LET – *Linear Energy Transfer.*
LLUMC – *Loma Linda University Medical Center*, Loma Linda, US.
LOR – *Line of Response.*
LSO – *Lutetium oxyorthosilicate* – Lu_2SiO_5.
LYSO – *Lutetium-yttrium oxyorthosilicate* – $Lu_{2(1-x)}Y_{2x}SiO_5$.
MCNPX – *Monte Carlo N-Particle eXtended.*
MedAustron – Center for ion therapy and research in Wiener Neustadt, Austria.
MGH – *Massachusetts General Hospital*, Boston, US.
MIT – *Marburger Ionenstrahl-Therapiezentrum*, Germany.
MLEM – *Maximum Likelihood Estimation Method.*
MRI – *Magnetic Resonance Imaging.*
MWPC – *Multiwire Proportional Chambers.*
NASA – *US National Aeronautics and Space Administration.*
NCI – *National Cancer Institute*, Bethesda, US.
NIRS – *Japanese National Institute of Radiological Sciences.*
OAR – *Organs at risk.*
OER – *Oxygen enhancement ratio.*
OSEM – *Ordered subset expectation maximization.*
PEANUT – *Pre–Equilibrium Approach to Nuclear Thermalization*, a pre–equilibrium Intra–Nuclear Cascade hadron interaction model.
PET – *Positron Emission Tomography.*
PIMMS – *Proton-Ion Medical Machine Study* performed at CERN for an optimized synchrotron for ion therapy.
PMMA – *Polymethyl methacrylate*, $[CH_2C(CH_3)COOCH_3]_n$, Plexiglass.
PTCOG –*Particle Therapy Co-Operative Group.*
QA – *Quality Assurance.*
RIB – *Radioactive ion beams.*
RIβ^+ – Radioactive ion beams of β^+ emitting particles.
RBE – *Radio Biological Effectiveness*, relative biological effectiveness.
rQMD – FLUKA embedded event generator based on the *Cascade-Relativistic Quantum Molecular Dynamics* model for nucleus–nucleus interactions.
SOBP –*Spread–out Bragg Peak.*
SPECT –*Single Positron Emission Computer Tomography.*
SPHIC –*Shanghai Proton and Heavy Ion Center*, China.
TERA –*Terapia con Radiazioni Adroniche*, Italian Foundation for Therapy with Hadronic Radiations.
TPS –*Treatment Planning Systems (or software).*
voxel –*voxelized unit* of volume on a regular grid in three dimensional space.

Em memória do meu avô António.

Zusammenfassung

Während Ionen in der Lage sind, strahlenresistente, tief sitzende Tumore effektiv zu zerstören, muss die Lage des Tumorgewebes im Rahmen einer Hadronentherapie exakt bekannt sein, um die Schonung des umgebenden gesunden Gewebes und die Wirksamkeit der Behandlung sicherzustellen. In der klinischen Praxis können Informationen über die Strahlreichweite *in-vivo* von größter Wichtigkeit sein, da sie eine Bestätigung dafür liefern, dass der Tumor effektiv angesprochen wird. Range–Verification–Techniken wie die positron–emission–tomography (PET) haben ein großes klinisches Potenzial, indem sie die Position des *Bragg Peak* in der verabreichten Behandlung durch Vergleich der erfassten Signale mit einem vorher festgelegten Zielbereich überprüfen. Im Falle der PET ergibt sich die Aktivitätsverteilung aus den Produkten inelastischer nuklearer Wechselwirkungen zwischen den Ionen und den Atomkernen im Gewebe. Es wird daher oft als vorteilhafter angesehen, den PET-Scanner in die Strahllinie integriert zu haben, wobei das Scannen während oder unmittelbar nach der Bestrahlung (*in beam PET*) erfolgt. Dies ermöglicht es, Erfassungsfehler im Zusammenhang mit Patientenpositionierung oder *biological washout* zu reduzieren, während gleichzeitig der Beitrag der β^+–Emitter mit kürzerer Halbwertszeit zum PET–Gesamtsignal beiträgt.

Der Gesamterfolg der Kohlenstoff–Ionen–Therapie–Projekte in Japan und Europa, zusammen mit den jüngsten Fortschritten in der Beschleuniger–Technologie und medizinischer Bildgebung, trug zu einem erneuten Interesse an innovativen Lösungen für Hadronentherapie-Anwendungen bei. Im Speziellen zielt diese Arbeit auf eine Untersuchung der Vorteile einer Verwendung der β^+–emittierenden, radioaktiven Ionen ^{11}C und ^{15}O in der Hadronentherapie, verglichen mit den erzielten Resultaten der Nutzung ihrer stabilen Gegenstücke. Zu diesem Zweck wurde der FLUKA–*Monte-Carlo*–Partikeltransport– und Interaktionscode verwendet, um radioaktive Ionenstrahlung in klinischen Umgebungen zu simulieren, einschließlich der Verwendung von PET-Scans mit äquivalenter Dosisabgabe für verschiedene *Online*– und *Offline-PET* Akquisitionsszenarien.

Die Evaluierung der dosimetrischen Ergebnisse mit FLUKA profitierte von den jüngsten Entwicklungen in Modellen für den geladenen Hadronentransport und Fragmentierung bei relativ niedrigen Energien von therapeutischem Interesse. Im Rahmen dieser Arbeit wurde der Code verwendet, um sowohl monoenergetische als auch *Spread Out Bragg Peaks* (SOBP) in Wasser und in einem anthropomorphen Kopf–VOXEL–Phantom zu simulieren. In der Modellierung der Bestrahlung mit ^{12}C und ^{16}O wurden Appro–ximation in der Abgabe der Synchrotronstrahlung und der Strahlführung, angewandt am Heidelberg Ionen Therapiezentrums (HIT), verwendet. Die Daten des Forschungs–

Behandlungsplanungssystems wurden dann in einer Extrapolation für radioaktive Ionenstrahlung benutzt. Das Bildgebungspotenzial, insbesondere für die Reichweitenüberprüfung, wurde mit den neu entwickelten FLUKA PET TOOLS bewertet. Dies erforderte eine detailliertere Modellierung der *Siemens Biograph mCT PET/CT* (PET-Scanner-Modell bei HIT verwendet) Geometrie und Signalantwort. Darüber hinaus wurden Berechnungen von Annihilations-Ereignissen bei Ruheenergie, die von den β^+-Emittern herrühren, durchgeführt. Die Zeitabhängigkeit entsprechender PET-Signale wurde ebenfalls in die Berechnungen einbezogen, so dass die Auswirkungen sowohl der Strahlzeitstruktur als auch der Abtastzeit im Endergebnis wiedergegeben werden.

Mit den Simulationen, die mit Synchrotron–ähnlichen Bestrahlungsschemata und den approximierten HIT–Strahlführungselementen durchgeführt wurden, konnte verifiziert werden, dass die Bildgebungsresultate der radioaktiven Ionenstrahlen bei einer vergleichbaren Dosisabgabe bei jedem PET–Akquisitionsszenario die Bestrahlungen mit stabilen Ionen deutlich übertreffen. Insbesondere wurde bei Verwendung radioaktiver Ionenstrahlen eine- im Vergleich mit stabilen Ionen - um etwa eine Größenordnung höhere Menge an Annihilationsereignissen bei Ruheenergie beobachtet, sowohl für *Online-PET*–Erfassungen (130 Sekunden, einschließlich Überlaufzeit) mit ^{15}O als auch für die *Offline-PET*–Erfassung (5 bis 30 Minuten Erfassung Zeit nach Strahl) mit ^{11}C. Darüber hinaus wurde nicht nur ein erheblicher Zugewinn an Koinzidenzereignissen beobachtet, sondern auch die Qualität der Rekonstruktionsbilder verbessert. Die Ergebnisse mit radioaktiven Ionenstrahlen ermöglichten eine bessere Identifizierung der distalen Kante des SOBP (innerhalb von 1 mm), mit einer besseren Definition der proximalen Anstiegszone bis hin zur distalen Fallzone (Faktor 2 mit ^{15}O *in room* und fast ein Faktor von 3 für ^{11}C in *Offline-PET*-Akquisitionen).

In einer zweiten Phase wurden experimentelle Daten, die am Heavy Ion Medical Accelerator in Chiba (HIMAC) gewonnen wurden, verwendet, um sie mit den Simulationsergebnissen zu vergleichen. Diese Daten wurden in Zusammenarbeit mit Kollegen des Physics Imaging Teams des japanischen Instituts für radiologische Wissenschaften (NIRS) gewonnen. Die Produktion von radioaktiven Ionenstrahlen von ^{11}C und ^{15}O wurde mittels Projektil-Fragmentierungs-Separations-Methode durchgeführt. Der FLUKA-Code wurde zur Berechnung von *Bragg Peak*-Kurven in Wasser und Polymethylmethacrylat (PMMA) herangezogen. Der Vergleich mit den experimentellen Ergebnissen in Wasser zeigte eine gute Übereinstimmung mit den Simulationen und es wurden keine Unterschiede über 1 mm beobachtet. Die Dichte und Form der β^+ Emitter–Aktivität wurde ebenfalls berechnet und mit den Werten verglichen, die mit einem Prototyp eines OPEN-PET–Scanners erhalten wurden, der zwischen den spills und einigen Minuten danach Daten sammelte. Trotz der verwendeten Produktionsmethode, die *Bragg Peak*–Kurven der radioaktiven Ionenstrahlen beträchtlich um einen Faktor 4–5 in Wasser verbreitert im Vergleich zu stabilen Ionenstrahlen, wiesen die in PMMA mit diesen Spezies rekonstruierten Bilder eine um etwa Faktor 2 bessere Definition der Region zwischen dem proximalen Anstieg und dem distalen Abfall auf. Diese Ergebnisse wurden auch durch die FLUKA-Simulationen bestätigt und stimmen mit früheren Beobachtungen überein. Darüber hinaus weisen die rekonstruierten Signale im Vergleich zu stabilen Ionenstrahlen einen beträchtlichen Größengewinn von mindestens einer Größenordnung auf, ebenfalls bestätigt durch FLUKA-Simulationen.

Zusammenfassend weisen die Ergebnisse dieser Arbeit darauf hin, dass β^+-emittierende

radioaktive Ionenstrahlung die für die Strahlreichweitenverifikation und die Behandlungsüberwachung verfügbare Bildsignalleistung bezogen auf stabile Ionenstrahlen in der Hadronentherapie verbessern können.

Keywords: `Hadronentherapie, Radioaktiver Ionenstrahl, Dosimetrie, PET imaging, Monte Carlo, FLUKA`.

Abstract

In the context of hadrontherapy, whilst ions are capable of effectively destroying radio resistant, deep seated tumors, their treatment localization must be well assessed to ensure the sparing of surrounding healthy tissue and treatment effectiveness. In clinical practice, information on the *in vivo* beam range can be of paramount importance, for it provides confirmation that the tumor was targeted effectively. Range verification techniques, such as positron–emission–tomography (PET) imaging, hold great potential in clinical practice, in order to check the accuracy of the *Bragg Peak* in the delivered treatment by means of the comparison of the acquired signal with a corresponding prediction. In the aforementioned case of PET, the activity distribution arises from inelastic nuclear interaction products between the ion and the tissue nuclei. It is therefore often deemed more advantageous to have the PET scanner integrated into the beam line, with scanning occuring during or immediately after irradiation, the so called *in beam PET*. This allows to mitigate acquisition errors related to patient positioning and biological washout, while benefiting from shorter half–life β^+ emitters contributing to the total PET signal.

The overall success of the carbon ion therapy projects in Japan and Europe, along with the recent advances in accelerator technology and medical imaging, contributed to a renewed interest in innovative solutions for hadrontherapy applications. In particular, this work aimed at investigating the advantages of using β^+ emitting, radioactive ion beams of ^{11}C and ^{15}O in hadrontherapy, in comparison to the performance of their stable counterparts. To this end, the FLUKA *Monte Carlo* particle transport and interaction code was used to simulate radioactive ion beams in clinical environments, including the use of PET scans with equivalent dose delivery for different *online*– and *offline*–PET acquisition scenarios.

The dosimetric performance evaluation with FLUKA benefited from its recent developments in charged hadron transport and fragment production models at relatively low energies of therapeutic interest. During the course of this work, the code has been used to simulate both mono–energetic and *Spread Out Bragg Peaks* (SOBP) in water and in an anthropomorphic head VOXEL phantom. ^{12}C and ^{16}O ion beam dose delivery was modeled in the simulations using an approximation of the synchrotron beam delivery and beam line applied by the Heidelberg Ion Therapy Center (HIT). The research treatment planning system data were then used in extrapolations for radioactive ion beams. The imaging potential, particularly for range verification, was assessed with the newly developed FLUKA PET TOOLS. This required a more detailed modeling of the *Siemens Biograph mCT PET/CT* (PET scanner model used at HIT) geometry and signal response. Furthermore, calculations of the annihilations events at rest ensuing from the β^+ emitters were performed. The time dependence of the corresponding PET signal was also included in the calculations, so that the effects of both the beam time structure and scan time could be reproduced in the final result.

In the simulations performed using synchrotron–like irradiation schemes and the approximate HIT beam line elements, it was verified that radioactive ion beams imaging results clearly outperform stable ion beam irradiations for every PET acquisition scenario, with a comparable dose delivery. In particular, it was observed approximately an order of magnitude higher amount of annihilation events at rest occurring when employing radioactive ion beams, for *online PET* acquisitions (130 seconds, including spill time) using ^{15}O as well as for *offline PET* acquisition (5 to 30 minutes acquisition time after beam) using ^{11}C compared to the stable counterparts. Furthermore, not only a considerable gain in coincidence events was observed, but also the quality of the reconstruction images was improved. Namely, radioactive ion beam results allowed for a better identification of the the distal edge of the SOBP (within 1 mm), with superior definition of proximal rise to distal fall–off regions with respect to their stable counterparts by up to a factor of 2 in ^{15}O, *in room* and almost 3 for ^{11}C, in *offline PET* acquisitions.

In a second stage, experimental data acquired at the Heavy Ion Medical Accelerator at Chiba (HIMAC) were used to benchmark the simulation results. These data were obtained in collaboration with colleagues from the Japanese National Institute of Radiological Sciences (NIRS) Physics Imaging Team. The synchrotron primary ^{12}C and ^{16}O ion beam were respectively converted into radioactive ion beams of ^{11}C and ^{15}O using the projectile fragmentation separation method. The FLUKA code was employed for calculating energy deposition of *Bragg Peak* curves in water and polymethyl methacrylate (PMMA). The comparison of simulations and experimental results in water showed a good agreement, with range deviations below 1 mm. The amount and shape of β^+ activity were also calculated, and later compared with the ones obtained with an OPENPET scanner prototype, which collected data in between spills and some minutes afterwards. Despite the production method employed, which broadened considerably the *Bragg Peak* curves of radioactive ion beams by a factor 4–5 in water in comparison to the stable ion beams, the images reconstructed in PMMA using these species featured approximately a factor 2 better definition of the region between the proximal rise and distal fall–off compared to stable ion beams. These findings were also confirmed by the FLUKA simulations and are in line with previous observations. Moreover, the reconstructed signals indicate a considerable gain in magnitude, of at least one order of magnitude compared to stable ion beams, which is as well corroborated by FLUKA simulations.

Concluding, the results in this work indicate that β^+ emitting radioactive ion beams can enhance the imaging signal output available for beam range verification and treatment monitoring with respect to stable ion beams in hadrontherapy.

Keywords: `Hadrontherapy, Radioactive ion beams, Dosimetry, PET imaging, Monte Carlo, FLUKA.`

Extended outlines

Chapter 1 – This is an introductory chapter, including the aim of the present work and a short overview of hadrontherapy, reviewing its physical, biological aspects and a more in–depth description of HIT and HIMAC facilities. The potential of radioactive ion beams will be highlighted. A brief description of PET scanner functions and applications will then follow, with particular emphasis on *in beam PET* and the motivation for range monitoring techniques.

Chapter 2 – A brief introduction to the *Monte Carlo* method and its application in particle transport will be given. Its role in treatment planning will be detailed. A more extensive description of the *Monte Carlo* particle transport and interaction code FLUKA will then follow.

Chapter 3 – Firstly, the methodology employed to generate SOBPs according to user input parameters, in line with a research treatment planning system (TPS) data used at HIT, will be described. Secondly, a summary description of the FLUKA PET TOOLS will be also provided, along with the elements implemented in the simulations for the various PET acquisitions scenarios studied.

Chapter 4 – Description, supported by FLUKA simulations, of the dosimetric and imaging properties of β^+ emitting radioactive ion beams ($RI\beta^+$) and comparison with their stable counterparts in water. These simulations will provide preliminary estimates of the $RI\beta^+$ figures of merit for the following studies in the voxelized phantom geometry and subsequent comparisons with PET reconstructions.

Chapter 5 – This chapter includes the results of comparisons between stable carbon and oxygen ion beams with ^{11}C and ^{15}O SOBPs. The first part simulates clinical–like irradiations in an antropomorphic head phantom. The reconstructed images of SOBPs of comparable dose are obtained via FLUKA PET TOOLS in various PET acquisition scenario, and subsequently a quantitative analysis is performed. The second part deals with the comparison between the experimentally acquired results obtained with NIRS's colleagues and FLUKA simulations of dose and β^+ activities. The dosimetric performance of these beams was assessed in a water phantom whereas the reconstructions were obtained via irradiations on a PMMA phantom, employing an OPENPET prototype for the acquisition.

Chapter 6 – This chapter includes the major conclusions of this work, as well as some remarks on future work.

Chapter 1

Introduction

> Bloch: “Space is the field of linear operators.”
> Heisenberg: “Nonsense, space is blue and birds fly through it.”
>
> — Felix Bloch, *Heisenberg and the early days of quantum mechanics*

Cancer is a disease characterized by an uncontrolled cellular division, which can propagate from tissue to tissue. By interfering with regular organ functions, eventually causing them to cease working properly, it can lead ultimately to death ([WHO]). Its causes are varied and chiefly associated to environmental, genetic and behavioral factors.

In fact, cancer is today in Europe the leading cause of mortality for people aged 45–64, accounting for one quarter of the continent's total death rate according to [EUR]. In the United States it is the second cause of death. The growing aging population, unhealthy lifestyle and pollution are the leading factors as per [WHO12] expected to increase cancer incidence worldwide[Fer13, AOS15]. Recent studies estimate that the number of cancer cases may increase more than 40% from 2014–2035, despite possible future favorable variations in the incidence and mortality rates[Smi16]. In addition to that, lower socioeconomic strata of the population are predicted to be the most affected by this trend ([IAEA–HHR–3]).

However, in spite of being a deadly disease, cancer is presently curable in $\sim 50\%$ of the cases provided it is early diagnosed and an adequate treatment is applied. Nonetheless, these numbers are averaged as some types of cancer may be particularly deadly due to their location, type and stage, (*e.g.* lung and pancreas), despite the great variety of treatment methods currently available ([NCI]). Nowadays, cancer treatment entails at least one of the modalities below, namely:

- Surgery;
- Radiotherapy;
- Chemotherapy & Immunotherapy.

Since W. Roentgen's discovery of X–rays in 1895, radiation and medical applications have been intertwined, laying the basis of what is now denominated Radiotherapy. Although its success varied greatly at its early stage, presently in Europe, radiation is involved in about 70% of cancer treatments according to [IAEA–TRS–461]. Besides its application in diagnostic medicine, it plays a major role in treatment when surgery is either impractical or not recommended, since it may allow a rather selective and localized effect within the tumor, relatively sparing the neighbouring healthy tissue. Radiotherapy is now divided in two categories[Gre12, Moh17]:

→ Conventional - Including *Brachytherapy*, a technique characterized by the implantation of radioactive sources nearby or in contact with the tumor; *targeted therapy*, entailing the use of radiopharmaceuticals to target the tumor for treatment or imaging purposes; and *external therapy*, involving the irradiation of the tumor with electrons or photons beams, in a non–invasive manner;

⇝ Unconventional - Includes hadrontherapy which, as the name indicates, consists of "treatment of tumors through external irradiation by means of accelerated hadronic particles"[Bra09].

The present work will focus on the unconventional domain of hadrontherapy, namely the application of radioactive ion beams, that decay by positron emission ($RI\beta^+$), in a therapy context replacing currently available stable ions.

Therefore, the main goal of this thesis is to investigate how the treatment and imaging performance of selected $RI\beta^+$, such as ^{11}C and ^{15}O, compare to their stable counterparts, and quantify their merits in scenarios as close to clinical environment as possible.

To this end, the FLUKA MC code was used to compare dosimetric and PET imaging performance, using a development version with updated fragmentation models and the recently developed PET TOOLS package. Also, synchroton–like irradiations, beam line and PET scanner elements were (approximately) reproduced for realistic simulations. Furthermore, the code was also compared with experimental data acquired at HIMAC, for both $RI\beta^+$ and stable beams.

1.1 Rationale for ion beams in hadrontherapy

The concept of hadrontherapy dates back to 1946 and the work of R. R. Wilson[Wil46]. It has, especially in recent years, developed considerably, following scientific and technical breakthroughs that made it more practical and accurate. The general advantages of charged hadrons compared to conventional therapy forms are: their more localized dose delivery, the finite range and the lower rate of late toxicity[AK05, Sui10]. Overall, it may lead to higher treatment/radiobiological effectiveness, with about half the integral body dose of conventional treatment forms and therefore lower risks of secondary tumors[Lom09, SES10].

Throughout 1950–80's many types of charged hadrons, from protons to argon ions, were studied intermittently at the LBNL, in the United States ([LBL77, LBL80]). At the time, it was the only machine capable of delivering heavy ions with the energy range required by medical treatments[SES10]. However, it was oriented towards research in nuclear physics and not optimally designed for therapy purposes. After that period, proton therapy became quickly popular through the 90–00's, and it is now considered an advanced clinical modality[Alo96, Pag12, BMM16]. However, it appeared that some ion species could be therapeutically more effective than the meanwhile well–established protons, with experimental work evidencing heavier ions lower lateral scattering for the same range, along with the higher energy transfer to matter and hence a higher biological effectiveness for tumor tissues[Cas80, Cas82, Alo96]. Consequently, the treatment effectiveness could be increased with respect to protons, even for radioresistant tumors[Cas80, Alo96, Ohn13].

On the other side, the use of heavier ions over protons implies some drawbacks, firstly a larger upfront investment and operational costs initially restricted their usage to research facilities[Sch14]. The physical properties of certain heavier ions, such as their fragmentation dose tail, a residual dose resulting from ion fragmentation mechanisms occurring during beam–media interactions, hindered their clinical application[CTL76, Alo96]. Lastly, their relatively high biological impact must not be overlooked, and dose delivery has to be properly assessed/monitored to preserve healthy tissues nearby from receiving critical doses. This is a non trivial task in view of the variation of biological effectiveness of ions in tissue along the beam path[Cas80].

Carbon ions were found optimal because of the balance between their destructive and ballistic properties, which lays the basis of carbon ion therapy[TK12, Ohn13]. Even though carbon ions are effective against radioresistant tumors, the destruction of tumors is more easily achieved with heavier ions, but collateral damage to normal tissue increases abruptly.

Carbon ion therapy was first applied at clinical scale in Japan by NIRS, at the HIMAC facility in 1994. Since then, HIMAC has treated more than 9 000 out of a total of 12 000 patients treated with carbon ions in all Japan, which alone hosts five carbon ion therapy facilities[EK16]. Shortly after its initial success in Japan, carbon ion therapy was introduced in Europe, in 1997 at GSI in Darmstadt, Germany[Nod14]. The latter operated as a pilot project until 2008, in collaboration with DKFZ Heidelberg, Radiological University Hospital Heidelberg and FZ Rossendorf. After the GSI success and pioneering work with carbon ion scanning technique and integration of an online PET camera, the German carbon ion therapy program was then reallocated in 2009 to a new facility, HIT, in Heidelberg[Sui10]. In the following year, CNAO started operations in Pavia, Italy. Two other facilities, albeit more recent, MIT in Marburg (started 2015) and MedAustron near Vienna (started 2017) complete the list of European carbon ion therapy centers. Finally, the worldwide listing of carbon ion therapy dedicated facilities is completed by two facilities in China, the HIRFL in Lanzhou and the SPHIC in Shangai. As of 2017, already more than 20 000 patients benefited from treatment with carbon ions, as detailed in figure 1.1 ([PTCOG]).

Chronology

1895	Discovery of x–rays (W. Röntgen)
1932	First cyclotron (E. Lawrence)
1946	Protontherapy proposed (R. R. Wilson)
1954	First patient treatment with protons (LBNL)
1957	First patient proton treatment in Europe (Uppsala, Sweden)
1969	Start of ITEP, Moscow (Oldest proton facility still in operation)
1994	First hospital–based facility dedicated to carbon ions (HIMAC, Japan)
1997	First patient treated with carbon ions at GSI, Germany
2009	First European proton/carbon ion facility (HIT, Germany)

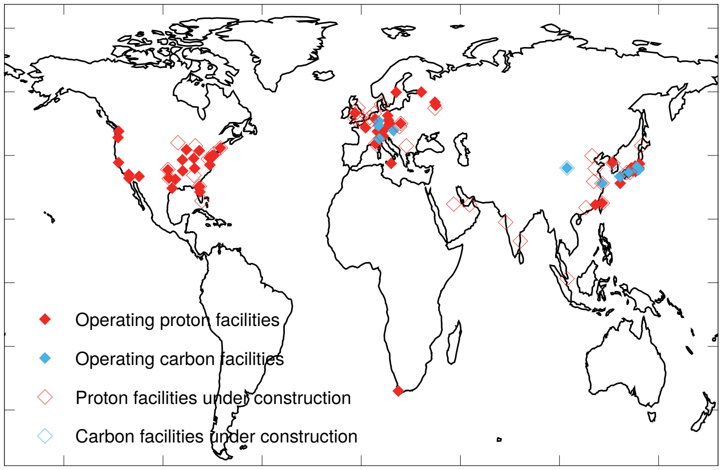

Figure 1.1: *On the left, a chronogical overview of hadrontherapy events as given by [ENLIGHT]. A world map detailing the Particle therapy facilities in operation (as of June 2017) is shown on the right ([PTCOG]).*

Despite the growing trend of carbon ion therapy, its conceptual challenges, inadequate reimbursement policies and data supporting its cost–effectiveness still limit its worldwide application, compared to the more well–established proton therapy[Sch14].

1.1.1 Physics of interaction of ions with matter

Medical treatments involving irradiation of tissue with heavy charged particles exploit the biological effects originating from physical energy loss processes as ions traverse matter, chiefly as a result of inelastic interactions between the impinging ion and the electrons of the media's atoms.

Atomic interactions of radiation in matter can be distinguished in two major forms: ionizing and non–ionizing. Moreover, two types of ionizing radiation can be identified ([IAEA–TCS–42]):

- ⋆ Directly ionizing radiation, leading to ionization and excitation of target atoms, through long range electromagnetic force (*e.g.* relativistic charged particles);
- ⋆ Indirectly ionizing radiation, which does not ionize atoms *per se.* Their interactions are dominated by short–range forces, without being hindered by the Coulomb barrier threshold (*e.g.* X–rays and neutrons). Nevertheless, they may generate secondary radiation such as electrons and protons that is directly ionizing.

It is thus paramount to understand radiation interaction with matter in order to estimate its consequences. In the particular case of ions traversing biological tissue, this implies evaluating properties such as range, rate of energy dissipation and characterize the distribution of secondary radiation spatially, as well as in time. A more biologically–driven description of radiation impact will be provided in the next section while the physical aspects will be herebelow described[Tur95, Tav10, Kno10].

As the ion exerts electromagnetic forces on the medium electrons, it incrementally imparts energy to them and thus (directly) ionizes the media atoms, leaving them in an excited state while the ion loses kinetic energy and gradually slows down, capturing electrons from the media until becoming neutral and stopping. Some excited electrons may even acquire enough energy to travel macroscopic distances in matter (δ–ray) and excite/ionize the surrounding media themselves. To a lesser degree, nuclear reactions or atomic nucleus scattering may also occur. Overall, energy deposition for ions in a medium results from the combination of three mechanisms[Leo94] as depicted in figure 1.2:

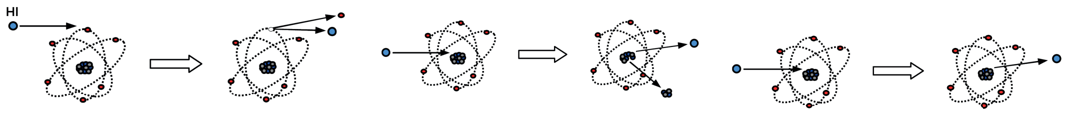

(a) ENERGY LOSSES – Collisions with atomic electrons

(b) FRAGMENTATION – Nuclear Interactions

(c) SCATTERING – Multiple Coulomb Scattering

Figure 1.2: *Adapted illustration of the major energy loss mechanisms for heavy charged hadrons (HI) through matter*[MGH].

Nuclear reactions are very relevant for high energies even though cross sections are lower. However, scattering is not to be neglected, particularly for lower energies. Nevertheless, the vast majority (80–90%) of the ion and secondary fragments energy is lost via (inelastic) collisions with atomic electrons, while atomic (elastic) collisions do not entail considerable energy losses at therapeutic energies. Also, the paths described by ions in matter are typically straight, making their lateral energy deposition profiles steeper than those of protons for instance[Bat16].

Energy losses. Most of the ions' energy is lost in (inelastic) collisions with atomic electrons and to a less degree with atomic nuclei[BMM16]. The maximum energy transferred to electrons (ΔE_{max}) in a single collision between a particle of mass M and kinetic energy E with a free atomic electron with mass m_e, is dictated by kinematics and given by

$$\Delta E_{max} = \frac{2m_e c^2\beta^2\gamma^2}{1 + 2\gamma\frac{m_e}{M} + \left(\frac{m_e}{M}\right)^2}, \tag{1.1}$$

with $\gamma = \left(1-\beta^2\right)^{-\frac{1}{2}}$ being the *Lorentz factor* and $\beta = v/c$ the velocity of the incident particle in units of c (c is the speed of light in vacuum). For ions at non relativistic energies, as $M \gg m_e$, it can be written simply

$$\Delta E_{max} = 2mc^2\beta^2\gamma^2. \tag{1.2}$$

As a consequence of this, a trail of excited or ionized atoms will be observed throughout the beam path. Given the multiplicity of collisions in materials it is customary to characterize the energy loss distribution as an average quantity and its fluctuations. The average energy loss per unit path length is denominated *Stopping Power* $S(E)$

$$S(E) = -\frac{dE}{dx} \quad \left[\mathrm{MeV\,cm^{-1}}\right]. \tag{1.3}$$

Alternatively, the concept of *Mass Stopping Power* is more often employed, for it is almost independent on the medium density ρ

$$S(E) = -\frac{dE}{\rho dx} \quad \left[\mathrm{MeV\,cm^{2}\,g^{-1}}\right]. \tag{1.4}$$

By exhausting their kinetic energy, ions will eventually come at rest. The distance travelled up to this point is denominated *Range.* Energy losses of heavy charged particles were first studied by N. Bohr through 1913–15[Boh15], by averaging the energy imparted to media electrons across a distance for different energies, but unaccounting for relativistic and quantum mechanical effects. Consequently, the mean range (R) of an heavy charged particle is influenced by the particle's speed, its mass, and the electron density of the material traversed. For ions it tends to be straight up to near its end. Assuming the slowing down of heavy charged particles to be a continuous process with always the average stopping power, the CSDA range can be used to estimate the range based on the inital energy (E_0) loss rate along its path, or the distance beyond which it "shall not pass" in view of its energy loss rate, as

$$R_{\mathrm{CSDA}} = \int_{E_o}^{0} \left(\frac{dE}{dx}\right)^{-1} dE. \tag{1.5}$$

The standard way of defining the penetration depth of ions is an approximation since it does not account for stochastic effects such as energy *straggling*, δ–ray production, nuclear interactions and *Multiple Coulomb Scattering* (figure 1.2), effects that will be described later on. Nonetheless, it can be considered a good approximation for heavy charged particles' mean range calculation, for these aforementioned effects have no considerable effect in ions' trajectory. A (very) approximate method to compare mean ranges, as a function of the material's density (ρ) and projectile atomic mass (A), can be obtained with the *Bragg–Kleeman's* rule[Kno10]

$$\frac{R_1}{R_0} \cong \frac{\rho_0\sqrt{A_1}}{\rho_1\sqrt{A_0}}.$$

Naturally, it is paramount to know in detail the exact range of these ions, since their therapeutic application is only effective if the energy deposition is confined to the tumor region. Failure to do so may imply the destruction of healthy cells, hindering treatment prospects.

In addition to that, the energy deposition of charged hadrons is not constant, as it peaks at range's near–end, an effect known as *Bragg Peak*[BK04, BK05], put into evidence in figure 1.3.

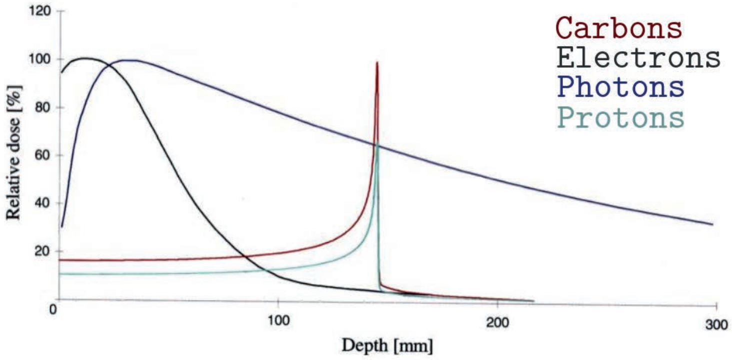

Figure 1.3: *Depth dependence of the deposited dose for different radiation types*[Man15].

The above mentioned effect, occurring at the very end of the continuous energy loss regime, and being characterized by an high energy transfer to the target material, was first identified by W. H. Bragg while investigating the slowing down of α particles in air[BK04]. The position at which it takes place is related to the electronic stopping powers of the projectile and *straggling* effects and can be adjusted for maximum impact at the tumor range[Bor97]. Such energy deposition profile contrasts greatly to that of X–rays and neutrons, which are thus rather inefficient for targeting deep tumors compared to charged hadrons. Note that, particularly for ions, a slight range offset can evidently lead to a possibly unnoticed large energy deposition out of the region of interest.

The mean energy loss per unit path length, accounting for the interactions of heavy charged particles with target electrons can be approximately estimated using the *Bethe–Bloch* equation for the *Stopping Power* per unit path length[Bet30, PDG14].

$$\left(\frac{dE}{dx}\right)_{e^-} = -4\pi N_A r_e^2 m_e c^2 \rho \frac{Z}{A}\frac{z^2}{\beta^2}\left[\frac{1}{2}\ln\left(2m\gamma^2\beta^2c^2\Delta E_{max}\right) - \ln\left(I\right) - \beta^2 - \frac{\delta}{2} - \frac{C}{Z}\right], \qquad (1.6)$$

being r_e the classical electronic radius, m_e the electron rest mass, z the projectile charge, Z and A are the material's atomic and mass numbers, respectively. N_A is the *Avogadro's number*, ρ the material's density and ΔE_{max} the maximum energy transfer as given in equation 1.1. As for I, it is a material–dependent parameter, called the mean excitation energy of atomic electrons and it is a logarithmic average of all possible excitation and ionization levels[Jan82]. Finally, C/Z and $\delta/2$ are the shell and density correction terms, respectively[Ste84, Bic92]. As the projectile slows down below few MeV/u (for light ions), it tends to "picks up" electrons from the medium more easily, the projectile charge in equation 1.6 is then approximately described via its effective charge z_e, using Barkas formula[BBS56, BDH63]:

$$z_e \approx z \left(1 - e^{-125\beta z^{-\frac{2}{3}}} \right). \tag{1.7}$$

Equation 1.6 was firstly improved with non–relativistic corrections (1930) and then relativistically (1932), since for therapeutic energies β can take values up to 0.7[Bet32, BH34]. Additional corrections were implemented, due to the fact that H. Bethe's original formula did not include terms beyond z^2 (leading order in perturbation theory). The full scope of the approximations and corrections considered in the framework of the *Bethe–Bloch* equation will be overviewed in chapter 2.

While shell corrective factors are of increasing relevance at low energies, density corrections are important for relativistic projectiles. The *Bethe–Bloch* equation performs well between the interval $0.1 < \gamma\beta < 100$, in which therapy applications are typically included. At energies $\lesssim 0.3$ MeV/u the particle eventually enters the *Lindhard region* where equation 1.6 is no longer valid due to the velocity of the projectile and of the orbital electrons becoming comparable[Kr15b].

The *Bragg Peak* and the related increase of energy loss as the particle velocity decreases is put into evidence looking at the z^2/β^2 factor in equation 1.6. Near the end of its path and according to equation 1.7, the slowed–down projectile picks up electrons and its charge is reduced, thus compensating the energy loss as $\frac{dE}{dx} \propto z_e^2$, causing the energy loss curve to fall off and resulting in the characteristic *Bragg Peak* curve. According to equation 1.6 and without accounting for statistical fluctuations, the range can be considered to scale approximately with the A/z^2 parameter, for a given β[Kur14]. As for the *Bragg Peak*'s relative height to entrance dose, it decreases with increasing kinetic energy of the beam particle and the *straggling effect*[Sui10].

Upon losing gradually energy from inelastic interactions with atomic electrons, elastic Coulomb interactions with nuclei become more likely. This nuclear stopping power contribution is only relevant for very low energies (typically $\lesssim 10$ keV/u), and thus negligible in therapeutic applications[SES10]. Other forms of energy losses beyond collisional ones are radiative energy losses via *Bremsstrahlung*[PDG14]. A last energy loss mechanism, albeit less relevant than *Bremsstrahlung*, is by emission of *Cherenkov* radiation. For ions at therapeutic energies the radiative energy loss component is totally negligible.

Nuclear reactions. Nuclear reactions and nuclear scattering imply an interaction of a particle or radiation with a nucleus. In this work non–elastic interactions are vastly more relevant than elastic scattering since the former induce the nucleus transformation into one or more nuclides. The consequent transformation is characterized by conservation of total energy, charge, nucleon number, as well as linear and angular momentum[Ber09].

Concerning hadrontherapy, and even though the stopping process of high energy hadrons is more affected by collisions with atomic electrons, nuclear reactions will play a major role in the treatment effectiveness. Interactions between nuclear particles are governed by the strong interaction force. In the case of ions, for these reactions to occur, either a kinematic or *Coulomb barrier* threshold needs to be overcome in the interaction between projectile and target. If the *Coulomb barrier* threshold is surpassed, the kinematic threshold applies and a reaction can occur only if the available energy is above threshold.

When within the nuclear force range, an interaction is typically very fast and can result in the exchange of energy or particles between the interacting particles or the fusion of the projectile with the target. In non–elastic nuclear interactions and at hadrontherapy's energy range, peripherical collisions are the most relevant, with ions transferring kinetic energy and nucleons[BMM16].

The *abrasion–ablation* model is commonly used to describe this process in two steps: firstly, the nucleons directly involved in the interaction are abrased and lead to the creation of an "hot reaction zone" (see figure 1.4), while the remaining nucleons that did not take part in the interaction are almost unaffected by the collision; subsequently, an ablation process ensues where the fragments and the "hot reaction zone" de–excite by evaporating lighter fragments and radiation[BMM16].

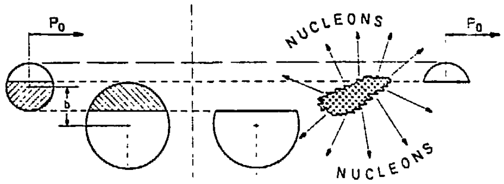

Figure 1.4: *Illustration of the possible outcome of a collision between an highly energetic projectile with momentum* p_0 *and a target nucleus*[BRT90].

In the earlier stage ($\sim 10^{-22}$ s), preliminary fragments are produced, which are partially excited. In the second stage the excited nuclei will produce nucleons and heavier fragments via evaporation, below an energy threshold for nucleon separation, foillowed by γ de–excitation which will expend the residual excitation energies in a process lasting up to 10^{-16} s [Som07]. These processes will be mentioned in more detail in chapter 2.

For ions impinging in matter, nuclear reactions pertaining to the ion, the media nuclei and subproducts are several and responsible for fragment production, loss of primary beam fluence and resulting emerging radiation, according to the reaction cross sections[Bat16]. Considering a monoenergetic ion beam impinging in a medium, the rate of nuclear reactions $\dot{r}$ [reaction cm^{-3} s^{-1}] will intrinsically depend on both the beam flux ϕ [particle cm^{-2} s^{-1}] and number of atoms $\mathcal{N}$ in the volume impinged [atoms cm^{-3}]. Given these elements, the reaction rate in a given volume $dAdx$ will be given by:

$$d\dot{r} = \sigma\phi\mathcal{N}dAdx \tag{1.8}$$

with σ (cm^2) being the microscopic cross section, essentially quantifying the probability of a specific reaction occurring. Its value is almost constant down to 100 MeV/u, below which value it increases as other mechanisms such as deep inelastic or fusion reactions start to contribute[SES10].

On average, about 20% of primary protons and half of the primary carbon ions will undergo fragmentation reactions in hadrontherapy irradiations[HIS06, Kr15b]. They are subdivided in target and projectile fragments, although only the former are produced with protons. While target fragments are approximately static the projectile fragments, due to the high projectile's velocity, will appear forward peaked in the laboratory frame as they approximately inherit the projectile's velocity and direction. Consequently, they will travel distances according to the already mentioned relationship $R \propto {}^{A}/_{Z^2}$ for a given β[Eng92, Fie06]. When ions heavier than protons impinge in a target, the build–up of secondary particles beyond the primary ion penetration depth will form the fragmentation dose tail, observed after the *Bragg Peak* and depicted in figure 1.5[Par04].

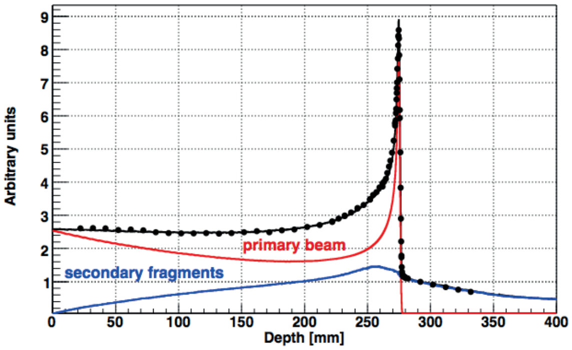

Figure 1.5: *Bragg Peak longitudinal profile in water for a 400 MeV/u* ^{12}C *beam (experimental data*[HIS06]*: points, FLUKA simulation: solid line), distinguishing the energy deposition from primary ion beam and secondary fragments*[Mai07].

From a dosimetric point of view these fragments can be of consequence given the regions their energy is imparted to, particularly in the case of heavier ions, as both the beam particles and their secondaries spread both longitudinally and laterally[Mat05, Bat16]. In spite of that, some clinical monitoring techniques (*e.g.* range verification) benefit from the emissions from radioactive fragments produced or other outgoing radiation due to nuclear reactions, in its prompt or delayed form[Kr15b].

Regarding radioactive fragments, a radioactive decay is characterized by an unstable nucleus spontaneously transforming itself into one or more types of particle/radiation, generating new nuclear species until a stable isotope is attained.

Lateral scattering & Range straggling. Although ions are characterized by having relatively straight paths, not all charged particles in a mono energetic beam travel equal distances. This is because of the stochastic nature of its interactions with matter, and the practical unattainability of a perfect mono energetic beam[BMM16].

When Coulomb interactions with atomic nuclei increase, considerable changes of direction can be observed. For light charged particles such as electrons, this effect is more evident, forcing a seemingly *zig–zagging* throughout their path. On the other side, more massive and energetic particles as ion beams are more hardly deflected. Therefore, the lateral scattering as consequence of accumulated small deviations at each step is less pronounced, which leads to remarkable advantages in tumor dose conformity.

Due to the large number of collisions the beam is "broadened" spatially, this is a result from cumulative multiple deflections which end up being of consequence to projectiles' trajectory, according to *Moliére's Theory* of *Multiple Coulomb Scattering*[Mol48, Bet53]. For such small angle deviations ($\lesssim 10^o$), the scattering projection angle Θ distribution can be approximated to a Gaussian whose standard deviation σ_Θ (rad) is approximately given by the *Highland's formula*, revised[Hig75, LD91].

$$\sigma_\Theta \approx \frac{13.6\ \mathrm{MeV}}{\beta p c} z \sqrt{\frac{L}{L_R}} \left[1 + 0.088 \log\left(\frac{L}{L_R}\right)\right], \tag{1.9}$$

where p is the projectiles' momentum and L and L_R the target thickness and radiation length [g cm^{-2}], respectively. The lateral scattering is higher for lower energy projectiles, approximately following the relationship $z/\beta pc$[Krä00, SES10, Kur14].

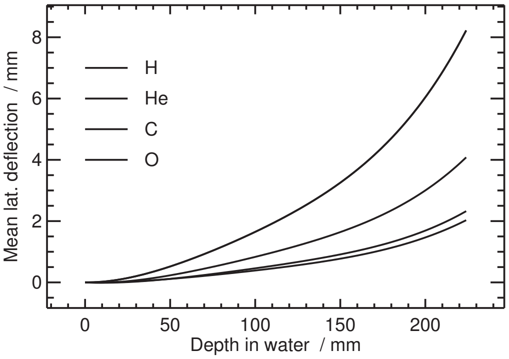

Figure 1.6: *Lateral deflection for various ion beams in depth*[*Par04*].

Moreover, the joint effect of statistical energy fluctuations in the projectile's slowing down process is described with *Vavilov distributions* for thin targets[Vav57]. These fluctuations result in the widening of the *Bragg Peak* and contribute to lower peak–to–entrance energy deposition ratios. Energy loss fluctuations can be approximately described as a Gaussian for thick targets with variance σ_E^2

$$\sigma_E^2 \approx 4\pi N_A r_e^2 m_e^2 c^4 \rho z^2 \frac{Z}{A} \Delta s \tag{1.10}$$

in which Δs denotes the target thickness[Pön04]. As a result of the above mentioned effects, a relatively small penetration depth variation in ions' travelled path can be observed, which is denominated *Range straggling* and whose width σ_R is given by

$$\sigma_R = \frac{R}{\sqrt{m}} f\left(\frac{E}{mc^2}\right), \tag{1.11}$$

with R being the mean range, m the particle's mass and f an absorber dependent function. As $\sigma_R/R \propto A^{-1/2}$, heavier ions tend to have sharper peaks than lighter ions such as protons[Krä00, SES10]. The *range straggling* variance is related to the *energy loss straggling* (σ_E) via

$$\sigma_R^2 = \int_0^{E_0} \left(\frac{d\sigma_E}{dx}\right) \left(\frac{dE}{dx}\right)^{-3} dE. \tag{1.12}$$

Relative *range straggling* in tissue attains 1% of the mean range for protons and 0.3% for carbon ions[Par04].

1.1.2 Biological effects of ions in tissue

Every living organism on Earth is subject to both a natural and artificial radiation background. Natural background comprises terrestrial as well as cosmic sources and is the chief background contributor. As for exposure to artificial radiation sources, it can have several origins, from atomic weapon test remniscences to medical treatments.

Radiation–related biological damage is a consequence of the interaction of radiation with biological tissue and ionization of cellular atoms, disrupting their activity and chemical balance. Ionizing radiation effects can be subdivided in two categories by [ICRP–103]:

- Deterministic: Manifested in a short time period, whenever radiation exceeds a threshold, leading to observable tissue or organ effects.
- Stochastic: The probability of radiation exposure effects' occurrence increases with dose, but neither a threshold applies, nor a time period can be set for quantifying its consequences (*e.g.* probability of cancer development or heritable disease, triggered by mutations in reproductive cells).

The International Commission on Radiological Units and Measurements (ICRU) and the International Commission on Radiological Protection (ICRP) are the entities responsible for providing scientific support and guidelines for radioprotection in view of chemical, material and biological effects of radiation, regulating dosimetric quantities's application.

Destroying a tumor in hadrontherapy implies destroying its tissue beyond repair through energy deposition, by attaining a certain dose, and at the same time ensuring that the healthy tissue in its vicinity is preserved. Absorbed dose ([ICRP–103]) can be quantified as

$$D = \frac{d\bar{E}}{dm}, \tag{1.13}$$

with $\bar{E}$ being the average energy imparted to a mass m by ionizing radiation. It is expressed in units of [Gy] $\equiv$ [J kg^{-1}]. Absorbed dose is measured with specific equipment, including calorimeters' measurement via temperature rise and ionization chambers, which measure ionization induced by the passage of radiation in a gas. The gas is contained in a chamber subject to an electric field. The ion–electron pairs produced by the beam interaction with the gas will then be attracted to the electrodes, generating an electric signal proportional to the ionization's, and thus dose, magnitude[San12]. Concerning absorbed dose from mono energetic ions, and provided a collimated beam is being used, it varies in depth as:

$$D(x) = \frac{1}{\rho}\left(-\frac{dE}{dx}\right)\Phi(x), \tag{1.14}$$

with Φ representing the (primary) ion fluence, approximately given by the following expression in depth

$$\Phi(x) = \Phi_0 e^{-\mathcal{N}\sigma x} \quad [\mathrm{ion\,cm^{-2}}], \tag{1.15}$$

being Φ_0 the entrance fluence, $\mathcal{N}_t$ the number of the medium atoms per unit of volume, whereas σ is the reaction cross section related to the ion interaction with the medium[Par04].

In a radiation protection context, absorbed dose is calculated using the equivalent dose (H_T) notion, which is defined in [ICRP–103] as

$$H_T = \sum_R w_R D_{T,R}, \tag{1.16}$$

with $D_{T,R}$ being the average dose absorbed in an organ or tissue T, for radiation R, and w the corresponding weighting factor for that radiation. Although the units are still [J kg^{-1}], its measurement unit is the *sievert* [Sv] instead of *gray* [Gy] to distinguish it in view of the former tissue's weighting factor ([IAEA–TCS–42]). A simplified version of these weighting factors can be seen in table 1.1:

Table 1.1: *Radiation Weighting Factors – [ICRP–103] 103 2007.*

Radiation type	**Radiation Weighting factor w$_R$**
Photons, all energies	1
Electrons, muons, all energies	1
Protons and charged pions	2
Alpha particles, fission fragments, heavy ions	20
Neutrons	$w_R = \begin{cases} 2.5 + 18.2e^{-\frac{[\ln(E_n)]^2}{6}}, & E_n < 1\text{ MeV} \\ 5.0 + 17.0e^{-\frac{[\ln(2E_n)]^2}{6}}, & 1 \leq E_n \leq 50\text{ MeV} \\ 2.5 + 3.25e^{-\frac{[\ln(0.04E_n)]^2}{6}}, & E_n > 50\text{ MeV} \end{cases}$

ICRP assumes that, for doses below 100 mSv, the stochastic effect incidence increases steadily and proportionally to the equivalent dose. Therefore, the dose to healthy tissue while targeting a tumor, should be kept as low as reasonably achievable, at least below deterministic repair thresholds. In hadrontherapy, the quantification of the dose delivered to a patient differs considerably, as will be later described. Before that, a brief mention to the clinical procedure will be given.

Clinical methodology. The decision for the use of any general form of radiotherapy results from a multidisciplinary medical committee evaluation ([IAEA–HHS–31]). The latter evaluation accounts for different treatment options for particular cases, defining treatment strategies depending on: whether the therapy is curative or palliative; the patient status (age, health); tumor location along with the identification of organs at risk (OAR) nearby, which should be preserved.

An optimal dose delivery in clinical practice is the baseline of conformal radiation therapy (CRT) and it should obey to five cardinal points: Dose should be sufficient to destroy the tumor; it should be uniformly delivered; exempt healthy tissue from lethal dose; irradiation should last as short time as possible and patient movement impact should be minimized.

Failure to cope with those points may result in repercussions to healthy tissue due to radiation's exposure, depending on the characteristics of the radiation and sensitivity of the irradiated tissue.

Typically, conventional radiotherapy encompasses daily fractions of 1.8–3 Gy throughout 5–8 weeks, for 5 days a week with dose to the tumor attaining $\sim$ 75 Gy without secondary effects in optimal scenarios. However, with carbon ions, the dose delivery is typically of $\sim$ 60 Gy, but weighted with a biological effectiveness factor which will be later described, over 4 weeks in 16 sessions for skull base tumors, the value varying depending on the tumor type, location and fractionation protocol[Ohn13].

Regarding the latter, dose delivery should be adequately fractionated in view of different tissues having distinct responses to dose, with normal cells typically recovering better than abnormal cells. At present, dose delivery protocols are based on the probability of healthy tissue of 5% of the population evidencing side effects after 5 years (TD5/5 value). For palliative treatments, higher doses/fraction can be envisaged ([IAEA–TCS–42]). According to NIRS data, for skull base chordoma patients, the overall local control rates at 5 years were 88%, and similar values were reported at GSI, whereas with conventional proton therapy a 73% value is generally attained[Ohn13].

Side effects can be avoided throughout various methodologies: Subdividing dose intake in fractions over a somewhat extensive period of time and allowing healthy tissue to regenerate after receiving sublethal dose, it reduces the impact of punctual overshooting but it has a negative influence on the treatment output rate; Also, the dose to adjacent healthy tissues may be kept below critical thresholds by targeting the tumor through different angles, using multiple irradiation fields (stereotactical) and/or intensity modulation techniques, with dose being delivered homogeneously throughout the tumor volume only employing intensity modulation techniques[AK05]. The latter approach will be mentioned in more detail in section 1.1.5.

The effects of radiation in tissue. Tumor cell destruction in ion therapy is a consequence of radiation effects over functional DNA segments, generally by secondary electrons in the ∼10 eV energy range, resulting from the beam particle's interactions and consequent ionization density[Gre12, LFO13].

As the human body is ∼ 80% water, the majority of the interactions of an ion beam, for instance carbon, affects water molecules, involving *Coulombic* but also nuclear interactions such as $^{12}\mathrm{C}(^{16}\mathrm{O},\mathrm{X})$ and $^{12}\mathrm{C}(p,X)$. Depending of the interaction type it may eventually lead to a transformation of the molecular structure which can prevent/alter its biological function.

The effects of radiation along particle tracks in tissue (dl) can be more accurately evaluated using the notion of (restricted) linear energy transfer (LET)

$$L_\Delta = \left(\frac{dE}{dl}\right)_\Delta \quad [\mathrm{keV}\,\mu\mathrm{m}^{-1}], \tag{1.17}$$

which, by excluding energies above a threshold Δ for secondary electrons, allows a more detailed assessment of radiation's localized effects[BMM16]. Necessarily, the slowing down of charged hadrons traversing a media implies an increase in ionization density and thus LET up to the *Bragg Peak*, increasing its destructive effectiveness ([IAEA–TCS–42]).

Among the various types of ionizing radiation, ions, being both directly and densely ionizing, are considered high–LET radiation, depositing great amounts of energy in relatively localized spots, favouring deep–seated tumor destruction. Furthermore, contrarily to protons that are sparsely ionizing and low–LET, ions are indeed able to treat radioresistant tumors by damaging directly the DNA[EK16, Sui10]. While protons modestly damage the DNA molecules mostly via singlestrand breaks, ions are more likely to cause doublestrand breaks, irreparable and usually leading directly to cell death via loss of reproductive integrity. Since DNA comprises about 5% of a cell nucleus, these effects take place at a relatively tiny scale, they are categorized in [IAEA–TCS–42] as:

Direct – Breaking up of biological molecules promoting unpaired electrons, due to the direct action of an impinging particle in a macromolecule involved in biological tasks which becomes disfunctional and reactive. High–LET radiation such as ions is extremely destructive in this way.

Indirect – The free radicals, such as hydroxyl, produced by the radiation in the cell, affect the DNA collaterally. The mixed field of an ion irradiation creates many indirect effects by interaction with cellular water in tissue and promoting radiolysis, which leads to highly reactive radicals.

Free radicals are intrinsically related with the oxygen amount in the medium, thus cells with low oxygen content (hypoxic) are relatively radioresistant, up to a factor of *circa* 3, than normal ones and they must be irradiated with higher doses to be destroyed, an effect quantified by the oxygen enhancement ratio (OER), defined as[Sui10, Sch14]:

$$\mathrm{OER} = \frac{D_h}{D_a}, \tag{1.18}$$

with D_h being the dose required to produce a deterministic effect in an hypoxic tissue, and D_a in an aerobic one. For low–LET radiation OER is ~ 3. Regarding carbon ions instead, OER varies with LET from 2.5–1 rendering them more effective at killing cells in the hypoxic, necrotic cores of solid tumors. Since ions with charge equal or above six can provide the same biological effectiveness using up to a third of the X–rays dose, the radioresistant effect, due to low oxygenation rate (poor re–oxygenation pattern/high repair capacity), is almost overcome using these ion species[Sui10, Moh17]. However, one needs to take into account also the loss of ballistic selectivity due to fragmentation and the possible high damage to healthy tissue in order to compare ions' effect with other radiation. One way to quantify the sensitivity of biological material, for different particles, with respect to a specific biological endpoint such as with X–rays, is done by applying the relative biological effectiveness (RBE) factor[SES10]:

$$\mathrm{RBE}_{iso} = \frac{D_{\mathrm{X-rays}}}{D_{ion}}, \tag{1.19}$$

which is here defined as the ratio between the X–rays (usually 250 kVp) and the test radiation (*i.e.* ions) dose required to produce the same biological effect as defined by [IAEA–TRS–461]. This effect was in fact one of the main driving factor for using high–LET and low OER particles, in cancer therapy. It becomes then necessary to distinguish between physical dose D and biological dose D_{bio}, as these are conceptually distinguishable quantities in view of dose's microscopic distribution in tissue, linked through RBE

$$D_{\mathrm{bio}} = \mathrm{RBE} \cdot D. \tag{1.20}$$

Moreover, since RBE is a dose dependent factor (among other factors such as particle type and tissue) its variations may therefore have a considerable impact on the dose delivered near OAR.

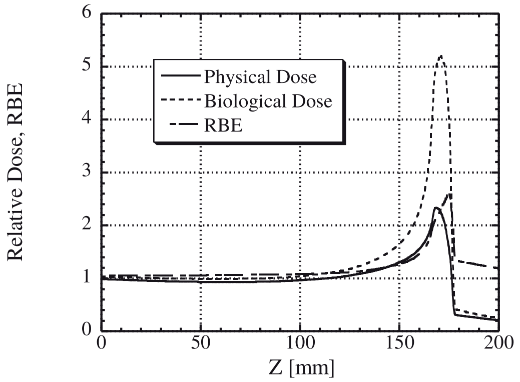

Figure 1.7: *Illustration of the difference between physical dose and biological dose, and respective RBE, calculated at the* 10% *survival level with a* ^{11}C *spot beam. Note the distal RBE increase*[Ura01].

Biological dependent quantities take into account all factors related to biological response to radiation that physical dose does not quantify, thus this weighted dose is often expressed in *gray equivalent* [GyE] units, or "RBE-weighted" [Gy (RBE)] ([IAEA–TRS–461]), its effect is illustrated in figure 1.7. Note that thoughout this work "Dose" will always refer to absorbed, physical dose [Gy], unless explicitly mentioned otherwise.

In figure 1.8, the clear advantage in using heavy ions instead of X–rays and protons can be appreciated. The latter exhibit RBE values of ∼ 1.1[Sui10] and therefore the same cell survival rate is achieved with less dose in the case of heavier ions.

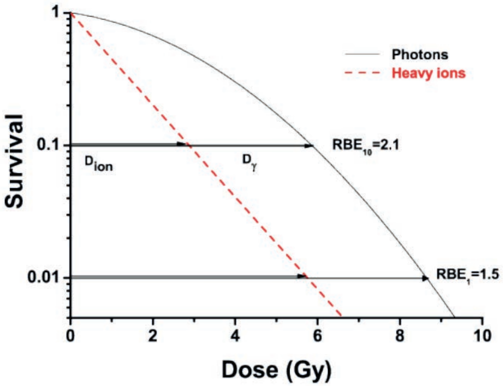

Figure 1.8: *Survival curves for heavy ions and photons*[SES10].

A typical endpoint for tumour killing corresponds to 10% survival. Cell survival — $\mathfrak{s}(D)$ evolution — in view of sparsely ionizing radiation's absorbed dose, can be described via the *linear quadratic model* as per [IAEA–TCS–42]

$$\mathfrak{s}(D) = \mathfrak{s}_0 e^{(-\alpha D - \beta D^2)}, \tag{1.21}$$

with α being the linear cell killing and β the quadratic cell kill specific coefficients, the latter less relevant for high–LET radiation. The former strongly varies as a function of LET *in vivo*, being the α/β parameter the value used to model cell survival[Sch14]. For densely ionizing radiation its tracks lead to an higher cell death rate regardless of the cell cycle, type, degree of oxygenation or repair capacity. It is commonly accepted that RBE increases with LET up to 100 [keV μm^{-1}], then for too high LET a saturation level occurs, an effect denominated *overkill* decreasing the RBE value.

The *local effect model* (LEM), developed at GSI, is a model presently in its fourth version employed to estimate biological damage due to cell killing by ions, it does so considering: the energy deposited by the radiation type; microscopic dose distribution in the vicinity of ion tracks; cell diameter and its sensitivity to X–rays according to α/β parameters. Thus it allows for the prediction of RBE values in ion therapy[Mai10, SES10, Bau14].

The ion's RBE will be deeply influenced by the tissue type, ion energy and biological endpoint/ion beam characteristics.[Sch14]. Consequently, ions may not have favorable outcomes with all types of tumors and the outcome prediction should account for the cell type and traits (*e.g.* the biological cycle), the type of tumor and the response of healthy tissue in its vicinity[Sch14]. Finally, the fragmentation of the ion beam would lead to different RBE values to be evaluated for each of the species produced, increasing greatly the complexity of the problem[Mai10].

Ions' LET (and RBE) variations can be very sharp along the beam path, going from 0.15 [keV μm^{-1}] up to LET $>$ 100 [keV μm^{-1}] before the *Bragg Peak*[Ura01]. This contrasts with protons, whose LET varies between 0.4–16 [keV μm^{-1}]. For carbon ions, RBE variation spans from ~ 1 at the plateau, where healthy tissue is affected within repair threshold, to more than 3–4 at the peak (there are reports from 2.5–5), hence maximizing the effect on the tumor site, as observed in figure 1.7[Ter09, Moh17]. As a consequence, 1 Gy of ion dose translates into $\sim$ 3–4 Gy of a photon beam, and slightly less for protons.

For ions heavier than carbons, an high LET and RBE is observed already at the entrance, mitigating the treatments' efficacy. However, oxygen ions are expected to be more efficient against some radioresistant tumors. Ideally, a compromise should be sought by evaluating both tumor response and usage of high–LET radiation, in view of different tissues' regeneration capabilities. Eventually, different kind of ions could also be used according to their biological effectiveness and, in facilities such as HIT, this is technically feasible with protons, helium, oxygen and carbon ions, combining high–LET and low–LET ions[KMP12].

Despite extensive work *in vitro* (*e.g.* NIRS) and the LEM or other models development, it is extremely important to have *in vivo* data. For the moment, a conversion factor between absorbed dose and RBE–weighted dose is used for treatment planning and an optimal model is still to be found, with several alternatives under study[SES10].

Regarding tissues' response to high–LET radiation, it is under investigation in which scenarios "hypofractionation" is preferrable to maximize treatment's efficacy, as well as the possible advantages of using different ions[Sch14, Ina17]. Clearly the high effectiveness of heavy ions open the possibility of "hypofractionation", ideally enabling a reduction of treatment time for some cancer types, with at least an equivalent treatment efficacy[TK12]. While conventional fractions will account for 1.7–2.1 Gy (RBE), "hypofractionation" will attain 3–14 Gy (RBE)[Sui10]. Another possible advantage of "hypofractionation" is the reduction of operational costs, in view of higher number of patients per year[Sch14].

For such evaluation, it is important to assess the outcome of different clinical protocols with ions and protons, the effects of OER, as well as other biological variables (*e.g.* glucose, iron metabolism)[Sch14]. This should be pursued in such a way that a cost *vs* benefit and treatment efficacy record history can be properly established, according to standard protocols[Sui10, Kam15].

So far, clinical outcomes of carbon ion beam facilities in Japan and Germany have been very promising [Ter09, TK12, Ohn13, EK16, Moh17]. The experience with high–LET radiation is expected to lead to an international consensus for converting physical into biological dose, assessing both deterministic and stochastic effects, especially important in ions[Sch14]. Finally, the study of steep RBE variations, cell survival rate and the improvement of biophysical models along with the assessment of tumor types and response, would be helpful to define the treatment approach, including "hypofractionation" effectiveness[Ohn13]. Overall, these studies have also opened a gateway to the therapeutic application of other ions species[Kit10].

1.1.3 Hadrontherapy with radioactive ion beams

Due to ions' favorable energy deposition profile, their clinical efficiency could be improved if optimally exploited. Still, entrance dose and the fragmentation dose tail, which is absent in protons, are limiting factors in clinical scenarios. At the entrance, heavier ions's RBE values are similar to protons but, because of fragmentation, the dose values may change according to the different fragments' biological effectiveness[Har17]. The fragments' energy transfer is much lower than the peak value, but still relevant considering that RBE could attain relatively high values in that region.

Even though ions are more hardly deflected in their paths than protons and consequently have better ballistic properties, their range uncertainties can have a more deleterious impact on the dose delivered to the patient in view of their enhanced biological effect and steep dose profile[Alo00]. This is a clear drawback in view of their suitability for treating deep–seated tumors or tumors located near sensitive organs, requiring an appropriate range assessment.

Overall, after dwelling over the physical and biological aspects of hadrontherapy, the three cardinal advantages of ions with respect to protons can be summarized as:

1. Less scattering and consequently better lateral dose profile while traversing tissue in depth;
2. Higher biological effectiveness, destroying cancer cells beyond repair threshold;
3. Sharper *Bragg Peak*, although with a "fragmentation tail".

However, the radiation from nuclear reactions involving the primary beam and its fragmentation products can be also useful. Since typically no primary beam particle emerges from the treatment in hadrontherapy, the detection of such secondary radiation will be the only source of information on the treatment effectiveness, during or afterwards. In fact, the β^+ emitter fragments produced by ions, prompt γ and even secondary protons, can still be used as peak's position indicator *e.g.* using a PET apparatus *in–situ*, to take advantage of the *autoactivation* of the beam through the β^+ emitting radionuclides generated by the impinging ions[Mac69, TCS71, Tob77, Eng92, Eng99, PE00, PEH2b].

The nuclei generated in fragmentation processes are generally depleted of neutrons, hence radioactive and decaying through either electron capture or positron emission[Tom03]. In fact, one of the leading fragmentation modes is the stripping of neutrons from the ion projectile. This occurs as a nucleus is "pushed" beyond the line of stability, increasing its proton–to–neutron ratio, originating a β^+ emitter (f_i). The latter emissions may contribute to the signals that can be of relevance for imaging characterization, as will be described later. Generally, the mixed field will mostly consist of neutrons, gammas and other light secondaries, proceeding from inelastic nuclear interactions and consequent fragmentation of either the projectile and/or target nucleus[Eng92, Tom03, Ina08].

Projectile fragmentation. As the chief mechanism of *autoactivation*, projectile fragments (*e.g.* p, He, Li, Be, B) are very energetic as they approximately inherit the primary particle velocity, and direction, at their current reaction point x_0. Due to the $R \propto {}^{A}\!/_{z^2}$[Eng92] relationship for equal velocity, they may travel longer distances than the projectile $(\mathfrak{p})$ *Bragg Peak*. If the interaction leads to a loss of neutrons in nuclei while not affecting the charge of the nuclei, a shorter range can occur instead[Som07]. Fragment's $(\mathfrak{f})$ stopping position will change in depth (x) due to variable impact points, along with energy losses in various interaction. Although this poses constraints on range monitoring with ions (*e.g.* for ^{12}C irradiation, ^{11}C and ^{10}C will come at rest before the *Bragg Peak*), it could be overcome using $RI\beta^+$, as it will be later described[Pa12a]. The number of β^+ emitters of a certain i^{th} type $(dN_{\mathfrak{p},\mathfrak{f}i})$, originating directly from a number of primary ions N_0 in a target $(\mathfrak{t})$, can be characterized at depth x by

$$dN_{\mathfrak{p},\mathfrak{f}i}(x) = N_0(x)\mathcal{N}_{\mathfrak{t}}\sigma\left[E_{\mathfrak{p}}(x), A_{\mathfrak{p}}, A_{\mathfrak{t}}, A_{\mathfrak{f}}, Z_{\mathfrak{p}}, Z_{\mathfrak{t}}, Z_{\mathfrak{f}}\right]dx, \tag{1.22}$$

where $\mathcal{N}_{\mathfrak{t}}$, σ, A and Z denote the number of target nuclei in volume, partial cross section for projectiles of energy E at depth x, mass and atomic number, respectively[Ina05]. On the other hand, the stopping position of these fragments will depend on the range of these fragments $(R_{\mathfrak{p},\mathfrak{f}i})$, after the reaction point x_0, and can be described as

$$R_{\mathfrak{p},\mathfrak{f}i} = x_0 + \int_0^{E_{x_0}} \left(\frac{dE}{dx}\right)^{-1} dE, \tag{1.23}$$

with E_{x_0} being the initial energy at the reaction point, the average overall stopping position $x_{\mathfrak{p},\mathfrak{f}i}$ will be then approximately given as a result of $x_0 + R_{\mathfrak{p},\mathfrak{f}i}$[Ina05]. For the β^+ emitter production through projectile fragmentation, ion beams with $Z \geq 5$ are required.

Target fragmentation. It consists of the nuclides which will travel very short distances, being thus indicators of the interaction location and the only mechanism responsible for β^+ emitter fragments production in therapy with ions with $Z<5$[Fie06]. If $dN_{\mathfrak{t},\mathfrak{f}j}$ is the number of β^+ emitters of certain j^{th} type, then their evolution in depth x is given by

$$dN_{\mathfrak{t},\mathfrak{f}j}(x) = N_0(x)\mathcal{N}_{\mathfrak{t}}\sigma\left[E_{\mathfrak{p}}(x), A_{\mathfrak{p}}, A_{\mathfrak{t}}, A_{\mathfrak{f}}, Z_{\mathfrak{p}}, Z_{\mathfrak{t}}, Z_{\mathfrak{f}}\right]dx. \tag{1.24}$$

However, please note that besides the production ascribed to the primary ion beam described in equations 1.22 and 1.24, secondary particles could also further induce β^+ emitter production in tissue[Ina05].

β^+ emitters. Such species, some highlighted in figure 1.9, decay through the following mechanism, denominated β^+ decay:

$${}^{\mathrm{A}}_{\mathrm{Z}}X \longrightarrow {}^{\mathrm{A}}_{\mathrm{Z-1}}X' + \beta^+ + \nu_e + Q_{e^-}.$$

In the above reaction, X denotes the parent nucleus, usually a neutron deficient radioactive nucleus, while X' is the daughter specie, in which a proton was converted into a neutron[Cur34]. The β^+ and ν_e are the ejected positron and electron neutrino, respectively. The latter is required for lepton number and momentum conservation. As for Q_{e^-}, it denotes the energy required to expell an extra orbital electron, to compensate for the positive charge lost[Bai05]. The β^+ is emitted with a continuous spectrum of energies up to a maximum *endpoint* energy, depending on the differences in atomic mass of parent and resulting isotope excited levels[SF02, CD06].

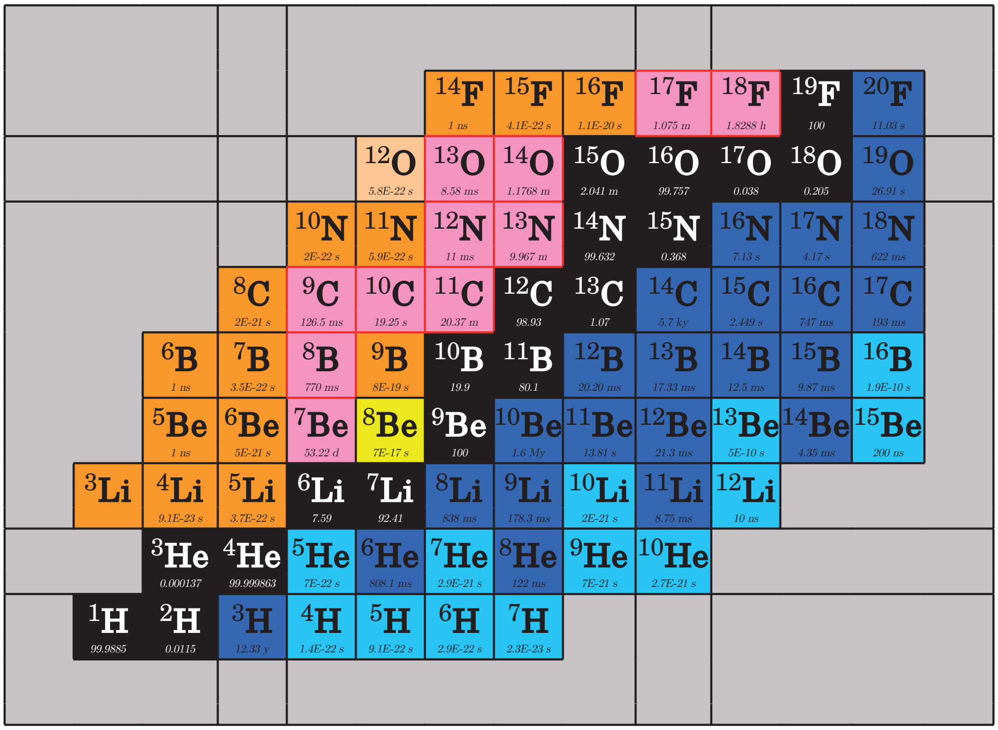

Figure 1.9: *Adapted chart of nuclides with the β^+ emitting isotopes coloured in pink and outlined in red ([IAEA–NDS]).*

Irrespective of the parent isotope, the positron emitted will annihilate with an atomic electron within few mm in range, upon exhausting its kinetic energy. At such point, it will capture an ambient electron, forming instantaneously ($\sim 10^{-10}$ s) a bound state named *positronium* that will annihilate shortly afterward. A *positronium* has two configurations, *ortho–* or *para–positronium*, with spin values of 1 or 0 and half–life in vacuum of $\sim$ 140 ns and $\sim$ 0.125 ns, respectively. The *ortho–positronium* formation is more probable (75%) but due to its much longer half–life compared to the *para–positronium*, the latter ends up being the dominant form annihilating by swiftly interacting with an atomic electron. Since the *positronium* rest mass is $E = 2m_ec^2$ and its momentum approaches zero it will typically generate two 511 keV photons travelling in approximately opposite directions ($\sim 180 \pm 0.5°$) if in the *para–positronium* form, as described in figure 1.10. Alternatively, other decay configurations with at least three photons emitted for *ortho–positronium* are also possible, although highly unlikely (0.003%)[Bai05]. Coincidence photons are neither exactly opposing nor energetically similar due to the shell electrons having a significantly higher momentum than the positron, which typically reaches thermal energies at the annihilation moment[Böh12].

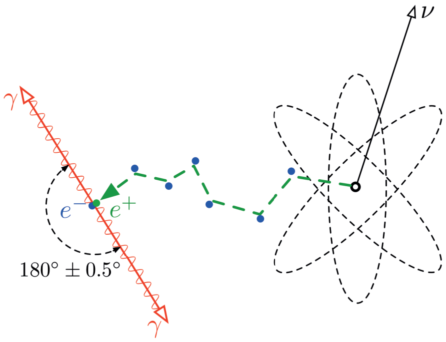

Figure 1.10: *Illustration of a positron emission and respective annihilation*[Lan08].

RIβ^+. In a stable ion beam irradiation, the range of β^+ emitters does not coincide with the projectiles' and therefore with the *Bragg Peak* due to the interplay between electromagnetic and nuclear processes[Pa12a]. Therefore, the estimation of beam range or dose delivered via the β^+ emitting pattern will not be straightforward, with uncertainities being a major concern[Pri08, Pri12].

Remarkable technical advances in computational, accelerator and detector physics, as well as imaging techniques in the past decades, have drawn attention to additional types of ion beams, including radioactive ones. If a projectile is itself a β^+ emitter, its range would be more easily pinpointed via its decay emission, with variations only due to range *straggling* and the β^+ endpoint energy. Consequently, the total number of β^+ emitters produced (P) at depth x can then be estimated for β^+ emitting projectiles as a result of:

$$P(x) = N_0(x) + \sum_{j=1}^{J} N_{\mathfrak{t},\mathfrak{f}j}(x) + \sum_{i=1}^{I} N_{\mathfrak{p},\mathfrak{f}i}(x), \tag{1.25}$$

whereas for stable ion projectiles, the final stopping place of the projectile does not coincide necessarily with that of the β^+ emitter[Ina05]. In this latter case, only two contributions are then considered, namely:

$$P(x) = \sum_{j=1}^{J} N_{\mathfrak{t},\mathfrak{f}j}(x) + \sum_{i=1}^{I} N_{\mathfrak{p},\mathfrak{f}i}(x). \tag{1.26}$$

The β^+ emitter target and projectile fragments contributions to the number of β^+ emitter produced are denoted by $N_{\mathfrak{t},\mathfrak{f}j}$ and $N_{\mathfrak{p},\mathfrak{f}j}$, respectively. In equation 1.25, N_0 refers to the additional contribution from the β^+ emitting beam particle. At the primary ion stopping position this aforementioned contribution is therefore of major relevance. If a proton or a light ion ($Z < 5$) is being used, the only contribution to the overall production in equation 1.26 will be limited to the first term, since no β^+ emitter projectile fragments will be produced as one can see from figure 1.9.

By combining the advantageous ballistic and tumor destructive properties of some ions with their imaging potential, the treatment efficacy could therefore be greatly improved[Ina05, MAT14, Kat15]. These aforementioned characteristics are combined if one considers a β^+ emitter radioactive ion beam. The annihilation event distribution will derive not only from the β^+ emitting fragments produced in fragmentation but rather it will be strongly dominated by those of the beam particle (as illustrated in figure 1.11), putting the *Bragg Peak* into evidence. Notwithstanding this, their dosimetric advantages are expected to be comparable to the stable counterparts.

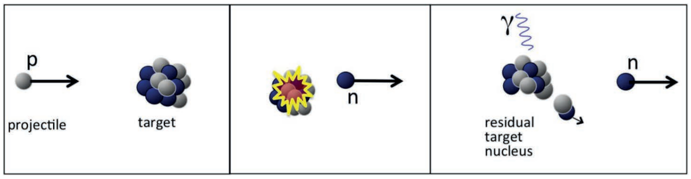

(a) proton

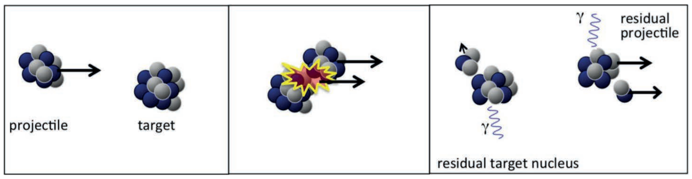

(b) stable ion

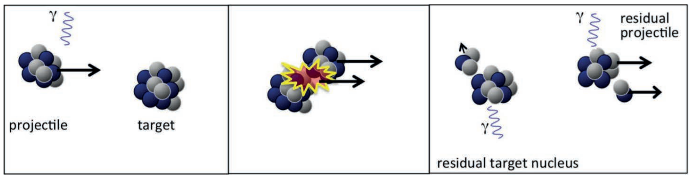

(c) radioactive ion

Figure 1.11: *Illustration of signal emission from residual projectiles with respect to different projectile types*[Kr15b]*, modified from the original with the inclusion of the bottom panel for* $RI\beta^+$.

Presently, in hadrontherapy, *autoactivation* β^+ emitter yield is relatively low and further reduced by physiological effects, typically being about two orders of magnitude lower than in diagnostic nuclear medicine, where it often reaches 50 [kBq cm^{-3}] at peak values[Bis17].

It is therefore clear that the clinical advantages of ion beams are only fully exploited if the uncertainities related to dose delivery and range estimation are overcome. Using $RI\beta^+$ as projectiles, and provided these species' half–lives allow an efficient usage in clinical practice ($t_{1/2}$ at most few minutes), the PET signal acquisition can be boosted, by enhancing the β^+ activity levels in the region of interest and thus improving the imaging quality.

The imaging potentialities of $RI\beta^+$ beams were recognized as early as late 70's at LBNL, and identified as a technique that could bring advantages to image guided radiotherapy, either to measure beams' range to be subsequentially used in treatment planning, as probes, to assess the beam range during treatment or monitor metabolic processes over time[Lla79, Cha81]. The enhanced signal rate achieved with $RI\beta^+$ could also compensate for the deterioration due to metabolic effects with respect to stable projectiles[Alo00]. However, these trials were made with low dose schemes and therefore faced insurmountable technical challenges such as diminished β^+ emitter signal with respect to background from detector activation. Even though results were promising, going as far as including the beam range monitoring in a living dog, research stopped with the BEVALAC's physics program shutdown in 1992[Lla84, Alo96].

The interest in this topic was, however, not lost. Studies were carried out at GSI in the 90's, using secondary RIB[Eng92, Paw96] and at HIMAC since early 2000's, with experiments in imaging and range verification[Sud00, Kan02, Ina05]. These studies concluded that signal from doses as low as 10 mGy could lead to range monitoring results within 1 mm, while peak doses of 96 mGy (RBE) rendered range uncertainities to as low as ±0.3 mm in a 15 cm diameter homogeneous PMMA phantom. The use of ^{11}C and ^{10}C as probes was also investigated, with *in situ* signal detection, just prior to treatment with ^{12}C[Ise04]. More recently, tests highlighting the possible advantages in using ^{15}O for imaging gain and efficacy in treating hypoxic tumors have been carried out[Moh16]. All studies so far performed with $RI\beta^+$ have indicated a potential advantageous effect in treatment quality by allowing the tracking of the beam in a more efficient manner[Kit06]. However, it remains still challenging to produce, accelerate and deliver those beams with clinical standard quality[MAT14, Aug16].

1.1.4 Positron emission tomography

PET designates a nuclear medicine imaging technique characterized by the indirect detection of β^+ emitting radionuclides, through their annihilation coincidence photons, and subsequent computation of a digital image representing the distribution of β^+ emitter activity[Tur11]. It is now well–established and characterized by a relatively high efficiency, high sensitivity even with nanomolar concentrations, relative non–invasiveness and a 3D imaging capability. PET has a broad range of applications, due to β^+ emitters from low–Z radionuclides that take part in metabolically relevant processes. Recent research has focused either on brain related pathologies (*e.g.* Alzheimer and Parkinson) or pinpointing cancer tissue locations in the body.

Since the first PET prototype, dating from 1975, the technique underwent many conceptual changes, leading to the modern PET design and functional specifications[Phe75, Zan04]. In its currently most widespread form, denominated PET/CT scanning, it consists of both a PET and CT scanners mounted in series (see figure 1.12-a), each with their respective field of view (FOV) and with images coregistered[Bey00, To08a]. It was originally developed in the United States, in 1998 and became commercially available in 2001, quickly replacing standalone PET solutions[Bey04, To08a, To08b]. The "fused" PET/CT concept allows the visualization of the inner body structure and, at the same time, identify the approximate location of positron annihilation, further improving the imaging accuracy[Bey00, To08b].

The major advantages in having the tomographs integrated in a single system is the needlessness of patient repositioning at a different device and that it allows CT images to be used for the attenuation correction of PET data. The need for these corrections derives from linear attenuation coefficients, that are measured with CT for the x–ray energy range (80–140 keV) and must be readjusted for γ (511 keV), allowing for a quantitative assessment via PET imaging[CD06].

Currently, PET/CT scanners are manufactured by five companies: *GE Healthcare, Hitachi, Philips, Toshiba* and *Siemens.* Among these, one can highlight the state of the art models *Siemens Biograph m*CT, *Philips* Gemini series and *GE* Discovery series. For the PET image reconstruction simulations in chapter 5, the *Biograph m*CT (TruePoint TrueV option) was modelled, in an attempt to reproduce possible PET acquisition scenarios[STP08]. Its parameters are included in the appendix.

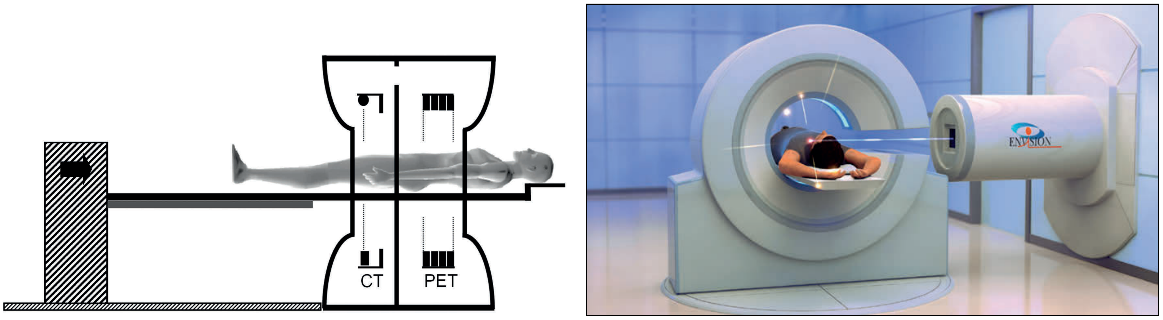

(a) (b)

Figure 1.12: *PET/CT scanner schematic, adapted*[To08b]*, in a common gantry and with a single patient couch (a). Artistic depiction of an in beam PET acquisition scenario (b)* [*ENVISION*].

PET role in Hadrontherapy. In recent years, imaging techniques that are PET–based have improved greatly, benefiting hadrontherapy and the development of online, *in situ*, treatment monitoring modalities. These are considered as very advantageous in view of the fact that *autoactivation*'s signal does not entail extra dose to the patient. At the moment, it is the most extensively clinically investigated technique for treatment monitoring and range verification in proton and carbon ion therapy.

Upon ion beam irradiation, two signal components can be distinguished, namely a prompt component, originating from nuclear reactions in a sub *ns* time scale, including photons, hadrons and leptons (*e.g.* prompt γ in the 1–10 MeV energy range) and a decay component with radiation emissions due to radioactive isotopes (*e.g.* β^+). In the latter case, the signal quality will depend on the amount of radioactive species', their half–life and β^+ range.

Additionally, PET can be exploited in diagnostic applications in a 4D framework, studying the tracer dynamics in time. In a hadrontherapy context, this allows for the characterization and follow up of lesions related to treatment. This feedback could be used to improve the target definition as a function of organ motion and even to refine the treatment approach in view of the irradiation consequences' effect, ideally, in real time. This is the main principle behind *in vivo* beam range verification, to ensure tumor–dose conformality and thus maximize hadrontherapy treatment success[Vyn93, OLA96, PE00]. A very promising technique to accomplish treatment monitoring and confirmation is to use PET–based systems *in situ* and fully integrated with the beam line as depicted in figure 1.12-b, denominated *in beam PET*[Paw96, En04a]. This method will be mentioned in greater detail in the next section.

PET/CT Scanning. Scanning procedure starts with the CT being used to computerize and assemble a picture of the target zones from X–rays data for anatomical information, within seconds. In this process, whole body effective doses within 20 mSv can be delivered, although for correction/verification purposes the exposure is lowered down to 3 mSv[To08b].

A PET scan will consist of the collection and reconstruction of 511 keV coincidence γ, produced in the annihilation events. After escaping the body these signals can be detected by the PET scanner, typically a cylindrical assembly of crystals, within an (ideally short) time and energy coincidence windows[Bey04].

An electronic apparatus will register a coincidence trigger whenever signals are detected in opposing coincidence detectors. This results in the establishment of a line of response (LOR), and throughout the PET scan time these will map the activity density of β^+ emitter nuclei, particularly in range. By collecting all the identified LORs, a projection of the activity distribution is obtained in 2D, or 3D if the projections are obtained at different angles[Zan04, Fah02].

Three major types of events (see figure 1.13) will contribute to the overall coincidences acquired, depending on the experimental conditions, namely true (T), scattered (S) and random (R) coincidences in PET imaging:

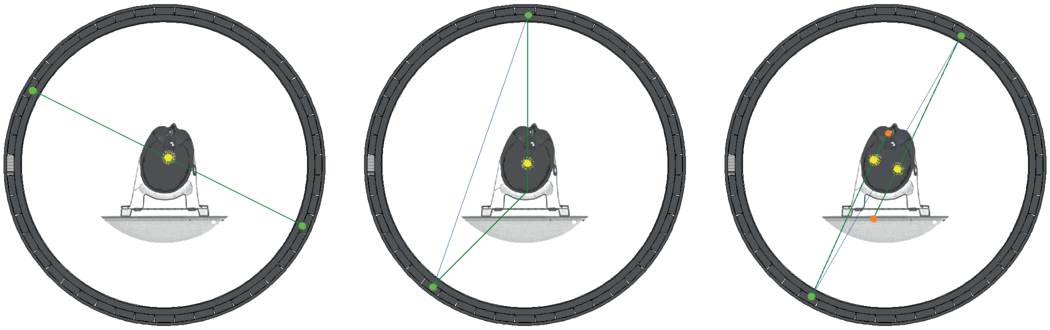
(a) True coincidence (b) Scattering coincidence (c) Random coincidence

Figure 1.13: *Scheme illustrating true, scatter and random coincidence detection within a coincidence window.*

Scattering coincidences share a common annihilation event but it does not lie within the LOR. Their occurence is intrinsically connected to the PET design and sensitivity, as well as the patient geometry, its body size and consequently attenuation chiefly via *Compton scattering*, being mostly constant throughout the acquisition time[Tur11].

Random coincidence events do not share the same annihilation event and are more affected by the beam microstructure in hadrontherapy scenarios, detector dead time and shifts in energy peaks. Their mitigation often implies a non trivial fine–tuning at instrumentation level (*i.e.* fast–response electronics). Reduced dead time and a delayed coincidence timing window, along with an optimal energy resolution window, contribute to the further reduction of random events.

Lastly, the true event rate is calculated from the subtraction of both scattering and random events to the total coincidence event rate. Among the true event rate, there may be also "spurious" true events, arising when a non coincidence photon interacts with a PET crystal within the coincidence time window of another photon proceeding from an actual annihilation event, but in which one element of the pair was attenuated or escaped the system. Also, there might be multiple coincidences occuring, in which case the position cannot be retraced, and the events should be discarded[CD06].

3D PET is now widely disseminated for its better performance than 2D PET in scenarios with lower counts and short acquisition times. It uses all rings for reconstruction, increasing almost fivefold the true detection sensitivity, albeit with an increase of complexity and background noise, particularly from scatter coincidence events[Tur11].

For these scanners, true and scatter coincidence rates vary linearly with activity, whereas random coincidence events do so quadratically, so more signal does not necessarily correspond to a better image[Zan04]. Consequently, a PET scanner performance is maximized by both higher count rates and lower noise from background ($R+S$) events[Tur11]. The noise equivalent count rate ($\dot{\mathcal{N}}_{eq}$), a parameter used to assess PET performance in view of the different types of events detected, is defined as

$$\dot{\mathcal{N}}_{eq} = \frac{T^2}{S+T+R}. \tag{1.27}$$

The maximum value of $\dot{\mathcal{N}}_{eq}$ corresponds to a particular scanner's optimized count rate[Tur11]. Such optimization can entail the use of simulations to understand the influence of different physics mechanisms involved in background coincidence generation and maximize the true count rate[Hir14, Poo15].

Noise is of particular relevance for *in beam PET* if not properly mitigated, as this technique sees a high rate of secondary particles that can affect image quality, as their LOR will not coincide with the annihilation site. Noise will originate from single counts, neutron induced events and the overall γ–ray background, along with the activated detector itself[Hir14].

PET image reconstruction Whole body imaging requires either the use of multiple detector rings for a 3D assessment of β^+ activity distribution or using multi–ring, septa separated, 2D PET, in which coincidences are compiled from a limited ring number. The former type is characterized by a larger solid angle and higher amount of true coincidences, but requires a more challenging image reconstruction procedure.

The acquired raw data, consisting of coincidence event counts and respective LOR, is typically stored in either lists or *sinogram* format[Def97]. The count number assigned to a LOR is proportional to a line integral of the β^+ activity along that LOR. It corresponds to a 2D matrix in which line integrals are arranged in parallel subsets, each representing a projection angle as a row in an image. Every LOR is identified as a specific pixel, whose value is incremented everytime a detection occurs. In the end, the *sinogram*'s pixel value will actually indicate the number of coincidence detections between the detector pair of the respective LOR[Fah02].

In list mode, a coincidence is recorded individually, preserving both time and spatial information of LORs. Conversely, a *sinogram* representation is obtained within a certain time interval. Thus, the former allows for greater flexibility in image generation but requires handling large datafiles. *Sinograms* are much lighter, but lack temporal and spatial resolution information.

For image reconstruction, one can resort to analytical (*e.g.* FBP) or iterative methods (*e.g.* MLEM), in which algorithms are employed to extract *sinogram* data in cross sectional images with the β^+ activity distribution[CD06, Tur11]. Subsequent normalizations can be applied, as corrective measures related to scanner specific parameters (*i.e.* efficiency) and to convert count rate into β^+ activity values. Also, the CT scan can be used to estimate attenuation and scatter corrections, so that a quantitative result is obtained while highlighting physiological information[Fah02, Zan04].

PET scanner characteristics. The detector in a PET scanner typically consists of scintillator materials transforming the coincidence signals into optical photons (≈ 1 eV), using photomultiplier tubes or the more recent avalanche photodiodes and silicon photomultipliers to convert these scintillation photons' into electronic signals. The detector material should be characterized by a high photoelectric effect cross section for 511 keV photons, high absorption (high Z and ρ) and efficiency (low dead time) with high light output yield in short time intervals. However, no material excels in all these aspects, for instance absorption is relatively high for *Discovery*'s BGO, while the luminosity for *Biograph*'s LSO can achieve values as high as 29 photon/keV, with a 40 ns decay constant. Also

GSO, in some versions doped with zirconium, and *Gemini*'s LYSO are other commonly used PET scintillator materials[Bai05, To08b, Hir16].

PET systems are in continuous evolution as the demand grows for higher sensitivity, and spatiotemporal resolution, properties that depend on crystal material and electronics. The sensitivity of a scanner is typically improved by increasing the scintillator thickness and density, providing more detector material, or extending the FOV.

Generally, photons will take few ns to reach the detector and their time–of–flight (TOF) will depend on the annihilation position along the LOR. An optimal time resolution requires both fast electronics for signal processing and low scintillator material decay time varying within 10–100 ns[Zan04]. The availability of LSO and LYSO materials with low coincidence timing resolution ($\lesssim$ 450 ps) led to TOF–PET, an enhanced PET modality which allows a more direct pinpointing of annihilation event location by calculating the TOF difference between the annihilation photons[Lop16]. This modality is featured in commercial *Gemini TF* and *Biograph* scanners, the latter attaining time resolutions lower than 500 ps and coincidence timing resolution of 4.1 ns[STP08]. This information can then be implemented in the PET reconstruction to improve the image quality[To08b].

Spatial resolution of a PET scanner, on the other hand, is instrinsically limited by two factors: the β^+ *endpoint* energy, which depends on the isotope, and the photon pair non–collinearity, technically limiting resolution to at least 1.5 mm and resulting in a blurring effect that is more relevant for larger diameter PET rings[CD06, Zan04, Bai05]. Presently, PET/CT systems spatial resolution varies slightly among different PET scanners, achieving $\sim$ 4.2 mm transaxially/axially for *Biograph mCT* and slightly higher values for *Gemini TF* and *Discovery STE*, but it can reach values as low as *circa* 2–3 mm using point spread function information.

1.1.5 Dose delivery and overview of range monitoring techniques

While intensity modulation of photon beams typically uses beamlets from different directions to target the tumor (IMXT), it still produces high entrance and exit dose levels. Intensity modulated particle therapy (IMPT) with charged hadrons allows for higher levels of dose conformity and homogeneity, achieved even within a single field SOBP[Krä00, Sui10]. A SOBP takes the shape of a dose "plateau" instead of a single peak, as in figure 1.14, allowing for the targeting of deep–seated tumours. The final shape is achieved throughout the use of multiple pristine *Bragg Peaks* of different energies, with overlapping dose profile leading to the delivery of high levels of dose along a given depth. As for the dose values, they are modulated by each peaks' intensity, their cumulative effect resulting in the aforementioned "plateau" shape.

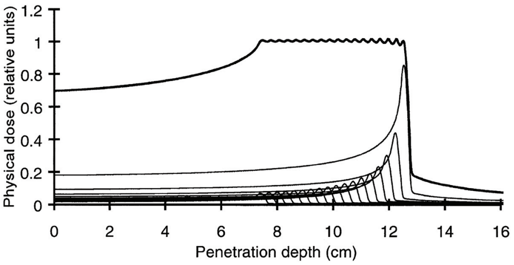

Figure 1.14: *Depth dose distribution of charged hadron beams in the form of a SOBP resulting from the cumulative effect of 18 different pristine Bragg Peaks*[Pin14].

The range of each particular beam can be set directly at accelerator level or by moderating the beam with attenuators, so as to target the tumor in depth. Range can be defined down to sub–mm accuracy in well defined media in quality assurance (QA) scenarios. However, in patients, multiple factors will add up to the range uncertainities, which should be addressed with mitigation strategies, particularly in the presence of OAR in the vicinity of the tumor[Pri12]. In fact, range uncertainties may amount to as much as 3.5% of the prescribed range +1 mm for protons, as reflected in MGH safety margin protocols[Pag12]. For this purpose, the use of gantries to deliver the beam from multiple angles is highly desirable to further ensure conformity to tumor volume. These gantries are equipped with a nozzle at their end for beam shape and monitoring.

The quality of the dose delivery in range will be affected by the beam energy spread, *straggling*, patient biological factors, CT QA and RBE variation. In practical terms, the range is defined at the *Bragg Peak* curve distal fall off to 80% of its maximum for a pristine *Bragg Peak* and 90% for a SOBP. Furthermore, a detailed knowledge of the range of different ions and subsequent *Bragg Peak*, as a function of energy, is relevant in order to evaluate SOBP biological dose delivery and treatment efficacy[Sui10].

Treatment Planning. Treatment planning and simulation consist of using an "inverse plan optimization approach", as it starts by defining a set of constrains that need to be fulfilled with an optimized procedure, iteratively[PMS13]. In hadrontherapy it includes ideally the following steps:

1. Anatomical imaging acquisition fused with tomographical information using MRI and/or CT. This generates a digital model of the region to be irradiated. Raw CT data, without enhanced contrast, will essentially represent the density of electrons in tissue.

2. Definition of tumor's dosage and fractionation plan. Also, boundary limits and OAR tolerances for irradiation by clinical practitioners are then set, corresponding to the regions of interest to be targeted and/or spared by the beam.

3. Simulation reproducing both the patient and setup geometry. Diagnostic X–rays are used to pinpoint OAR. The optimal tumor targeting paths are then defined with respect to OAR in the vicinity. The absorbed dose to be applied is then computed in 3D, either in the CT directly or in water–equivalent coordinate system. Subsequently, if heavier ions than protons are being used, the biological effect in the tumor and healthy tissue in its vicinity needs to be evaluated using a radiobiological model.

4. The radiation treatment planning is then established if a clinically acceptable solution is found, accounting for the data from the previous step using: the TPS database, the clinical data and specific models and algorithms for RBE and dose conversion.

Hounsfield Units (HU) conversion protocols translate the CT results into a map of relative stopping power. Such protocols are based on CT scans of tissue/phantom materials with known density/elemental composition. The photon attenuation factor is expressed in HU, quantified via

$$HU = 1000 \times \left(\frac{\mu - \mu_{H_2O}}{\mu_{H_2O}} \right), \tag{1.28}$$

where μ_{H_2O} is the attenuation coefficient in water and μ the attenuation coefficient of the material. Once a stopping power ratio map is defined, a detailed plan can be calculated, typically iteratively. However, conversion errors may result in some millimeters uncertainities in range as reported for protons[Pag12].

Most comercial TPS are still based on fast–performing analytical pencil–beam dose calculation algorithms and range predictions using the water–equivalent's stopping power estimates from CT scan data (*e.g. Syngo PT Planning* from *Siemens*)[Pa12b]. These systems project ranges based on the water equivalent depth in the patient, nuclear reactions and scattering effects are therefore accounted for in water only and subsequent corrections are necessary for heterogeneities in the beam path[Pa12b]. Although the proton therapy mixed field is relatively less complex than that of heavier ions, the uncertainities deriving from heterogeneities (*e.g.* at bone/soft tissue interfaces, air cavities), as well as different I from tissues, may result in higher under–/over-dosage for protons due to their larger scattering[Sui10].

A more in depth evaluation of the biological and physical consequences ascribed to complex physical processes in hadrontherapy is indeed the major motivation for current ongoing work aiming at employing MC codes to aid inverse treatment planning[Krä00, Bau14].

Dose delivery systems. In hadrontherapy, dose should be delivered accurately and homogeneously to a target volume. Two methods, employing active and passive techniques are employed for that effect[Kit10]. The latter are simplier to implement, since they adapt the existing beam to the target volume, using[Sui10, SES10]:

- Beam–scattering – The lateral tumor outline is covered using double scatterers with an apperture. The range is modulated with ridge filters and/or a range modulator. In both ways an homogeneous SOBP with appropriate width and depth, is achieved. However, degraders such as ridge filters widen the physical dose distribution in range, but also laterally, requiring compensators which are patient specific. Distal conformity to the tumor often produces a proximal overdosage with this method.

- Layer–stacking – Similar to the above referred method, but it attains a better dose delivery "shaping" and consequently higher conformity to tumor's volume. Wobbling/uniform scanning is followed by further elements, such as rotating wheels of variable thicknesses for both range/shape compensation. Multiple SOBPs are then collimated and attenuated to comply with the tumor shape.

Passive methods tend to lose efficacy at the tumor's boundaries and have a more limited maximum range. Plus, the use of energy degraders lead to additional nuclear reactions, altered RBE values and produce secondaries such as neutrons that disrupt dose delivery/imaging quality. Additionally, vendor information may actually differ in the equipment provided, leading to additional uncertainties[Pag12].

On the other hand, active scanning techniques rely on magnetic steering of ion beams, possibly with different intensities and/or over other modulating devices, as well as energy modulation for a better conformity to the tumor. These can attain mm–level precision, without employing degraders and therefore with less debris production, allowing for a more accurate LET quantification. Beam targeting position is controlled transversally with a pair of dipole magnets and longitudinally through change of beam energy in steps[Bou08, Par10]. Two modalities are generally included in this method[Sui10]:

- Spot scanning: Achieves an uniform dose distribution employing multiple discrete dose spots of a particular energy/direction. After usage, a spot is switched off and both the scan magnets and the accelerator energy are adjusted for the next irradiation. It was developed in Japan but first clinically applied at PSI[Ped95].

- Raster scanning: Uses pencil beams to cover the tumors' volume in layers. Each layer corresponds to a particular energy, range and intensity in a certain area. It requires the beam to be scanned quickly transversally. This methodology was first developed at HIMAC, later being introduced at GSI and subsequently HIT[Hir90, Hab93].

An intermediate method between passive and active techniques, which will be here denominated semi–active, can be considered as well:

- Wobbling: Beams are scattered and then scanned magnetically in predefined paths, without intensity modulation but with varying energy. It was first developed at NIRS[Sui10].

Despite the favorable evolution of dose delivery accuracy, its adaptation to dynamic patient target volumes is most desirable to ensure precision treatments. In clinical usage, adaptive radiation therapy (ART) denotes the adaptation of dose delivery to tumor changes during treatment session or throughout the whole treatment (*e.g.* tumor shrinkage/regression; weight loss/gain; interference of cavities and respiratory motion of organs).

As these anatomical changes may result in range uncertainties, the TP should be updated accordingly and often CT rescanning would have to be performed. This approach is made possible by technological advances which can be put into effect at TP level for a more efficient treatment.

Range verification in hadrontherapy. In the framework of hadrontherapy, getting information from irradiation effects is limited by the fact that the beam is stopped inside the patient. Therefore, only secondaries can be used for obtaining information on the treatment, via imaging[Kr15b]. Range verification techniques require radiation dose calculations, and (ideally) MC to describe dose delivery and nuclear fragmentation. This is highly desirable in the context of IMPT, where the consequences of over/under shooting are more drastic than in conventional IMRT, even if properly fractionated. Furthermore, it allows feedback upon variations detected by imaging in the TP. This can eventually lead to a more efficient exploitation of charged hadrons' advantageous dose delivery, a better monitoring and confirmation of treatment.

Ideally, the consequences of anatomical changes (*e.g.* position, motion) over the predicted dose and range should be assessed not only in between treatment fractionation (inter fraction) but during treatment (intra fraction), with *in vivo* range verification and dose monitoring. The two most promising beam delivery monitoring techniques currently exploit the detection of:

β^+ **emitters** – Employing PET–based solutions (*e.g. in beam PET* and *offline PET*), as well as planar positron cameras[Paw96, En04b]. The use of a commercial PET scanner implies having the patient moved, after treatment, in a different room (offline) or in the same room (*in–room PET*), which can lead to significant signal losses[PBH08, Kr15b, Bis17]. *Offline PET* solutions have as major disadvantage the need for a relatively long acquisition time after beam delivery and consequently degradation caused by physiological/metabolic effects, as well as a non–linear correlation between signal and delivered dose[Par04]. Contrary to commercial PET scanners, *in beam PET* solutions can be used *in situ* during or after irradiation. However, for planar positron cameras this can imply the loss of 3D imaging capability and more complex image reconstruction techniques[PEL03].

Prompt γ – Originating from the de–excitation of target nuclei along the particle path or from the projectile itself. These γ rays are characterized by energies up to *circa* 10 MeV, yields of 10^{-4} photons per primary carbon ion and ten times less for primary proton are produced almost instantaneously (up to few ns) during the irradiation, theoretically overcoming some of the inherent limitations of the PET technique[Kr15b]. The use of this radiation in monitoring is enabled by correlating the fall off of the dose distribution with that of γ emission typically detected at 90º from the beam direction[Ag12a]. Several detectors have been developed for hadrontherapy monitoring, since standard Single Positron Emission Computer Tomography (SPECT) is unsuitable for such high photon energies[BMM16]. Some of these detectors include collimated gamma cameras in various geometries and functional forms[Rob13]. Despite that, prompt γ detection is still challenging and considerably affected by the high background from neutrons and delayed photons, requiring complex detector customization[Pol14].

Additionally, studies were also conduced on secondary charged particle detection[Ag12b] and ion radiography and tomography[Par14]. Although these are easier to detect than neutral particles, the scattering and energy loss will affect signal acquisition, making it difficult to establish a correlation between the measured secondary charged particle profile and the primary beam range[BMM16].

Although recently prompt γ clinical use has been reported[Xie17, Ric16], PET–based techniques are still the most investigated method for *in vivo* range verification and treatment monitoring[CSE06, Bau13, Kr15a]. Nevertheless, PET techniques clinical use is limited to retrospective information after fraction delivery due to the high background during irradiation, this also implies loss of range information if multiple treatment fields are employed[PBH08, Com12].

As already mentioned, dose deposition is chiefly ascribed to electromagnetic interactions with tissues' atomic electrons. On the other hand the β^+ activation profile derives from delayed emissions from the decay of unstable nuclei formed by nucleon–nucleus or nucleus–nucleus interactions. As these species, resulting from the beam interactions, have different ranges, their contribution will not reflect exactly the positions of the dose distribution directly at the *Bragg Peak*, as illustrated in figure 1.15 for carbon ion beams and protons.

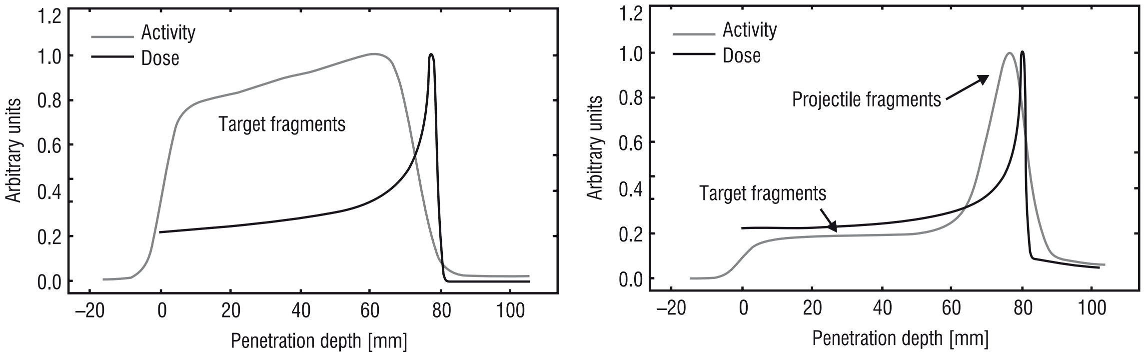

Figure 1.15: *^{12}C (212.12 MeV/u) and proton (110 MeV) pristine Bragg Peak measured β^+–emitter activity in depth in PMMA, on the right and left side, respectively. The calculated dose distribution is shown in dashed lines*[Pa12a].

The detection of β^+ activity is a particularly important topic in ion therapy since the activity levels are generally lower, by a factor of 2–3 orders of magnitude, than in nuclear medicine PET applications. The use of carbon ions implies even less PET statistics than protons, as it induces activities of *circa* 200 [Bq Gy^{-1} cm^{-3}], but the presence of projectile fragments (*e.g.* ^{10}C, ^{11}C) allows for a better spatial correlation between the *Bragg peak* and the β^+ activity fall–off at distal edge (see figure 1.15)[PEH2a, En04a, Par04, Ina08]. However the correlation is still not straightforward, especially if many different contributors are present or if the signal emitters decay significantly. Since protons, and in fact most particle beams with Z < 5, produce chiefly target fragments and lack β^+ emitter projectile fragments, range correlation is more challenging due to the lack of a distinctive peak along the particle's interaction trail, particularly at *Bragg Peak* (see figure 1.15)[Par04]. On the other hand, the activity induced by protons is 2–3 times higher than in carbon ion irradiations, reaching 600 [Bq Gy^{-1} cm^{-3}], and it is still possible to establish a correlation with the *Bragg Peak*, in a similar methodology as that applied to prompt γ[En04a, En04b].

Models are employed to estimate the magnitude and spatial distribution of those fragments, for instance based on the beam type and energy[PEH2b]. In clinical routine, this result is then compared with the reconstructed activity, with a strong dependence on the patient's CT, the TP and the time course of the irradiation and imaging. This methodology resulted in monitoring and QA of almost all GSI treated patients[Eng99, Par04].

Currently, it is envisaged that $RI\beta^+$ could provide a clearer correlation of dose and activity, as β^+ emitters will come at rest at the *Bragg Peak*.

Regarding the PET image acquisition methodology, it can vary greatly. For instance at HIT, PET imaging is performed in a different room, during the patient positioning it is expected that the tumor can be displaced[Bau13]. However, even when immobilized, if the signal acquisition time is long (*e.g.* 30 min), additional effects can disrupt the initial distribution of β^+ emitters, due to the *biological washout*, depending on the anatomical location. At the moment, *in beam PET* and *offline PET* experiments and clinical trials report 1– to 2–mm accuracy at best for verification of the beam range, provided no motion occurs and in favourable anatomical regions. As for *in room PET*, it reports *circa* 2–3 mm range differences between measurements and predictions[Min13]. Using online imaging information in a wider variety of clinical indications, the general goal is to achieve 1 mm of the lateral and range deviations from the planned treatment, considering the coarse resolution of PET. In this work the following PET data acquisition modalities are distinguished in figure 1.16[PBH08, Sha11, Pa12a].

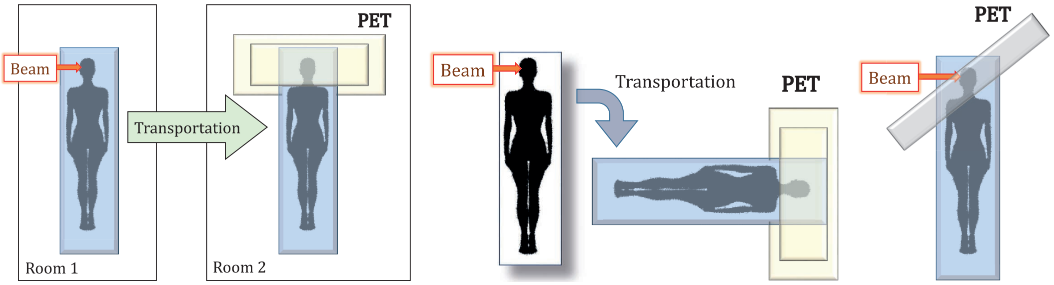

(a) *Offline PET* (b) *In room PET* (c) *In beam PET*

Figure 1.16: PET *imaging acquisition modalities.*

In beam PET. While commercial PET scanners can be used to detect coincidences after treatment with *offline* and *in room PET*, a part of the signal emitted during treatment will be lost in these modes. In view of this, it is highly desirable to have the scanner integrated with the beam line, to provide a deeper insight on the efficacy of treatment and monitoring irradiation effects (*i.e. in beam PET*) online or slightly after irradiation, without compromising much the treatment time by doing the acquisition *in situ*[PEH2a, PPE05, CSE06, PBH08, Pa07a].

By using *in beam PET* and *in vivo* range verification, one could get information on patient specific stopping power or low dose image guidance at the region of interest[Fie10, Pa12a]. This would open the possibility to adjust the treatment inter fraction (*e.g.* using probes), and even at some point during fractionated dose delivery, for range corrections as a function of mismatches detected against the plan. A disadvantage of using probes is that the incoming signal will be too weak due to the short irradiation time, requiring advanced detection and signal processing techniques.

However, if enough beam particles are delivered and the detectors efficiency is adequate, a valid signal could be acquired and processed with PET techniques, leading to a clearer assessment of dose distribution, and a more direct comparison with the prescribed dose in the TPS. Although studies with proton irradiations of PMMA phantoms denote a sub mm range monitoring accuracy[PPE05, Kr14a], the offline range monitoring in patients with protons reported deviations within 2.0 mm in between measured and calculated PET profiles in head and neck tumors, particularly in the presence of bony structures[Pa07b]. Online acquisitions are expected to benefit from the existence of short lived β^+ emitters, such as ^{8}B, ^{9}C, ^{10}C, ^{14}O and especially ^{15}O, whose production/position can be correlated with fragmentation and dose delivered in shorter time, mitigating the *biological washout* deleterious effect on imaging[PBH08]. Still, some organs, particularly those in the abdominal cavity, move as a function of the body position/breathing, along with blood flow or other metabolic elements. This affects the co–registering and CT stoichiometric calibrations for tissue classification in CT–based MC simulation of the expected activity patterns, being one of the main reasons limiting application of *in vivo* in humans[PEL03, Pa12a].

However, the most considerable drawback of these *in beam* solutions is the high integration cost, as they need to be custom made since they are not yet commercially available[Att09, Hir14]. Also, much effort is required in suppressing background and coping with the inherent angular detection limitation when resorting to dual–head configurations (figure 1.12-b). In fact, noise interference likely due to background radiation deterred the first prototype planar coincidence camera developed at LBNL from clinical application ([LBL77]).

Eventually, this limitation was overcome with BASTEI at GSI, consisting of dual–head positron camera integrated with the beam line for *in beam PET* imaging and treatment[Eng92, Eng99, Paw96, En04a]. It successfully correlated some β^+ emitters, particularly ^{11}C produced by fragmentation of ^{12}C, using MC calculations, later applying this information in clinical practice using *in beam PET* imaging for verification against MC calculations based on TP[En04b]. It was therefore the first example of *in vivo* verification procedures based on *in beam PET* and its clinical feasibility in reducing range uncertainities for carbon ions[En04a]. The scanner was essentially used to detect the distal edges of the irradiation, and verify the positions of air filled cavities, washout zones and bones based on the activity levels. PET monitoring was employed during treatment of more than 400 patients with carbon ion beams in head/neck and pelvic tumors between 1999–2008. A similar approach was followed for NCC Kashiwa but with protons, monitoring beam range or lateral position shifts[Nis06]. Notable research done by NIRS in Japan has focused on PET scanner development for *in beam PET*, aiming for range verification of $RI\beta^+$ probes with planar positron cameras[Kou98, Sud00].

More recently, integrated *in beam PET* solutions included (planar) positron cameras developed in Italy, one example being the INSIDE collaboration setup, envisaging (proton) treatment monitoring at CNAO[Bis17, Fer17]. Another example of recent *in beam PET* developments is the more complex full ring solutions, such as NIRS OPENPET prototypes, detailed later in this chapter and in chapter 5, which demonstrated the feasibility of signal acquisition from ^{11}C irradiation with a full ring PET[Yam08, Att09, Yos12, Tas12, Hir14, Yam17].

Online verification is technically very challenging as it requires the ring of detectors to be either opened or shifted so that the beam can pass through the ring in its way to the patient, losing detection efficiency with the reduced detection coverage and requiring often more complex image reconstruction procedures[CSE06, Sha11, An12].

Considering an 1 Gy irradiation, signal acquisitions with *online PET* and a synchrotron or cyclotron based facility, the former employs a pulsed beam and can typically deliver a field in 2–3 min, the latter in even shorter time (< 2 min) with a continuous beam. For synchrotrons, the chief requirements are still random coincidence suppression, which makes PET acquisition *in–spill* ("beam on") often deemed unfeasible due to high background (*e.g.* prompt γ, neutrons) affecting image acquisition quality and performance of some scanners[Sha11, Bis17]. On the other hand, *inter–spill* acquisition implies a loss of very short lived β^+ emitters, albeit dealing with less background[Hir14]. For cyclotrons, since it features a continuous beam, the acquisition will be affected by substantial noise levels (*e.g.* activated elements in the beam line). Noise effect mitigation and integration of the scanner with the beam line increase considerably the cost of these solutions.

Comparing with in room or offline acquisitions, typically starting 5 min after treatment and lasting for up to 30 min, and provided noise is mitigated, online acquisitions can attain even 10 times more signal than offline, provided the *in–spill* component is accounted for.

For the present work, *in beam PET* will refer to an *online PET* acquisition coinciding with beam time. However, whenever acquisition continues beyond the treatment time, as in the case of the approach at GSI, also lasting 40 s afterward or at the HIMAC's experiment described in chapter 5, without the patient/target being moved it will still be considered an *in beam PET* scenario, but not an *online PET* acquisition. Therefore, for the HIT–based simulations, performed for different PET acquisition scenarios in chapter 5, *online PET* acquisition refers to acquisition during beam time only. In addition to that, this work will consider that *online PET* includes the sum of *inter–spill* (in–between spills) and *in–spill* (during spill) as acquisition's sub–modalities. Later in chapter 5, this distinction will be employed to investigate whether the use of $RI\beta^+$ could potentiate acquisitions in *in–spill* or *inter–spill* acquisition scenarios.

In room PET. An immobilized patient is moved few minutes (~ 2.5 minutes) after treatment to a PET scanner, located in the same room where irradiation occurs[Zhu11, Min13]. It is preferable to do so mechanically and with computerized precision, avoiding patient re–positioning. Furthermore, the performance can be enhanced using a mobile PET/CT scanner, avoiding errors due to the co–registration between the CT scan taken for TP's CT and the PET images' CT. Its merit compared to *in beam PET* technique lies in the balance between decay effect and acquisition efficiency gain. It greatly benefits from the possible use of commercial PET scanners, meaning a full ring can be applied and few minutes suffice for an acquisition, the maximum acceptable time allocated for an in–room measurement generally corresponds to one field's irradiation time, or ~ 3 minutes, which does not delay greatly the image acquisition time[Zhu11, Sha11]. There is also an economical impact associated with the required access control/interlocking, extra space and all software guaranteeing movement precision, but much lower than *in beam PET*[Sha11].

On the other hand, the short delay and acquisition time contrarily to the offline acquisiton allows for the collection of short lived isotopes' signals from ^{15}O, mitigating *biological washout* effect. Additionally, it also leads to lower positioning related uncertainities.

Using protons, MGH employed an *in room PET* approach, requiring 5 minutes starting from 2 minutes end of beam (EOB). In its earlier stage, the project reported results equivalent to a 20 minute–long scan offline and range agreement within ± 3 mm of the predicted activity. At that time, 2 mm co–registration errors with robotic couch and radioactive markers, as well as the scanner bore size, limited its application to pediatric and cranial treatments[Min13].

Offline PET. The patient is moved into a different room after irradiation, for an acquisition that can last 15–30 minutes[PBH08, Sha11]. Ideally, the irradiation and acquisition location should be within a short walking distance. Patient preparation/installation usually leads to acquisition starting 5–12 minutes after EOB[Bau13]. Maximum benefit is attained with acquisition starting as close as possible to the irradiation, and have it lasting as long as logistically feasible, taking into account patient confort and treatment throughput. Its major advantage lies in the lack for the need to install a scanner in the irradiation room, which entails non–negligible costs. On the other side, induced activity levels will be much lower than in conventional nuclear medicine[Pa12a] (mostly ^{11}C) with only a fraction of this value being actually acquired. Furthermore, the superimposition of the activity of different irradiation fields delivered will also lead to considerable image deterioration, making it difficult to disentangle the uncertainties ascribed to each irradiation field.

In addition to that, it is most affected by *biological washout* and anatomical changes due to patient transportation and repositioning. Nevertheless, it is a relatively economical choice and has been investigated in many centers such as MGH (protons) and HIT[Pa07a, Bau13]. At HIT, a full ring, commercial PET/CT scanner is used with relatively low integration effort, although with considerably high cost. PET/CT imaging is performed in a special room nearby the treatment rooms. CT images are used for attenuation corrections, improving accuracy but leading to extra dose. Patient repositioning is reported to delay 5–20 minutes from irradiation to imaging acquisition, which can promote washout and decrease statistics. In such cases the image may only be recovered applying specific reconstruction algorithms[Com12, Kur13]. Still, good QA and imaging results with carbon ions and protons have been reported for distal edges where activity from the long–lived ^{11}C concentrated, enabling range verification typically within ± 3 mm and good correlation with dose delivery[Han17].

1.1.6 Hadrontherapy facilities and state of the art

Despite the fact that carbon ion therapy continues to grow steadily, its complexity, high upfront cost and unclear clinical benefits still hinder its expansion compared to proton therapy[AK05]. However, given its superior dose distribution and biological effectiveness, it is envisaged that favourable histological and longterm clinical data from tumor control, along with the lowering costs, could make ion therapy more viable in the future[Sch14, Kam15, Moh17].

Whereas in the past ion therapy was primarily explored in research centers, nowadays hadrontherapy facilities are essentially "hospital–based" centers, consisting of both a conventional and technical area. The former includes the patient, personnel and medical zones while the latter hosts the accelerator, beam line and all aspects involved in the conversion of a beam into a clinical instrument. To this effect, a beam line should be capable of selecting and deliver beams up to 30 cm depth, which translates into particle energies up to 230 MeV for protons or 430 MeV/u for carbon ions. Moreover, the accelerator should be capable of delivering a maximum dose rate of

1 [Gy min^{-1}] with an accuracy within 2% over a 25×25 cm^2 field for a *Bragg Peak* at 30 cm, thus implying the use of 15 nA of protons or 0.48 nA of carbon ions[EWA11]. In clinical practice, treatments typically require 2 [GyE dm^{-3} min^{-1}], with beam intensities at the target attaining at least 1 nA and 0.1 nA for protons and carbon ions, respectively[Bra09, AB11]. Fractions are often delivered in a couple of minutes[EWA11]. In the case of proton therapy centers, this translates into an annual output of $15000 - 25000$ irradiation sessions, encompassing 20–30 minutes each, totalling an yearly throughput of ~ 1000 patients[AK05]. In carbon ion therapy, HIMAC currently reports a throughput of 900–1000 patients per year, using an average of 11–12 fractions per patient, depending on the clinical case[EK16]. Irrespective of the particle employed in the treatment, beam size, emittance, energy modulation step and repetition rate are all key technical aspects ensuring tumor conformity during treatment, reducing side effects.

Achieving ion beam energies and intensities of therapeutic relevance implies a substantial cost due to its technical complexity. A typical carbon ion therapy center can cost more than 100 M€, 30% higher than proton therapy facilities[AK05, Sch14]. One example of the complexity in using carbon ions, instead of protons, is that accelerator (synchrotron) diameter must be increased from about 8 to 25 m.

In terms of accelerator technologies, all existent proton and heavier ion beam facilities rely on cyclotrons (proton only) and synchrotrons (all ions). A cyclotron is a circular accelerator in which the particles perform a spiral path and is characterized by having a continuous duty cycle at a fixed energy, high reliability, compactness and being relatively easier to operate than a synchrotron[SES10]. A synchrotron is a circular accelerator ring usually linked with a linear accelerator (LINAC) for pre–accelerating particles up to several MeV/u[VAF11]. Due to the ions' relatively high momentum, substantially high magnetic beam rigidities are required, attaining 6.3 Tm for 400 MeV/u ions whereas only 2.2 Tm are needed for proton beams of 250 MeV, requiring larger and hence more costly magnets. The latter factor greatly hinders the avaliability of carbon ion gantries, which amounts to only two worldwide, at HIT and HIMAC, since they need to be much bulkier than for protons.

The first hospital based proton therapy center equipped with a synchrotron was LLUMC in 1990. It was the first center with a gantry and was capable of delivering a pulsed beam every 2.2 s, with energies from 70–250 MeV to the treatment rooms. Additionally it also featured one research room.

Contrarily to cyclotrons, in a synchrotron the beam is delivered in spills every few seconds, with intensities of 2×10^{10} protons/cycle or 10^9 C ions/cycle, a feature which can be exploited for clinical purposes. For instance, synchrotrons' beam delivery stratification in spills, lasting fron ms to few seconds, punctuated by a few seconds pauses (inter–spill) makes it ideal for *in beam PET*[EWA11]. Also, beams of different energies are more easily achievable in a synchrotron, adjusting the cavity frequency and the magnetic field accordingly, although it may take up to 1 s to attain the desired energy. This energy–changing ability also avoids the use of complex attenuation components to achieve tumor conformity, mitigating beam quality loss after extraction and shielding needs. As for cyclotrons', movable absorbers can be employed for beam energy changing, and they can be faster, within tens of ms, than cycle changes in a synchrotron. Since a cyclotron still produces a continuous background, it can limit the application of *in beam PET*[Bou08]. At present, synchrotrons are considered the only viable solution to accelerate ions heavier than protons to therapeutic energies, with cyclotrons remaining the proton therapy standard chiefly for economical reasons[SES10].

Currently, proton cyclotrons are provided by *IBA*, *Sumitomo* and *Varian/Accel*, whereas *Optivus*, *Hitachi*, *Protom* and *Mitsubishi* provide synchrotrons, the latter with a smaller HIMAC model for proton and carbon ions. Also in combined carbon ion and proton therapy, synchrotrons were manufactured by *Siemens*, with exclusive licences of the GSI patents and know–how up to 2012, while *IBA* and *Varian/Accel* are developing carbon ion superconducting cyclotrons[AK05]. Furthermore, recently single–room facilities featuring synchrocyclotron proton therapy were also made available. Another product, an optimized medical synchrotron – PIMMS, can provide both types of particles for therapy applications. It results from a proof of concept design study consortium between CERN, TERA foundation, Oncology 2000 and MedAustron, with know–how input from GSI. This solution was partially adopted at CNAO and MedAustron[Bry00, AK05].

The main challenges of hadrontherapy with ion beams can be summed up as: the collection of treatment outcome history and comparison of treatment protocols between the different existing facilities; improve techniques for dose delivery with respect to tumor conformity and dose delivery verification; optimize the cost of the whole facility and R&D in biological effectiveness; range monitoring in real time and evaluation of the therapeutic effects of different ion species such as $RI\beta^+$ or ions lighter than carbons[Kit10, AB11]. Regarding accelerator development, research has focused on more efficient devices, to downsize costs[AB11, MAT14, Aug16, BMM16].

Among the various hadrontherapy facilities existing worldwide, HIT and HIMAC are held in high regard due to their role in both clinical and technical developments in carbon ion therapy. Due to these factors and their relevance to this work they will hereby described in greater detail.

HIT. After the overall success of the GSI pilot project, an entirely dedicated facility was justified, thus HIT was proposed and approved in 2001. Its irradiation system and the medical equipment was supplied by *Siemens* and the total cost amounted to 119M€[AK05]. It “inherited” the accummulated expertise at GSI, upgrading it in scale and equipment, an example being the first worldwide carbon ion gantry[Pa12b]. The gantry has a diameter just below 15 m, 670 tons in weight and 25 m in length. This huge size is justified because of the increase of efficacy in therapy achieved throughout the 360° angular coverage, while the patient is immobilized and the tumor targeted within sub–mm accuracy.

The facility hosts three treatment rooms, two equipped with horizontal beam lines and one with a gantry. Up to the end of 2016, it treated almost 4000 patients ([PTCOG]). A room for QA and experiments is also included, with horizontal beam line and the beam scanning technology. Up to May 2017 it was the only facility with a carbon ion gantry, allowing 360° rotation as visible in figure 1.17. It has the capability to perform treatments with protons, helium, carbon and oxygen ions, albeit with an energy limitation for the latter. From a clinical point of view, its results have been remarkable, with some neck and head tumors attaining excellent control and survival rates[Moh17].

From the main synchrotron, it is capable of delivering carbon and oxygen ion beams of up to 430 MeV/u, and protons and helium ion beams up to 221 MeV/u. These maximum beam energies correspond to particle ranges in water from 2 until up to 30 cm (23 cm for oxygen ions)[Har17, Tes17]. Helium and oxygen ion beams are currently in pre–clinical stage, as research is ongoing for clinical translation[KMP12]. A pulse can be delivered every 3 s, and the extraction spill can be maintained up to 10 s. Extraction cycles can also vary in time, their period generally in the 5–10 s range[Par10].

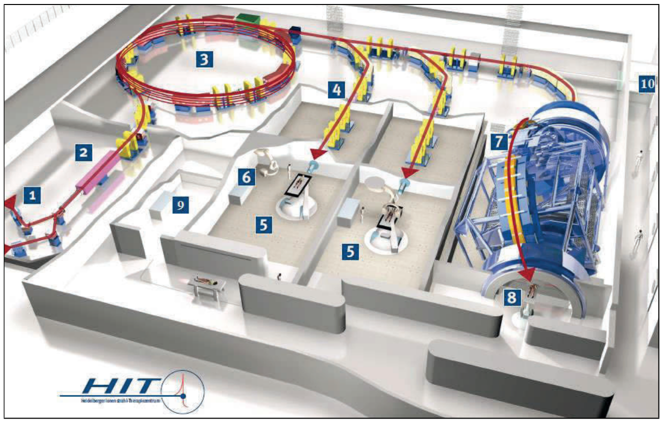

1 Ion sources
2 Linac
3 Synchrotron
4 High energy beam transfer line
5 Horizontal treatment room
6 x–ray positioning control system
7 Gantry
8 Gantry treatment room
9 PET/CT room
10 Experimental room

Figure 1.17: *An artistic depiction of the [HIT] facility and its description*[Tes17].

Similarly to GSI, raster scanning is applied to all treatments at HIT, adjusted at accelerator level in 255 steps (205 for oxygen ions) to cover the range desired with initial beam energy, typically 2–30 cm in water. In clinical practice, 4 foci, or beam sizes, and 10 intensities from $2 \times 10^6 - 8 \times 10^7$ ^{12}C ions/s are typically employed. For protons, intensities from 8×10^7 up to 2×10^9 protons/s can be attained[Par10, Pa12b, Tes16a]. The beam intensity in an experimental framework can be regulated to as low as 10^6 particle/s. High level of accuracy is attained using almost monoenergetic pencil beams with $\Delta p/p \approx 0.1\%$[Par10] laterally covering the tumor volume using scanning magnets for optimal conformity and homogeneity. Beam delivery quality is ensured in real time by feedback in intensity–controlled raster scanner. This is provided to the magnet units handling the dose delivery via the ions passing the vacuum exit window into a beam and application monitoring system (BAMS, *Siemens AG*), monitoring beam fluence and position with ionization chambers and MWPC. If abnormalities are detected, beam extraction can be interrupted within 250 μs[Par10] in the case of carbon ions or protons. A ripple filter (*Siemens AG*) can be placed after the aforementioned elements, to smoothen the dose delivery at the SOBP plateau for ^{12}C ions or very low energy protons. A schematic of the beam line elements is provided in chapter 3.

Treatment planning is performed using the first commercial CE–labelled TPS for ions – *Syngo PT Planning* (*Siemens AG*) – which was based on a `TRiP98` code created and clinically applied in the GSI framework. It has been improved in the meantime using FLUKA simulations for patients, including a realistic description of the HIT beam line. Considerable simulation work resulted in the generation of basic input data for TPS and its validation, accounting for the ripple filter effect for all these energy steps in water, for proton and carbon ions dose delivery, fragment spectra and lateral profile[Mai07, Pa12b, PMS13, Bau14].

HIMAC. An heavy ion synchrotron complex, designed and commissioned by NIRS, HIMAC is not only the first, but also a flagship among carbon ion facilities worldwide, having undergone multiple and innovative improvements since the starting of its clinical operation in 1994[Yam98]. Clinical outcome has been excellent so far, with cancer therapy applied effectively on various organ types with a 90% local control, including bone and soft tissue sarcoma, which are typically radioresistant[Kam15]. It featured a strong research focus towards the increase of beam intensities and accuracy over the years, with pioneering studies on "hypofractionation" success rate, in particular early stage lung cancer. Experience with carbon ions let to a broad clinical history accumulated over time, providing data on which types of tumors and organs were more efficiently treated, dose fractionation and records of re–incidence/late toxicity and other side effects[Tak00, Nod14, Alo00, EK16].

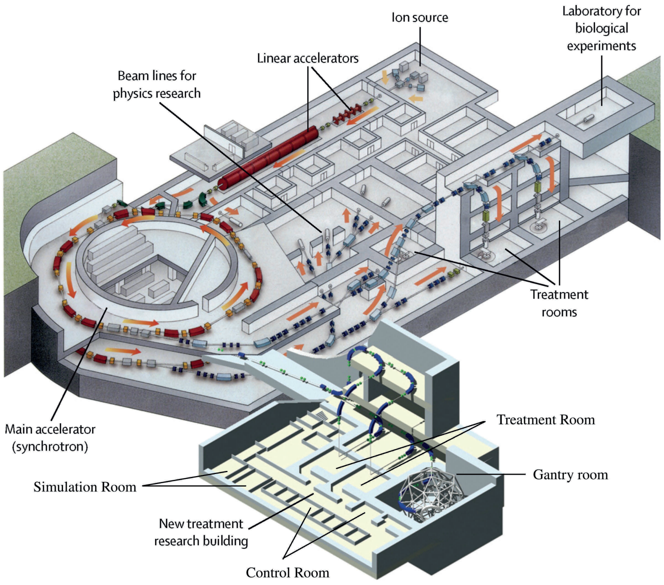

Figure 1.18: *Artistic depiction of the HIMAC facility*[Kam15].

Among its remarkable achievements, one can highlight the extremely fast raster scan implementation, respiratory motion control as well as $RI\beta^+$ studies in biology and treatment verification. Its new treatment facility is entirely dedicated to ART technology and it is also notably equipped with a 4–magnet superconducting rotating gantry system (*Toshiba Corp.*) as from May 2017, visible in figure 1.18. It is relatively compact, with 5.5 m in radius and length of 13 m[Iwa12].

The facility contains six treatment rooms as depicted in figure 1.18, they operate during daytime on normal clinical schedule. Beam switching between rooms can be done within ~ 5 minutes. There are two rooms for physics irradiation purposes and four rooms, dedicated to experimental activities also available, accounting for: Secondary beams' irradiation with online isotope separators for $RI\beta^+$ production, a low energy experimental room with the 6 MeV/u from the injector LINAC and a biology irradiation room that replicates treatment conditions for experimental purposes[Kit16].

The synchrotron consists of a dual ring with ~ 40 m diameter. In an experimental framework, and due to recent improvements, the synchrotron ring can accelerate $\sim 2 \times 10^{10}$ C^{6+} ions during a single synchrotron cycle, enough to perform single–fractional irradiation for most tumors treated with 3D scanning method. However, in a clinical environment, the dose rate required is established as 5 [GyE dm^{-3} min^{-1}] with average 14 fractions and intensities of 3.6×10^8 particles per second (pps), as weekly–averaged value, with pulses every 3.3–2 s. Note that typically 1.8×10^9 carbon ions/s yield an average dose rate of 3 [Gy min^{-1}] in a diameter of 10 cm and thickness of 6 cm at the SOBP plateau. Regarding the production rate of secondary/radioactive beams, a minimum intensity must be achieved due to treatment time requirements. Therefore, if primary beam intensities of $\sim 2 \times 10^9$ pps are reached, the production rate of secondary beams has to be at least 0.3% to match clinical requirements[Sud00].

The irradiation system was initially passive, HIMAC employed a double wobbler magnet–scatterer method, used to enlarge and homogeneize the dose field delivered, providing uniform (below ±2.5%) irradiation carbon ion beam fields at the isocentre[Kan99]. To avoid overdosage of healthy tissue, layer–stacking method (3D range-stacking) was also employed, confining dosage to the boundaries of a volume by application of multiple degraders (ridge filters), creating multiple small SOBPs. The subsequent collimators, multi–leaf and bolus, are responsible for the adaptation of the SOBPs range and shape accordingly[Sud00]. Since this earlier methodology was characterized by low beam utilization efficiency, and inhomogeneities in dose delivery were sometimes unavoidable, 3D scanning methods, including spot scanning and raster scanning were later adopted in the new treatment research facility[Ura99, Ura01, Kit08, Nod11, Nod14, Nod17].

This new facility, completed in 2011, added three rooms to the overall structure and applied 3D fast raster scanner technology only, devised for ART. Using intensity modulation techniques, greater accuracy can be achieved using dynamic beam control with fast 3D pencil–beam scanning technique, applied multiple times to reduce the error and thus mitigating repercussions to the patient[Miz11, Nod17]. Scanning methods require isoenergetic layers for depth scanning, at HIMAC this is achieved through a combination of synchrotron energy change at machine level and thin energy degraders. As a result, carbon ion beams can be delivered in 201 energy steps between 56 and 430 MeV/u[Nod17]. The new treatment research facility also hosts the gantry, depicted in figure 1.19, which is notable for allowing intensity modulated carbon ion therapy combined with 3D fast repainting method in 360°, without adjusting the treatment couch which further increases accuracy of treatments in the vicinity of critical organs. X–ray imaging of the tumor zone provides guidance to respiratory–gated scanning in real time.

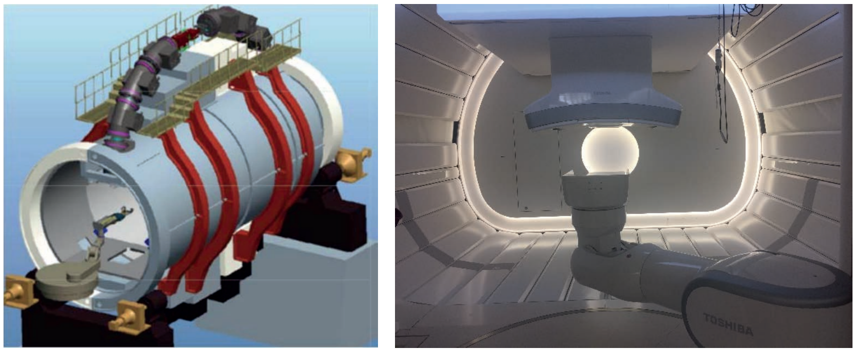

(a) Gantry view[Nod14]

(b) Patient couch position port (image courtesy of W. S. Kozłowska).

Figure 1.19: *The HIMAC gantry seen from two different perspectives.*

During nights and weekends, HIMAC provides a wide range of beams, from protons to heavier ions, including research purposes other than medical, such as space, biophysics and material radiation studies, as well as nuclear and atomic physics. Biology–related ion experiments take about 1000 hours and 70 users/year[Kit16]. RBE experimental methods for life science studies regarding biological effectiveness are of two kinds: irradiation of cell samples to investigate radiation effects at microscopic level, as well as the study of highly energetic heavy ion beams biological effects in the framework of space or hadrontherapy applications.

New developments in the experimental area are being performed with $RI\beta^+$ to facilitate range assessment, particularly in situations involving OAR[Kan04, Kat15]. Although production of $RI\beta^+$ is still not optimal and currently resorts to a projectile fragmentation "in–flight" separation method, one can convert $\sim 0.1 - 1\%$ of primary beam into $RI\beta^+$ (*e.g.* ^{11}C), by means of a secondary beam line acting as an online $RI\beta^+$ separator[Kou98, Kan98, Sud00, Kan02, Ise04]. Despite having approximately the same velocity as the projectile, and being in general forward directed, fragmented beams obtained with such method are characterized by relatively wide momentum spreads and large size/emittance[Ura01, Moh16]. Consequently the primary beam needs to be well shielded around the fragmentation target and other relevant beam line segments. More details on this secondary beam line will be provided in chapter 5.

The main limitation in the projectile fragmentation approach is the $RI\beta^+$ beam intensities and purity. Due to the low reaction yields, the secondary beam can achieve intensities of up to 7×10^6 ions/s, which is enough for PET tests, TP verification and even preliminary treatments[Tom03]. However, for a treatment, one would need to achieve a total of $\sim 10^{9-10}$ ^{11}C ions, ideally with intensities of 10^8 ions/s. This would require intensities of 10^{11} for the primary beam[Fie11]. Still, the secondary beam purity needs to be improved to reach clinical standard. Relatively high purity levels, over 90%, and activities of about $10^3 - 10^5$ [Bq Gy^{-1} cm^{-3}] for ^{10}C and ^{11}C beams have been reported in an irradiated volume[Ura01, Kan02, Kit06, Fie11]. These values are comparable to PET tracer imaging, but require highly efficient and not commercially available PET solutions for monitoring in the framework of *in beam PET*. This research topic has been very promising, with ^{15}O and ^{11}C beams being observed to indicate within 0.7 mm and 2.3 mm the *Bragg Peak* in an *in beam PET* test in PMMA, respectively[Moh16, Yam16].

Recent studies have attempted ^{11}C production with higher purity with a more direct, albeit challenging approach, consisting of injecting ^{11}C in the LINAC connecting to the synchrotron after application of an isotope separation online (ISOL) technique. The aforementioned technique implies a molecular separation process, followed by an isotope separation process, so as to attain high purity yields of ^{11}C, to be used as ion source. Considering the overall efficiency losses involved, it is expected that this alternative ISOL technique could deliver $\sim 10^9$ ^{11}C ions in few seconds, with high purity for therapy with *online PET* monitoring[Kat13, Kat15, Boy15, Nod17, Kat16].

Investigations with *in beam PET* at HIMAC culminated in the conceptual design and construction of various OPENPET prototypes[Yam17]. In its early stage, the system consisted of two full rings setups separated axially, with the beam passing in between them, hence allowing collection of signal with full rings[Yam08]. However, since only oblique LOR were collected and reconstructed, the image quality was somehow hindered, also multiple noise sources during *in–spill* limited its application to *inter–spill* and offline only[Hir14]. A small, single ringed, OPENPET prototype followed, collecting signals for phantom and mouse brain irradiation[Yam11]. This second generation, with a single full ring, but slanted, allowed for the collection of some direct LOR. Moreover, its geometry allows for more space and rotation for the beam passage[Tas12]. This new model was found to have a sensitivity improvement of a factor 1.2 compared to its predecessor[Hir14]. The latest version consists of a human sized, single ringed and axially shifted OPENPET[Yam17]. This latest version was employed in the data collection analysed in chapter 5, and subsequent comparison of experimentally acquired PET images with FLUKA simulations of stable ion and $RI\beta^+$ beams in a PMMA phantom.

Chapter 2

The Monte Carlo particle interaction and transport code FLUKA

> "Then are you so certain that your roulette–playing will get us out of our difficulties?"
>
> — F. M. Dostoyevsky in *The Gambler*

2.1 A brief introduction to the *Monte Carlo* method

The *Monte Carlo* (MC) method applies probability theories and statistical methods to model physical/mathematical systems and processes that are stochastic in nature[Vas17].

Its official invention dates back to 1946, in the framework of the *Manhattan project* at *Los Alamos National Laboratory*, where S. Ulam devised it for thermonuclear weapons research. Recognizing the significance of this invention, von Neumann attempted to implement the method computationally, using rudimentary "pseudo random numbers" generation techniques and the early computer ENIAC to model thermonuclear reactions[Eck87].

As the project was under governmental secrecy, a code name had to be attributed. N. Metropolis suggested naming it "Monte Carlo", alluding to the method's random nature and the gambling addiction of S. Ulam's uncle. Despite its official date of discovery, E. Fermi had already been applying it successfully to neutron moderation for the prior 15 years, albeit in a limited manner due to the unavailability of heavier computational power[Met87].

In fact, even before the advent of computers the method was already applied. Some historical examples being Buffon's needle problem in 1777 and later Laplace's π determination method. With the growth of computational power, MC methods became more popular for different research topics[Bie].

The first stage of MC method application is the definition of the problem in mathematical terms, so that one can calculate the quantities of interest. In order to do so, a statistical interpretation of the problem is performed. The MC mathematical core is the notion of moments of a distribution and the *Central Limit Theorem*[FFS11]. The former states that, for a variable x and probability density function $f(x)$, the mean of a function $g(x)$ over an interval $[a, b]$ is

$$\bar{g}(x) = \frac{\int_a^b g(x)f(x)dx}{\int_a^b f(x)dx}. \tag{2.1}$$

By applying the normalized probability density function $\mathcal{F}(x)$ as

$$\mathcal{F}(x) = \frac{f(x)}{\int_a^b f(x)dx}, \tag{2.2}$$

and for $\bar{g}(x)$

$$\bar{g}(x) = \int_a^b g(x)\mathcal{F}(x)dx, \tag{2.3}$$

where if $g(x) = x$, one directly obtains

$$\bar{x} = \int_a^b x\mathcal{F}(x)dx. \tag{2.4}$$

In a similar manner, the mean of a distribution can be extended to multiple dimensions, according to various probability density functions, *e.g.* integrating over $g(x, y, z)\mathcal{F}(x)\mathcal{G}(y)\mathcal{H}(z)\ldots$ This is often advantageous considering that calculations of multidimensional integrals are usually impractical, but necessary for solving physical problems.

The sampling $\mathfrak{S}_N$ of N values of g, for example $g_i(x_i, y_i, z_i)$, while averaging over the number of times this process occurs

$$\mathfrak{S}_N = \frac{\sum_1^N g_i(x_i, y_i, z_i)}{N}, \tag{2.5}$$

leads to a mean value for the solution. In the event that these terms follow the distribution of g, then the integration process corresponds to an analogue MC simulation.

Regarding the *Central Limit Theorem*, it is the centerpiece for the MC method. It states that if N is sufficiently large, the normalized $\mathfrak{S}_N$ value of N independent random variables identically distributed will tend to a normal distribution (except in cases when the second central moment is infinite), with mean $\bar{g}$ and variance σ_g^2/N. Therefore:

$$\lim_{N \longrightarrow \infty} \mathfrak{S}_N = \bar{g}, \tag{2.6}$$

hence,

$$\lim_{N \longrightarrow \infty} \mathcal{P}(\mathfrak{S}_N) = \frac{1}{\sqrt{\frac{2\pi}{N}}\sigma_g} e^{-\frac{(\mathfrak{S}_N - \bar{g})^2}{2\sigma_g^2/N}}. \tag{2.7}$$

Consequently, MC can be used to solve integrals with multiple dimensions throughout sampling from appropriate stochastic distributions, becoming in a sense a “mathematical experiment”. Convergence will eventually not depend on the number of variables n, as in general integration methods, in which convergence is governed by $N^{-1/n}$, but on the number of samples as $\sigma \propto N^{-1/2}$ instead[Jam90]. Therefore, for problems with $n > 2$, which is the rule in particle transport, MC becomes extremely convenient and is often the most advantageous technique for scenarios of dimensionality above four[Bie].

2.2 Application of Monte Carlo to particle interaction and transport

The MC method is particularly well suited for particle transport problems, as these are systems of great complexity and radiation interaction is ultimately stochastic in nature. MC allows the user to set up a virtual framework where particle detection can be performed in a controlled environment and with access to all physics processes, with the possibility of repeating the virtual experiment as often as required[FFS11].

Irrespective of the particle type, the baseline of either particle beams or radiation source products' transport should always be sound physics models, in order to replicate all physical mechanisms involved. This of course assuming that the geometry, materials and hence the real experimental setup, is properly defined and its properties replicated[FFS11].

When applied to particle transport, the MC method relies on "pseudo random numbers" and sampling techniques to model the transport of particles throughout media. Random sampling techniques are paramount in MC codes, since given a probability density function $\mathcal{F}(x)$ of a variable x, samples of x should be generated accordingly. True random numbers can neither be predicted nor reproduced, being generated by random physical processes (*e.g.* nuclear decay events). MC codes resort instead to sequences of random numbers generated by algorithms named "pseudo random numbers", while they are practically random with respect to the correlation they are still reproducible[Jam90]. They still exhibit periodicity, albeit with prolonged periods (*e.g.* 10^{61}), proceeding from an initial number or "seed", whose changing implies a different random number sequence generation[MT04]. Regarding the MC method's application, since it dwells with stochastic problems, it requires modeling of random variables. In particle transport this becomes essentially an integration problem of probability density function in a phase space with multiple variables.

As a primary particle travels throughout matter it is evaluated at certain steps, its "fate" (*e.g.* fission) is then decided by random selection from the given $\mathcal{F}(x)$. For an oversimplistic case, concerning the photon beam attenuation, one may attempt to exemplify based on

$$p(x)dx = \Sigma e^{-\Sigma x}dx, \tag{2.8}$$

where $p(x)$ is the probability density function of the photon travelling a distance x. In its turn, x varies between $0 < x < \infty$, governed exponentially by the macroscopic cross section Σ. By integrating, an estimation of the mean free path $\lambda(x)$ can be obtained as

$$\lambda(x) = \int_0^\infty xp(x)dx = \frac{1}{\Sigma}. \tag{2.9}$$

In a MC approach, the problem would be rewritten as

$$\int_0^x \Sigma e^{-\Sigma y}dy = \zeta \tag{2.10}$$

with $0 \leq \zeta < 1$ being a randomly generated number. Solving the integral, one would obtain

$$1 - e^{-\Sigma s} = \zeta \Leftrightarrow s = -\frac{\ln(1-\zeta)}{\Sigma}.$$

Thus, starting from a "pseudo random number" $\zeta \in [0, 1[$ the distance travelled by a photon can be computed[Lui13].

However, the aforementioned example is oversimplistic as MC methods should reproduce the different phenomena during particle transport (*e.g.* solving the *Boltzmann transport equation*) from its creation until its destruction, transformation, absorption or discard by any transport–imposed condition. Also, in the event that secondary particles are produced as a result of interactions, they are to be placed onto a "stack", and in turn transported iteratively until a new primary particle is considered again.

Transport should also be performed in a realistic geometry, with reasonable statistics and the particles reflecting changes as a result of interactions (*e.g.* energy loss, directional change) for consistency. However, one must be aware that the MC method has many important limitations. In fact, the geometry, material and chemical parameters do not change during the simulation (*e.g.* composition, temperature, homogeneity and shape are constants). Also, the transport of a particle will have its outcome dependent on its properties at that moment, irrespective of the previous occurrences experienced by other particles. This implies that the particles generated do not interact in between them, but just with the medium defined in the simulation *ab initio*[FFS11].

A basic underlying concept behind particle transport in a MC framework is the phase space. In classical mechanics, a particle is described in a phase space by at least 7 dimensions. Typically, the position and linear momentum components in each *Cartesian* coordinate, and the time. An "history" of a particle can be regarded as the recording of position and momentum coordinate changes in time as the particle travels through the phase space.

Let one consider the simplified example of a neutron traversing a certain material, with the macroscopic cross section given as

$$\Sigma = \Sigma_a + \Sigma_s, \tag{2.11}$$

with Σ_a and Σ_s referring to the absorption and scattering macroscopic cross sections[Lui13]. Once again, the expected distance at which an interaction occurs is given by equation 2.9, and the mean free path $\lambda = 1/\Sigma$.

At this point, since there are two types of macroscopic cross sections to be considered, the interaction will result from an interplay between absorption and scattering probabilities, ζ_a and $(1 - \zeta_a)$, respectively. The outcome becomes analogue to the schematic description in figure 2.1:

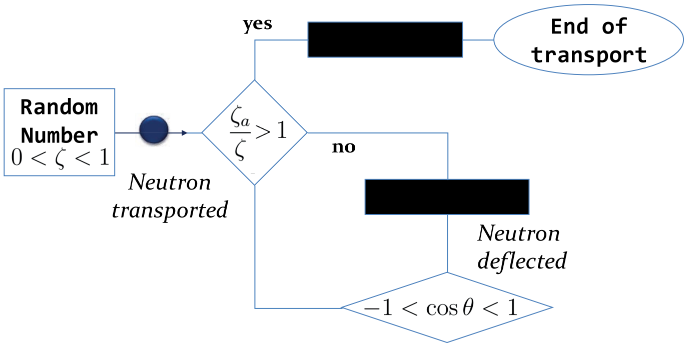

Figure 2.1: *(Over)simplistic example of MC application to neutron transport.*

The scattering happening with a polar angle θ, assuming an isotropic scenario, given by an uniform distribution for $\cos\theta \in [-1, 1]$ as

$$\cos\theta = 2\zeta - 1, \quad \phi = 2\pi\zeta,$$

in the center of momentum frame and with an azimuthal angle ϕ, $\zeta \in [0,1[$ being a random number. From then onward, the particle is retracked, until the next interaction occurs throughout the geometry defined. Obviously, there should be additional parameters taken into consideration in order to obtain a realistic result (*e.g.* absorption by capture or fission). Also, scattering can be elastic or inelastic, possibly entailing secondary particle production, which in turn would need to be tracked.

Finally, depending on the complexity of the problem that is being modeled (*e.g.* media type, geometry), a large number of particle "histories" may be required to obtain a more accurate result estimation[FFS11].

On the other hand, an accurate result can be obtained attending to the method's convergence to a solution in the phase space by increasing the density of particles in the region of interest of the phase space and decreasing it elsewhere. In such cases, the process simulated is a modified version of the real one, or a "biased" version of it, in fact[FFS11].

Hence, MC simulations can be separated in two types, analogue and non–analogue, depending on whether they are biased or not, respectively.

Given that the full potential of the MC method is mainly exploited by its (relatively) fast convergence in integration problems, a simple example of calculation of an integral $\mathcal{A}_{\triangledown}$, corresponding to a surface area is

$$\mathcal{A}_{\triangledown} = \int_0^{2\pi} f(t)dt, \tag{2.12}$$

in which f defines a curve, denominated "cat curve" according to the parametric set of functions $f(t)$[Wolf]. The calculation of this integral over the whole domain analytically would be demanding. One way to do it using the MC method would require enclosing it in a boundary, visualized as the black square, with surface area $\mathcal{A}_{\square}$ surrounding the "cat" outline as defined in figure 2.2.

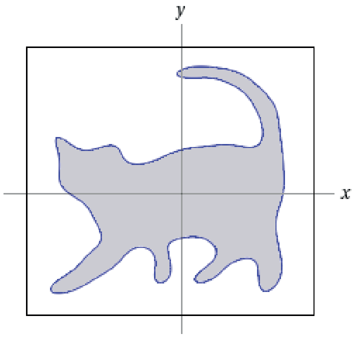

Figure 2.2: *"Cat curve" (adapted from Wolfram Alpha).*

Then, one may generate N random points with an uniform distribution for t over the squared domain $\mathcal{A}_{\square}$ and count the resulting $f(t)$ values belonging to the shaded area, or $\mathcal{A}'_{\triangledown} \subseteq \mathcal{A}_{\triangledown}$ in figure 2.2. The integral solution could then be estimated as

$$I \approx \mathcal{A}_{\square} \frac{n}{N},$$

where n is the number of times the condition was verified. Naturally, the estimated result will converge to the exact result for $N \longrightarrow \infty$. The example could also be extended to an arbitrary number of dimensions. The method's application would be equally valid, even though the complexity of the problem would increase significantly.

In the context of particle physics the number of particles in a phase space, or phase space density $n_{(x,y,z,p_x,p_y,p_z,t)}$, is the key parameter to describe particle transport. Other components (*e.g.* spin) could also be added to those dimensions, if deemed relevant. The product $n\vec{v}$ translates into the angular flux Ψ:

$$\Psi = \frac{d\Phi}{dtdEd\vec{\Omega}} = \dot{\Phi}_{E\vec{\Omega}}. \tag{2.13}$$

The above mentioned notion is a building block for particle transport, being essentially the fluence (Φ) derivative carrying the information on time, energy and direction over the phase space[FFS11]. The resulting fluence is given as

$$\int_E \int_{\vec{\Omega}} \int_t \dot{\Phi}_{E\vec{\Omega}} dtd\vec{\Omega}dE. \tag{2.14}$$

Evaluating the quantity 2.13 using the MC method requires considering not only the transport of particles, but also the interaction and consequently secondary production. This is accomplished using the *Boltzmann transport equation*, which can be regarded as a balance equation that, for any phase space point, evaluates the particle density as a result of ingoing and outgoing terms[FFS11].

$$\frac{1}{v}\frac{d\Psi(x)}{dt} + \vec{\Omega} \cdot \nabla\Psi(x) + \Sigma_t\Psi(x) - \mathcal{S}(x) = \int_\Omega \int_E \Psi(x)\Sigma_s(x' \longrightarrow x)dx'dEd\Omega \tag{2.15}$$

On the left side, the first term describes the variation of angular flux (*e.g.* altered as a consequence of decay). As for the second term, it accounts for flux changes through motion without change of energy/direction, while the third term denotes absorption by accounting for the total macroscopic cross section (Σ_t). The particle sources contribution is accounted for with the negative term $\mathcal{S}(x)$. On the other side, scattering is considered using Σ_s, the macroscopic scattering cross section. This latter represents the changes in flux due to either energy or directional changes of particle position. The evaluation of cross section data in MC codes often resorts to data libraries, for different energies, particle types and materials.

Depending on the phase space of interest and the quantity to be evaluated, various estimators can be considered and some examples will be provided in the next section. Various detector elements can be used to provide a result (estimate), in a mesh, for instance.

The variance of the mean of x thus calculated, in N batches, comes as

$$\sigma^2_{<x>} = \frac{1}{N-1}\left[\frac{\sum_1^N n_i x_i^2}{n} - \left(\frac{\sum_1^N n_i x_i}{n}\right)^2\right], \tag{2.16}$$

with x_i representing the average of x and n_i being the number of particle histories in the i^{th} batch. On the other hand, $n = \sum_i^N n_i$ is the total number of histories in the N batches. As a result of the *Central Limit Theorem*, if the system convergence criteria are met, the sample average will tend to the actual distribution if $N \longrightarrow \infty$.

In the domain of medical physics and hadrontherapy in particular, MC has gained popularity and its models have contributed to[BMM16, Vas17]:

1. Detector development for image monitoring (*e.g.* prompt γ, PET) and dose delivery optimization purposes;
2. A better understanding of ion beam interactions with matter and their secondary particle production;
3. Improvements of radiobiological models;
4. General accelerator design and beam line development;
5. TP validation and optimization.

Monte Carlo role in Treatment Planning. Besides its use for design and commissioning of a clinical facility, MC simulations are nowadays considered the tool of choice for an accurate description of physical dose in hadrontherapy[Pa12b]. This recognition results from its enhanced physical capabilities for reproducing ion interactions in complex geometries in comparison to predictions of most commercial TPS relying on analytical dose calculation engines[PPE05, Mai13, Bau14]. Some examples of TPS are `TRiP` (GSI), HIPLAN (HIMAC), the *Syngo PT Planning* (*e.g.* HIT) and *RaySearch RayStation* (*e.g.* MEDAUSTRON)[Bat16]. Provided with adequate anatomical data, a MC code should be able to:

- More accurately reproduce the heterogeneous composition of human tissue in the simulation model based on CT images[Pa07b];
- Adequately describe radiation transport and interaction[Rob13];
- Properly assess primary beam and secondary particle production, leading to a possibly better intensity modulation as well as *in vivo* range and dose delivery verification[En04b, Bat16].

Regarding the volume elements in tridimensional space (VOXEL) density/composition conversion from CT scan data, in a MC code, it can be made directly with density and material composition instead of relative stopping power ratio maps in water as used in analytical TPS[Pa07b, Pa07c]. This also allows for the adjustment of the stopping power calculation to follow the clinically established HU to stopping power ratio conversion. Also, MC codes are able to estimate physical dose within few percent accuracy, since they handle nuclear interactions, tissue composition and energy losses more realistically[Kr15b, Bat16]. However, MC simulations often entail large execution times, which can be prohibitive in clinical applications context. Still, MC codes can provide basic data for representative settings (*e.g.* beam energy) to be employed in the TPS, for fast TP recalculation, using databases to accomplish a SOBP over the tumor volume[Bau14].

MC codes are also very relevant in treatment monitoring for example, evaluating β^+ emitter activities and subsequently compare them against measurements to infer the correctness of the treatment delivery as done for instance at HIT, supported by FLUKA calculations[Som09, Pa12b]. As mentioned in chapter 1, the spatial distribution of β^+ emitters or de–excitation products varies in time according to beam–target and secondaries interactions, due to non–elastic nuclear reactions. MC codes can model these reactions, the acquisition time, detector setup and disentangle the signal from background, thus being very useful in either *in beam PET* monitoring or prompt γ studies[Kr14b]. An [INSIDE] collaboration proposed workflow, including FLUKA calculations for *in* *beam PET* monitoring online, is depicted in the schematic of figure 2.3. It is based upon the methodology pioneered at GSI and later at MGH Boston and HIT, where PET was employed as a tool for range verification by comparing measurements with simulated results[En04b, Par04, Pön04, Pri12].

PET–based treatment monitoring consists of measuring β^+ emitter activity distribution and then compare it to the simulated β^+ emitter activity distribution, accounting for the time effects (*i.e.* beam time structure, decay time during signal acquisition). If a mismatch in the activity of the two results is identified, a TP evaluation is performed, otherwise the treatment will proceed to the next fraction. Additionally, the TP re–evaluation may require a new CT scan to assess anatomical changes and possibly redefine the TP[Bau14].

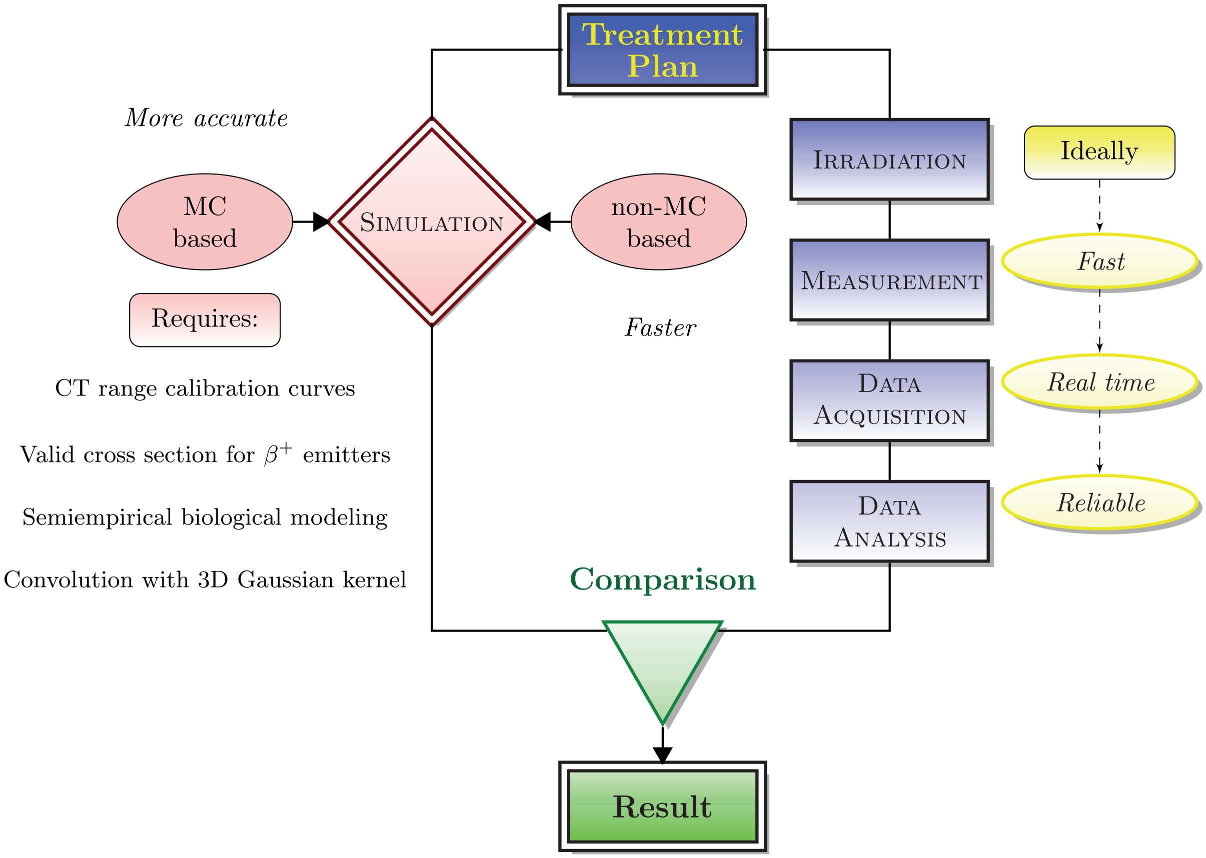

Figure 2.3: *A schematic depiction of a MC code possible use in online, in beam PET, treatment monitoring ([INSIDE]).*

Many MC codes can deal, with varying degrees of success, with hadrontherapy applications' problems: FLUKA[Böh14, Bat16]; PHITS[Sat13]; GEANT4/GATE[Ago03, LIK10, Gre12], MCNPX[Mas11], SRIM[Zie08] and SHIELD[Gei06, Bass14], among others[Rob13].

The selection of FLUKA for the present work was heavily influenced by its use in HIT and CNAO start–up, commissioning and operational stages, including as well extensive validation work[Pa12b, PMS13, Bau13, Bis17]. At HIT, FLUKA was used as the MC framework of choice to generate the beam library parameters (*e.g.* energy, focus values), including physical basic data to be used as input in the commercial TPS[KMP12]. This culminated in an extensive validation of TPS dose calculations based in water equivalent thicknesses and FLUKA CT–based recalculations, resulting in comparisons between MC dose with TPS predicted dose[Tes16a, Bau14, Pa12a]. Dosimetric calculations were validated by dose measurements in water, whereas β^+ activity simulations were subsequently compared with measured radiation for treatment verification[Kr14b]. The CT–based FLUKA MC calculations of physical and biological dose are implemented in clinical routine, for QA but also in physics experiments and biological dose assessment, for example via predictions through an interface with the *Local Effect Model* dose effect, extensively applied at HIT and CNAO[Mai13, Bau14, Bat16]. Recently, FLUKA was also compared with NIRS analytical TPS and biological dose calculation system[Mag17].

In recent years, FLUKA underwent various developments and validation of ion fragmentation and secondary particle emissions for imaging studies, with intensive investigations on the produced fragmentation tail dose and spectra, including repercussions on biological dose calculations[Mai10, Böh10, Rob13]. In addition to these investigations, the introduction of a framework enabling PET studies contributed to the decision for its use in this work[Ort13]. FLUKA nuclear models will be detailed in the next section of this chapter, whereas the PET TOOLS will be described in chapter 3.

As a consequence of the growing reliance of hadrontherapy on MC codes, several groups are studying nuclear fragmentation processes occuring during irradiation, as well as their angular distribution, in order to further improve the reproduction of the β^+ emitters' activity yield and spatial distribution, which is very relevant for *in beam PET*[Pri08]. In 2005, fluence and LET of various fragments have been studied at HIMAC to assess their impact in the depth dose profile and compare with calculated fluences[Mat05]. Recently, a remarkable effort has been carried out at GANIL (Grand Accélérateur National d'Ions Lourds)[Sal16], obtaining cross section information for some β^+ emitters of interest. However, the study covered a limited energy range. Also, the MEDIPIX–TIMEPIX collaboration succeded in obtaining experimental data via ion identification from fragmentation[Har17].

Given the limited direct availability of experimental cross section data at clinical relevant energies, the comparison of β^+ emitter distribution against the signal detected originating from secondary emissions can be used not only to identify the species produced, but also benchmark and improve the underlying nuclear models available in MC codes. This process is still ongoing as it requires a large amount of data to be properly validated[PPE05, LIK10, Böh10, Rob13, Kr15b].

2.3 The FLUKA code

FLUKA is a fully–integrated, multipurpose, *Monte Carlo* particle transport and interaction simulation code[Fer05]. In its present version (`2011.2x.0`) it can transport more than 60 different particles and handle complex geometries. The code benefits from a versatile graphical user interface – *flair* – providing an user–friendly environment regarding many routine tasks (*e.g.* input editor, interactive geometry builder)[Vla08]. FLUKA functionalities can be further extended, by linking user routines, enabling additional features for specific calculations.

The code is propriety of CERN and INFN, and is freely distributed (`http://www.fluka.org`) for academic purposes, with its development being carried out in the framework of an international collaboration with dozens of institutes. Its applications vary greatly, including space, medical applications, accelerator & particle physics, shielding, dosimetry and general radioprotection, among many others[PCF01, Bal06, Böh14, Bat16].

Its history can be traced back to the work of J. Ranft in the 60's to assess the implications of high energy proton induced cascades in shielding studies at CERN[Ran65]. The challenges of proton colliders up to the TeV energy range renewed the interest in FLUKA and its capabilities, hence leading to a total redesign of the code to face more complex radiation physics domains. The present generation of FLUKA dates back from 1989 and has been undergoing development up to the present day, during this period the code became a multipurpose particle code, now applied in a wide range of fields and energies[Bat15]. Since 1989, the present generation saw the addition of major features such as: magnetic fields, energy deposition in limited volumes, high–energy effects and low-energy neutron interactions, as well as an original *Multiple Coulomb Scattering* algorithm for all charged particles, enhanced electromagnetic and hadronic parts, low–energy neutron transport, extended usage of *Combinatory Geometry* package and introduction of new scoring and biasing functionalities[Fer92, Fas97b]. This code version is characterized by extensively benchmarked and tested microscopic physical models, being designed and structured to ensure self–consistency, which is particular evident in its handling of various components of the hadronic and electromagnetic cascades, where mutual interaction between the different components, and respective correlations, are preserved[Fer05].

In particular, heavy ion transport in FLUKA and interaction models were subject to many upgrades, due to their importance in hadrontherapy and space applications problems[Bia99, Bal06]. A collaboration with NASA contributed to the development related to FLUKA heavy ion transport and interaction models[And04, Bal07].

Considering all its models, it is today one of the few codes able to simulate transport of particles in matter, dealing with hadron–hadron, hadron–nucleus, nucleus–nucleus, neutrino, neutrons, electromagnetic, μ and γ interactions over wide energy ranges (from TeV to the *Coulomb barrier* for charged particles). Also, since 2004 a model for electromagnetic ion dissociation, of relevance for highly energetic and heavy ion interaction, has been added[Bal05, Fer06, Bra14]. Another model, particularly relevant to this work, has been added in 2012 which allows for a better description of Compton scattering and positron annihilation[Böh12]. Regarding the latter, the code effectively distinguishes between annihilation events in flight or with the electron at rest, even though annihilation events in flight are by far less frequent than at rest. The distinction is made via the proper sampling of atomic electron momentum values, with the acollinearity of the photons emitted in the annihilation being therefore reflected in the model[Böh12].

Nuclear reactions

Nuclear reactions modeling with an MC code starts with sampling the probability of a nuclear event occuring, according to the incident particle and energy. Then the nuclear interaction is sampled using the MC code's internal models or database informations. In FLUKA, it can be subdivided in the following categories[FS96, Bat05]:

Hadron–nucleon interactions. Up to 5 GeV, the code uses models based on individual resonance production and decays. At higher energies, and up to 20 TeV/u, parton string models are used[FS96, Fas03]. Beyond 20 TeV/u, DPMJET-III is employed instead[RER01].

Hadron–nucleus interactions. Below 20 TeV, the PEANUT model is applied, whilst above that energy the DPMJET-III model takes over[FS97]. PEANUT features both a detailed (Generalized)

Intra–Nuclear Cascade (G)INC, describing multiple independent nucleon–nucleon interactions in the target nucleus and subsequent transition to pre–equilibrium models[Ser47, Ber74, Fer06]. The transition is continuous and the compound nucleus excitation energy is handled by the "exciton" formalism, where the excitation energy is shared among the presently excited nucleons and holes. Particles and light fragments (from coalescence) are emitted from the excited nucleus until a configuration where equilibrium is attained[Bla83, Fas03]. These models are responsible for reproducing interactions involving nucleons (and various exotic particles) at a wide energy range, including modeling proton and neutron interactions in hadrontherapy[Böh14]. Different generators will apply based on the projectile energy in case of heavier ions, as will be briefly described later[Böh10].

Nucleus–nucleus interactions. Contrarily to nucleon–nucleus reactions, in nucleus–nucleus interactions the incoming nucleons are not free[BMM16]. Three event generators are used depending on the energy range:

DPMJET–III – It is interfaced with FLUKA for energies $E \geq 5$ GeV/u for ions and 20 TeV for hadrons, based on the *Dual Parton* and *Glauber–Gribov* approaches[RER01]. It is the event generator applied to high energy hadron–nucleon, hadron–nucleus and nucleus–nucleus interactions, featuring also a photo–production off nuclei event generator.

rQMD-2.4 – It is based on an original "relativistic quantum molecular dynamics" model, extensively modified from the original code[SSG89, Sor95]. It is interfaced with FLUKA in its faster cascading version for ion interactions at intermediate energies, from 125 MeV/u $\lesssim E <$ 5 GeV/u, where DPMJET-III takes over[And04, Bat05]. Its modifications led to energy/momentum balance accounting for experimental binding energies, and accurate calculations of excitation energy, with the evaporation and de–excitation processes being handled by FLUKA modules[And04, Aig05, Gar07].

BME – This model covers the lowest energy range, from the *Coulomb barrier* to $\sim$ 125 MeV/u. It deals with the thermalization processes in compound nuclei created in the complete or incomplete fusion of two ions, using a MC event generator, incorporating as input the results of the numerical integration of the *Boltzmann Master Equations*[Bat03, Cer06] (equation 2.15). In such scenarios, MC would have to use as input pre–equilibrium particles' evaluated angle–energy multiplicity spectra, including those emitted both in the primary and the secondary interactions along the nuclear reaction chain. Such calculations are too lengthy to be made at run–time, therefore an internal database is used for interpolation, covering the pre–equilibrium emissions throughout the reaction chain for many pairs of interacting ions. In this process, accurate computation of double differential cross–sections of all residuals created in a reaction, involving a projectile with variable energy, is performed. Moreover, momentum distribution of the residual particles produced, their decay properties and respective emissions, are also calculated[Cav01, Bat03].

Given the hadrontherapy energy range, ion interactions are mostly handled by BME and rQMD modules and thus DPMJET–III will be henceforth excluded from the present discussion. These models play an important role in simulating heavy ion interactions with matter, ensuring the correct reproduction of double differential cross–section for all particles emitted in the reactions. If in hadron–nucleus interactions radioactive products originate generally from the target nucleus, in nucleus–nucleus interactions both target and projectile nuclei are produced[Fas03, Fer06].

In the framework of hadrontherapy, simulating the interaction of an ion beam with tissue requires describing various projectile–target pairs within a broad energy range. RQMD–2.4 and BME models and their interplay are relevant for they will eventually govern the fragmentation build–up and β^+ emitter production[Som09].

For intermediate energies, the original rQMD–2.4 assumes, in its initial condition, that the projectile and target can be described as two Fermi gases. The Fermi momentum (p_F) is given by

$$p_F = \hbar\left(3\pi^2\frac{A}{2V}\right)^{\frac{1}{3}}, \tag{2.17}$$

with $V = \frac{4}{3}\pi\left(r_0 A^{\frac{1}{3}}\right)^3$ and $\rho = \frac{A}{V}$, where $r_0 = 1.12$ fm and $\rho_0 = 0.17$ [nucleon fm^{-3}]. The nucleon momentum can then be described as:

$$p = p_F\left[\frac{\rho(r)}{\rho_0}\right]^{\frac{1}{3}}\zeta^{\frac{1}{3}}, \quad \zeta \in [0,1] \tag{2.18}$$

Where ζ is a “pseudo random number”. The final momentum states in every coordinate system will then be characterized by

$$p_x = p\sin\theta\cos\phi, \quad p_y = p\sin\theta\sin\phi, \quad p_z = p\cos\theta,$$

with $\phi = 2\pi\zeta$ and $\cos\theta = 1 - 2\zeta$, with the condition that the sum of momenta values in each of the coordinate frames is null. To identify projectile and target like nuclei, one needs to account for the experimental binding energies, nuclear potentials and both attraction and repulsion effects in the formation of spectator nucleon clusters[And04]. These functions, which are relevant in the overall nuclear stability, are not present in the rQMD original version but are included in the module interfaced with FLUKA[SSG89, And04].

Regarding low energy ion interactions, these are gradually handled with BME event generator as rQMD becomes less reliable below 125 MeV/u. In a first step, the reaction cross sections (σ) are calculated based on models, defining the probability of either complete fusion ($\mathcal{P}_f$) or peripheral collision ($\mathcal{P} = 1 - \mathcal{P}_f$) occuring as[Kar75, CCG05]:

$$\mathcal{P} = 1 - \frac{\sigma_f}{\sigma}, \tag{2.19}$$

where σ_f is the complete fusion partial cross section and $\mathcal{P}$ the probability of a peripheral collision taking place[Man15]. Peripheral collisions are typically the most probable for higher ion bombarding energies, in which complete fusion is less likely. Consequently, as depicted in figure 1.4, this results in an “hot reaction zone” along with projectile and target fragments.

Subsequently, the thermalization process of a compound nucleus thus produced is described with the BME theory[Cav98]. It consists of using the transport equation to find the momentum distribution variation in time, as a result of mutual interactions. However, this is made in volume partitions of the nucleon interaction phase space $\Delta V = 2\pi m \Delta E \Delta p_z$, where m is the nucleon mass, E its energy and p_z its momentum in the beam axis reference frame. The occupational probability n in a bin i hosting a number of states g, for proton states (a variation of it can be applied for neutrons), evolves in time according to the following set of differential equations:

$$\begin{aligned}\tfrac{d(n_i,g_i)^P}{dt} = \textstyle\sum_{j,l,m} \Big[& \omega^{PP}_{lm\to ij} g^P_l n^P_l g^P_m n^P_m \left(1-n^P_i\right)\left(1-n^P_j\right) + \\ & -\omega^{PP}_{ij\to lm} g^P_i n^P_i g^P_j n^P_j \left(1-n^P_l\right)\left(1-n^P_m\right) \Big] + \\ + \textstyle\sum_{j,l,m} \Big[& \omega^{PN}_{lm\to ij} g^P_l n^P_l g^N_m n^N_m \left(1-n^P_i\right)\left(1-n^N_j\right) + \\ & -\omega^{PN}_{ij\to lm} g^P_i n^P_i g^N_j n^N_j \left(1-n^P_l\right)\left(1-n^N_m\right) \Big] + \\ & -n^P_i g^P_i \omega^P_{i\to i'} g^P_{i'} \delta\left(E^P_i - E^P_F - B^P - E^P_{i'}\right) - \tfrac{dD^P_i}{dt},\end{aligned} \tag{2.20}$$

with P and N indicating the proton and neutrons, respectively[Cav01, Gad03, Man15]. As for the coefficients $\omega_{ij\to lm}$ and $\omega_{i\to i'}$, these correspond to the transition probability in time of two interacting nucleons, from an initial bin configuration (i,j) to the next one (l,m), and the emission probabilities into the continuum. Integrating equation 2.20, one can obtain the nucleon evolution in time through the phase space. Regarding the last term in equation 2.20, it is denominated the "depletion term" and it pertains the proton emission bound in a cluster c. The latter is formed as nucleons coalesce into a system, in which the momentum of a constituent nucleon lies within the compound nucleus' sphere center of mass momentum[Cer92]. A cluster of N' neutrons and P' protons is therefore formed with an energy E_c and at an angle θ_c from the beam axis and bin i, with a probability in time $\mathcal{P}_c$:

$$\mathcal{P}_c(E_c,\theta_c,t) = \prod_i \left(n^P_i\right)^{V_i(E_c,\theta_c)P'} \cdot \prod_i \left(n^N_i\right)^{V_i(E_c,\theta_c)N'}, \tag{2.21}$$

in which $V_i(E_c,\theta_c)$ is the volume fraction of the i^{th} bin within the compound nucleus' sphere center of mass momentum, with center E_c,θ_c in the phase space[Man15]. The multiplicity M spectrum can then be calculated up to the equilibrium time (t_e), for the emitted nucleons with energy E' and at angle θ:

$$\frac{d^2M(E',\theta)}{dE'd\Omega} = \frac{1}{2\pi\sin\theta}\int_0^{t_e} n(E,\theta,t)\frac{\sigma' v}{V}\rho(E,\theta)dt. \tag{2.22}$$

As well as for a cluster (M_c):

$$\frac{d^2M_c(E_c,\theta_c)}{dE_c d\Omega} = \frac{R_c}{2\pi\sin\theta}\int_0^{t_e} \mathcal{P}_c(E_c,\theta_c,t)\frac{\sigma' v_c}{V}\rho_c(E_c,\theta_c)dt. \tag{2.23}$$

R_c corresponds to the probability of a cluster being emitted after it is formed, while Ω is the solid angle[Cer92, Gad03]. As for v and v_c, these are the nucleon and cluster velocities, relatively to the residual nucleus, respectively. Regarding σ', it refers to the inverse process cross section (*i.e. absorption*), while V is the laboratory volume which cancels with a similar factor appearing in the density of nuclear or cluster states in the continuum (ρ), depending on whether a nucleon or a cluster is being considered, respectively. The integral of equation 2.23 allows one to find the number of fragments produced in time. However, given the large multiplicity and complexity of emissions, a database with pre calculated parameterized results from the original BME code is called, with predetermined emissions' double differential spectra, to enhance the calculation speed as previously mentioned[Cav98].

Overall, the evaluation of the nucleons involved in the pick up, stripping, break up or incomplete fusion scenarios is based on the impact parameter selection, while the kinematics and excitation energy sharing is found via break up studies.

At the very end, when the nuclei are in equilibrium, BME transits to the FLUKA common de–excitation modules, as depicted in the schematic of figure 2.4[Bat16].

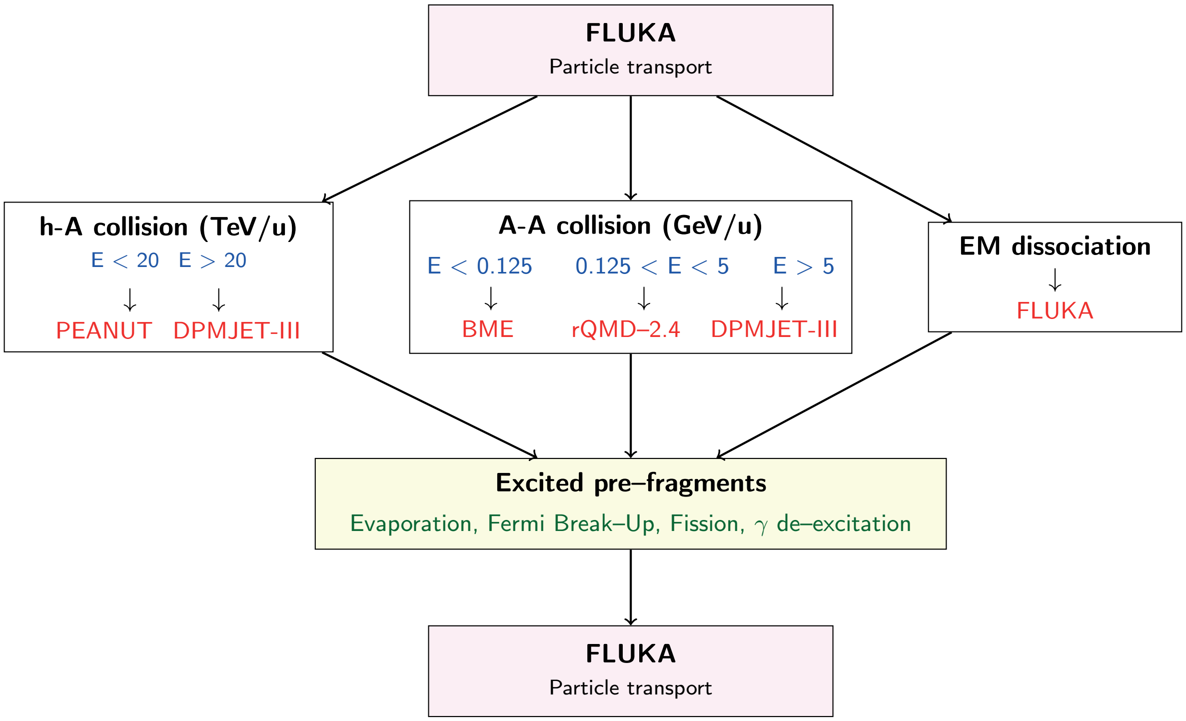

Figure 2.4: *Schematic view of the major FLUKA modules for particle transport. h–A refers to hadron–nucleus, A–A denotes nucleus–nucleus and EM to electromagnetic.*

De–excitation modules. These modules describe the last stages of a nuclear interaction, after the precedent collisions and emissions, when fragment production takes place from a thermally equilibrated system. At this point, the system is characterized by its excitation energy U, residual momentum and number of protons/neutrons. The constituents of the final compound nucleus de–excitation can be summarily described as:

A≥17 – Depending on the mass and excitation energy, fragments can undergo:

- *Evaporation*, where de–excitation will occur mainly with emission of low kinetic energy (few MeV) nucleons and light fragments (d, t, α). It is handled throughout a version of *Weisskopf–Ewing* formalism[Wei37, Dre62, Fas01]. It states that a system has an equal probability $\mathcal{P}$ of evolving in between stage 1 and 2, as a function of the density of states ρ of the two systems: $\mathcal{P}_{1\to2}\rho(1) = \mathcal{P}_{2\to1}\rho(2)$. Conversely, $\mathcal{P}_{2\to1}$ refers to the probability of capturing a particle and forming a composite nucleus. The evaporation probability $\mathcal{P}_j$ of a particle j and spin $S \cdot \hbar$ is obtained by

$$\mathcal{P}_j(E)dE = \frac{(2S+1)m}{\pi^2\hbar^3}\sigma' \frac{\rho_2(U_2)}{\rho_1(U_1)} EdE, \tag{2.24}$$

with $U_1 \equiv U$ and $U_2 = U - E - Q_j$ being the excitation energy of the evaporating and evaporated nucleus, respectively, while σ' is the inverse process cross section. Q_j refers to the reaction Q for emitting a particle j from the original compound nucleus[FS96].

- *Fission*, which may occur in excited heavy compound nuclei, whenever the excitation energy is greater than the fission barrier B_f, when considerable deformations may take place with eventual splitting. The probability of its occurrence competes with that of evaporation, and is given by

$$\mathcal{P} = \frac{1}{2\pi\hbar}\int_0^{(U-B_f)} \frac{\rho(U - B_f - E)}{\rho(U)} dE, \tag{2.25}$$

with ρ being the nuclear level densities[FS96]. B_f varies according to the fissibility parameter Z^2/A and can be practically neglected for $Z < 70$ and thence is of no relevance in hadrontherapy.

A<17 – Statistical evaporation of excited lighter residuals is not feasible given the sparse and wide excitation levels, therefore requiring a more detailed treatment. This process attains a high relevance in hadrontherapy for most biological tissue consist of nuclei with A<17[Kr15b].

- To this effect, a modified version of the *Fermi Break–Up Model* is employed for de–excitation of an excited nucleus[Fer50]. The disassembling into $n \geq 2$ fragments of a residual nucleus is characterized by a probability $\mathcal{P}$[Böh14, Man15]:

$$\mathcal{P} = \frac{S_n}{G}\left[\frac{V}{(2\pi\hbar)^3}\right]^{n-1}\left(\frac{1}{M}\prod_{i=1}^{n} m_i\right)^{\frac{3}{2}} \frac{(2\pi)^{\frac{3(n-1)}{2}}}{\Gamma\left[\frac{3(n-1)}{2}\right]} E^{\frac{3n-5}{2}}, \tag{2.26}$$

where V is approximately the volume of the initial residual nucleus, M is the total mass (comprising U and the nucleon mass – $M_{P,N}$), m_i the i^{th} fragment mass and E the total kinetic energy of the nucleus at the breaking up. S and G correspond to the spin $\prod_{i=1}^{n} 2S_i + 1$ and permutation $\prod_{j=1}^{k} n_j!$ factors, respectively. Regarding n_j, it is the number of identical j^{th} particles. As for Γ, it denotes the *gamma* function[FS96].

The resulting fragment is then obtained by computing equation 2.26 for all possible combinations and then randomly selecting one. In this process, *Coulomb barrier* (B_c) is accounted for in the total kinetic energy calculation at the breaking up, via

$$E = U - \left(\sum_{i=1}^{n} m_i c^2 - M_{A,Z}c^2\right) - B_c. \tag{2.27}$$

The final state is obtained using a MC procedure over equation 2.26[FS96]. If the fragment is radioactive, decay will apply and the subsequent fragment(s) configuration(s) will be evaluated according to kinematic quantities.

γ *de–excitation* occurs at the last stage, with cascades of γ–rays being produced as a by–product of the nuclear de–excitation process whenever the excitation energy is below the threshold for particle emission. It includes a statistical treatment for various transitions at high excitation energies, and a discrete treatment for low excitation levels. The probability of emitting a γ–ray with energy E_γ is given by

$$\mathcal{P}(E_\gamma)dE_\gamma = \frac{\rho_2(U_2)}{\rho_1(U_1)} \sum_L f(E_\gamma, L)dE_\gamma, \tag{2.28}$$

with L being the multipolarity of the γ transition, and f functions either calculated or derived from photoabsorption cross sections[FS96]. The data employed follows the photon energies and branching ratios as given in the *Reference Input Parameter Library* (RIPL-3) database from IAEA[Bat16].

The cumulative effect of the above mentioned processes ensures the physical consistency of remaining residuals. In addition to that, the mass spectrum of residuals is further constrained by the excitation energy distribution at each step leading up to de–excitation. The accurate production of these residuals is extremely relevant for treatment monitoring, due to the modelling of β^+ emitting fragments, prompt γ and fast secondary charged particles[BMM16]

FLUKA implementation of transport and energy–loss mechanisms for charged hadrons

FLUKA accurately accounts for continuous energy losses of heavy charged particles, energy loss *straggling*, δ—ray production, and *Multiple Coulomb Scattering*[Fer92, Fas97b, Bat16].

Bethe–Bloch formalism in FLUKA. The energy loss mechanism for charged hadrons in hadrontherapy is based on the *Bethe–Bloch theory*[Bet30, Bet32, BH34, Blo33a, Blo33b] with higher order corrections, summarily described in chapter 1. In FLUKA, electronic stopping powers are computed based on an improved *Bethe–Bloch* formalism, starting from 1 keV energies onwards, ranging out particles below the energy cut–off. Higher order corrections accounts for *Barkas, Bloch* and *Mott corrections*, effective charge parameterizations and a sophisticated *straggling.* Also, it includes nuclear form factors, at high energies, and charge exchange effects, for lower energies.

The major correction factors and their effect on the accuracy of stopping power calculations by FLUKA will be discussed. For the sake of simplicity, equation 1.6 will be rewritten, omitting explicitly the correction factors later derived using relativistic quantum mechanics perturbation treatments[Bic92]:

$$\left(\frac{dE}{dx}\right)_{e^-} = -4\pi N_A r_e^2 m_e c^2 \rho \frac{Z}{A} \frac{z_e^2}{\beta^2} (\mathcal{L} + \mathcal{M}). \tag{2.29}$$

For large velocities or light ions, the projectile charge approaches the atomic charge number, as all the atomic electrons are stripped off. However, for light ions $\lesssim$ 10 MeV/u the description of average quadratic charge state decreases as the projectile slows down and it is partially neutralized by capturing electrons[BBS56, BDH63]. FLUKA follows a previous implementation, modified to include the effect of various $\mathcal{L}$ and $\mathcal{M}$ corrections[HBG89]. Regarding $\mathcal{L}$, it consists of the dimensionless stopping number term per target electron and contains three major subterms:

$$\mathcal{L} = \mathcal{L}_0 + z_e\mathcal{L}_1 + z_e^2\mathcal{L}_2. \tag{2.30}$$

Each of whose will be evaluated individually:

$\mathcal{L}_0$ is the *Bethe term* and includes the basic stopping power formula, namely[Por99]:

$$\mathcal{L}_0 = \frac{1}{2}\ln\left(2m_ec^2\beta^2\gamma^2\Delta E_{max}\right) - \beta^2 - \ln I - \frac{C}{Z} - \frac{\delta}{2}. \tag{2.31}$$

It includes the following correction factors:

C – The sum of target *shell corrections*, used to correct for atomic binding effects, as electrons are not at rest[Zie99]. Its importance increases as the projectile slows down ($E <$ 100 MeV/u), no longer yielding velocities larger than the atomic electrons, rendering the *Bethe–Bloch* approximation no longer valid.

δ – Density effect corrections, introduced by E. Fermi, are mainly important for relativistic projectiles with $E > 1$ GeV/u, and they are needed due to the polarization of the electric field, leading to a decrease in distant–collision contribution factor, as $\ln(\beta\gamma)$[Zie99]. Thus, the energy loss is reduced due to the polarization of the medium and the electrons getting screened farther[Ste84].

I – Target mean excitation energy, as well as density effect parameters in FLUKA, derive from [ICRU–37] data[Ste84]. Variations in range arise from uncertainties on the mean excitation energy. For instance, a change of 5 eV in I (from $75 \rightarrow 80$ eV) can result in a $0.8 - 1.2\%$ difference in the predicted stopping power in water[Pag12]. Even changes of 2 eV can lead to ~ 1 mm variation in range for 400 MeV/u carbon ions. In 1993, [ICRU–49] issued a recommended a value of 75 ± 3 eV for water, which is the default in FLUKA. Experimental data and recent ICRU publications point towards a slightly higher I values (~ 78 eV), which can be input in FLUKA[Pag12].

The radiative contribution to energy losses for positrons and electrons was adopted so as to be consistent with *Bremsstrahlung* data as well[SB86]. Differences between the positron and electron are taken into account concerning both stopping power and *Bremsstrahlung*[Kim86]. The latter and electron pair production at high energy by heavy charged particles is described through either a continuous or discrete energy loss regime.

$z_e\mathcal{L}_1$ denotes the *Barkas-Andersen effect* (z_e^3) correction, which accounts for a stopping power slightly smaller for negatively charged particles[Pit95]. $\mathcal{L}_1$ is defined as a parametric function (*Barkas effect*)[BBS56, BDH63, Ash72]. It becomes relevant at $E < 10$ MeV/u and is implemented in FLUKA as per [ICRU–49].

$z_e^2\mathcal{L}_2$ is the *Bloch* (z_e^4) *correction*, introduced by F. Bloch[Blo33a, Blo33b]. It is defined by [ICRU–37] as

$$\mathcal{L}_2(y) = \psi(1) - \Re[\psi(1+iy)], \tag{2.32}$$

with ψ being the *digamma function* (logarithmic derivative of the *gamma function*) and $y = z_e{}^{\alpha}/_{\beta}$, where α is the fine structure constant and $\Re$ denotes its real part. Its importance increases at lower energies, being particularly relevant for distant collisions of ions within an 10 MeV/u $< E <$ 1 GeV/u energy range. Alternatively, a simplified version of equation 2.32 is sometimes employed[BP82]:

$$\mathcal{L}_2(y) = -y^2 \left[1.20206 - y^2 \left(1.042 - 0.8549y^2 + 0.343y^4\right)\right]. \tag{2.33}$$

Regarding $\mathcal{M}$, it is a correction important for medium/heavy relativistic projectiles, related to the electron–ion *Mott*[Mot29] cross–section (*Mott correction* to *Rutherford scattering* cross section) introduced in FLUKA in 2010. This higher order correction is required whenever $z_e{}^{\alpha}/_{\beta} \ll 1$ is no longer satisfied, since the *Bethe-Bloch* equation does not account for electron–ion scattering cross–sections beyond the *1*st *Born approximation*[Bat16].

The *Mott correction* is applied as a parameterized factor in FLUKA based on offline calculations, to yield the appropriate stopping power factor based on the relationship between *Mott* and *Bethe* differential cross–section $\left(\frac{d\sigma_M}{d\varepsilon} \text{ and } \frac{d\sigma_B}{d\varepsilon}\text{, respectively}\right)$:

$$\mathcal{M} = \int \left(\frac{d\sigma_M}{d\varepsilon} - \frac{d\sigma_B}{d\varepsilon}\right) \varepsilon d\varepsilon, \tag{2.34}$$

where ε is the transferred energy. Secondary electron production and energy loss fluctuations are corrected as well[LQZ95, JKE09]. Overall, *straggling* in FLUKA simulations, using the 1st *order Born approximation* and *Mott* cross sections, was verified to be within the intervals of measured variances for various combinations of relativistic ions and targets[Sch96].

Summarizing, these corrections result in the following equations, for spin 0 projectiles:

$$\left.\left(\frac{dE}{dx}\right)_{e^-}\right|_0 = -4\pi N r^2 mc^2 \rho \frac{Z}{A}\frac{z^2}{\beta^2}(\mathcal{L} + \mathcal{M}); \tag{2.35}$$

and for spin $^1/_2$,

$$\left.\left(\frac{dE}{dx}\right)_{e^-}\right|_{\frac{1}{2}} = -4\pi N r^2 mc^2 \rho \frac{Z}{A}\frac{z^2}{\beta^2}\left(\mathcal{L} + \frac{1}{8}\frac{\Delta E_{max}}{(mc^2 + Mc^2)} + \mathcal{M}\right). \tag{2.36}$$

Regarding the elastic interactions via the *Coulomb* force with atomic nuclei, and although these energy losses are much less relevant than those with atomic electrons at therapeutic energy, they are accounted for in FLUKA as non–ionizing energy losses. Also, *displacements per atom* (DPA), can be also estimated in FLUKA[Fas11].

Energy loss fluctuations. As the *Bragg Peak* characteristics are notably affected by charged particles' average ionization and its fluctuations, an accurate modeling of those effects is particularly important. The *Landau–Vavilov distribution* is typically used to describe energy losses in thin absorbers but it is difficult to implement in MC, FLUKA uses instead an alternative implementation exploiting statistical properties of cumulants of distributions applied to both heavy charged particles and e^+/e^-[Vav57, Fas97b]. This includes full compatibility for δ–ray emission as well as the already mentioned effect of *Mott* corrections, matching the average restricted stopping power[Bat16].

Multiple Coulomb Scattering. Transport of charged hadrons and muons in FLUKA is accomplished with an original implementation of multiple scattering, based on the *Molière theory* of *Multiple Coulomb Scattering*, improved by *Bethe*[Mol48, Mol55, Bet53]. This implementation of the model is characterized by a "condensed history" approach, speeding up the calculation since it does not sample all interactions individually. It accounts for correlations between the final step angular distribution, lateral deflections (average/second moment) and path–length corrections. A rejection technique is used to apply nuclear form factors and spin–relativistic corrections at the 1st or 2nd *Born approximation* level[Fer92]. Additionally, it includes the *Fano correction* for heavy charged particle multiple scattering[Fan54].

Optionally, the code can work in *Single Scattering mode*, an algorithm based on the *Mott* formula with a screening factor consistent with *Molière theory* implementation in FLUKA. It is also capable of reproducing electron backscattering and energy deposition in very thin material layers where *Molière theory* does not apply. It is not a default setting because it is penalyzing in terms of CPU[Fas97a].

Overall, the transport and energy loss mechanisms implemented in FLUKA have been verified to be well in agreement with data for heavy ions (carbon, oxygen and helium ions) and provided experimental parameters (*e.g.* I) are consistent. Some benchmarking examples are provided in literature for medical applications[Som07, Mai07, Man15]. The use of FLUKA for generation of input data to the clinical TPS at HIT and its validation in terms of depth dose distributions in water, yielding range agreement within 100 μm in range and absolute 1.5% in dose in ion therapy in general exemplifies the accuracy the electromagnetic physics models but also of the nuclear models capability in predicting non–elastic nuclear interactions[Bat16, Tes17].

Chapter 3

Tools developed using FLUKA

> "When you want to know how things really work, study them when they're coming apart."
>
> — William Gibson, *Zero History*.

This chapter details the various tools conceived for:

1. Generation of SOBPs using FLUKA, according to preset parameters defined by the user and checked against a research treatment planning system;
2. Enabling the simulation of PET acquisitions in *in beam PET* scenarios, using the newly developed FLUKA PET TOOLS.

3.1 Generating stable SOBP according to clinical irradiation parameters

In order to compare the dosimetric properties of different beams in clinical–like scenarios, SOBPs with an uniform physical dose at the "plateau" were systematically generated for this work. A plateau value of 1 Gy was considered optimal, since it was assumed to translate into 3 Gy (RBE), which are values of biological dose prescribed, per fraction, for scanned carbon ion treatments reported in clinical cases[Bau13, Bau14]. Moreover, [IAEA–TRS–461] stipulates a RBE value of around 3 for carbon ion beams at the SOBP "plateau" center depending on the tissue and tumor type, based on GSI and NIRS studies, further supporting the present work approach[KS00, Suz00]. However, one must recall that, even though dose intake can only be completely evaluated using the notion of biological dose, the present study is limited to a physical dose evaluation.

Using FLUKA built–in estimators, absorbed dose was scored for dose delivery verification. This value was normalized to [$\mathrm{Gy} \equiv \mathrm{J\ kg^{-1}}$] (see equation 1.13). Water was used as target material for optimization with `TRiP` TPS, which was developed at GSI and used at HIT for research purposes only. The dose profile scored consisted of ^{12}C and ^{16}O ions SOBPs, with subsequent extrapolation for $RI\beta^+$.

As the creation of these SOBPs requires inverse planning, some SOBP results optimized at HIT in water with the research TPS for ^{12}C and ^{16}O ions, were provided for this work. The dose optimization process consists of the automatic generation of pencil–like beams with modulated intensities so as to achieve proper longitudinal and lateral prescribed doses[Bau14]. The research

TPS data provided were not entirely based on the standard `TRiP98` code developed and used for clinical purposes at GSI[Krä00, Kra08], being instead upgraded with an older FLUKA version, hence it will be referred simply as OLDTPS in this work. At HIT, an improved version of `TRiP` is used for research purposes, further upgraded with a detailed model of the HIT beamline using a more recent FLUKA version[KMP12, Bau14, Ian15]. FLUKA was also used for validation and generation of the dosimetric TPS input, such as laterally integrated depth dose, double Gaussian parametrization and fragment spectra, for each of 255 energy steps for protons, carbon and oxygen ions as already mentioned in chapter 2. From here onward, whenever referring to this newer research TPS version, or when both are mentioned, this latter version will be denominated explicitly NEWTPS and the older OLDTPS. Moreover, one should note that at HIT the *Syngo PT Planning* is employed for clinical applications with carbon ions, but no data from this commercial TPS has been used in this work.

For the comparisons hereby included in this work, OLDTPS data were provided by HIT. They include the initial ion kinetic energy (tabulated) and number of ions per beam spot, as well as the focus information, which is the beam lateral size in air at isocenter, for each of the isoenergetic layers. An initial beam size in vacuum of 2.5 mm FWHM was considered in the simulations for all the beams at each spot.

The data were used to check whether a valid SOBP in water could be obtained for an *in silico* comparison. Six therapy plans were provided in total, their characteristics are depicted in table 3.1:

Table 3.1: *Treatment plan details.*

Beams	SOBP length [cm]	SOBP dose [Gy]	Field area [cm^2]	Depth in water [cm]
^{12}C	3	1	5×5	10
^{12}C	3	1	5×5	15
^{12}C	3	1	5×5	20
^{16}O	3	1	5×5	10
^{16}O	3	1	5×5	15
^{16}O	3	1	5×5	20

The SOBP dose refers to the dose value at the SOBP "plateau", whereas the field area consists of the surface covered by the beam spots at each isoenergetic layer, later depicted in figure 3.4. The SOBP length indicates the "plateau" longitudinal length. As for the SOBP depth, it refers to the longitudinal isocenter of the "plateau". Please note that the data were valid for water phantoms only.

The geometry setup in FLUKA had to make use of minor approximations, as some of the elements along the beam path were either far too complex to be implemented, or their information was undisclosed due to confidentiality issues[Rin15, Tes16a]. Besides the geometry approximations, the description of materials in terms of water equivalent thicknesses could amplify the inconsistencies, particularly in the case of oxygen ion beams, due to a larger impact of nuclear reaction effects[KMP12].

All beam line elements are manufactured by *Siemens AG* and consist of: vacuum window, a beam and application monitoring system (BAMS) with two multiwire proportional chambers (MWPCs), separated by three ionizing chambers (IC) for beam monitoring, and finally a Ripple Filter (RiFi)[PMS13]. These elements are depicted in figure 3.1.

In the FLUKA simulations in this work, water equivalent thicknesses were employed in the beam attenuation for all these beam line elements, except the RiFi.

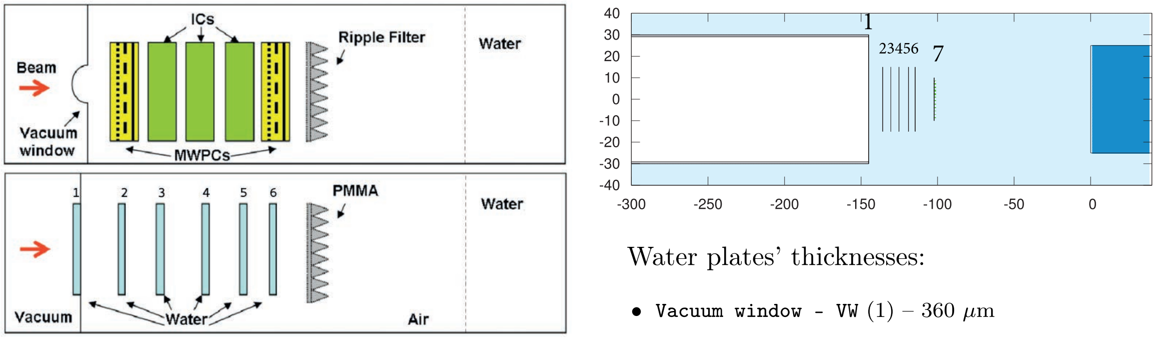

- `Ripple Filter` (7) material: PMMA

Water plates' thicknesses:

- `Vacuum window - VW` (1) – 360 μm
- `MWPC` (2,6) – 160 μm
- `Ionizing Chambers` (3,4,5) – 230 μm

Figure 3.1: *On the left, a schematic view of the beam line geometry*[*Pa12b*]*. On the right, a description of water equivalent approximations as implemented in this work into FLUKA's Geoviewer.*

In addition to these geometry elements, the water density was changed to 0.998 [g cm^{-3}] to account for the temperature during the data taking, and the mean excitation energy was set to 77.3 eV for consistency with the setting used at HIT for the basic data put into `TRiP`. The simulation transport thresholds for all charged hadrons were set to 100 keV, for electrons and positrons to 50 keV and for photons to 5 keV.

Regarding the RiFi, its effect could not be reproduced simply with water equivalent approximations, as evidenced in figure 3.2[Bou08, Krä00, Rin15]. Therefore, a RiFi model was devised for this work as a set of triangular–shaped structures with 3 mm height in a vertical plate, the full set being made of PMMA with density of 1.19 [g cm^{-3}], as displayed in figure 3.3. It acts as a passive energy modulator, degrading the beam, attenuating the peaks' maximum values and smoothing its resulting distribution[Rin15]. The homogeneization of the field dose delivered is ensured by the triangular structures' design (height, spacing), which is optimized to the present beam delivery setup[WK99].

The major consequence of using a RiFi is the reduction of the number of isoenergetic layers needed to achieve a smooth plateau at the SOBP level. Consequently, the number of energy steps required for the dose delivery is also reduced, translating into less overall irradiation time, as energy changes can be time–consuming in some accelerator setups[Rin15].

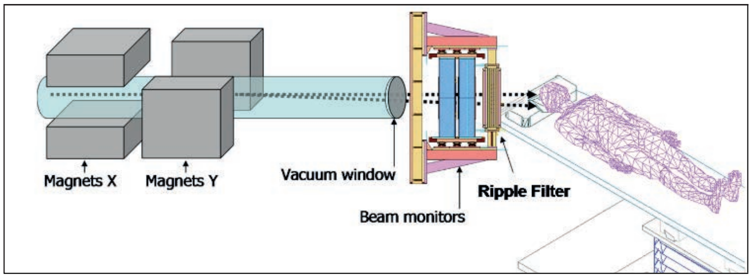

(a) Conceptual beam delivery system, with the RiFi highlighted[Bou08].

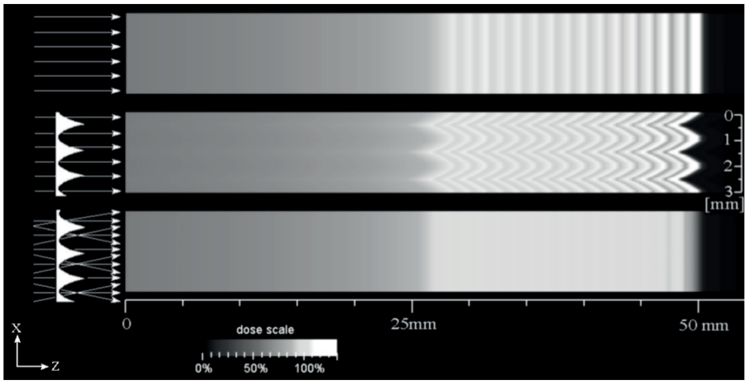

(b) Dose distribution without RiFi (up), with RiFi but not accounting for the scattering effect (middle) and finally accounting for scattering effect (bottom).

Figure 3.2: *RiFi positioning in the beamline and effect on the dose delivered*[*WK99*].

The correct design of a RiFi is particularly important for ion beams since, given their narrower *Bragg Peak* compared to protons and less *straggling*, they are more sensitive to a faulty RiFi geometry[Pa12b]. Furthermore, as a physical obstacle, it implies *per se* a loss of energy, quantified as $\sim 1\%$ in simulation tests, leading to a beam range shift as well as beam quality degradation.

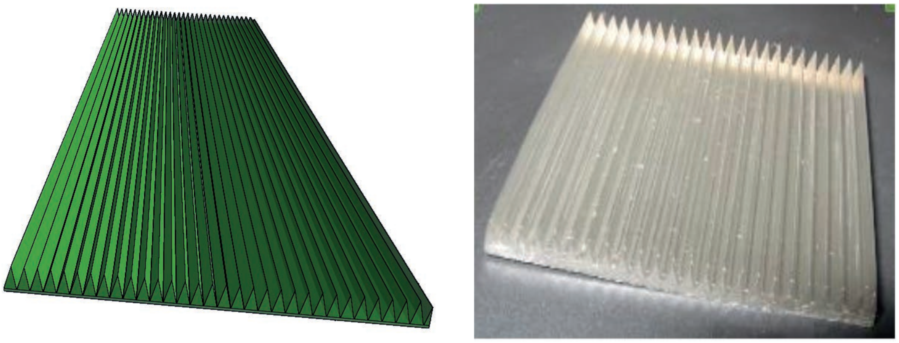

(a) Simulated (b) Realistic view

Figure 3.3: *Example of simulated and real RiFi samples.*

In order to accomplish a simulation employing the TPS data, multiple beams had to be generated simultaneously from different spots over a squared grid, attaining the desired radiation field. This procedure is illustrated in figure 3.4 (a). These data consisted of a total of 625 beam spots, each created at different coordinates, evenly distributed and separated from the neighbouring spot by 2 mm, as depicted in figure 3.4 (b) in a simulation scoring only the beam particle fluence (`BEAMPART`).

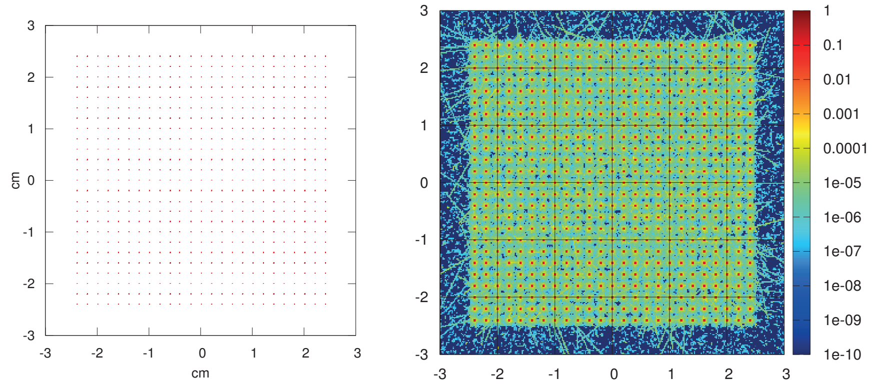

(a) Initial beam spots' distribution in the squared grid.

(b) Transverse view of `BEAMPART` fluence (particle cm^{-2}) as the ions traverse the vacuum window.

Figure 3.4: *`BEAMPART` scoring before (a) and at (b) vacuum window, using source.f for the grid–like field generation.*

Due to the fact that every beam in such scheme has equal energy, and predefined number of particles per spot, the overall structure is denominated as an isoenergetic layer. The latter is characterized by an average range and intensity and, by combining different isoenergetic layers, a SOBP is obtained[Pa12b, Tes16a]. Besides the particle type, energy, intensity and positional distribution of beams in space, each beam spot in this work was set with momentum spread $\Delta p/p = 0.1\%$ (FWHM), its shape gaussian with a FWHM of 2.5 mm in vacuum, broadened after traversing air and beam line elements[PMS13]. This value was implemented in `source.f`, in the appendix A.

3.1.1 SOBP creation method

The `TRiP` data from HIT consisted of ^{12}C and ^{16}O ion beams. In order to perform an inverse optimization and create SOBPs for ^{11}C and ^{15}O, a set of scripts was developed that, for a particular geometry:

1. Calculate the energies to produce pristine *Bragg Peaks* at the specific ranges desired in a FLUKA simulation. A database `bpgen.cpp` comprising fitted energy *vs* range values, for multiple ions, was created for the purpose.

2. After selecting the desired SOBP depth in water, one can simulate the desired number of pristine *Bragg Peaks* according to the database energy parameters for the beam particle chosen.

3. Once finished, the laterally integrated output, in the form of energy deposition $\mathcal{E}$, is optimized so that the weights (*i.e.* number of ions) for each of the pristine *Bragg Peaks* are calculated.

This leads to a SOBP "plateau" dose level as defined by the user, upon unit conversion as detailed in equation 3.3.

4. The subsequent SOBP is then automatically plotted, generating a table with the corresponding number of ions for each field/peak. The number of ions calculated in this process will be denoted as $\mathcal{I}$.

The three last items are handled by a program `supra.cpp` which, as `bpgen.cpp`, can be found in the appendix. The following scheme details the main steps to generate a SOBP:

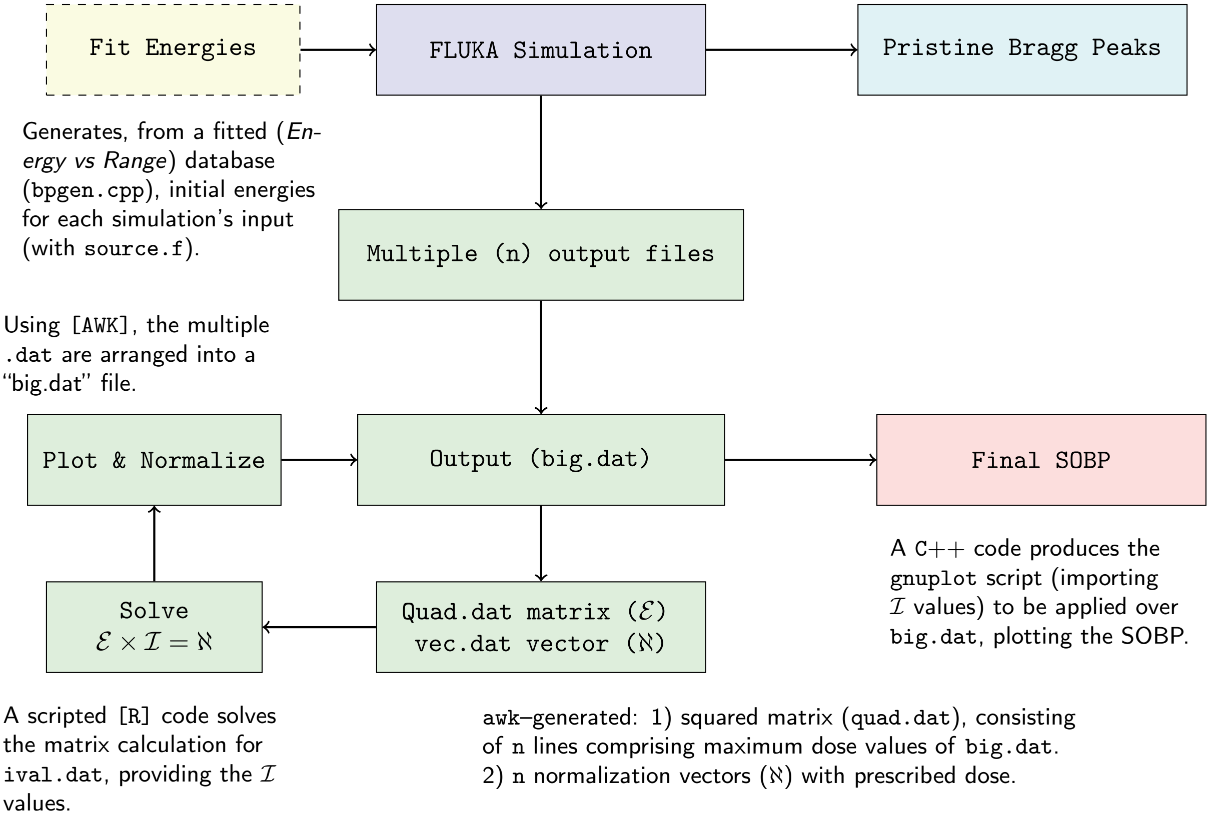

Generates, from a fitted (*Energy vs Range*) database (`bpgen.cpp`), initial energies for each simulation's input (with `source.f`).

Using `[AWK]`, the multiple `.dat` are arranged into a "big.dat" file.

A `C++` code produces the `gnuplot` script (importing $\mathcal{I}$ values) to be applied over `big.dat`, plotting the SOBP.

A scripted `[R]` code solves the matrix calculation for `ival.dat`, providing the $\mathcal{I}$ values.

`awk`–generated: 1) squared matrix (`quad.dat`), consisting of `n` lines comprising maximum dose values of `big.dat`. 2) `n` normalization vectors ($\aleph$) with prescribed dose.

Figure 3.5: *Schematic view of the* SOBP *creation process, the green–coloured entries are handled by* `supra.cpp`

Considering a circular Gaussian shaped beam spot, the transverse beam profile is obtained as

$$I(x,y) = \frac{I}{2\pi\sigma^2_{(x,y)}} \exp\left[-\frac{(x^2+y^2)}{2\sigma^2_{(x,y)}}\right], \tag{3.1}$$

with $I(x,y)$ being the intensity at position (x,y) with respect to the isocenter and I the total intensity, in particles per second[HL15].

The partial energy deposition from a pencil ion beam with initial energy E (at the isocenter) can be described as dose D in the following manner[Bor97, Krä00, Kra08]

$$D(E,r) \quad [\mathrm{Gy}] = 1.602 \times 10^{-10} d(E,z) \left[\frac{\mathrm{MeV}}{\mathrm{g\ cm^{-2}}}\right] \frac{\mathcal{I}}{2\pi\sigma^2} \left[\frac{\mathrm{particles}}{\mathrm{cm^2}}\right] \exp\left(-\frac{1}{2}\frac{r^2}{\sigma^2}\right), \tag{3.2}$$

with $d(E,z)$ being the laterally integrated dose at depth z, r the lateral distance from the central axis of the beam, σ the Gaussian beam profile standard deviation and $\mathcal{I}$ the ion number. The constant factors ensure the proper numerical conversion from [MeV] to [J], as $\left[Gy \equiv \mathrm{J\,kg^{-1}}\right]$

However, assuming an homogeneous, squared field dose delivered over an area $\mathcal{A}(x,y)$, as will be the case in the present work, and adapting equation 3.2 to FLUKA estimators, one can rewrite it instead as

$$D(E,x,y,z) \quad [\mathrm{Gy}] = \kappa \left[\frac{\mathrm{J}}{\mathrm{GeV}}\right] \frac{1}{\rho} \left[\frac{\mathrm{cm^3}}{\mathrm{kg}}\right] \mathcal{E}(z) \left[\frac{\mathrm{GeV}}{\mathrm{cm\,\texttt{ppp}}}\right] \frac{\mathcal{I}}{\mathcal{A}(x,y)} \left[\frac{\mathrm{particles}}{\mathrm{cm^2}}\right], \tag{3.3}$$

where $\mathcal{E}$ is the energy deposition. In FLUKA, as it is scored in a volume it is given in units of $\left[\mathrm{GeV\,cm^{-3}\,\texttt{ppp}^{-1}}\right]$, with `ppp` referring to “per primary particle”. For the subsequent calculations, this result comes integrated over the area $\mathcal{A}(x,y)$ of the estimator, with the resulting `USRBIN-1D` yielding then $\left[\mathrm{GeV\,cm^{-1}\,\texttt{ppp}^{-1}}\right]$ as indicated in equation 3.3. Please note that $\kappa = 1.602 \times 10^{-10} \left[\mathrm{J\,GeV^{-1}}\right]$ and ρ the density chosen according to the room temperature.

The notion of dose area product (DAP) will be sometimes introduced throughout this analysis to highlight the area $\mathcal{A}(x,y)$ selected for the energy deposition calculation. DAP is given in units of [Gy cm^2]. The field dimensions used to score the data in the water phantom consisted of a square with area of 4×4 cm^2. This surface was smaller than the original 5×5 cm^2 generated before interaction with beam line elements [figure 3.4 (b)], so as to ensure that the dose delivery was homogeneous over the surface chosen and not laterally degraded for the following calculation.

Three major weaknesses can be identified in the scripted procedure described in figure 3.5, namely: reliance on a database which would have to be modified to calculate SOBPs in different material or geometry; statistical requirements limiting its application in complex scenarios without heavy CPU power; since the calculation is performed for a laterally integrated volume, it may fail when applied to heterogeneous materials. Nevertheless, for the scope of this work the procedure followed can be considered adequate.

Provided the database `bpgen.cpp` is properly set, `supra.cpp` will generate a table containing all the simulation outputs from the multiple `.dat` files. Each column will correspond to the energy deposition in depth of a pristine *Bragg Peak*, integrated laterally, the so called `big.dat` file.

For the present case, 16 isoenergetic layers and pristine *Bragg Peak* results, were used for the sake of consistency according to the `TRiP` data provided. However, other valid combinations could be attained with the present method, for different ranges, with different number of isoenergetic layers and alternative SOBP plateau lengths. One should note that the database fits are only valid within the considered ranges of 2–30 cm.

The last step of the calculation is accomplished by representing `big.dat` file into a squared matrix (`quad.dat`), consisting of the lines that contain the maximum value of energy deposition per individual beam. In this manner, the lines of the squared `quad.dat` matrix are to be regarded as the unweighted isoenergetic layers contributions, whereas the columns correspond to pristine *Bragg Peaks* values.

The peak normalization values are then extracted, properly weighting the contributions from all beams to the final SOBP result. Once in the form of a squared matrix `n`×`n`, or `quad.dat`, it can then be described as $\mathcal{E} \times \mathcal{I} = \aleph$:

$$\begin{array}{ccccc} \texttt{quad.dat} & & \texttt{ival.dat} & & \texttt{vec.dat} \\ \begin{bmatrix} \mathcal{E}_{11} & \mathcal{E}_{12} & \mathcal{E}_{13} & \cdots & \mathcal{E}_{1n} \\ \mathcal{E}_{21} & \mathcal{E}_{22} & \mathcal{E}_{23} & \cdots & \mathcal{E}_{2n} \\ \mathcal{E}_{31} & \mathcal{E}_{32} & \mathcal{E}_{33} & \cdots & \mathcal{E}_{3n} \\ \vdots & \vdots & \vdots & \ddots & \vdots \\ \mathcal{E}_{n1} & \mathcal{E}_{n2} & \mathcal{E}_{n3} & \cdots & \mathcal{E}_{nn} \end{bmatrix} & \cdot & \begin{bmatrix} \mathcal{I}_1 \\ \mathcal{I}_2 \\ \mathcal{I}_3 \\ \vdots \\ \mathcal{I}_n \end{bmatrix} & = & \begin{bmatrix} \aleph \\ \aleph \\ \aleph \\ \vdots \\ \aleph \end{bmatrix} \end{array}$$

As for n, it is now strictly equal to the number of pristine *Bragg Peaks* simulated, this assuming each has a unique maximum value. $\mathcal{E}(z)$ is the energy deposition value in depth, directly given by FLUKA as output $\left[\mathrm{GeV\,cm^{-1}}\,\texttt{ppp}^{-1}\right]$, with the maximum of each beam diagonalized.

In the present case considered, the normalization constant $\aleph = \kappa/\rho\mathcal{A}$, is the factor required for a single peak to reach a dose D, and obeys the following relationship extracted from equation 3.3

$$D \quad [\mathrm{Gy}] = \frac{\kappa}{\rho\mathcal{A}}\mathcal{E}\mathcal{I}, \tag{3.4}$$

where the simulation media density ρ and estimator area $\mathcal{A}$ are given by the user in `supra.cpp`. A vector column of $\aleph$–value entries is then generated with as many elements as there are isoenergetic layers (`vec.dat`). These act as a normalization factor, and ensure that the sum of peak values of each pristine *Bragg Peak* of the SOBP will attain the prescribed dose. Hence, it sets the system as $\mathcal{E} \times \mathcal{I} = \aleph$ automatically. Note that in this work D was set to 1 Gy, but the method is also valid for other values, in which case the normalization factor would be rescaled accordingly.

$\mathcal{I}_n$, on the other hand, is the number of ions required to achieve the prescribed dose value. Obtaining the number of ions corresponding to each beam, and thus with a certain energy, can be achieved solving for $\mathcal{I}$:

$$\begin{bmatrix} \mathcal{I}_1 \\ \mathcal{I}_2 \\ \mathcal{I}_3 \\ \vdots \\ \mathcal{I}_n \end{bmatrix} = \begin{bmatrix} \mathcal{E}_{11} & \mathcal{E}_{12} & \mathcal{E}_{13} & \cdots & \mathcal{E}_{1n} \\ \mathcal{E}_{21} & \mathcal{E}_{22} & \mathcal{E}_{23} & \cdots & \mathcal{E}_{2n} \\ \mathcal{E}_{31} & \mathcal{E}_{32} & \mathcal{E}_{33} & \cdots & \mathcal{E}_{3n} \\ \vdots & \vdots & \vdots & \ddots & \vdots \\ \mathcal{E}_{n1} & \mathcal{E}_{n2} & \mathcal{E}_{n3} & \cdots & \mathcal{E}_{nn} \end{bmatrix}^{-1} \cdot \begin{bmatrix} \aleph \\ \aleph \\ \aleph \\ \vdots \\ \aleph \end{bmatrix}$$

The inverse of the squared matrix is obtained implicitly by solving the system $\mathcal{E} \times \mathcal{I} = \aleph$, by `supra.cpp`, retrieving $\mathcal{I} = \mathcal{E}^{-1} \times \aleph$ under the form of a `.dat` file, denominated `ival.dat`.

The values in `big.dat` are plotted in units of DAP [Gy cm^2], using an expression of the form used in equation

$$\mathrm{DAP} \quad [\mathrm{Gy\,cm^2}] = \mathrm{D} \times \mathcal{A}' = \aleph\mathcal{E}\mathcal{I}\mathcal{A}', \tag{3.5}$$

ultimately obtaining the DAP values at different positions in depth. Here, $\mathcal{A}'$ is an area value that behaves *de facto* as a normalization factor, to scale the dose according to the area chosen for the plot. The reason for using DAP is to explicitly convey the information of the lateral limits of the isoenergetic layer for the plot. For a direct comparison with OLDTPS data provided, $\mathcal{A}'$ was set as a squared area with 4 cm length, yielding a maximum dose 1 Gy, thus the DAP value at the SOBP corresponded to 16 [Gy cm^2]. SOBP plots were directly obtained from the simulated $\mathcal{E}$ result values, contained in `big.dat`, while applying `ival.dat` as $\mathcal{I}$ in equation 3.3, resulting in the final SOBP.

Regarding the OLDTPS data provided in table 3.1, it contains the total number of particle for obtaining a SOBP of 1 Gy at each of the 16 isoenergetic layers $\mathcal{I}'_n$, where $n = 1, 2, 3 \dots 16$. However, it has been observed by the TPS provider that when recalculated with FLUKA, the `TRiP` plan for ^{12}C yielded 0.95 Gy and not 1 Gy at the SOBP “plateau”. This has consequences that will manifest in chapter 5.

The number of particles, for each isoenergetic layer provided in the OLDTPS, is equally divided among the 625 raster scan spots ($i_{x,y}$) that compose the dose delivery cross section 5×5 cm^2 surface before interaction with the beam line elements. Then, each isoenergetic layer n is accounted for with their respective i values, so that the total number of particles delivered in the plan $\mathcal{I}_\mathrm{T}$ to accomplish a SOBP are given by:

$$\mathcal{I}_\mathrm{T} = \sum_{n=1}^{16} \mathcal{I}'_n = \sum_{n=1}^{16} \left(\sum_{x=1}^{25} \sum_{y=1}^{25} i_{n,x,y} \right). \tag{3.6}$$

Note that the resulting dose distribution was seen to correspond to an homogeneous dose only over a surface of 16 cm^2 at the SOBP, even though the initial surface covered by the beam spots was of 25 cm^2, as displayed in figure 3.4.

3.2 Developments for the application of FLUKA PET TOOLS to ion beam range verification scenarios

FLUKA PET TOOLS are one of the major medical themed features currently under development in FLUKA, extending its functionalities in the medical imaging domain[Ort13, Ort14, Bat16, Au18a].

Using these tools, the first reconstruction of PET signals from a beam irradiation was accomplished, its results will be presented later in chapter 5. For consistency, the signals were collected employing the same geometry setup described in section 3.1, but now featuring a PET scanner model and patient geometry, in various acquisition modalities. Contrary to the previous section procedure, customized estimators had to be used, such as user–routine defined lists of particle events occurring in a PET–shaped geometry (`USERDUMP`) along with other PET TOOLS specific scoring elements.

With these tools, it is expected to confirm the imaging advantages of $RI\beta^+$ over stable ions beams, generated in the form of SOBPs with the procedure described in section 3.1. For SOBPs with equal dose, $RI\beta^+$ should boost the amount of annihilation events at rest, leading to considerable improvements in the reconstructed PET signal. Presently, the FLUKA PET TOOLS package consists of[Ort15]:

PET geometry tools – Allows the construction of different PET scanners employing reproducible geometrical elements (lattices) and their roto–translation. The user can either select from some existing commercial models or define a customized model. Scanner construction takes place in three stages, of increasing complexity: blocks → modules → rings (see appendix B).

Scoring routines – All the simulation data relevant to the reconstruction (*e.g.* coincidence γ hit coordinates) is collected by these routines and associated with the detector's geometry, in either binary or ASCII file format. The user can activate flags for obtaining additional information, at the expense of data size increase (*e.g.* parent isotope flags). Dead time and energy window constraints are enforced through the FLUKA input parameters.

Post–processing routines – Consist of routines embedded in the FLUKA code and an external file (`postprocess.param`) to parse detector information to the routines. The latter allows for the processing of output files, creating both a coincidence list or *sinogram* representation, based on the coincidence timing window. In both representations, scatter, random, true and total coincidences are produced.

The *sinogram* is a set of projections obtained from different angles, as a linear transform of the original image. Each projection will consist of parallel one–dimensional rays across the two–dimensional target, yielding the integral of the object contrast along each ray to a single projection pixel. In this representation, a single row describes the projected view of the intensity throughout a single angle (*Michelogram*)[Def97]. For each pair of crystal rings defined by the user, a *sinogram* storing either 2D or 3D images in a binary file will be created[Fah02, Ort13]. For the *Siemens Biograph m*CT, 109 *sinograms* were created, in a 3D mode. In order to apply iterative reconstruction algorithms to 3D data and mitigate the computational burden, the data is first rebinned into 2D *sinograms* employing *Fourier rebinning*. This methodology results in relatively fast reconstructions, but may incur into resolution losses. The characteristics and quality of these sinograms can be improved with several post–processing parameters, such as: *arc correction, maximum ring difference, number of segments, span* and *mashing factor*[Ort15]. The parameter options employed in this work are shown in table C, in the appendix B

Imaging tools – The current version includes a fast 2D reconstruction *filtered–back–projection* (FBP) algorithm, for fast *sinogram* reconstructions with limited quality. This version also features an embedded iterative *maximum-likelihood–estimation–method* (MLEM) based reconstruction algorithm, to transform coincidence lists into images[Tou16]. The latter is capable of producing better quality images than the FBP, but it also requires longer reconstruction times. Moreover, it lacks attenuation corrections, which are currently under development. External reconstruction algorithms can be applied to both the coincidence list or *sinogram* produced as output. For the results that will be later presented in chapter 5, image reconstruction algorithms optimized for the scanner model were employed[Gia14, Gia16].

With this package, mainly developed by P. G. Ortega *et al.*, one can exploit the full predictive power of FLUKA, to validate not only treatment scenarios (dosimetry), but also reproduce PET/CT scanner response in R&D environment and perform diagnostics (imaging). However, the PET response simulation was limited to predefined β^+ emitter source scenarios. In order to perform realistic *in beam PET* simulations with FLUKA PET TOOLS, the following tasks were accomplished:

1. Creation of a realistic PET device in the *flair* library similar to the scanner found at HIT, using the *Siemens Biograph m*CT model online information[STP08].
2. Usage of a patient VOXEL phantom, instead of a water phantom, for a more realistic dose distribution[Bat16].

3. Integration of an approximate beam time structure and inclusion of the possibility of filtering the events, according to the acquisition time, in the tools post–processing routines[Au18a].

The *Siemens Biograph m*CT PET/CT scanner (*Siemens Molecular Imaging, Knoxville, USA*) is now available in the FLUKA PET TOOLS scanner database in *flair*. The full extent of both geometry and operational parameters, implemented in the TruePoint TrueV option (which extends the FOV by 33%), can be found in table 2, annexed.

Regarding the overall scanner geometry, it was defined so as to be in line with the setup found at HIT, depicted in figure 3.6, just next to the treatment room, for *offline PET* acquisitions. The setup simulated in this work corresponded effectively to an *in beam PET*, in the sense that scanner and beam line are coupled, while at HIT the scanner and the beam line are in different rooms, as mentioned in chapter 1. As a consequence, the irradiation and acquisition scenarios hereby presented for PET acquisition, namely: *online* (*i.e.* resulting from both *in–spill* and *inter–spill*), *in room* and *offline*, were all simulated with the scanner and beam line coupled. This was intended as the simplest way to evaluate all acquisitions without altering the simulations. This implementation is illustrated in figure 3.7

Figure 3.6: *Siemens PET mCT Biograph model version available at* HIT[*STP08*].

The beam line elements employed were those delineated in figure 3.1, but with the scanner setup positioned as in a fully operational *in beam PET* scenario. However, the PET/CT scanner was neither shifted nor open as in typical *in beam PET* setups, so as to keep the system as simple as possible for the performance evaluation of the different ion beams.

Even though this scanner model is currently applied in *offline PET* acquisitions, it has successfully passed tests to validate its performance in *online* mode[Sha11]. Please note that the present work is not intended as a clinical or technical validation of any PET acquisition scenario, the purpose is instead to set a proof of concept for the FLUKA PET TOOLS with subsequent evaluation of the different ion beams performance. Furthermore, one must note that the hereby proposed *in beam PET* modality uses a full ring and thus the images obtained could have an increased quality (*e.g.* more statistics, more efficient image reconstruction) than in previously reported *in beam PET* setups[CSE06]. However, the aforementioned effect is common to all ion beam species studied.

In addition to the PET/CT setup, an antropomorphic head VOXEL geometry was also used instead of a water phantom, as depicted in figure 3.7 (a). It was used for obtaining the PET reconstructed results that will be shown in chapter 5. The water phantom setup displayed in figure 3.7 (b) will be used in chapter 4 for the scoring of different quantities in water.

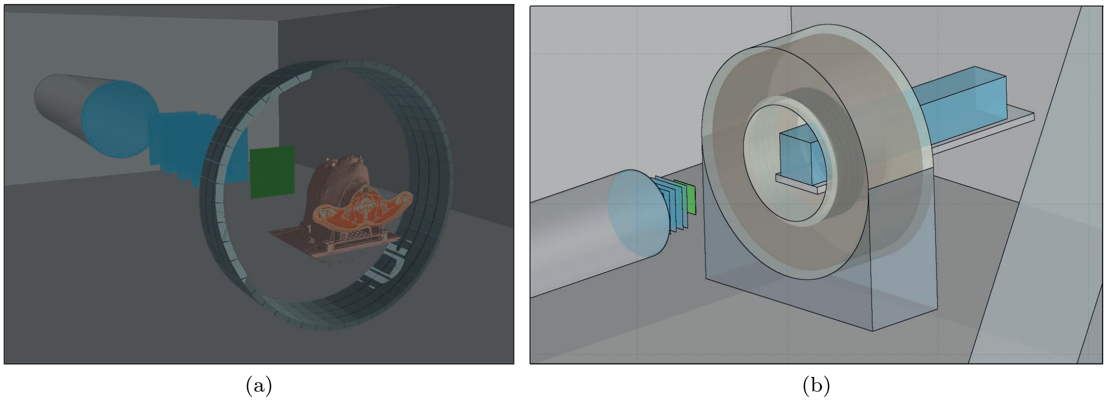
(a) (b)

Figure 3.7: PET *scanner device, with the* VOXEL *phantom and other* HIT *approximated geometry elements for image reconstruction (a). Realistically implemented geometry in flair with PET Biograph mCT device around an enlarged water phantom for testing purposes (b).*

While the use of water as an approximation to human tissue can be justified for tests, an heterogeneous/realistic distribution is preferable. This is because even though tissue is composed mostly by hydrogen and oxygen, bones and other differentiated structures in tissue may lead to lateral scattering, range *straggling* effects and different β^+ emitter formation/yield beoyond those predicted in water, affecting dose delivery and the corresponding PET signal[Tur95]. Therefore, a more realistic model, using a voxelized patient–like geometry was sought for a more representative result. The FLUKA implementation consists of 30 different main materials, with a given composition and nominal mean density, varying from air to titanium implants in a $-1024 < \text{HU} \leq 3060$ range with a continuous stopping power and density scaling factors attributed for each HU value[SBS00, JP04, Fer06, Pa07b].

Before detailing the FLUKA PET TOOLS image reconstruction procedure, it is firstly necessary to illustrate the tools' workflow, summarized in figure 3.8. In the flowchart, the functions handled by the FLUKA PET TOOLS are colored in tones of blue while the green colored functions denote the FLUKA simulation's elements of relevance[Au18a].

These tools, as mentioned earlier, are embedded into FLUKA, therefore supporting all its functionalities (*e.g.* radiation source generation, built–in estimators). Using a set of prepared tools, supported by documentation, a user can extract PET acquisition results from a predetermined radioactive source with minimal coding. However, this is not (yet) the case for a beam irradiation. For the latter, the user must alter the post–processing procedure to accommodate both the beam time structure and acquisition time effects. In this work, the output `USERDUMP` of the various simulations was modified *a posteriori*, according to the beam time structure and acquisition times considered, using scripts that complement the existing post–processing procedure.

The SOBP tools described in section 3.1 were employed in generating SOBPs of 1 Gy for ^{11}C, ^{12}C, ^{15}O and ^{16}O ions in water for tests, and later for the voxel phantom. The latter results are shown in chapter 5 while the former can be seen in the next chapter.

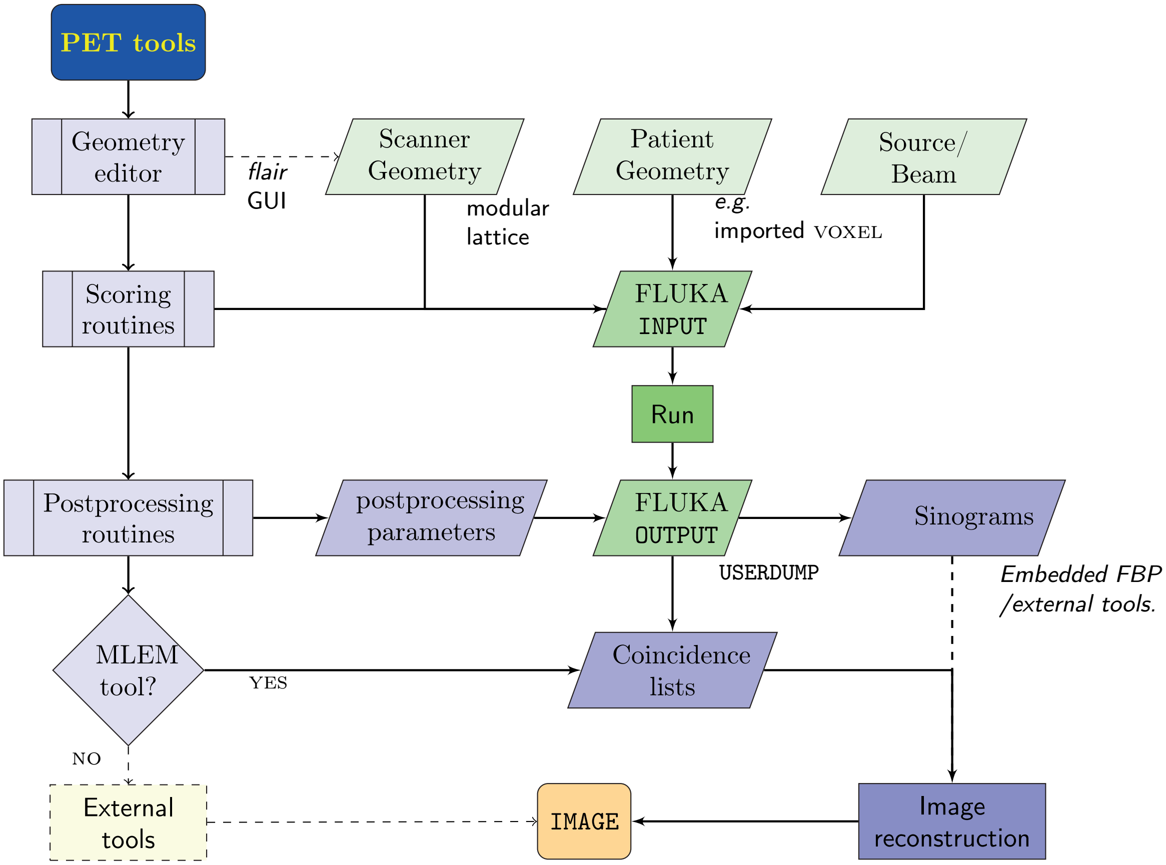

Figure 3.8: FLUKA's PET TOOLS *description, from simulation setup to the final image reconstruction: The dashed lines correspond to optional features whereas the functions connected by solid lines are automatically handled by the tools.* ***USERDUMP*** *corresponds to the built–in FLUKA estimator's output (in* ASCII*), to be used as input in the post–processing stage and subsequent image reconstruction.*

Due to the large amount of particles and inherent computational burden, it was decided to use only a range of 10 cm as a representative irradiation scenario for both water and antropomorphic head VOXEL geometries. For each input, the output results in an `USERDUMP`, whose general structure and columns of interest are highlighted in table 3.2.

Table 3.2: ***USERDUMP*** *structure, with the post–scripting elements highlighted and different abbreviations explained in the text.*

EV-NUM	SOU-NUM	PART-ID	SOU-ID	IRADL	IANGL	IRING	SOU-X	SOU-Y	SOU-Z
SOU-T	SOU-KinE	HIT-X	HIT-Y	HIT-Z	HIT-T	DEP-E	WEIGHT	N-CMPT	N-RAYL

`EV-NUM` (red) is an unique number identifying the event detected, in every simulation. The yellow entries $\mathtt{HIT}_{\mathtt{X,Y,Z}}$ are the coordinates on the lattice at which the energy is deposited, $\mathtt{SOU}_{\mathtt{X,Y,Z}}$ are the origin coordinates of the particles leading to the aforementioned hit. As for the orange entries (`-T`), they denote the time (in ns) of these respective events, for each simulation.

For the ensuing irradiation scenarios, the above mentioned `USERDUMP` file can be subsequently postprocessed to obtain the *sinogram* and a list of coincidences reflecting the beam–time and PET acquisition effect. The advantage of doing this retrospectively is that one can test as many plausible irradiation scenarios as desired. In order to have a final image, obtained only with coincidence events acquired during those pre–determined periods, one needs to manipulate the "time" information dumped, highlighted in orange in table 3.2. This is presently a constraint of *in beam PET* simulations with FLUKA PET TOOLS, in view of the missing ability to reflect the `IRRPROFI` card information, which includes the irradiation time and intensity, in the `USERDUMP` output. Furthermore, since various simulations were required for the different isoenergetic layers of every SOBP, a code was devised, acting in the following manner:

1. During the simulation, as the particles are transported, they will hit ($\mathtt{HIT}_{\mathtt{X,Y,Z}}$) and deposit energy (`DEP-E`) on the lattice elements constituting the PET detector. If within a certain energy window, a line is printed in the `USERDUMP`, containing the source ($\mathtt{SOU}_{\mathtt{X,Y,Z,ID}}$) information that originated the hit (see table 3.2).
2. The reconstruction is then applied considering the time window (using `HIT-T`) information, and the hit coordinates' values. If these criteria are properly space/time–correlated, they are later reconstructed as coincidence events. Moreover, it is also distinguished between types of coincidences: scattering, random or true coincidences. This is done automatically while processing the output.
3. The `SOU-T` (source time in ns), refers always to the time at which the source particle (*e.g.* ^{11}C, neutron) produced the particle originating the hit (*e.g.* photons, electrons) in time `HIT-T`. Therefore, to re–structure the dataset, both `SOU-T` and `HIT-T` values in the same line must be equally shifted in time, otherwise the particle's flight travel would not be physically consistent. For instance, considering a ^{11}C beam simulation, in the `USERDUMP`#2 resulting from `INPUT`#2 and hence the 2$^{\text{nd}}$ energy layer of the SOBP:
    (a) Let one assume that the `USERDUMP` obtained from an isoenergetic layer used ~`5.977E6` primary beam ions, with the subsequent detection registered. One of its events was chosen, corresponding to a ^{11}C decay, originally at `SOU-T=100.000` ns and a photon hitting the PET structure at `HIT-T=101.612` ns.
    (b) According to the beam time structure, and since it corresponds to the second energy layer, the transport should occur between the beginning and the end of the second spill. In this example, it will be considered that the spill occurs between the 9$^{\text{th}}$ and 10$^{\text{th}}$ second, in terms of absolute time in the overall irradiation.
    (c) Naturally, a "shift" of the decay time of the ^{11}C is required, extended to the resulting photon hit time by the same factor `+T`, for the sake of consistency. This factor `+T` being, in this particular case, a *pseudo random* value between 9 and 10 seconds. The decision to use such procedure to generate the `+T` value in fixed time intervals ensures the reproduction of the collective performance of the 625 beam structure in the grid, while adding to it a realistic time structure.
    (d) Completing the example, assuming the shift $\mathtt{+T}_{\mathrm{n}}$ is of 9.6 seconds, where n identifies the irradiation interval, `SOU-T` will then become `SOU-T`+9.6 s and `HIT-T` will be also

incremented by 9.6 s in that `USERDUMP` line. When applied to all beams it results as depicted in figure 3.9.

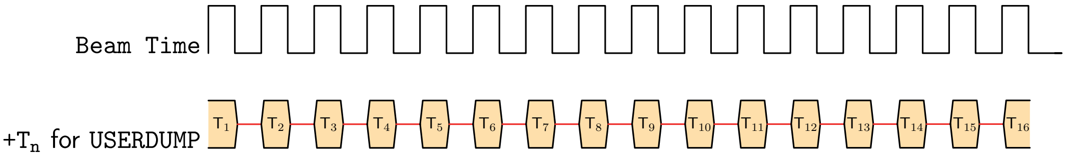

Figure 3.9: *Schematic view of the time structure ordering in the* ***`USERDUMP`*** *.*

where each `+T`$_n$ value is randomly placed only within the boundary conditions of the corresponding spill. This method automatically ensures that every line in the output will reflect the beam time effect.

4. For consistency, the `EV-NUM` entries (red, in table 3.2) in each of the n `USERDUMP`s will have to be changed accordingly, to avoid repetition during post–processing.

Merging all the `USERDUMP`s will gather the full dataset, now properly time structured as illustrated in figure 3.10:

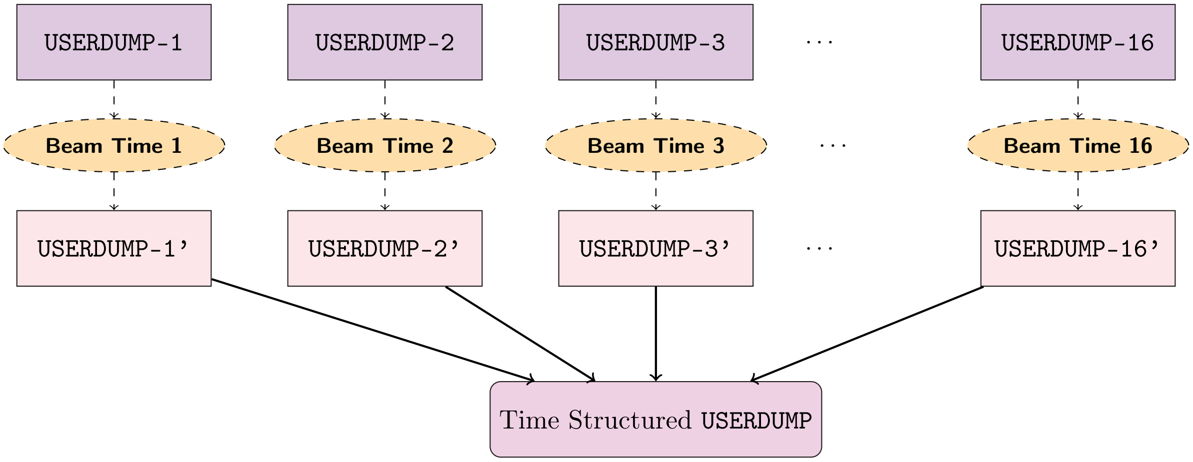

Figure 3.10: *Flow diagram illustrating the merging of the results scored for different beam times in a single* ***`USERDUMP`*** *for subsequent post–processing.*

Once the beam time structure is correctly enforced, and all events ordered, the acquisition time may be accounted for. As the current output contains events from the first particle that hits the detector (*e.g.* a prompt γ) to the last (*e.g.* resulting from the decay of some long–lived isotope), to account only for the events in the time window(s) desired, a filtering based on the `HIT-T` column must be employed. The final `USERDUMP` thus obtained will be ready to be processed with the standard tools.

The standard tools will produce coincidence list–mode data or *sinograms*, but now properly ordered and containing only the events acquired at the respective acquisition time windows. The resulting images will be shown in chapter 5, along with the coincidence details of these acquisitions.

Chapter 4

Basic dosimetry and imaging studies of ion beams using FLUKA

> “Es ist nicht das Ziel der Wissenschaft, der unendlichen Weisheit eine Tür zu öffnen, sondern eine Grenze zu setzen dem unendlichen Irrtum.”
>
> — Bertold Brecht, *Leben des Galilei (1939)*

In this chapter, the dosimetric and imaging properties of different ions were assessed by means of FLUKA simulations of irradiation in water, using the beam species listed in table 4.1. Particularly, their fragmentation products were studied by decomposing the various contributions to the final *Bragg Peak* curves.

Table 4.1: *Ion species evaluated in this work and relevant properties*[*Som07*] *)*

Ion	Half–life ($t_{1/2}$)	Decay emission	β^+ endpoint energy [MeV]
^{12}C	Stable	—	—
^{11}C	20.38 min	β^+	0.96
^{10}C	19.31 s	β^+	1.91
^{9}C	136.50 ms	β^+ (60%)	15.47
^{16}O	Stable	—	—
^{15}O	2.03 min	β^+	1.73

Regarding ^{12}C, it was chosen due to its established use in ion therapy[Kam15]. As for ^{16}O, it is being considered a next candidate for therapy at HIT, and it is deemed particularly relevant due to its higher efficacy against radioresistant tumors, less lateral scattering and higher LET[KMP12]. In addition to that, they are the stable counterparts of ^{11}C and ^{15}O, which are ion species of relevance in the framework of advanced studies at HIMAC, as mentioned in chapter 1. The produced intensities of ^{11}C and ^{15}O may soon match therapy needs and ^{11}C LET is almost equivalent to ^{12}C[Tom03]. Regarding ^{15}O, it is also an interesting species for treatment of hypoxic tumors[Kit06, Moh16]. At HIMAC, ^{10}C, ^{11}C and ^{15}O were employed as probes in range verification. Even though of limited use as a probe, since probes should have half–lives no longer than a couple of minutes to be effective, ^{11}C is potentially interesting to verify dose delivery in range *a posteriori*, either in *offline* or *in* *room PET* modalities. Moreover, ^{11}C, ^{15}O and ^{10}C are also of potential imaging interest in view of their half–lives in *in beam PET*[Ina08]. In this work's fragmentation study, ^{10}C and ^{9}C were only partially evaluated, in order to compare their trend with other heavier carbon ion beams. Even though ^{10}C has been used as a probe by NIRS, its study is far less advanced than ^{11}C, whereas ^{9}C has too short a half–life for direct clinical application and its use is restricted to cellular damage evaluation[Ise04, Kit06]. In addition to the aforementioned species, ^{8}B, ^{13}N and ^{17}F beams were occasionally simulated, for testing purposes, during the generation of different SOBPs detailed in chapter 3 and shown in the appendix A.

The β^+ originating from ^{11}C decay has a rather low *endpoint* energy with respect to ^{10}C and ^{15}O (table 4.1). While the maximum range for β^+ from ^{11}C is about 4.2 mm, for ^{15}O and ^{10}C it can reach 8.4 and 9.2 mm in water, respectively[Ise04, CE16]. The blurring due to this β^+ range for ^{11}C is thus smaller than the resolution of commercial PET scanners. Note that the PET imaging spatial resolution is ultimately limited by the β^+ range and non–collinearity in addition to the detector granularity[Der79, Bai05]. Conversely, ^{13}O, ^{12}N and ^{9}C have all *endpoint* energies above 15 MeV and half–lives much below 1 s, rendering them less suitable for PET applications[Som07]. Since the mean kinetic energy of emitted β^+ is approximately one third of the *endpoint* energy value, the distribution of β^+ emitted by ^{13}O, ^{12}N and ^{9}C was estimated with FLUKA to be higher by factors of ~ 1.5, 2.5 and 2 with respect to ^{11}C, resulting in a stronger blurring effect.

Several built–in estimators in FLUKA were used to acquire (*i.e.* "score") the simulation data in various geometries. Particularly, physical absorbed dose and annihilation events at rest were scored in 3D geometries (`USERBIN`) and employed in dosimetric and imaging studies, respectively. The annihilation event at rest (`ANNIHRST`) is a newly developed estimator, its output consists of "Annihilation events at rest per primary particle". As a quantity directly associated with decay, it must be coupled with the `DCYSCORE` card either for a certain decay time or in *semi-analogue* mode, to be retrieved in the form of a rate or in absolute value, respectively. The imaging potential was evaluated by quantifying the annihilation events at rest arising from the use of different beam types in the simulations.

Unless explicitly said otherwise, the simulation plots will assume that all radioactive species produced decay, with the result being therefore "time integrated" and with the radiation emitted accounted for.

4.1 Dosimetric evaluation of pristine Bragg Peaks for different ion beams

As the primary ion beam traverses a medium, it loses energy in an ever–increasing manner, culminating at the *Bragg Peak* region. Being heavy projectiles, many types of ionizing radiation will be produced as secondaries. A portion of this radiation will consist of lighter secondary nuclei, which will form the fragmentation tail[Har17]. Although not analyzed in this work, such fragments may have a different RBE value than the primary particle, hence requiring their impact to be well assessed for clinical applications.

The experimental "mapping" of those secondary particles is nowadays a topic of great interest, as it can provide better insight on the nuclear reactions taking place, particularly due to the fact that the projectile and most of its fragments are "lost" inside the body in hadrontherapy. However, comparison with experimental data is still not optimal, as data for carbon and other ions are scarce[Pri12, Rob13, Har17]. Given the reliance of TP on MC engines for basic data calculations in ion beam therapy, validation of various secondary production and distribution could not only demonstrate the adequacy of the models implemented in the MC codes, but it could also prove itself most useful in the prediction of dose delivery and also imaging[Som06, Böh10, Mai10, Rob13]. The latter is chiefly due to the relationship between fragmentation and subsequent signal output for example through β^+ emitter nuclei production[Sal16].

In figure 4.1 it is illustrated a *Bragg Peak* dose delivery profile with various species, calculated with FLUKA in a water phantom. The event generators rMQD–2.4 and BME, mentioned in chapter 2 were activated, along with `EVAPORATion` and `COALESCEnce` physics cards. Among the fragments by–products, there will be species decaying through the β^+ mechanism which are centerpiece in this work. These can be an imaging asset due to their occurence exactly at the *Bragg Peak*, for $RI\beta^+$, or in its vicinity for stable beams' irradiation scenarios. However, the mixed field of secondary radiation (*e.g.* p, γ, n *etc...*) is definitely going to contribute to the dose both in the direct beam path as well as in its proximity, depending on the type and energy of the radiation. Low energy neutron transport in FLUKA, below 20 MeV and down to thermal energies, was activated using the `LOW-NEUT` card. As for the energy transport thresholds, they were set at 100 keV for charged hadrons, 80 keV for electrons and positrons and 10 keV for photons.

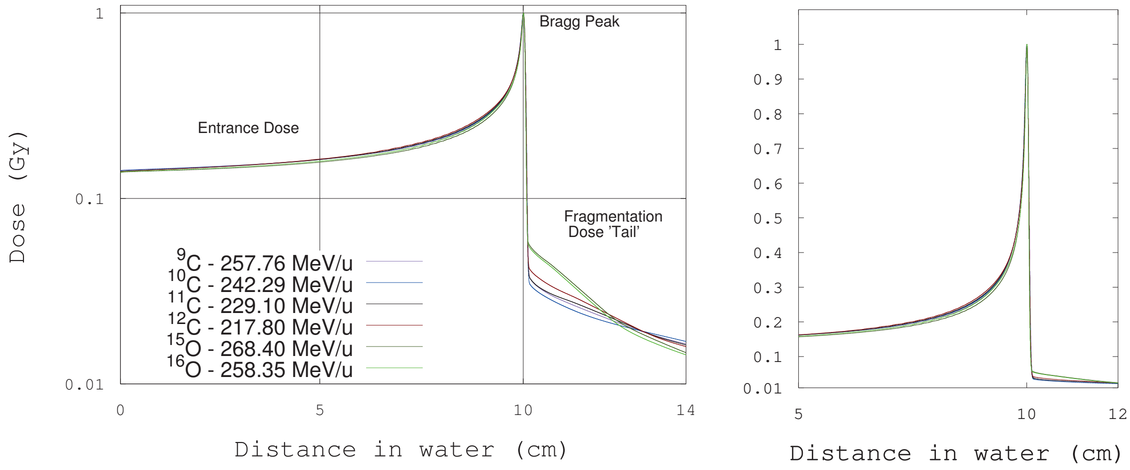

Figure 4.1: *Simulation of Bragg Peak curves for the four major ion species studied in this work, with two additional carbon $RI\beta^+$, for equal range in water. On the left, a logarithmic scale is used whereas on the right the result is plotted using linear scale and a shorter range margin. The peak dose is normalized to 1 Gy in both cases.*

The importance of the mixed field surpasses the prediction of patient dose intake, it also leads to a more accurate imaging potential estimation. Nonetheless, the dosimetric study should remain prioritary with respect to any subsequent imaging potential assessment.

Fragmentation is present throughout the three zones depicted in figure 4.1, but its effect becomes more visible in the fragmentation tail, beyond the *Bragg Peak*. This effect becomes a limiting factor in the selection of heavy charged particles in hadrontherapy, especially for the treatment of deep seated tumors or near OAR.

As discussed in chapter 1, ^{12}C ions are regarded as optimal in view of their high peak–to–entrance RBE differential effect and therefore it is important to understand how $RI\beta^+$ perform with respect to it. In fact, it remains to be seen whether the radioactive species considered in this work, despite their expected imaging potential, would display a comparable dosimetric performance for equivalent–in–range *Bragg Peaks* dose profiles. On the other hand, if it is demonstrated that fragmentation tail doses, or the overall mixed fields, for $RI\beta^+$ are comparable or more advantageous than those of their stable counterpart (*e.g.*^{11}C *vs* ^{12}C ions), their enhanced imaging properties would make them an asset in clinical practice.

Indicatively, in preliminary simulations no significant surplus of dose has been identified using $RI\beta^+$ in the fragmentation zone, as seen in figure 4.1[Aug16]. It has also been observed that the peak–to–entrance dose was equivalent in all beams included in the analysis.

The dose ratio between ^{11}C and ^{12}C yields an approximately $\sim 20\%$ reduction in dose immediately after the peak (figure 4.1). The trend beyond the *Bragg Peaks* has been investigated for irradiations of different ranges in water, resulting in the figure 4.2.

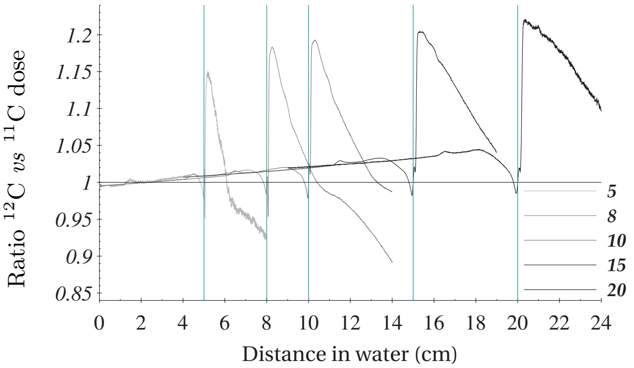

Figure 4.2: *1 Gy Bragg Peak, $^{12}C/^{11}C$ dose ratio at 5, 8, 10, 15 and 20 cm ranges in water. The turquoise vertical lines denote the Bragg Peak position.*

The fragmentation dose tail ratio attains 15% for *Bragg Peaks* at 5 cm depth and surpasses 20% for *Bragg Peaks* at 20 cm. Even more advantageous ratios were observed for either ^{10}C and ^{9}C with respect to ^{12}C, although not quantified here since studies for medical applications of these ions are far from advanced. Regarding ^{15}O, no major advantage with respect to ^{16}O is observed. This fragmentation dose tail ratio effect is also visible in the more realistic SOBPs, which will be presented later in the section 4.1.2.

Throughout the projectile interaction with water, many types of nuclear reactions will occur and each component of the resulting mixed field of radiation will deposit energy of its own at different ranges, depending on their energy, production angle and particle type. Regarding the angle, fragments were seen to be essentially forward projected[Böh10, Rob13]. The fluence evolution can be visualized by means of a reduction of primary ions and thus an increase in secondary particles' fluence (see figure 4.3).

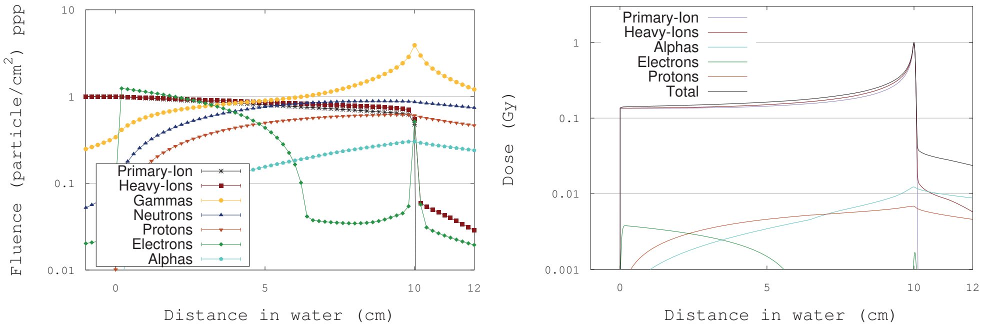

(a) ^{11}C (b) ^{11}C

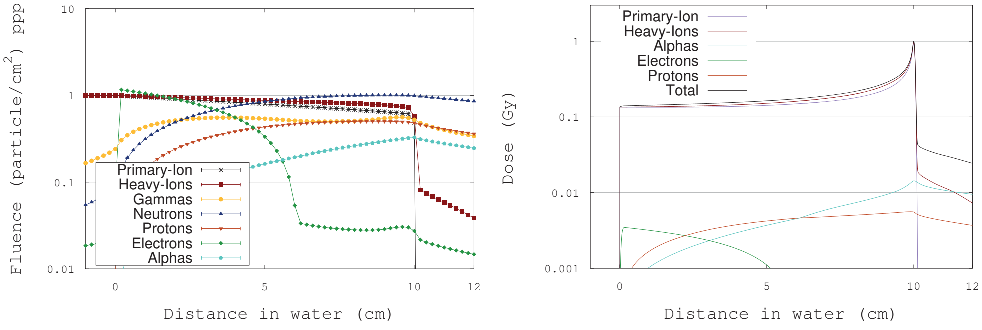

(c) ^{12}C (d) ^{12}C

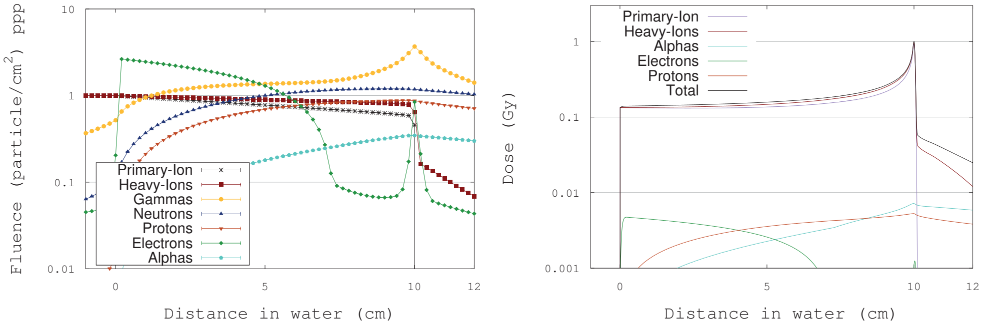

(e) ^{15}O (f) ^{15}O

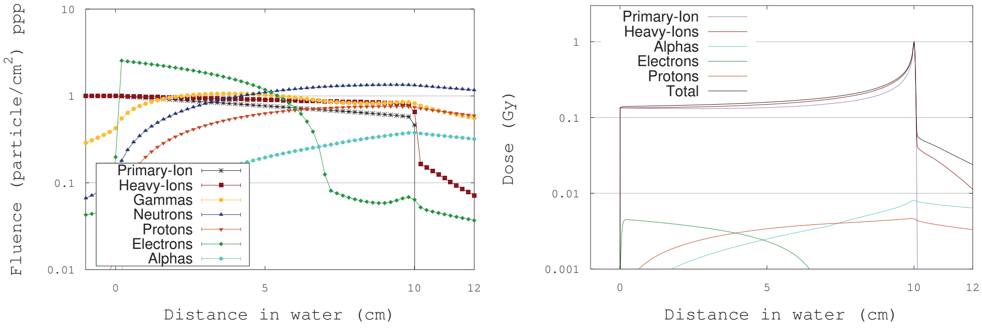

(g) ^{16}O (h) ^{16}O

Figure 4.3: *Comparison of physical dose (right side) and fluence of different particles in depth (left side), obtained with FLUKA. The fluence is normalized to the primary ion value at the entrance of the water phantom (0 cm), whereas the dose values are normalized to 1 Gy, according to the total dose value at the Bragg Peak.*

Depending on the primary ion, some resulting secondary particles may travel considerable lengths as visible in figure 4.3, including light and/or neutral particles but also projectile fragments. This is the rationale of the studies of protons and gammas as an indicator for *Bragg Peak* position mentioned in chapter 1, provided adequate detectors are available to counteract the neutron background (figure 4.3)[Ag12b]. For the $RI\beta^+$ irradiations studied, and compared to their stable counterparts, the value of electron fluence is substantially increased (figure 4.3), particularly at the *Bragg Peak*, by a factor of ~ 20 and ~ 12 for carbon and oxygen ions, respectively. Note that the electron fluence includes also positrons (`E+&E-` estimator) as well as δ–rays. The latter production was explicitly set using the `DELTARAY` transport card to an energy threshold of 300 keV, this value was quite high and consequently it results in an artificially abrupt decrease in electron fluence at approximately half–way to the *Bragg Peak* position, as δ–rays cease to be produced below that threshold. However, in this way one can better identify the sharp raise in electron fluence near the *Bragg Peak* due to the contribution from the β^+ emitters coming at rest. As for the gamma fluence, it increases at the *Bragg Peak* for oxygen ions by 60% and for carbon ions over a factor of ~ 2.5. Neutron fluences are found to be rather comparable between radioactive and stable beams in figure 4.3.

On the other hand, energy deposition as a result of gammas and neutrons is not relevant in the *Bragg Peak* region, due to their neutrality and longer range. Despite the high electron fluence seen in figure 4.3, the energy deposited by electrons is very low. In fact, and as expected, energy deposition is mostly dominated by the primary and other secondary ion's ionization effect.

Regarding the aforementioned $\sim 20\%$ gain in ^{11}C over ^{12}C at the fragmentation dose tail, observed in figure 4.1, it appears to be chiefly influenced by an interplay between α particles and heavier ion contribution, as seen in figure 4.3. The validity of these results requires however experimental verification.

Gamma and neutron particle fluences might increment the dose elsewhere depending on their energy. If for the former the biological impact is relatively low, the latter can be as relevant as ions, depending on their energy. Also, they are characterized by a wider spatial distribution with respect to ions for instance.

The information in figure 4.3 is insufficient to fully characterize the radiation produced by the different beams, for it conveys no indication on the energy of particles exiting the *Bragg Peak* region, nor does it provide full spatial information. To characterize the energy spectra of this radiation, FLUKA `USRBDX` estimators were used to score the differential fluence, as a function of energy, integrated over solid angle, traversing an one cm diameter detector sphere centered at the *Bragg Peak* position and in the outward direction only. These plots are seen in figure 4.4.

Gamma coincidences, originating from the annihilation events (*i.e.* 511 keV), differ by more than an order of magnitude in favor of $RI\beta^+$ irradiation in figure 4.4. This is in line with the gamma fluence simulation trend in figure 4.3.

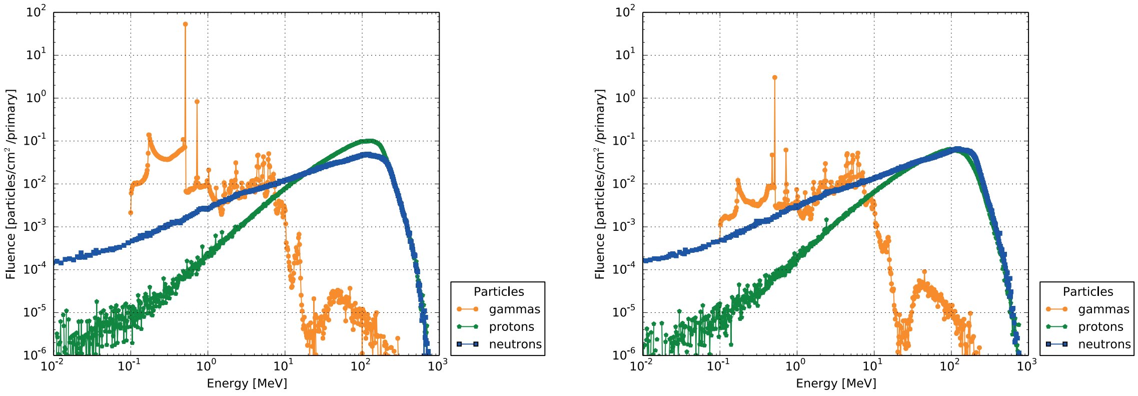

(a) ^{11}C (b) ^{12}C

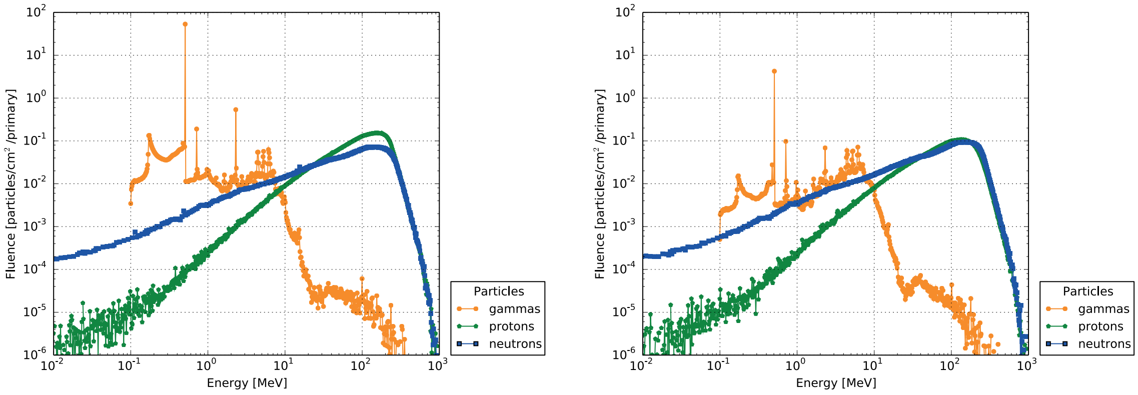

(c) ^{15}O (d) ^{16}O

Figure 4.4: *Differential fluence of neutrons, gammas and protons as a function of energy, exiting the Bragg Peak zone (integrated over solid angle) per primary particle.*

Many neutrons of relatively high energy ($\sim$ 100 MeV) also exit the *Bragg Peak* region, although with comparable fluences and energies among different beams. The most striking feature is perhaps the difference between protons and neutrons for $RI\beta^+$ irradiations, explained by their intrinsic neutron deficiency. A lower number of high energetic neutrons for $RI\beta^+$ irradiations is actually advantageous, as neutrons, having an high LET due to the low energy of recoiling particles and subsequently higher ionization density, could be of consequence elsewhere in the body. Instead, protons, being charged, are more likely to deposit their energy near the *Bragg Peak* and their impact is easier to assess.

A disentaglement of the prompt and decay dose components (figure 4.5) was required to ascertain the impact of the latter in $RI\beta^+$ irradiation scenarios. In a therapy scenario employing $RI\beta^+$, it is undesirable to have a too high amount of dose originating from radioactive emissions at the target zone, compared to ^{12}C or ^{16}O irradiations. The energy deposition components were thus singled out by whether they proceed directly from *Coulombic* energy losses or nuclear reactions (prompt), or were instead created through radioactive decay mechanism (decay). Additionally, the energy deposition ascribed to the primary beam particle only was also scored. Radioactive decays were evaluated by means of user routines `comscw.f` and `stuprf.f`, annexed. FLUKA was thus used in *Semianalogue* mode applying `DCYSCORE` cards coupled with the various `USRBIN`s estimators.

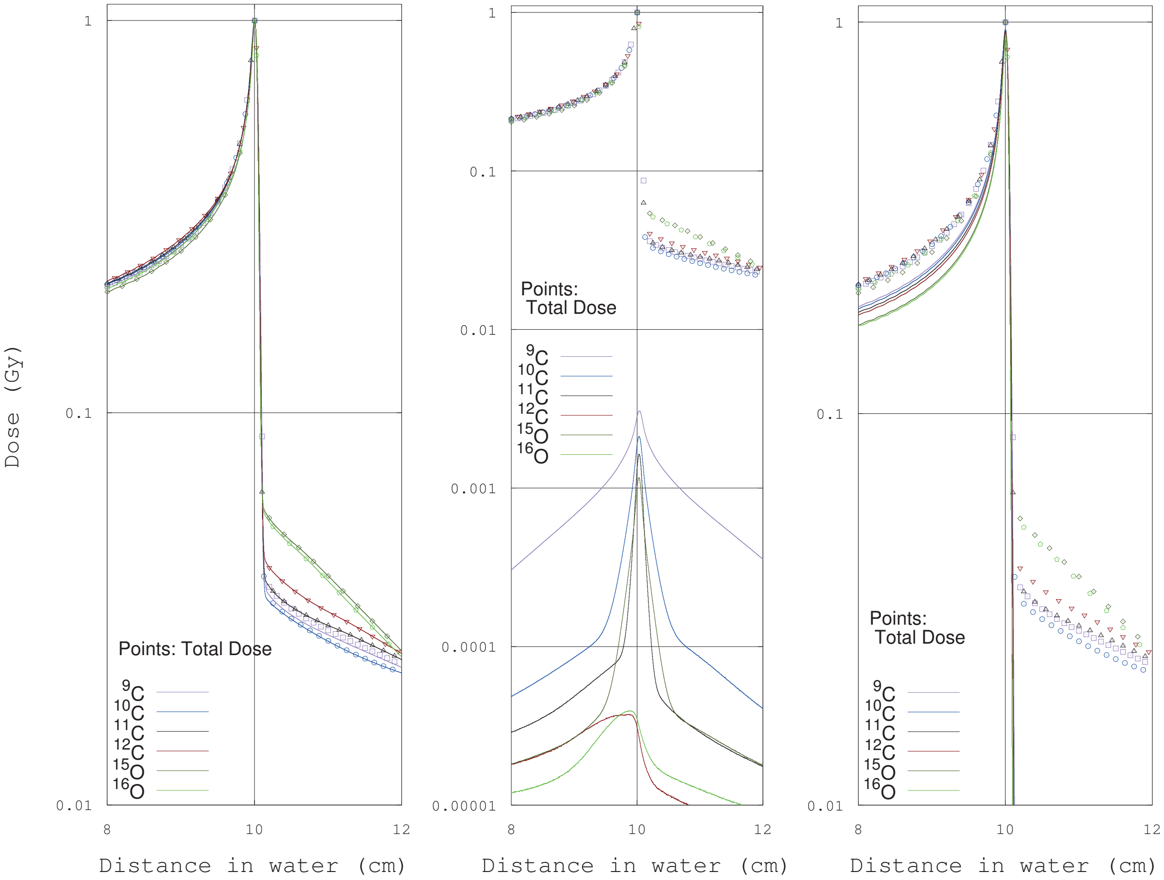

(a) Prompt (b) Decay (c) Projectile

Figure 4.5: *Evaluation of prompt, decay and primary ion contributions to the total dose for the different ion species Bragg Peaks in water, using FLUKA. The plots are normalized to 1 Gy at the total dose peak value.*

Clearly the decay component in figure 4.5 (b) is almost three orders of magnitude lower at the peak value compared to the prompt energy deposition, which is dominated by the primary particle up to the *Bragg Peak*. In fact, the combined (prompt) effect of primary ion and heavy ions produced is definitely responsible for the vast majority of energy delivered in the vicinity of the *Bragg Peak* region.

4.1.1 Influence of nuclear models on fragments contribution to the Bragg peak

A modified version of both `stuprf.f` and `comscw.f` user–routines was prepared for a more in–depth analysis of the fragmentation dose tail composition (the appendix A), accompanied with ^{9}C and ^{10}C results (figure A, also annexed). As mentioned in chapter 2, FLUKA uses its rQMD–2.4 implementation down to $\sim$ 125 MeV/u energy range, at which point ^{12}C and ^{16}O ions are typically still able to travel few cm in water[Som09]. The BME model in FLUKA becomes then the sole responsible for handling ion interactions at energies below 100 MeV/u. Since these models are entirely different entities, it was important to verify their performance around the 125 MeV/u frontier.

Additionally, a previous work featuring an earlier BME implementation displayed discontinuities on the activity profiles resulting from ^{12}C and ^{16}O irradiations, at the boundary between the two models[Som09]. These discontinuities were ascribed to the production of ^{11}C and ^{15}O, having been overcome since then. In fact, this improvement has a positive effect in the present work, as the transition between the above referred models in figures 4.6 and 4.7 was verified to be both gradual and without discontinuity. For the secondary ions, the rQMD component in all plots is going down as the *Bragg Peak* starts to build–up, typically around 7–8 cm in range for the considered energy, depending on the particle type. At those ranges, some of the projectile energy drops below the 125 MeV/u threshold while some fragments are produced at various energies, including below the 125 MeV/u level and thence their interactions start to be handled by BME[Cer06]. In the latter case, energy deposition profile typically peaks at the *Bragg Peak*. As for the rQMD model, it contains certainly mostly projectile fragments and thus their range varies in some cases by more than 1 cm. The formation of the double peaked shapes in the BME plots, for ions with higher Z than the projectile's, is due to the complete and incomplete fusion model (not present for rQMD), although the peak importance appears to be overestimated at the higher energy component (the initial peak).

Among all secondary ions energy deposition scored in figure 4.6 at the *Bragg Peak*, the most important inelastic collision energy contribution is from carbon isotopes ($2 - 3\%$ at the peak), particularly by BME. At that range in water, boron isotopes and α particles only attain 1% of the total energy. The fragment energy distribution peak shapes are broadened considerably by the influence of BME interactions, notably involving carbon and boron isotopes. The fragmentation dose tail is mostly "fed", immediately after the peak in ^{12}C, by boron ions and to a less degree α particles, although the latter contribution dominates beyond the $\sim$ 11 cm depth, after the peak of boron isotopes. More than 50% of the fragmentation dose tail is, in fact, ascribed to α particles at 14 cm in depth (see annexed figure A). For ^{11}C, α particles contribution clearly dominates. Furthermore, it can also be concluded from figure 4.6 that the previously observed effect in figure 4.2 does not derive from a single fragment type dominance, it results instead from a combination of various fragments.

With respect to oxygen irradiations in figure 4.7, the main isotopes contributing to the inelastic interactions at the *Bragg Peak* are nitrogen and carbon. At the aforementioned range, the contribution from oxygen isotopes inelastic collisions differs by more than a factor 2, between ^{16}O and ^{15}O, and becomes irrelevant after the peak. This aforementioned effect can be attributed chiefly to the rQMD component. In both ^{15}O and ^{16}O, the fragmentation dose tail is essentially formed by contributions of boron and carbon ion isotopes interactions via rQMD. Contrarily to the carbon irradiations in figure 4.6, α particles only dominate 2–3 cm after the *Bragg Peak*, consistent with the observation in figure's 4.3 energy distribution in range beyond the *Bragg Peak*, where heavy ions were seen to be of major relevance to oxygen compared to α particles.

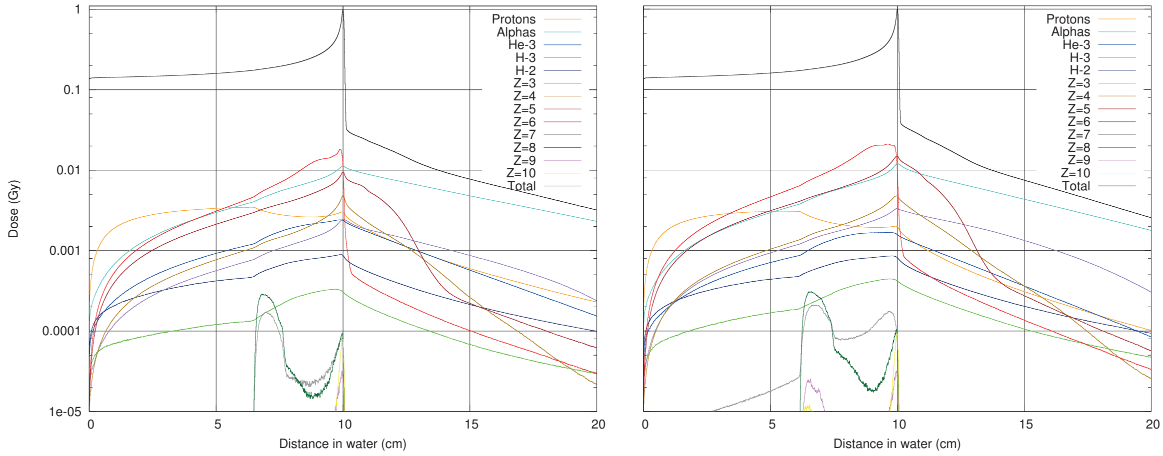

(a) ^{11}C (`BME+rQMD`) (b) ^{12}C (`BME+rQMD`)

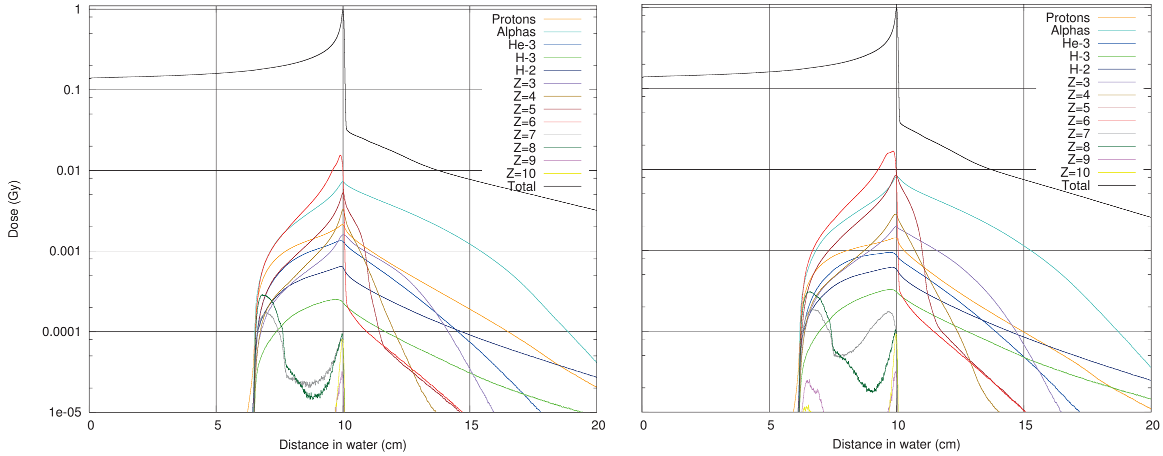

(c) ^{11}C (`BME`) (d) ^{12}C (`BME`)

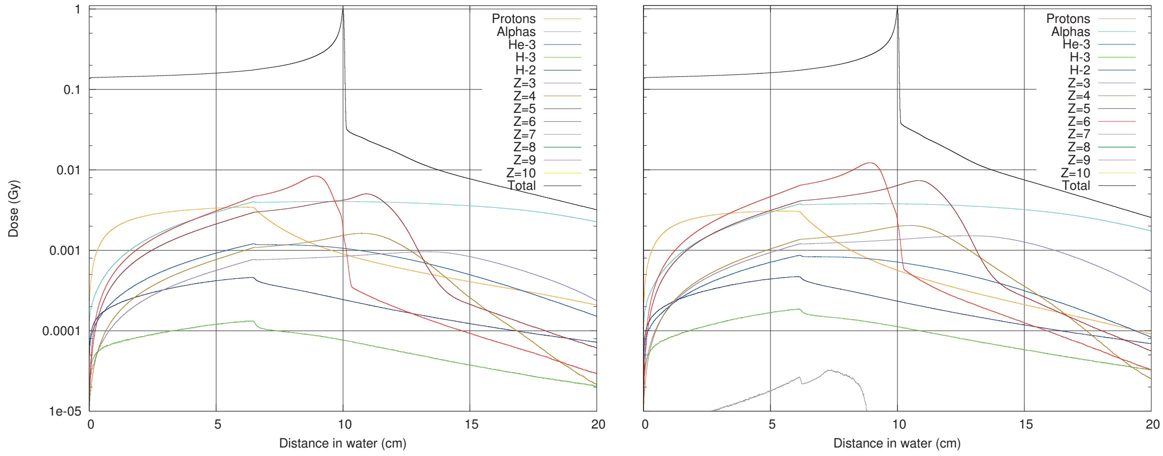

(e) ^{11}C (`rQMD`) (f) ^{12}C (`rQMD`)

Figure 4.6: *Absorbed dose by carbon ion beam fragments in inelastic collisions for a 10 cm deep Bragg Peak in water, normalized to 1 Gy at its total dose maximum, and filtered by Z and intervening model.*

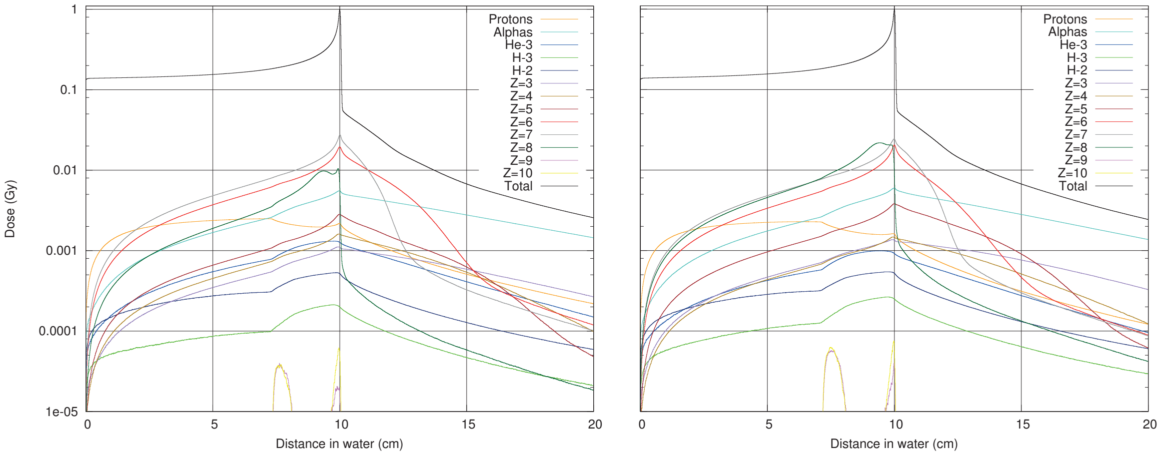

(a) ^{15}O (`BME+rQMD`)

(b) ^{16}O (`BME+rQMD`)

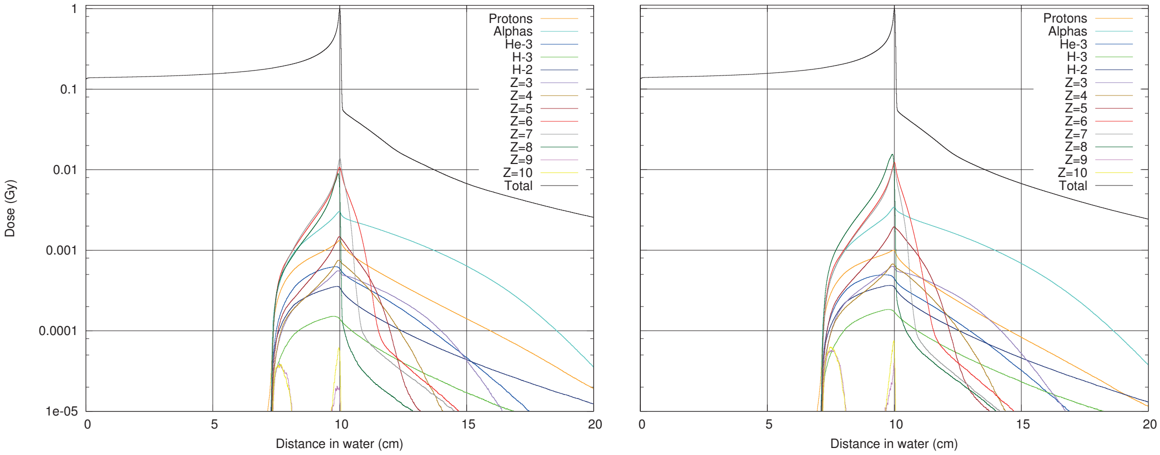

(c) ^{15}O (`BME`)

(d) ^{16}O (`BME`)

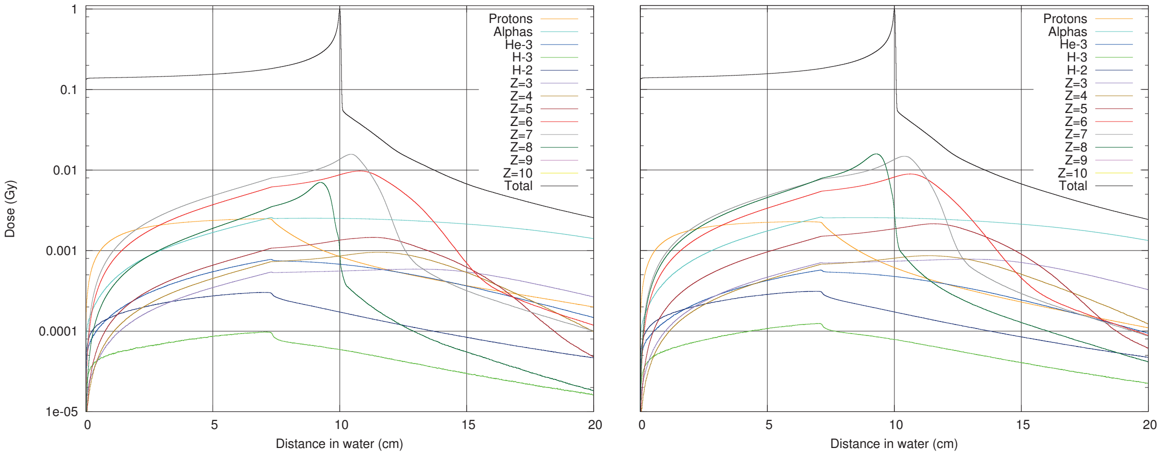

(e) ^{15}O (`rQMD`)

(f) ^{16}O (`rQMD`)

Figure 4.7: *Absorbed dose by oxygen ion beam fragments in inelastic collisions for a 10 cm deep Bragg Peak in water, normalized to 1 Gy at its total dose maximum, and filtered by Z and intervening model.*

Regarding ^{9}C and ^{10}C results (annexed figure A), the importance of secondary ions decreases. In fact, the major contributions via inelastic collisions to the energy deposition at the *Bragg Peak* attain no more than 1% for boron (^{9}C) and for carbon (^{10}C). In the latter case, α particle contribution dominates entirely after the *Bragg Peak*. The remaining major isotopes contributing to the fragmentation dose tail 1 cm after the peak are beryllium fragments and ^{3}He.

4.1.2 Simulating SOBPs for radioactive ion beams

The method described in the previous chapter, and detailed in the appendix A, was employed to obtain both the beam kinetic energies and number of particles calculated with the present work systematics ($\mathcal{I}_{\mathrm{S}}$) corresponding to 1 Gy SOBPs of ^{12}C and ^{16}O, or alternatively 16 Gy cm^2 DAP, with the desired characteristics in water of TPS data detailed in table 3.1. The procedure was then extended to $RI\beta^{+}$. The disentangled (DT) pristine *Bragg Peak* ion numbers at each isoenergetic layer for ^{11}C and ^{15}O are shown in figure 4.8, compared with ^{12}C and ^{16}O, for a SOBP with center at 15 cm in water.

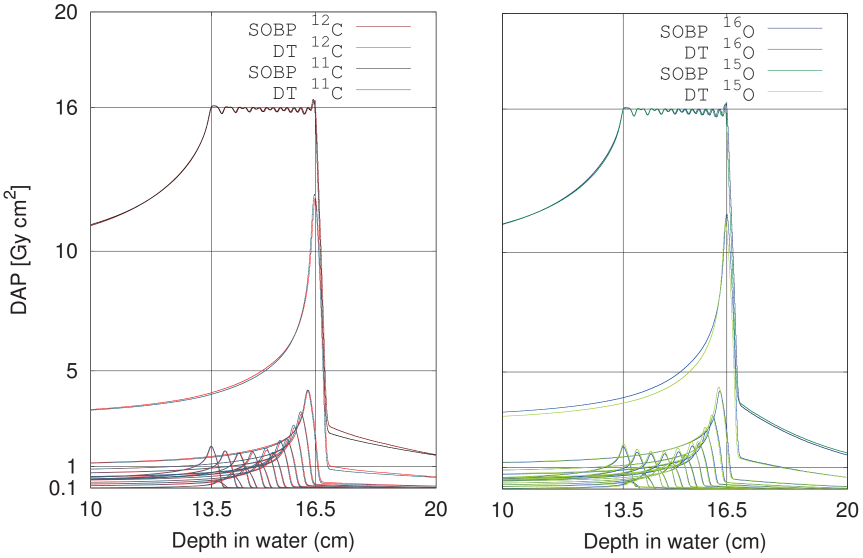

(a) ^{12}C and ^{11}C (b) ^{16}O and ^{15}O

Figure 4.8: *SOBPs centered at 15 cm in water, with the individual contributions at each isoenergetic layer disentangled.*

An attempt to validate this work's methodology with FLUKA recalculations based on the TPS data will be presented in chapter 5. However, from figure 4.8, it appears that the developed method does not show considerable variations in the number of primary ions, at each of the different isoenergetic layers, for the various ion beams employed. A more detailed dataset is provided in table A, annexed, for various SOBPs of $RI\beta^{+}$ at different depths in water. The ^{11}C, ^{12}C, ^{15}O and ^{16}O SOBPs generated are shown in figure 4.9, for a qualitative assessment of their dose distribution when centered at different depths (10 and 20 cm) in water.

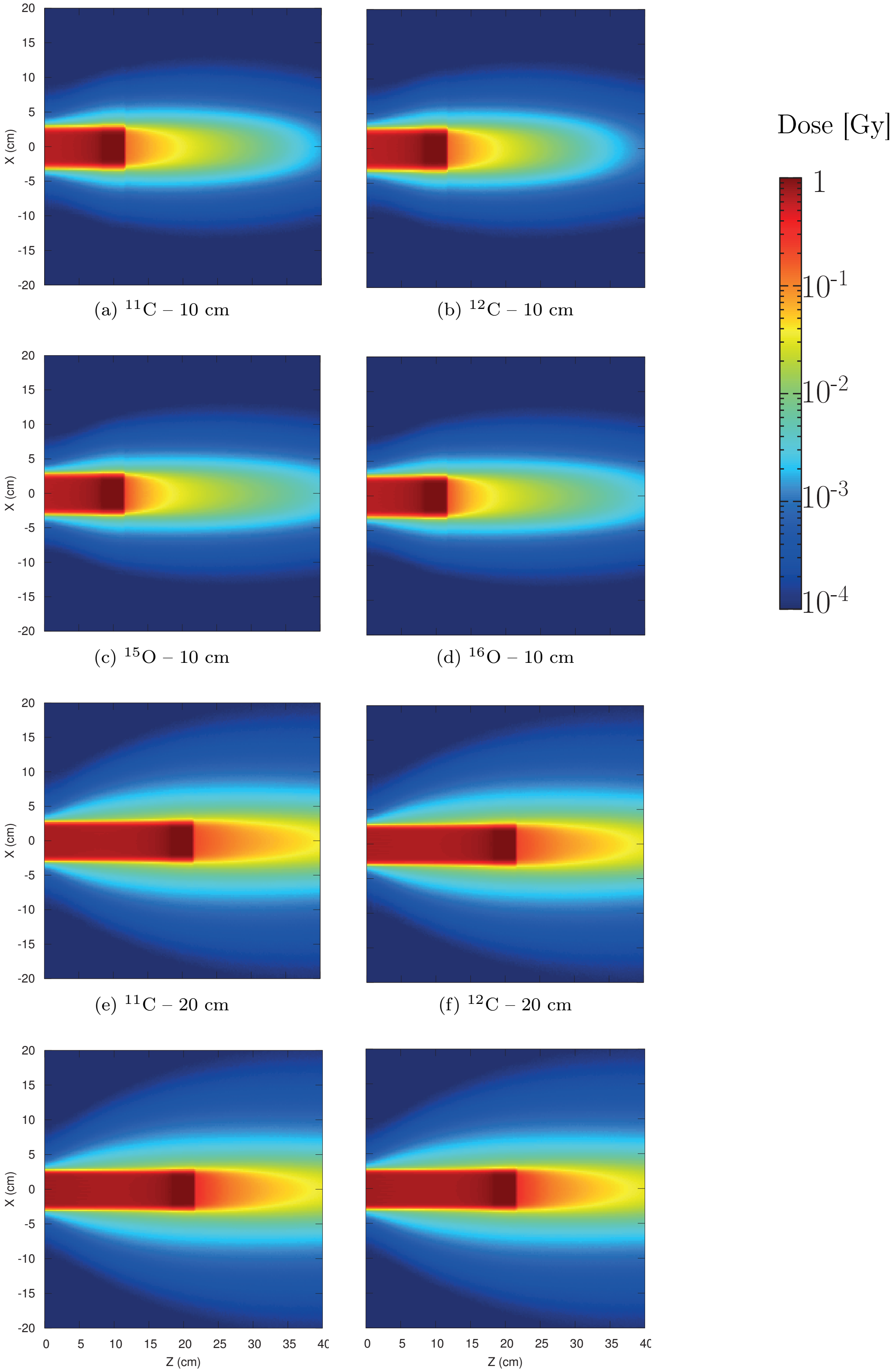

(a) ^{11}C – 10 cm

(b) ^{12}C – 10 cm

(c) ^{15}O – 10 cm

(d) ^{16}O – 10 cm

(e) ^{11}C – 20 cm

(f) ^{12}C – 20 cm

(g) ^{15}O – 20 cm

(h) ^{16}O – 20 cm

Figure 4.9: *Dose maps for 1 Gy SOBPs centered at different depths in water (10 and 20 cm), for the various ion beams.*

The fragmentation tail ratio trend reported in figure 4.1 for pristine *Bragg Peaks* is still visible in figure 4.10, in spite of the interplay between different isoenergetic layers and the effect of multiple projectile fragments in range, which could mitigate the advantageous effect highlighted in figure 4.2. On the other hand, a difference of $\sim 3\%$ is observed at the entrance dose, in favor of the stable ion species. Even though this difference is rather low, the dose levels at that range are much higher than in the fragmentation tail zone.

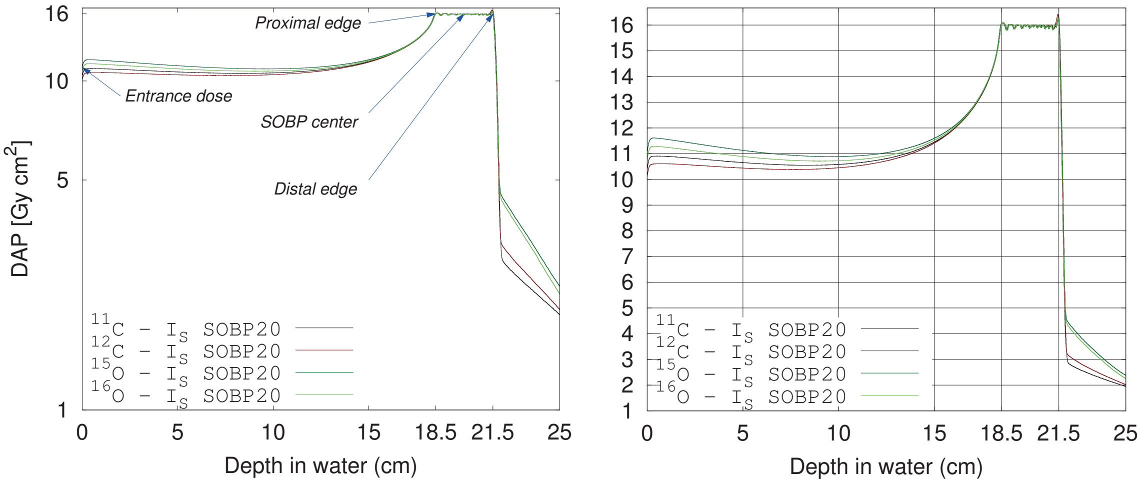

Figure 4.10: *SOBP for different ion beams, centered at 20 cm depth in water, using the number of ions ($\mathcal{I}_S$) calculated to attain an equivalent SOBP dose. On the left a logarithmic scale is employed whereas on the right side a linear scale is used instead.*

For oxygen beams, and in line with the observations in figure 4.1 for mono energetic beams, the simulations did not show a considerable difference in fragmentation tail dose, although it appears that ^{15}O leads to slightly higher doses both at the fragmentation tail and entrance zones.

4.2 Imaging potential of radioactive ion beams

The verification of the imaging potential of $RI\beta^+$ requires a direct PET imaging comparison, ideally within the framework of a patient irradiation scenario, with equivalent irradiation and acquisition parameters (*i.e.* comparable acquisition time, PET model, dose delivered). However, given the unavailability of patient data for $RI\beta^+$ irradiation scenarios, simulated stable ion beam irradiations were used as a basis for extrapolations of $RI\beta^+$ with the same dose delivery characteristics. This work methodology was further extended to VOXELIZED phantoms, but only considering physical dose, without accounting for the RBE effect in the different irradiations.

Once comparable SOBP doses are attained, one can estimate the imaging potential of $RI\beta^+$ via:

1. Direct calculation of the annihilation events at rest produced, evaluating their spatial distribution and time evolution, considering also the isotope of origin.

2. Usage of FLUKA PET TOOLS to obtain a reconstructed image from comparable *in beam PET* irradiation with acquisition scenarios of clinical relevance, using an anthropomorphic VOXEL phantom, an *in silico* version of PET scanner model used at HIT and an approximate description of its beam line elements using a RiFi and water equivalent approximations.

The second point is considerably more complex, as it requires scoring and processing data using external tools developed in the previous chapter, its results will be shown in chapter 5, after comparison of the SOBPs produced in this chapter. Note that although annihilation events at rest maps can be useful to assess photon emission origin, and therefore the events' distribution, they do not replace PET reconstruction images acquired during irradiation, which are more realistic.

4.2.1 Assessment of radioactive ions potential in PET imaging for SOBPs

In hadrontherapy, the distribution of β^+ emitters, either introduced with a biologically active molecule or produced by an ion beam, is an important information. Apart from the *biological washout*, the distribution is dynamic in both time and space due to the irradiation profile and subsequent decay. When employing PET techniques to visualize irradiation induced activity, the reconstructed image can be used to monitor the beam range. The following results assess the intrinsic imaging potential prior to image reconstruction by estimating the increment of annihilation events at rest using $RI\beta^+$, and their spatial distribution for the *in beam PET* scenarios studied.

In order to be consistent with the SOBP data, the scored annihilation events at rest must account for the weights applied to each of the pristine *Bragg Peaks* composing the SOBP generated using the tools described in the last chapter. This was accomplished using `ival.dat` as normalization factor, an example is found in the annex, in program `ultra.cpp`. In this way, the annihilation events at rest distribution in space and their total yield integrated over time can be assessed for SOBPs of equivalent dose. Since the time information of each isoenergetic layer, and their respective decay, is not yet considered, the following results are to be regarded as "integrated over time", or as an infinitely long acquisition time to score all annihilation events at rest produced.

The annihilation event at rest distribution resulting from each 1 Gy SOBP, time integrated for three different depths in water, can be seen in 1D and 2D in figures 4.11 and 4.12, respectively. Additionally, table 4.2 quantifies the simulated results, with annihilation events at rest abbreviated to Æverest for simplicity.

Table 4.2: *Analysis of the annihilation events at rest, integrated over time, with respect to the SOBP dose profiles, in water.*

Scenario	Beam	Æverest value [1×10^6 Events] at:			Distance between Æverest peak and SOBP distal edge [mm]
		proximal edge	distal edge	maximum	
SOBP 10 cm	^{11}C	1.28	13.00	14.60	0.8
	^{12}C	0.26	0.27	0.52	5.0
	^{15}O	0.68	6.00	7.10	1.0
	^{16}O	0.19	0.32	0.44	4.0
SOBP 15 cm	^{11}C	1.7	13.00	13.50	0.4
	^{12}C	0.36	0.30	0.57	10.0
	^{15}O	0.91	6.80	6.80	0.2
	^{16}O	0.26	0.35	0.51	6.8
SOBP 20 cm	^{11}C	1.50	10.00	13.00	1.3
	^{12}C	0.47	0.32	0.64	14.5
	^{15}O	1.08	6.13	6.37	0.8
	^{16}O	0.33	0.41	0.56	8.8

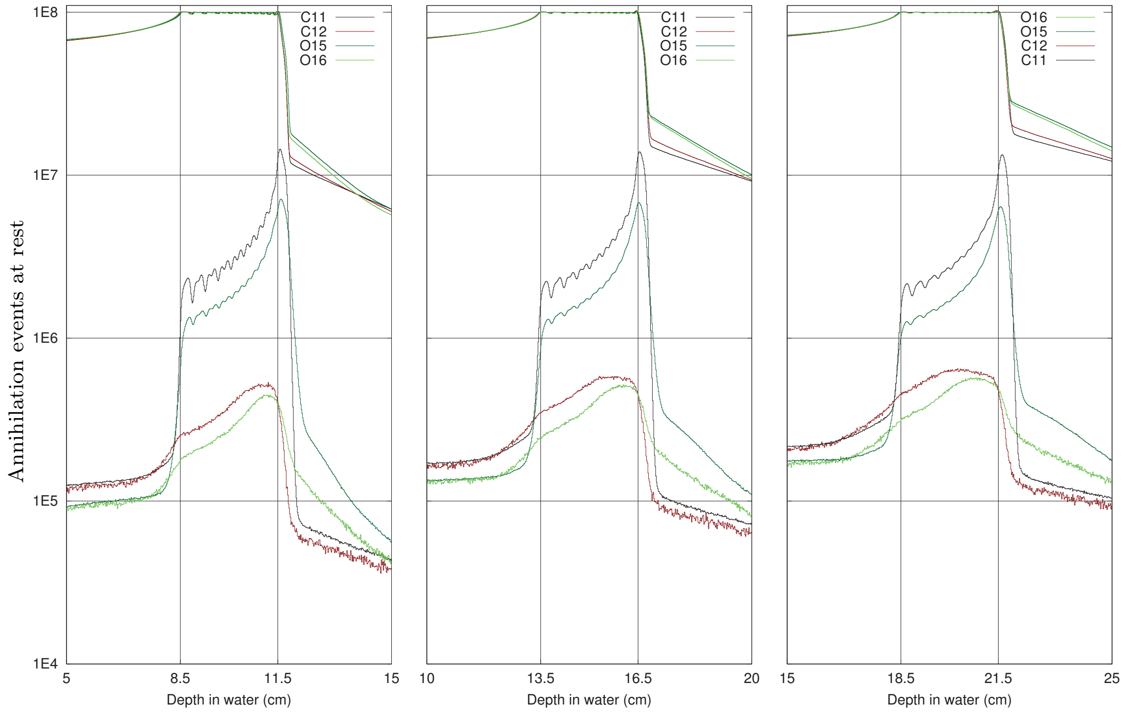

(a) SOBP – 10 cm (b) SOBP – 15 cm (c) SOBP – 20 cm

Figure 4.11: *Total annihilation events at rest, laterally integrated, from different SOBPs with the same physical dose in water. The dose profile is superimposed in arbitrary units for visualization purposes.*

Considering the dose distribution of pristine *Bragg Peaks* composing the SOBP previously highlighted in figure 4.8 and the distributions plotted in figure 4.11:

1. The annihilation events at rest resulting from stable ion beam irradiations do not evidence a clear peak, and their maximum do not coincide with the range of the distal edge of the SOBP. Note that SOBP dose distal edges are observed at 11.5, 16.5 and 21.5 cm in range, and these positions correspond exactly to the dominant *Bragg Peaks*, where the highest number of ions is delivered as observed in figure 4.8. In fact, for ^{12}C, the maximum of annihilation events at rest occurs at 11.0, 15.5 and 20.1 cm in depth. For ^{16}O, the deviation to the SOBP dose distal edge is smaller, but still the maximum of annihilation values correspond to 11.1, 15.8 and 20.6 cm in depth. Conversely, the maximum for $RI\beta^+$ are all within 1.3 mm from the distal edge of the SOBP. Also for the latter species, the distal dose fall–off, consisting of the distance corresponding to the distal curve decreasing from 90 to 10% of the SOBP edge value, coincides with the annihilation events at rest distribution distal fall–off.

2. Most notably, the annihilation events at rest resulting from irradiations with $RI\beta^+$ lead to a considerable gain in magnitude of annihilation events throughout the SOBP. Comparing the carbon ion distributions, this gain is of a factor 4.9, 4.7 and 3.2 for the proximal rise edge of the SOBP, at 8.5, 13.5 and 18.5 cm respectively. As for the distal edges at 11.5, 16.5 and 21.5 cm, the gain reaches over a factor 30. With respect to oxygen ions, the gains are overall lower but still considerable: for the proximal edge the gains are 3.6, 3.5 and 3.3, approximately, whereas for the distal edge the gain corresponds to a factor 15–20.

It is noteworthy to point out that the extremely favorable distal distribution of annihilation events at rest hereby seen is ascribed to the last isoenergetic layer having an higher weight, as seen in figure 4.8. Should the dose delivery being altered in terms of this layer weight, or sequence, this would reflect in the distribution of annihilation events. However, the overall gain with $RI\beta^+$ would be of course not altered, provided the total number of particles used is maintained. A reverted dose delivery in layer weight is often used when accounting for the RBE effect and consequently to quantify the biological dose.

In figure 4.12, one can appreciate qualitatively the lateral distribution of annihilation events at rest, which was integrated in figure 4.11. It varies approximately from 4 to 5 cm between the proximal and distal edges for ^{11}C and from 4.0 to 4.7 for ^{15}O due to the smaller lateral scattering. Comparing with the dose maps shown in figure 4.9, it is possible to see a clear correspondence between the higher dose zones and the higher annihilation events at rest distributions, both in range (Z) and laterally (X). In fact, the dose distribution is laterally homogeneous between the proximal and distal edge, at least within a 4 cm lateral interval. Therefore, the annihilation events at rest gain observed with $RI\beta^+$ over stable ion beam irradiations can be also useful to highlight the shape of the dose distribution.

Annihilation events at rest can provide an estimate of the ideal imaging potential, but the results shown so far did not account for its evolution in time. In a PET clinical scenario, the distribution of β^+ emitter activity observed for a specific radionuclide depends on the total number of primary ions employed, beam time structure and time of PET acquisition[Bau13]

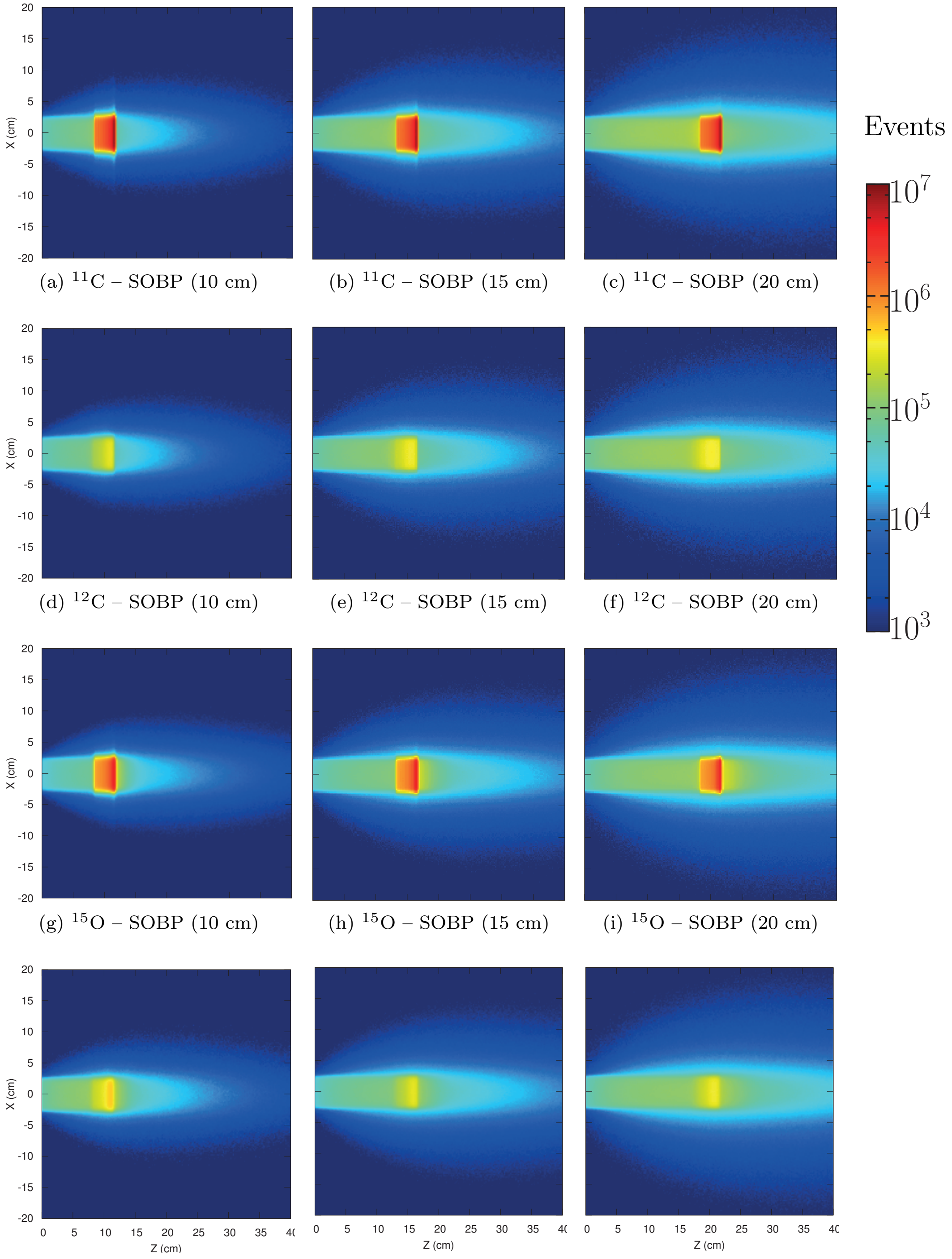

(a) ^{11}C – SOBP (10 cm) (b) ^{11}C – SOBP (15 cm) (c) ^{11}C – SOBP (20 cm)

(d) ^{12}C – SOBP (10 cm) (e) ^{12}C – SOBP (15 cm) (f) ^{12}C – SOBP (20 cm)

(g) ^{15}O – SOBP (10 cm) (h) ^{15}O – SOBP (15 cm) (i) ^{15}O – SOBP (20 cm)

(j) ^{16}O – SOBP (10 cm) (k) ^{16}O – SOBP (15 cm) (l) ^{16}O – SOBP (20 cm)

Figure 4.12: *Annihilation events at rest 2D maps, integrated over time, proceeding from the various 1 Gy SOBPs of different ranges in water.*

Assuming an *offline PET* acquisition, once the beam delivery is finished, decay mechanisms will be the sole responsibles for the production of β^+ emitter isotopes. This in contrast to β^+ emitter production taking place during irradiation, where decay and inelastic nuclear reactions compete. This competition becomes more complex to evaluate if one has to account for multiple β^+ emitters, decaying during beam time. Decay dynamics is considered to be affected ultimately by the β^+ emitters' rate of production and decay according to the *Radioactive Decay Law* in expression 4.1. The spontaneous decay products will, in time, contribute to the imaging signal according to their activity[SF02, Pri12]

$$A(t) \equiv -\frac{dN(t)}{dt} = \lambda N(t) = \lambda N_0 e^{-\lambda t} = A_0 e^{-\lambda t} \quad [\mathrm{Bq}], \tag{4.1}$$

where λ is the decay constant and N the radionuclide number, λ is given by

$$\lambda \equiv \lim_{\Delta t \longrightarrow 0} \frac{({}^{\Delta N}/{}_{N})}{\Delta t} \quad [\mathrm{s}^{-1}],$$

and is specific of each radionuclide. If only one type of β^+ emitter is contributing or if there is a predominant contribution from a specific species over all others, the activity can be calculated easily. However, multiple concentrations of β^+ emitters are typically produced by the primary beam interactions with the target.

The decay evolution in an *online* scenario at time t, where production and decay compete, is described analytically by the differential equation[SF02]

$$\frac{dN(t)}{dt} = \mathcal{Q}(t) - \lambda N(t), \tag{4.2}$$

where $\mathcal{Q}(t)$ is the production rate of the specific radionuclide in [nuclei s^{-1}], its solution can be obtained in the form of

$$N(t) = N_0 e^{-\lambda t} + \int_0^t \mathcal{Q}(t') e^{-\lambda(t-t')} dt', \tag{4.3}$$

where N_0 stands for the initial number of radionuclides[SF02]. If $\mathcal{Q}(t)$ is constant, then

$$N(t) = N_0 e^{-\lambda t} + \frac{\mathcal{Q}}{\lambda}\left(1 - e^{-\lambda t}\right). \tag{4.4}$$

In a more complex scenario, described in a previous work[PBH08] for a synchrotron with spills of a certain duration (t_s) and respective pauses (t_p), the activity evolution of a certain β^+ emitter can be described for the first spill as

$$A(t) = \mathcal{Q}\left(1 - e^{-\lambda t}\right) \quad 0 < t < t_s, \tag{4.5}$$

with the decay ensuing during the subsequent pause being described as

$$A(t) = \mathcal{Q}\left(1 - e^{-\lambda t_s}\right) e^{-\lambda(t-t_s)} \quad t_s < t < t_s + t_p. \tag{4.6}$$

Consequently, the number of decays of a β^+ emitter, in an acquisition time Δt, is given by

$$N(t, \Delta t) = \int_t^{t+\Delta t} A(t') dt', \tag{4.7}$$

provided that a 100% β^+–decay branching ratio applies. For an *in beam PET* acquisition, the two contributions pertaining *in–spill* and *inter–spill* PET acquisitions, for $\mathcal{S}$ spills, can be identified as detailed in the above mentioned work[PBH08]. The number of radionuclides of a certain type decayed during spill (N_s) and respective pauses (N_p) being as:

In–spill:

$$N_s = \mathcal{S}\left[\mathcal{Q}t_s - \frac{\mathcal{Q}}{\lambda}\left(1 - e^{-\lambda t_s}\right)\right] + \frac{\mathcal{Q}}{\lambda}\left(1 - e^{-\lambda t_s}\right)^2 e^{-\lambda t_p}\sum_{i=1}^{\mathcal{S}-1}\left(\mathcal{S} - i\right)e^{-(i-1)\lambda(t_s+t_p)}, \tag{4.8}$$

Inter–spill:

$$N_p = \frac{\mathcal{Q}}{\lambda}(1 - e^{-\lambda t_s})(1 - e^{-\lambda t_p})\sum_{i=1}^{\mathcal{S}-1}(\mathcal{S} - i)e^{-(i-1)\lambda(t_s+t_p)} \tag{4.9}$$

The *online PET* acquisition scenario described in this work would result therefore from the sum of equations 4.9 and 4.8. Extending the PET acquisition after beam delivery by a time t_{ext}, a situation which was excluded in section 5.1 but which was considered in section 5.2, the number of decays N_{ext} of a certain radionuclide is obtained via[PBH08]

$$N_{ext} = \frac{\mathcal{Q}}{\lambda}\left(1 - e^{-\lambda t_s}\right)\left(1 - e^{-\lambda t_{ext}}\right)\sum_{i=0}^{\mathcal{S}-1}e^{-i\lambda(t_s+t_p)}. \tag{4.10}$$

Finally, for both an *offline/in–room PET* acquisition[PBH08], spanning from t_1 to $t_2 = t_1 + \Delta t$, the amount of decays N_{off} of a certain species is calculated with:

$$N_{off} = \frac{\mathcal{Q}}{\lambda}(1 - e^{-\lambda t_s})e^{-\lambda t_1}(1 - e^{-\lambda t_2})\sum_{i=0}^{\mathcal{S}-1}e^{-i\lambda(t_s+t_p)}. \tag{4.11}$$

The scenarios depicted above can be also converted for a cyclotron, by employing a single spill of time t_s without t_p and $\mathcal{S} = 1$ in equations 4.8, 4.10 and 4.11[PBH08].

It is expected that the higher signal emission from $RI\beta^+$ could lead to PET detection improvements within the acquisition time interval Δt. The average radioactivity A_a available for an acquisition can be estimated with

$$A_a = \frac{A_0}{\lambda\Delta t}\left(1 - e^{-\lambda\Delta t}\right), \tag{4.12}$$

with the caveat that, depending on the PET sensitivity, the expected count rates actually acquired by the setup may vary. Furthermore, assessing the evolution of the β^+ emitters distribution with respect to a set of possible time acquisition windows, enables understanding which ion beams are actually more adequate in the PET acquisition modalities considered (*e.g. online* and *offline PET*).

This information complements the aforementioned discussed data on the magnitude of annihilation events at rest for the various SOBPs, enabling a deeper understanding of the reaction channels involved. In order to find which isotopes are "parenting" the β^+ emission, evaluating their individual impact on the annihilation events at rest mapped throughout the different acquisition times, it was necessary to implement:

1. An irradiation with a suitable beam time structure profile;
2. Acquisition times compatible with clinical applications;
3. Simulations that were no longer time integrated, scoring the rates of annihilation events at rest, at different time stamps.

This required implementing additional settings such as `RADDECAY`, `DCYTIMES` and `IRRPROFI` in the FLUKA simulation, to reproduce the appropriate irradiation and acquisition pattern. The chosen time structure and acquisition settings for SOBPs of ^{11}C, ^{12}C, ^{15}O and ^{16}O in water is shown in table 4.3, consisting of the intensities, in 10^6 ions/s and the spill spawn time, in seconds.

Table 4.3: *Intensities [10^6 ions s^{-1}] for each of the 16 isoenergetic layers to attain a SOBP of 1 Gy, at 10 cm in water, including the respective intervals Δt, in seconds, as implemented in* `IRRPROFI` *card in FLUKA.*

Layer	Δt	^{11}C	Δt	^{12}C	Δt	^{15}O	Δt	^{16}O
1	5	5.8042	5	5.5668	4	4.7645	4	4.5303
–	4	0	4	0	4	0	4	0
2	1	5.977	1	5.8649	1	4.367	1	4.0035
–	4	0	4	0	4	0	4	0
3	5	5.2526	5	4.9536	4	4.2475	4	4.1038
–	4	0	4	0	4	0	4	0
4	2	5.536	2	5.5325	2	3.858	2	3.4704
–	4	0	4	0	4	0	4	0
5	5	5.1996	5	4.7266	4	4.1393	4	3.9848
–	4	0	4	0	4	0	4	0
6	3	5.191	3	5.173	2	5.258	2	4.9076
–	4	0	4	0	4	0	4	0
7	5	5.3716	5	4.951	4	4.2688	4	4.1258
–	4	0	4	0	4	0	4	0
8	4	5.119	4	4.9088	3	4.5593	3	4.243
–	4	0	4	0	4	0	4	0
9	5	5.8864	5	5.4756	4	4.6988	4	4.5053
–	4	0	4	0	4	0	4	0
10	5	5.2884	5	5.0324	4	4.3215	4	4.0828
–	4	0	4	0	4	0	4	0
11	5	6.9016	5	6.4454	5	4.405	5	4.1482
–	4	0	4	0	4	0	4	0
12	5	7.0152	5	6.8298	5	4.6532	5	4.355
–	4	0	4	0	4	0	4	0
13	5	9.1966	5	8.5708	6	4.8248	6	4.5332
–	4	0	4	0	4	0	4	0
14	5	10.943	5	10.639	7	5.0116	7	4.8343
–	4	0	4	0	4	0	4	0
15	5	15.01	5	14.908	7	7.1324	7	6.8716
–	4	0	4	0	4	0	4	0
16	5	39.736	5	37.566	8	15.039	8	14.919

An irradiation time of ∼130 s was considered in every irradiation scenario. The irradiation length and intervals chosen for this work was based on values found in literature for synchroton–like beam time structure with ^{12}C ions, which reported 5 s long spills with few seconds of interval in between them[Mar11]. In this work the beam pauses were of 4 s and the spill time was not fixed, but varied typically around the 5 s value for carbon ions. Such extended spill time intervals are still technically feasible but can affect the PET imaging quality, due to the combination of background and *biological washout* contributions.

Furthermore, in this work, the spill distribution varied slightly between carbon and oxygen ion species as shown in table 4.3, even though the overall beam time of 130 s was kept unchanged. It was decided to keep the beam delivery profile of oxygen ions consistent with that of carbon ions in most layers, preserving at least a minimum of $\sim 4 \times 10^6$ ions/s spill intensity and thus reducing the spill time in some of the initial layers. Since the pause times were kept constantly at 4 s, the last layers' spill times were consequently extended considerably with respect to carbon ions. The carbon ion intensities chosen varied within $\sim 5 \times 10^6 - 4 \times 10^7$ ions/s and were similar to those in the experiment previously reported, namely $\sim 5 \times 10^6 - 8 \times 10^7$ ions/s[Mar11]. As for the sequence of irradiation, it took place from the lowest isoenergetic layer to the highest, following the procedure done at GSI and also initially undertaken at HIT.

Furthermore, even though there were 625 beam spots disposed in a squared grid for each of the 16 isoenergetic layers, the time structure "within spill", for any given energy layer, was neglected. Note that for very short–lived beams and/or a more realistic online acquisition evaluation the fully detailed time structure should be accounted for. Therefore, to reproduce the beam time structure, only 16 major intervals of irradiation, or spills, and 15 pauses were considered in the `IRRPROFI` card. Note that the values presented in table 4.3 result from the number of particles delivered ($\mathcal{I}_S$) for each isoenergetic layer, directly from `ival.dat` file, corresponding to 1 Gy SOBP.

With the time structure properly defined, some intervals–of–interest to score the rates of annihilation events at rest were selected, for their relevance in clinical context.

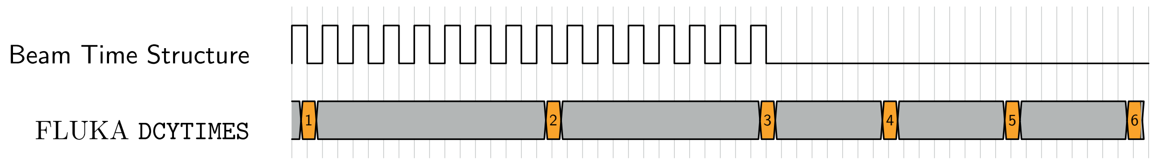

Figure 4.13: *`DCYTIMES` and `DCYSCORE` are time values, in seconds, relative to the end of beam (EOB), which is denoted as `DCYTIMES` #3. This latter value can be considered the origin (0) in the beam time structure.*

The time stamp values, in seconds and with respect to the origin of the beam time structure (`DCYTIMES` #3), considered in figure 4.13 are listed below:

1 -125 (for carbon ions) or -126 (oxygen ions); End of first layer.

2 -63 (for carbon ions) or -70 (for oxygen ions); End of 9th layer.

3 0 (EOB)

4 60

5 300

6 600

The choice of decay time stamps, including values during irradiation time up to 10 minutes afterwards, ensured the inclusion of most fragments of interest in this analysis, even short lived β^+ emitters. An illustration of how decay will affect the annihilation events rate, in time, is shown in figure 4.14.

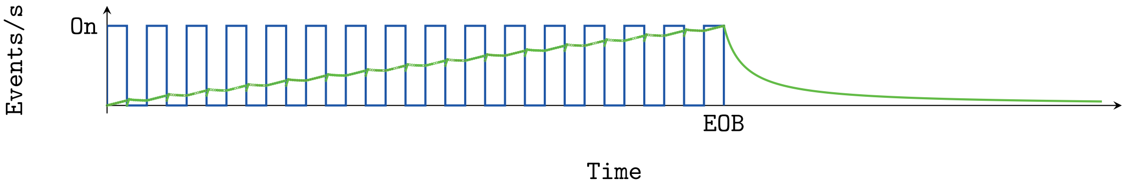

Figure 4.14: *Scheme illustrating how decay during beam time can affect the event rates seen during acquisitions both before and after EOB. The green line denotes the annihilation event rate [Events/s] trend observed for a single* β^+ *emitter, whereas the blue line denotes the beam time structure, with "On" meaning that a spill is being delivered. This depiction is not numerically accurate.*

An example of a qualitative assessment of rate of the annihilation events at rest 2D distribution, obtained at 5 minutes after EOB, is shown in figure 4.15. This example is relevant for it corresponds to the decay time at which rates of annihilation events at rest resulting from ^{11}C and ^{15}O are equivalent.

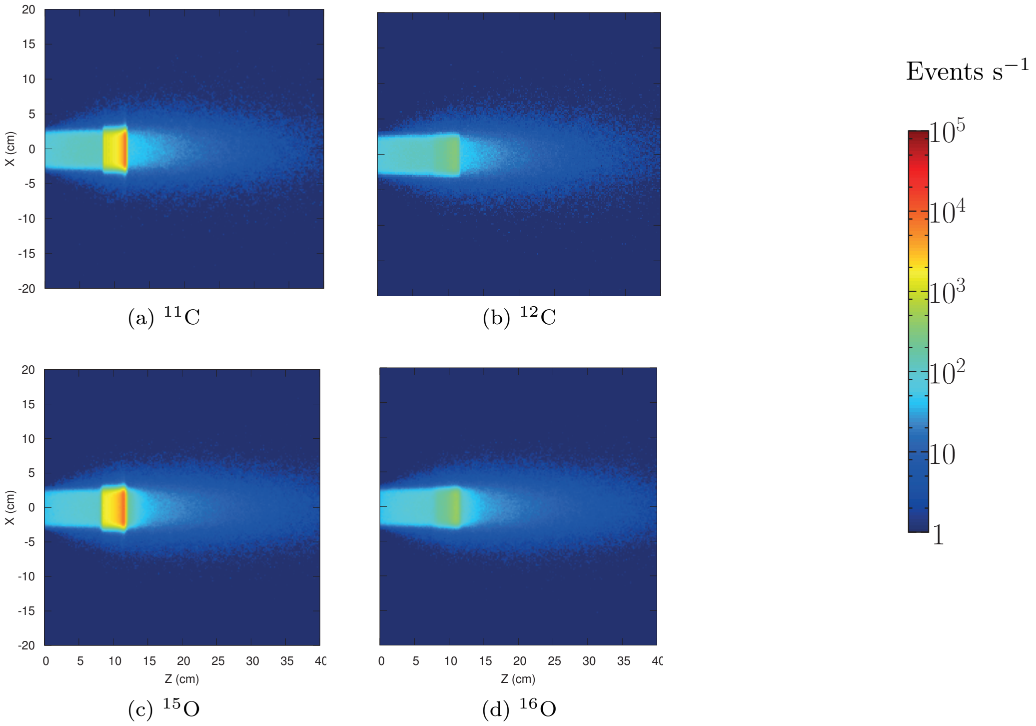

(a) ^{11}C

(b) ^{12}C

(c) ^{15}O

(d) ^{16}O

Figure 4.15: *Rates of annihilation events at rest for the different* SOBP*s, at 5 minutes after EOB.*

In figure 4.16 the distribution of annihilation events at rest is obtained in time–integrated mode, hence with the FLUKA card `RADDECAY` set to *semi–analogue*, to include all events in time and provide a broader overview of the species contributing to the total signal acquired.

The subsequent figures 4.17 and 4.18 depict the rates of annihilation events at rest [events s^{-1}] at the decay times studied, discriminated by parent isotope. The accounting of the different contributions was accomplished in FLUKA by filtering out the parent isotope information using `comscw.f` with the code given in the appendix A.

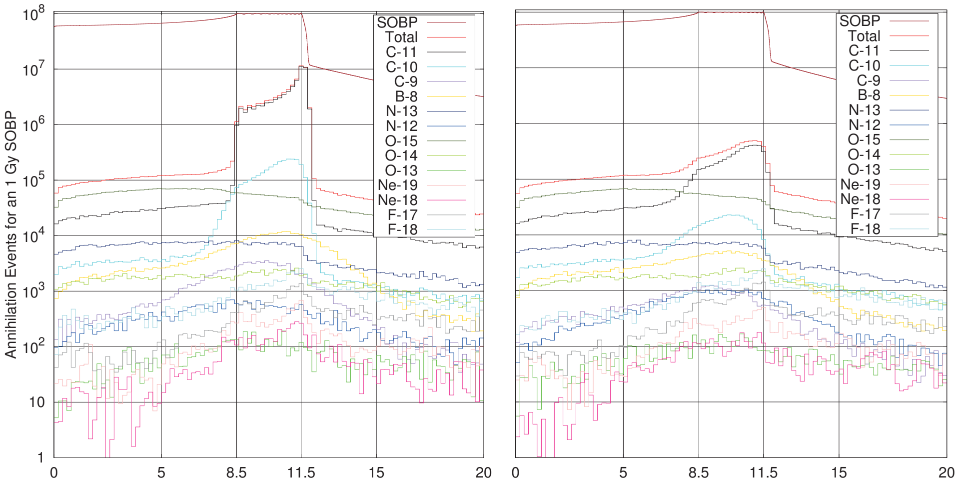

(a) ^{11}C (b) ^{12}C

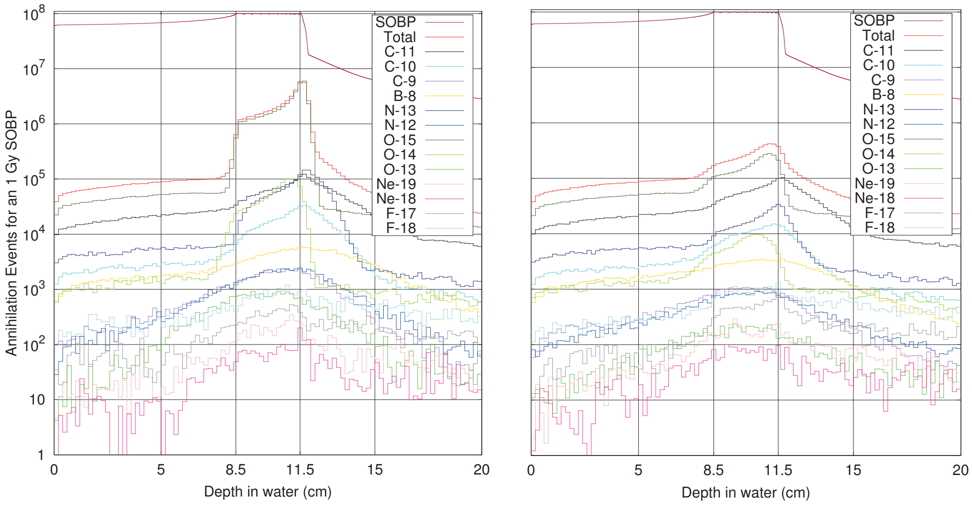

(c) ^{15}O (d) ^{16}O

Figure 4.16: *Total annihilation at rest events of different primary beams, stable (on the right) and radioactive (on the left), integrated over time and filtered according to parent isotope, for SOBPs of 1 Gy at 10 cm in water. The dose profile of the SOBP is superimposed, in arbitrary units.*

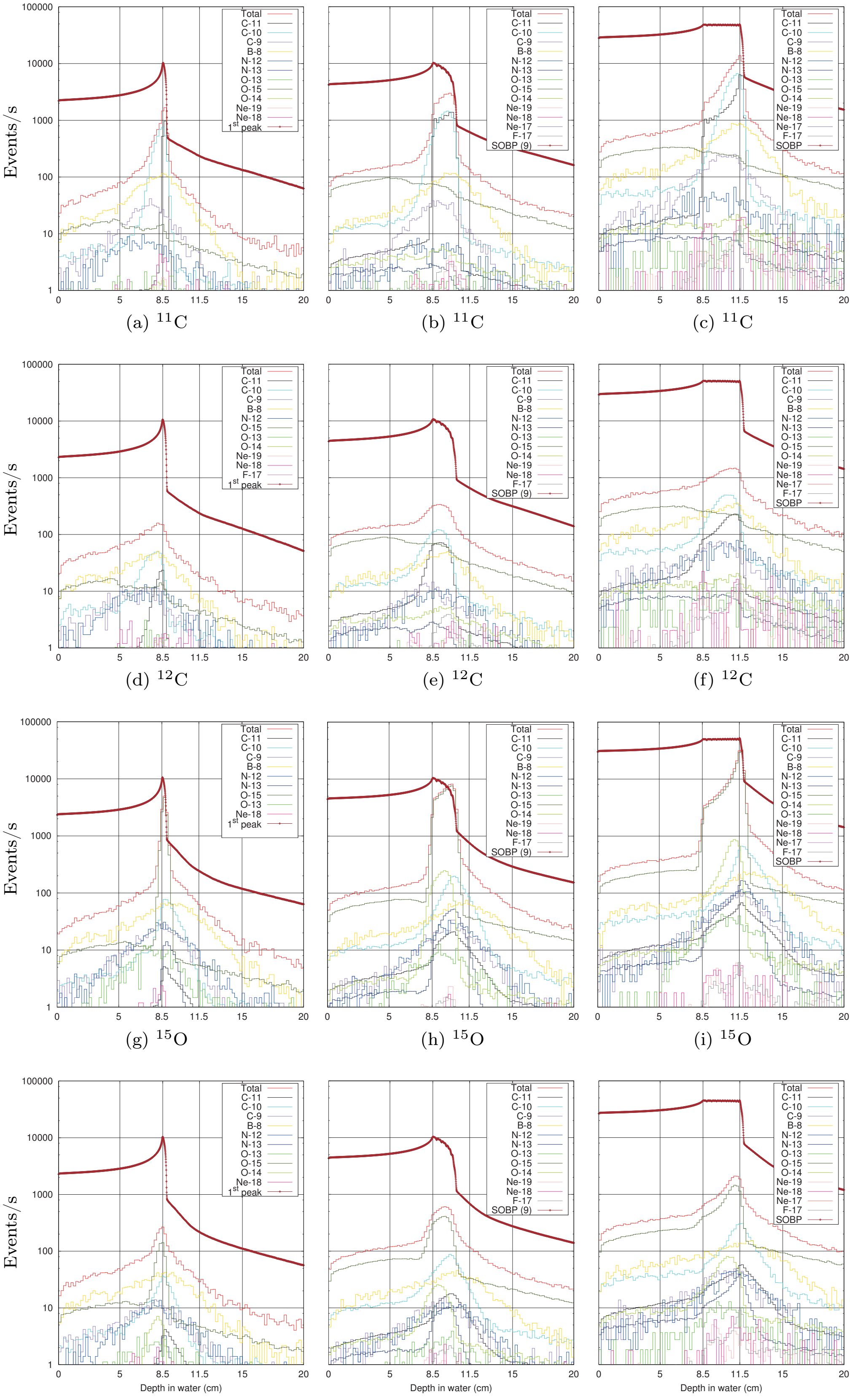

(a) ^{11}C (b) ^{11}C (c) ^{11}C

(d) ^{12}C (e) ^{12}C (f) ^{12}C

(g) ^{15}O (h) ^{15}O (i) ^{15}O

(j) ^{16}O (k) ^{16}O (l) ^{16}O

Figure 4.17: *Instantaneous annihilation events at rest rate [Events/s], filtered by parent isotope for SOBPs of 1 Gy at 10 cm in water, at the time corresponding to the end of first energy layer (1st column), end of ninth energy layer (2nd column) and EOB (3rd column). The SOBP dose profile is superimposed (arbitrary units).*

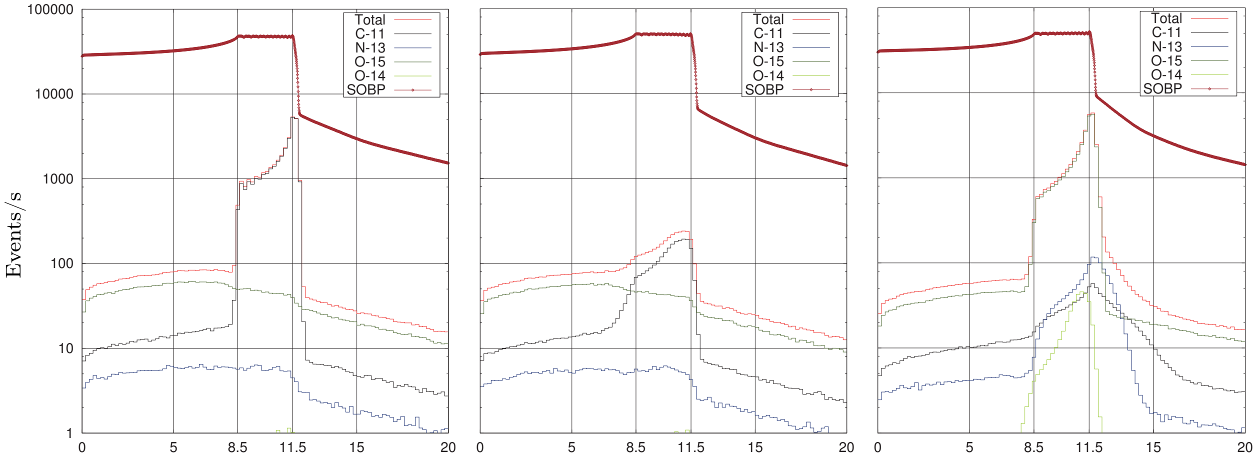

(a) ^{11}C (b) ^{12}C (c) ^{15}O

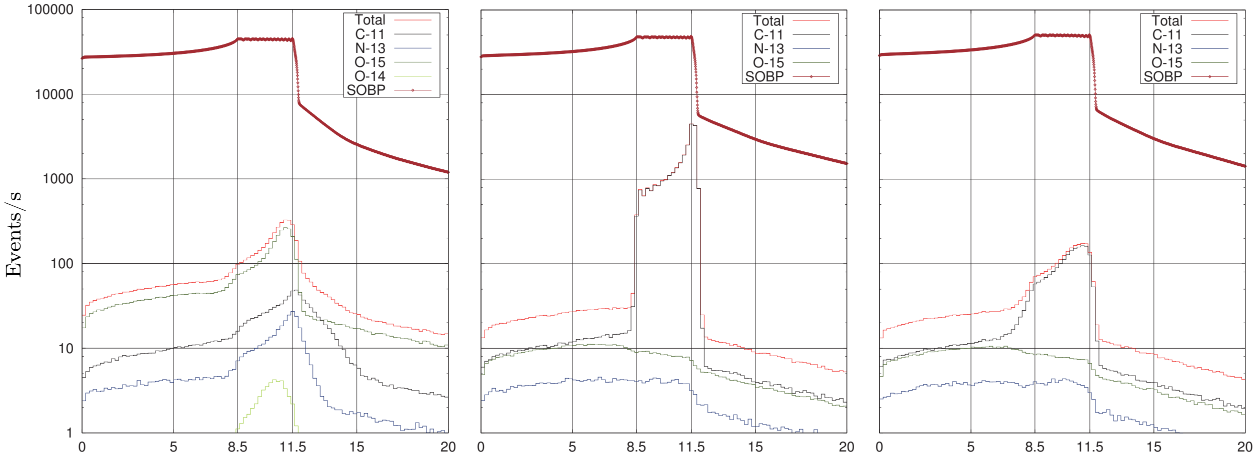

(d) ^{16}O (e) ^{11}C (f) ^{12}C

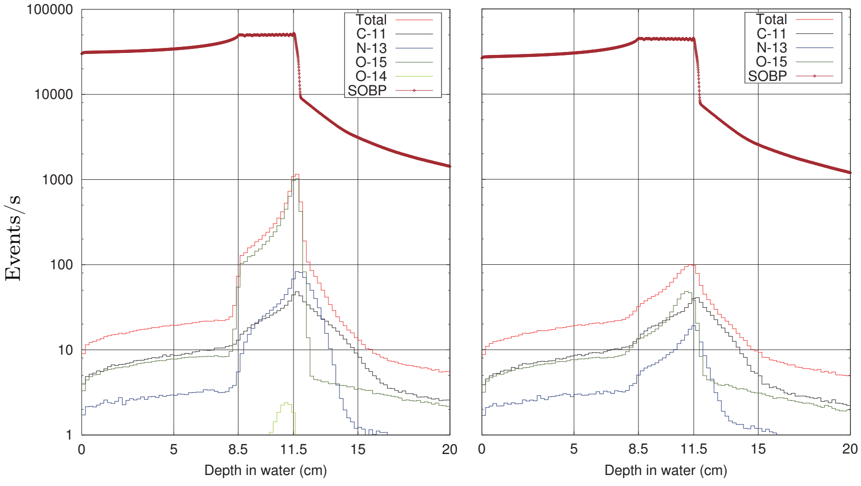

(g) ^{15}O (h) ^{16}O

Figure 4.18: *Annihilation at rest event rate in events/s, for SOBPs of 1 Gy at 10 cm in water, according to parent isotope, at 5 minutes (a–d) and 10 minutes after EOB (e–h). The SOBP profile is superimposed (arbitrary units).*

As illustrated in figure 4.16, one can observe that indeed the major contributors to the overall annihilation events at rest are ^{11}C and ^{15}O. In particular, for irradiations with radioactive beams, the aforementioned radioactive species contribute with over 95% of the time integrated annihilation event, at the peak value. The contribution of ^{15}O is seen to lead to a major background effect, over 70% of the total production, out of the SOBP target region, in all irradiation scenarios. This is mainly due to the ^{15}O target fragmentation production which is dominant in the considered water target. Regarding ^{12}C irradiation, the observed abundances of ^{11}C and ^{10}C are in line with cross section data collected for 250 MeV/u ^{12}C ions in water, corresponding to approximately 56 ± 4 and 5 ± 0.8 mbarn, respectively[Fie11]. For ^{16}O irradiations at 290 MeV/u in water, the cross sections of ^{15}O, ^{11}C, ^{13}N and ^{10}C correspond to approximately 28, 16, 6 and 1.7 mbarn[Fie11], with these proportions being approximately in line with the abundances verified in the simulation as well.

Through the irradiation, multiple species contribute to the total rate of annihilation events at rest (figure 4.17). For the ^{11}C ion irradiation, ^{10}C and ^{11}C each account for almost $\sim 45\%$ of the events observed at SOBP target region, with less than 10% being ascribed to ^{8}B and other species. In the ^{12}C ion SOBP target region, during irradiation, the rate of annihilation events at rest is mainly composed of ^{10}C ($\sim 50\%$) and to a less degree ^{8}B, with the ^{11}C contribution building up later on. In SOBPs of ^{15}O and ^{16}O, during irradiation, the contribution of ^{15}O predominates over all others. For the ^{15}O ion SOBP, one observes that its advantageous distribution at the distal zone of the annihilation event at rest rate is already present at EOB time, whereas for the ^{11}C ion SOBP this is not the case, due to the longer half–life of ^{11}C compared to ^{15}O. At EOB, in figure 4.17, the peak value for $RI\beta^+$ annihilation rates is at least one order of magnitude higher than in stable ion beam irradiations, and its range coincides with the distal edge of the SOBP dose profile. For ^{15}O it peaks at $\sim 40\,000$ events/s while for ^{11}C it surpasses slightly the $10\,000$ events/s threshold. At 5 min after EOB, as depicted in figures 4.18 and 4.15, the annihilation event rate distribution is comparable for both $RI\beta^+$ irradiation cases ($\sim 6\,000$ events/s) and is here seen to be strongly dominated by the primary ion species, a trend that is observed also later at 10 min after EOB. For the $RI\beta^+$ irradiations, both the rates of annihilation events at rest and the SOBP dose profiles are seen to coincide at their respective distal–fall off.

At 10 min after EOB, as seen in figure 4.18, ^{11}C annihilation rate at the peak region is only slightly below $6\,000$ events/s, but it is almost a factor 6 higher than ^{15}O, which in the meanwhile underwent a strong decay. Nevertheless, the rates of annihilation events at rest resulting from $RI\beta^+$ irradiations are at least one order of magnitude higher than the rates resulting from stable ion beams, at the peak value.

As previously mentioned, the gain is more evident distally, in view of the irradiation sequence. The last energy layer, and leading dose peak, is the least affected by the ongoing decay as it is generated only at the end of the irradiation and has consequently less time to decay.

From these simulation results, one can estimate that the annihilation events at rest gain with $RI\beta^+$ is more than an order of magnitude compared to stable ion beams. Moreover, this higher annihilation rate magnitude is seen to be more advantageously localized within the SOBP target region throughout the time stamps under analysis. The annihilation rate observed for SOBPs of ^{15}O ions outperforms that of ^{11}C ion SOBPs until up to 5 minutes after EOB, underperforming from then onwards as consequence of ^{15}O decay. The general decay trend is in line with the half–life of the respective primary beam ions for $RI\beta^+$, since their effect dominates after the EOB.

Chapter 5

Computational and experimental assessment of radioactive ion beams for PET imaging

> "(...) Leben Sie jetzt die Fragen. Vielleicht leben Sie dann allmählich, ohne es zu merken, eines fernen Tages in die Antwort hinein."
>
> — Rainer Maria Rilke, *Briefe an einen jungen Dichter (1908)*

5.1 Dosimetric and imaging results using a synchrotron–like TP

5.1.1 Verification of *Bragg Peaks* of ^{12}C and ^{16}O ion beams

A demonstration that the *Bragg Peak* energy deposition results using an established TPS (see section 3.1) could be compared directly with those produced in this study was performed, ensuring the latter validity. The SOBPs simulated with FLUKA in this work are based on calculations in water for the geometry defined in figure 3.1, using approximate elements of the HIT beam line. The initial kinetic energy and number of particles employed to generate each *Bragg Peak* (E_{S}, $\mathcal{I}_{\mathrm{S}}$) were obtained using the procedure described in chapter 3 and detailed in the appendix A.

These results were compared with ^{12}C SOBPs at 10 cm in water, recalculated using FLUKA based on data from HIT's OLDTPS, and can be seen in figure 5.1. As previously stated in chapter 3, OLDTPS stands for an earlier version of the research TPS, meanwhile outdated. The parameters used in the recalculation with FLUKA to generate the SOBP consisted of the isoenergetic layer energy value and number of particles, E_{T}, $\mathcal{I}_{\mathrm{T}}$, respectively.

Additionally, data from the newer version of the research TPS (NEWTPS) were provided for this test purpose only, already in SOBP form as a FLUKA simulation result[Tes16a]. This aforementioned SOBP data was therefore optimized using updated beam line elements, hence being denoted as "calibrated" (*i.e.* cross–checked). The isoenergetic beam layer energy and ion number employed were not disclosed but, in the normalization for its plotting in figure 5.1, the overall number of particles delivered was assumed to be equal to $\mathcal{I}_{\mathrm{T}}$.

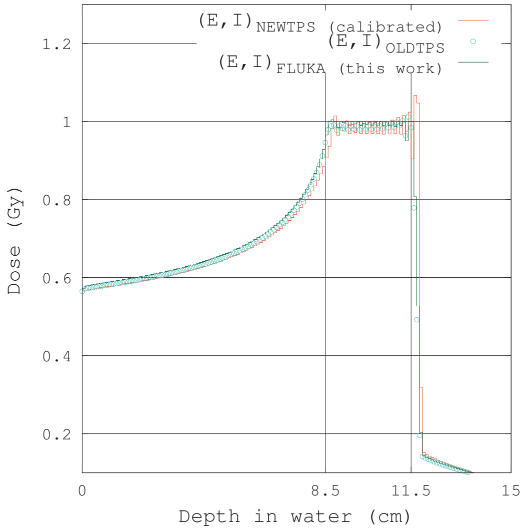

Figure 5.1: *Comparison of the ^{12}C SOBP centered at 10 cm depth in water calculated in this work with* OLDTPS *research TPS data, recalculated with FLUKA. The* NEWTPS *result (courtesy of T. Tessonnier) is also plotted.*

All the SOBP considered in figure 5.1 were laterally integrated over a surface of 20×20 cm^2 and plotted in range in intervals of 1 mm. To compare the lateral profile, NEWTPS and this works's SOBP FLUKA simulation were plotted directly in figure 5.2, integrating over their respective SOBP plateau. The OLDTPS data was not included in figure 5.2 since its recalculation was laterally integrated over a single binning unit.

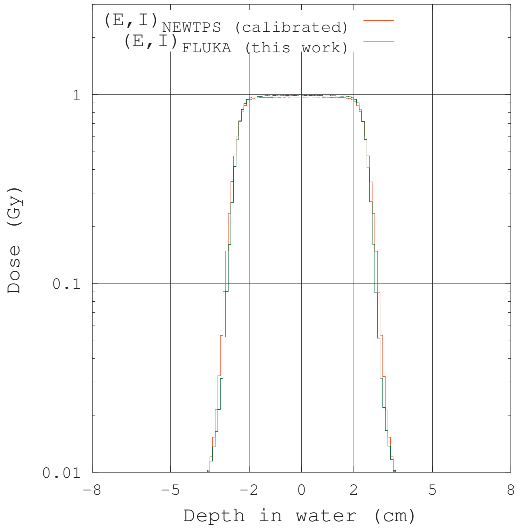

Figure 5.2: *Comparison of the ^{12}C SOBP lateral profile calculated in this work with* NEWTPS *research TPS version (this latter gently provided by T. Tessonnier). Both results are integrated over the SOBP plateau.*

A longitudinal shift of $\sim$ 3.5 mm in the distal edges between NEWTPS and this work SOBP results was verified, as shown in figure 5.1. In order to perform a more direct comparison with the NEWTPS, the last pristine *Bragg Peak* of the SOBP was provided by HIT, again for ^{12}C ions in water, and the following corrections were performed:

1. As inconsistencies between the real shape of the RiFi[WK99] (right) and the simulations (figure 3.2) could lead to considerable discrepances, the RiFi was removed for a more direct comparison.
2. Water density was modified from 1.0 to 0.998 [g cm^{-3}]. As water temperature was ~25°C, instead of 4°C as SI–defined.
3. The ionization potential value in water was adjusted from 77.3 to 76.8 eV, to be consistent with the NEWTPS simulation data provided.

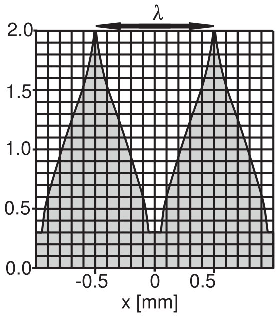

The resulting shift, depicted in figure 5.3, was reduced to $\sim$ 0.4 mm and can be considered within acceptable limits.

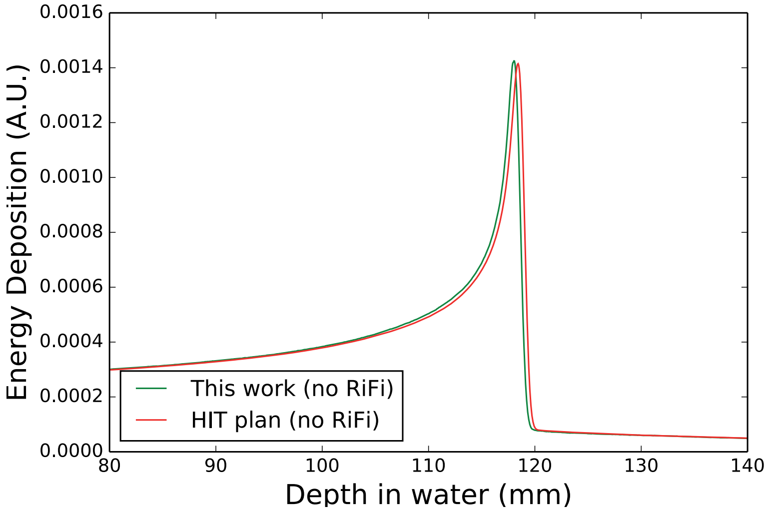

Figure 5.3: *Benchmarking performed for a ^{12}C ion pristine Bragg Peak, using the energy calculated by this work's model and comparing against the HIT's* NEWTPS *result, without RiFi. Research TPS data courtesy of T. Tessonnier.*

This "remaining" shift in range could be attributed to differences in beam line elements description and also simulation settings.

Since the NEWTPS is therefore adapted to more updated beam line components, and this works' models are adapted to earlier water equivalent approximations of the beam line, a range shift is likely to occur even if the same beam kinetic energy is employed using the same simulation code.

Nevertheless, an 0.4 mm shift lies within the 0.5 mm tolerance and is within the fluctuations that can be observed when repeating measurements in subsequent days.

Table 5.1 summarizes the benchmarked SOBP and pristine *Bragg Peak* characteristics in figures 5.1, 5.2 and 5.3. The peak to entrance ratio (PER) is defined as the ratio between the dose value at the proximal edge, in case of a SOBP, with respect to the dose value at the water phantom entrance (see chapter 4 figure 4.10). For a pristine *Bragg Peak*, the peak value is used instead. The value ΔW50% is the length, in range, between the half proximal edge value and the half dose value at the distal edge. As for the distal fall–off value, it consists of the distance in range between its decreasing from 90 to 10% of the distal edge value (again as depicted in chapter 4 figure 4.10). The FWHM value was calculated considering the lateral profiles obtained in figure 5.2.

Table 5.1: *Quantitative evaluation of the SOBPs and Pristine Bragg Peaks characteristics.*

	SOBP			Pristine Peak	
Characteristic	OLDTPS	NEWTPS	This work	NEWTPS	This work
PER	1.754	1.791	1.754	6.168	6.294
ΔW50% [cm]	4.2 ± 0.1	4.0 ± 0.1	4.3 ± 0.1	0.35 ± 0.01	0.35 ± 0.01
Distal fall–off [mm]	2.0 ± 0.1	1.5 ± 0.1	2.1 ± 0.1	0.97 ± 0.01	1.06 ± 0.01
FWHM [cm]	—	5.0 ± 0.1	5.0 ± 0.1	—	—
Ions delivered	6.00×10^8 ($\mathcal{I}_\mathrm{T}$)	$\equiv \mathcal{I}_\mathrm{T}$	6.07×10^8 ($\mathcal{I}_\mathrm{S}$)	—	—

Since the OLDTPS data used in the FLUKA recalculation was based on the `TRiPs` code, which in turn relied on an older FLUKA (2006) version for its basic input data and was optimized for older beam line elements, one should expect to observe intrinsic differences with respect to the NEWTPS data based on a more recent version of the FLUKA code (*e.g.* beam deflection, nuclear reactions). Moreover, differences ascribed to the beam line elements description, particularly for the RiFi, lead to inconsistencies in between the E and $\mathcal{I}$ values used from the research TPS (T) and from this work (S), which can be appreciated in table 5.2. The impact of range shifts was mitigated by employing E_S data fitted from a database, generated by `SOBPGen.cpp`, so as to match OLDTPS E_T range, within 100–300 μm accuracy. On the other hand, the intensity modulation discrepances were more difficult to address. The research TPS recalculation, laterally integrated over a relatively large surface (20×20 cm^2), rendered satisfatory results as seen in figure 5.1 and table 5.1. However, while extending this calculation for smaller integration volumes with lateral areas of 4×4 cm^2, it was found that the recalculated number of ions delivered for each of the Pristine *Bragg Peaks*, or the `Supra.cpp` $\mathcal{I}_\mathrm{S}$ values for each isoenergetic layer, did not match OLDTPS data $\mathcal{I}_\mathrm{T}$ values.

The main reason for this discrepance is that the recalculated OLDTPS plan was found to homogeneously yield 0.95 Gy in a 4×4 cm^2 surface at the SOBP region, instead of 1 Gy for ^{12}C in water at 10 cm in range, hence translating into ~ 15.2 [Gy cm^2]. Consequently, the energy deposition results obtained in the reduced volume differed systematically whenever directly compared. Increasing the volume would lead to a better agreement, but the dose homogeneity in this work was seen to deteriorate steeply beyond the 4×4 cm^2 surface, as one can see in figure 5.2 where the dose falls by approximately two orders of magnitude between 2 and 2.5 cm from the isocenter, a trend that is indeed confirmed by NEWTPS data.

Table 5.2: *This works' simulated (S) and* OLDTPS *research TPS TRiP parameters (T) for stable beams. The comparison is done directly for each of the 16 isoenergetic layers and the three different SOBP depths, namely 10 cm (top), 15 cm (middle) and 20 cm (bottom) in water; E – initial kinetic energy (MeV/u), $\mathcal{I}$ – number of ions ($\times 10^6$ ions), e_a and e_r – absolute and relative error, respectively. Each of the error values for a given isoenergetic layer pertain either $\mathcal{I}_S$ and E_S and use respectively $\mathcal{I}_T$ and E_T as reference.*

layer	^{12}C						^{16}O					
#	E_S	$\mathcal{I}_S$	E_T	$\mathcal{I}_T$	$e_r(E)[\%]$	$e_a(\mathcal{I})$	E_S	$\mathcal{I}_S$	E_T	$\mathcal{I}_T$	$e_r(E)[\%]$	$e_a(\mathcal{I})$
1	205.26	26.509	206.91	20.585	0.80	–5.92	243.33	17.363	244.15	12.539	0.34	–4.82
2	207.88	6.324	209.53	12.676	0.79	+6.35	246.48	4.622	247.26	8.914	0.32	+4.29
3	210.48	23.957	212.12	18.284	0.77	–5.67	249.61	15.295	250.36	11.219	0.30	–4.08
4	213.06	11.197	214.70	16.344	0.76	+5.15	252.72	8.073	253.54	11.546	0.32	+3.47
5	215.62	23.346	217.25	18.941	0.75	–4.41	255.80	14.609	256.59	11.530	0.31	–3.08
6	218.16	15.543	219.79	19.060	0.74	+3.52	258.87	10.804	259.55	12.231	0.26	+1.43
7	220.68	24.037	222.31	20.724	0.73	–3.31	261.91	15.264	262.65	13.792	0.28	–1.47
8	223.18	19.845	224.81	22.084	0.73	+2.24	264.93	13.530	265.66	14.025	0.28	+0.50
9	225.67	26.465	227.29	24.207	0.71	–2.26	267.94	17.006	268.64	15.428	0.26	–1.58
10	228.14	25.163	229.76	26.382	0.71	+1.22	270.92	16.853	271.59	16.644	0.25	–0.21
11	230.60	31.119	232.20	30.051	0.69	–1.07	273.89	20.233	274.51	18.281	0.23	–1.95
12	233.04	33.640	234.64	36.096	0.68	+2.46	276.84	21.771	277.41	20.998	0.21	–0.77
13	235.46	42.035	237.05	42.972	0.67	+0.94	279.77	27.037	280.29	25.179	0.19	–1.86
14	237.87	52.132	239.45	67.295	0.66	+15.16	282.69	33.596	283.19	33.319	0.18	–0.28
15	240.27	73.419	241.84	18.694	0.65	–54.73	285.59	47.362	286.05	38.701	0.16	–8.66
16	242.65	186.63	243.03	205.22	0.16	+18.59	288.47	118.29	288.92	130.79	0.16	+12.50
Total	–	621.36	–	599.62	–	–21.74	–	401.71	–	395.14	–	–6.57
1	265.79	29.860	267.20	24.624	0.53	–5.24	316.48	20.849	316.67	16.624	0.06	–4.23
2	268.04	7.922	269.43	13.357	0.52	+5.44	319.21	4.915	319.29	7.848	0.03	+2.93
3	270.28	26.538	271.66	20.574	0.51	–5.96	321.92	18.663	321.97	14.182	0.02	–4.48
4	272.51	13.427	273.88	18.028	0.50	+4.60	324.62	8.943	324.64	11.733	0.01	+2.79
5	274.73	25.396	276.09	20.263	0.49	–5.13	327.31	17.435	327.31	16.593	0.00	–0.84
6	276.94	18.615	278.29	20.934	0.49	+2.32	329.99	12.358	331.25	20.455	0.38	+8.10
7	279.14	26.208	280.48	22.574	0.48	–3.63	332.65	17.730	333.91	12.452	0.38	–5.28
8	281.33	23.058	282.67	24.275	0.47	+1.22	335.31	15.686	336.58	18.191	0.38	+2.51
9	283.51	29.448	284.84	27.115	0.47	–2.33	337.95	19.135	339.22	17.054	0.37	–2.08
10	285.69	29.304	287.02	30.630	0.46	+1.33	340.58	19.235	341.84	20.205	0.37	+0.97
11	287.85	35.808	289.18	34.873	0.46	–0.94	343.20	22.990	344.44	22.094	0.36	–0.90
12	290.00	39.481	291.34	42.451	0.46	+2.97	345.81	25.195	347.03	28.124	0.35	+2.93
13	292.15	49.573	293.50	50.017	0.46	+0.44	348.41	31.645	349.64	22.839	0.35	–8.81
14	294.29	60.601	295.65	79.946	0.46	+19.35	350.99	39.334	350.95	28.601	0.01	–10.73
15	296.41	82.440	297.79	17.966	0.46	–64.47	353.57	54.510	353.56	50.580	0.00	–3.93
16	298.53	236.24	298.87	248.27	0.11	+12.03	356.14	150.10	356.20	155.57	0.02	+5.47
Total	–	733.92	–	695.90	–	–38.02	–	478.72	–	463.15	–	–15.57
1	319.28	34.357	320.07	27.612	0.25	–6.75	381.33	24.603	381.74	19.301	0.11	–5.30
2	321.31	7.981	322.17	15.364	0.27	+7.38	383.80	5.745	384.27	10.516	0.12	+4.77
3	323.33	30.650	324.26	22.908	0.29	–7.74	386.27	21.822	386.77	15.812	0.13	–6.01
4	325.35	14.808	326.34	20.582	0.30	+5.77	388.73	10.020	389.28	14.906	0.14	+4.89
5	327.36	29.049	328.41	23.052	0.32	–6.00	391.18	20.979	391.82	16.446	0.16	–4.53
6	329.36	20.064	330.48	26.491	0.34	+6.43	393.63	13.406	394.31	14.000	0.17	+0.59
7	331.36	30.754	332.98	31.939	0.49	+1.19	396.07	21.061	396.17	18.093	0.03	–2.97
8	333.35	26.193	334.94	24.304	0.48	–1.89	398.50	17.186	399.77	26.634	0.32	+9.45
9	335.33	34.031	336.89	33.610	0.46	–0.42	400.92	22.612	402.13	14.553	0.30	–8.06
10	337.31	34.818	338.83	36.182	0.45	+1.36	403.34	22.015	404.50	24.957	0.29	+2.94
11	339.28	42.495	340.77	25.282	0.44	–17.21	405.76	27.484	406.83	24.209	0.26	–3.28
12	341.24	46.215	341.73	52.850	0.14	+6.64	408.17	29.923	408.92	20.655	0.18	–9.27
13	343.20	58.298	344.94	102.29	0.50	+43.99	410.57	38.354	410.71	42.047	0.03	+3.69
14	345.15	73.221	346.42	15.468	0.37	–57.75	412.96	47.097	414.33	77.468	0.33	+30.37
15	347.10	89.093	347.90	84.105	0.23	-4.99	415.35	65.060	–	–	–	–65.06
16	349.04	299.82	349.37	270.40	0.10	-29.42	417.74	187.60	417.90	206.77	0.04	+19.17
Total	–	871.85	–	812.44	–	–59.41	–	574.97	–	546.37	–	–28.60

The stable ion beam SOBPs calculated in this work for 10, 15 and 20 cm depths in water at the SOBP center are shown in figures 5.4 and 5.5, modulated in number of ions at each isoenergetic layer according to $\mathcal{I}_\mathrm{S}$ and $\mathcal{I}_\mathrm{T}$, laterally integrated over a 4×4 cm^2 surface. For the reasons already mentioned, the OLDTPS parameter $\mathcal{I}_\mathrm{T}$ does not match this works' results for the number of ions, $\mathcal{I}_{\mathrm{S}}$. In addition, it is also shown on the right side of figures 5.4 and 5.5 the individual peak disentanglement from the respective SOBP (DT), so as to verify whether the number of ions calculated at each isoenergetic layer was adequate. This verification was necessary, since considerable deviations between the calculated and TPS number of particles delivered could denote an inconsistency with the methodology adopted to generate the $\mathcal{I}_{\mathrm{S}}$ values. Moreover, the number of ions delivered in time and at each spill, and hence energy layer, would affect the PET acquisition simulation results. This is particularly true for *online PET* acquisitions, but to a lesser degree also for *in room* and *offline* PET acquisitions.

In the figures 5.4 and 5.5, only the last SOBP in range is shown disentangled, this had to do with the fact that, from the data presented in table 5.2, it was found that these SOBPs have highest discrepance between $\mathcal{I}_{\mathrm{T}}$ and $\mathcal{I}_{\mathrm{S}}$. Hence they represent a worst case scenario, more interesting for the present work analysis. Indeed, both in ^{12}C and ^{16}O SOBPs, and even in the worst case scenario detailed, it appears that the deviations are almost entirely ascribed to the systematic deviation with respect to the OLDTPS ion number, with the relative weight of each pristine *Bragg Peak* seemingly adequate.

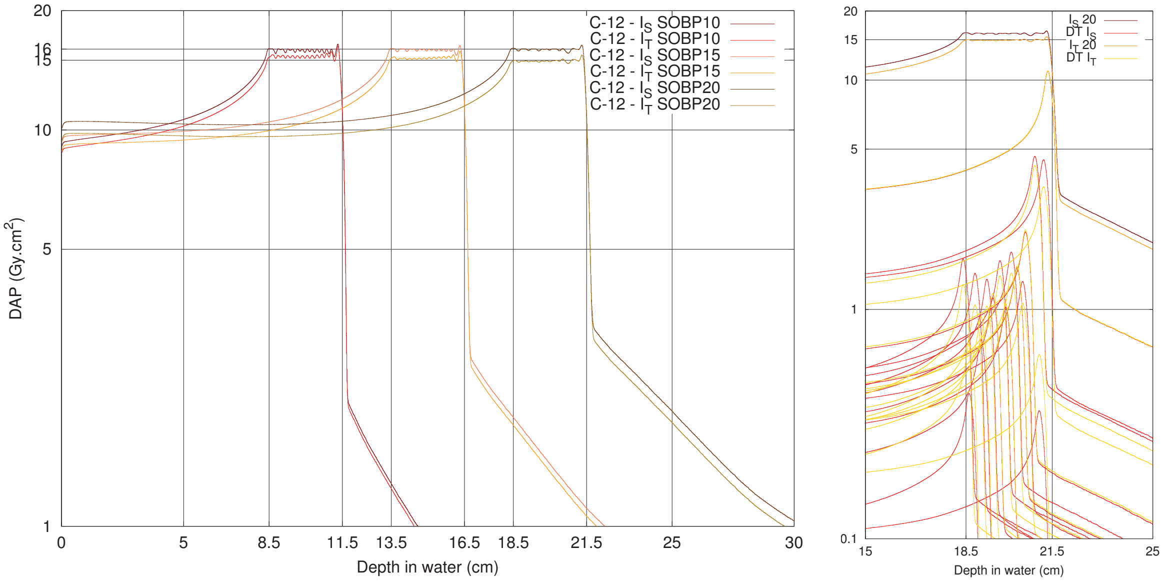

(a)

(b)

Figure 5.4: *(a)* ^{12}C SOBP*s as obtained by this work's FLUKA simulations ($\mathcal{I}_S$), and using TRiP's plan information ($\mathcal{I}_T$) in the FLUKA recalculation, at different ranges in water. (b)* ^{12}C *SOBP's individual peaks' disentanglement detailed at 20 cm range.*

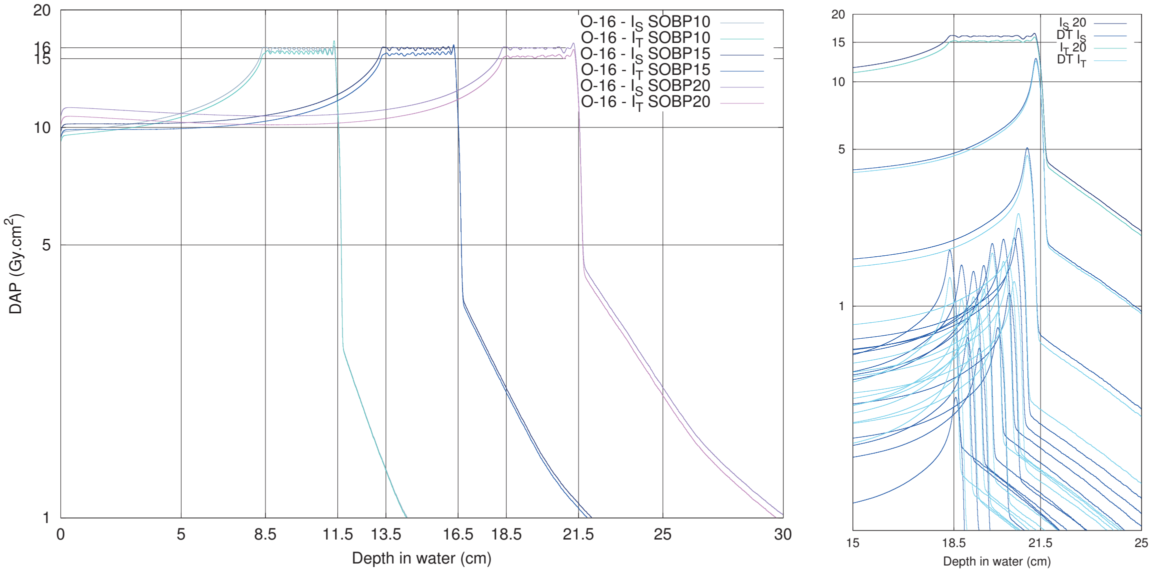

(a) (b)

Figure 5.5: *(a)* ^{16}*O* SOBP*s as obtained by this work's FLUKA simulations* ($\mathcal{I}_S$)*, and using TRiP's plan information* ($\mathcal{I}_T$) *in the FLUKA recalculation, at different ranges in water. (b)* ^{16}*O SOBP's individual peaks' disentanglement detailed at 20 cm range.*

Summarizing, it has been found that:

- The tools devised in this work led to a good agreement with the data laterally integrated in the water phantom, as in table 5.1. The energy parameters employed, based on the OLDTPS research TPS version and employing beam line approximations, matched the NEWTPS data in range within 0.4 mm, provided the RiFi was removed for the comparison and some relevant simulation parameters were adapted (water density and ionization potential).

- For volumes with smaller lateral width, namely 4×4 cm^2, the intensity modulation result agreement with OLDTPS deteriorated, although the lateral profile was inline with the NEWTPS values, as displayed in figure 5.2. The OLDTPS data provided, integrated over a 4×4 cm^2 surface, was found by HIT colleagues to attain 95% of the expected dose[Tes16b] and this has been also reflected in the total number of ion values calculated and the deviations in table 5.2, which ranged between ~ 1 and 7 % for ^{16}O SOBPs at 10 cm and ^{12}C at 20 cm range, respectively.

- Regarding the individual *Bragg Peaks* composing the SOBP, both the number of ions calculated in this work's models and recalculated from the OLDTPS are not completely in line, even if a 5% factor is accounted for in table 5.2. Nevertheless, the SOBP shape and the individual *Bragg Peaks* trend observed in the right side of figures 5.4 and 5.5 indicates major similarities in the way that both SOBPs are constructed. This is also supported by observations when comparing $\mathcal{I}_\mathrm{S}$ and $\mathcal{I}_\mathrm{T}$ values in table 5.2.

- Irrespective of the inconsistencies mentioned, no range discrepance above 300 μm was observed in between the SOBPs predicted ranges' for ^{12}C and ^{16}O. The methodology employed to generate $\mathcal{I}_{\mathrm{S}}$ was seen to render nominal values of 16 [Gy cm^2] for all scenarios simulated and was seen to be in line with the ^{12}C NEWTPS data provided by HIT.

5.1.2 Extrapolation for radioactive ion beam SOBPs in a water phantom and in a voxelized patient's head geometry

In spite of the fact that the SOBPs produced differed from the recalculated OLDTPS `TRiP` data, they match well NEWTPS ^{12}C data as previously mentioned. Therefore it will be assumed that the methodology employed can be extended to $RI\beta^+$, in view of the arguments discussed in the previous section.

The method was seen to be able to use FLUKA simulation data to obtain beam kinetic energy and number of ions for each isoenergetic layers (E_{S}, $\mathcal{I}_{\mathrm{S}}$) to generate SOBPs of ^{12}C and ^{16}O within the range intervals and at the nominal dose levels required, namely 1 Gy or 16 Gy cm^2. An extrapolation was performed for radioactive ion beams of ^{11}C and ^{15}O, in order to obtain comparable SOBPs, these results are shown in figure 5.6:

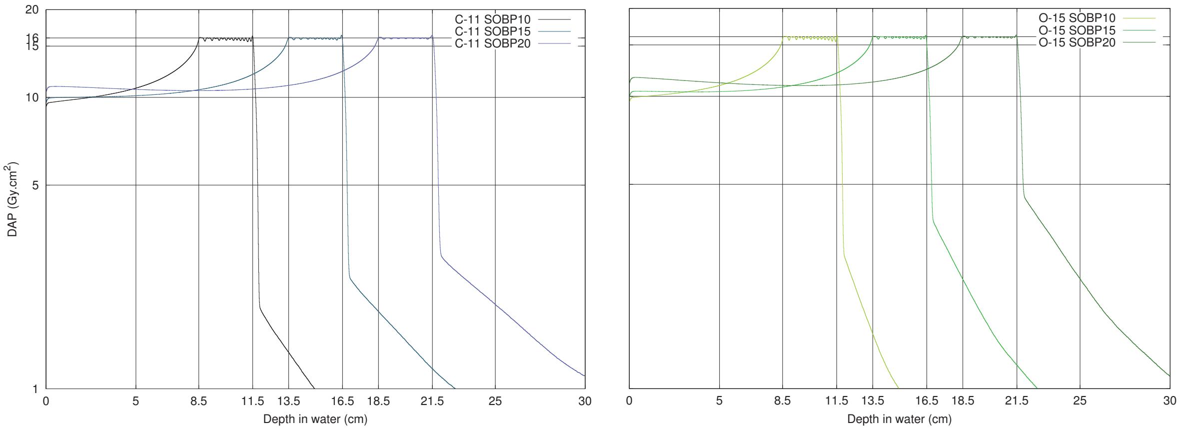

(a) ^{11}C (b) ^{15}O

Figure 5.6: *Radioactive ion beams'* SOBP*s at different ranges in water, as obtained by FLUKA ($\mathcal{I}_S$) in water.*

The next step included a patient head VOXEL scenario, instead of water, with comparable SOBPs of both stable and $RI\beta^+$ being obtained at equivalent ranges in the voxelized geometry[Bat16]. The full process of SOBP creation was accomplished in steps, the complete procedure is detailed in the appendix A: "Auxiliary programs".

Additionally, the *Siemens Biograph mCT (TrueV)* PET setup created in chapter 3 and shown in figure 3.7, was adapted to the present geometry, as depicted in figure 5.7. This enabled the generation of reconstructed images while accounting for the beam time structure and PET acquisition intervals in an *in beam PET* mode, diverging effectively from HIT's *offline PET* procedure. Finally, it allowed the testing of the FLUKA PET TOOLS' in its first application to an *in beam PET* scenario[Au18a].

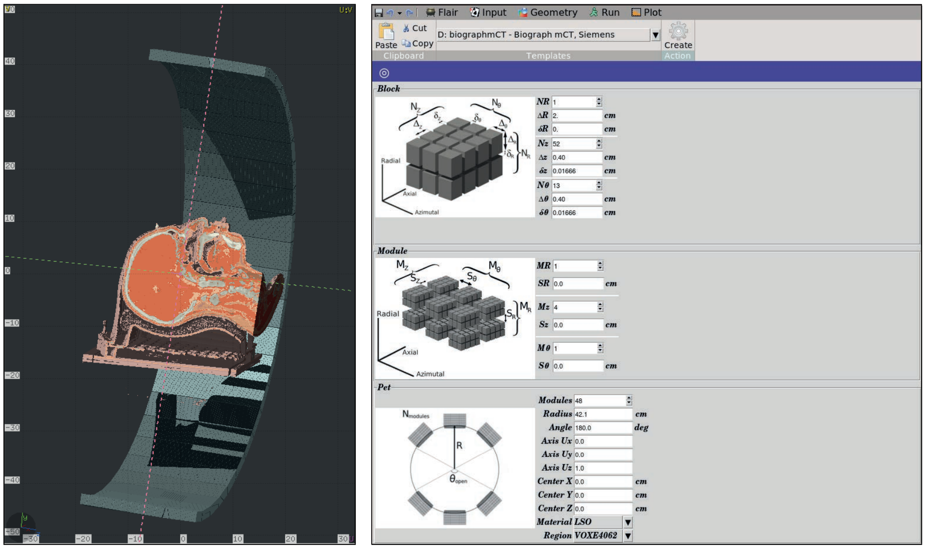

D: biographmCT - Biograph mCT, Siemens

Block

NR 1
ΔR 2. cm
δR 0. cm
Nz 52
Δz 0.40 cm
δz 0.01666 cm
Nθ 13
Δθ 0.40 cm
δθ 0.01666 cm

Module

MR 1
SR 0.0 cm
Mz 4
Sz 0.0 cm
Mθ 1
Sθ 0.0 cm

Pet

Modules 48
Radius 42.1 cm
Angle 180.0 deg
Axis Ux 0.0
Axis Uy 0.0
Axis Uz 1.0
Center X 0.0 cm
Center Y 0.0 cm
Center Z 0.0 cm
Material LSO
Region VOXE4062

(a) *PET Biograph m*CT (b) *Flair* PET model parameter setup

Figure 5.7: *Geometry view and setup in flair environment of the Siemens Biograph mCT (TrueV)*

By generating realistic SOBPs in the same PET+VOXEL scenario, and with beam line elements reproduced, different PET acquisition and beam time scenarios were simulated, as depicted in the schematic:

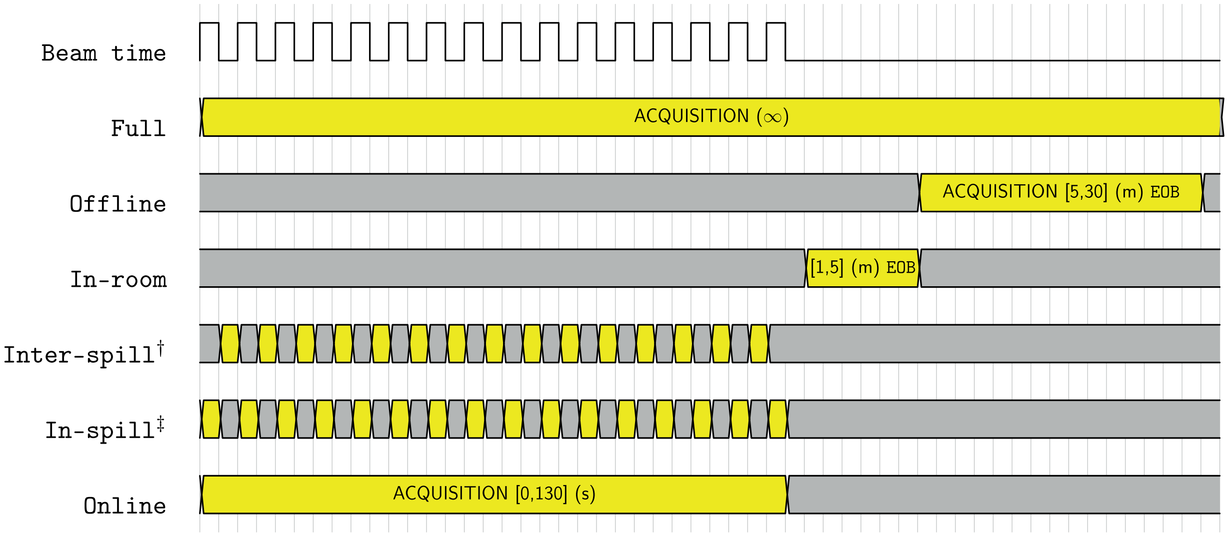

In the schematic above, "m" refers to minutes. EOB — End of Beam: defines the time counting from the irradiation's end.

† Inter–spill acquisition of events: totalling 60 seconds, comprising 15 periods of 4 second acquisition time.

‡ In–spill acquisition: accounting for 70 seconds in total, preserving the irradiation profile displayed in table 4.3.

The reconstructed images were then evaluated in order to assess the four ions' performance in different therapy modalities. These PET acquisition modalities, time and intensity parameters, were (arbitrary) variations of feasible scenarios at GSI/HIT reported in earlier works[PBH08, Sha11].

The *offline* and *in room PET* acquisition modalities spawned considerable minutes in time, whereas the *online PET* acquisitions were rather short, with 130 s only. An attempt was made to be consistent with a previous study, which reported that with 180 s *online PET* acquisition, with random suppression techniques, one could obtain a (tenfold) advantage in signal acquisition compared to a 30 minute *offline PET* acquisition[PBH08].

This work is not aimed at assessing the merit of any of these PET acquisition modalities or compare the results with literature, since the present work is only a simulation and a rather simple one. Instead, it will be attempted to highlight the merit of the different beam species for imaging with comparable dose delivery.

As the VOXEL phantom contained an heterogeneous material/density distribution, the previous methodology to calculate the total number of ions delivered in chapter's 3 equation 3.3 was replaced with a more complex, differential evolution iterative optimization method gently provided by W.S. Kozłowska, yielding the values displayed in table 5.3[KV17]:

Table 5.3: *Parameters for SOBPs of 1 Gy, centered at 10 cm depth in an anthropomorphic* VOXEL *phantom; E – initial beam kinetic energy (MeV/u), $\mathcal{I}$ – number of ions ($\times 10^6$ ions).*

Layer	^{11}C		^{12}C		^{15}O		^{16}O	
#	E	$\mathcal{I}$	E	$\mathcal{I}$	E	$\mathcal{I}$	E	$\mathcal{I}$
1	229.13	52.650	217.82	46.714	268.37	24.665	258.43	32.601
2	231.95	5.529	220.49	7.226	271.70	13.299	261.64	0.049
3	234.75	0.025	223.15	7.694	275.01	9.642	264.84	8.531
4	237.54	42.360	225.79	23.886	278.30	4.071	268.01	19.414
5	240.30	3.169	228.40	22.015	281.58	12.239	271.16	4.885
6	243.05	25.547	231.00	3.554	284.83	29.029	274.30	17.635
7	245.77	28.181	233.58	43.937	288.06	0.088	277.41	7.786
8	248.48	13.934	236.15	15.128	291.28	23.517	280.51	26.980
9	251.17	33.514	238.70	9.189	294.48	9.740	283.58	5.336
10	253.84	22.433	241.23	41.199	297.66	20.618	286.64	12.963
11	256.49	42.132	243.74	29.842	300.82	30.285	289.68	33.360
12	259.12	27.124	246.23	37.074	303.97	14.100	292.70	26.884
13	261.73	54.307	248.71	30.128	307.10	31.405	295.70	1.099
14	264.33	35.066	251.17	42.233	310.21	27.286	298.68	49.301
15	266.91	88.235	253.61	89.073	313.31	57.370	301.64	43.972
16	269.47	218.81	256.04	212.74	316.39	136.58	304.58	140.37
Total	–	693.01	–	661.63	–	443.93	–	431.16

The distributions of both dose and annihilation events at rest on the VOXEL, using the aforementioned ion numbers and energy parameters for ^{15}O can be, respectively, seen in figure 5.8

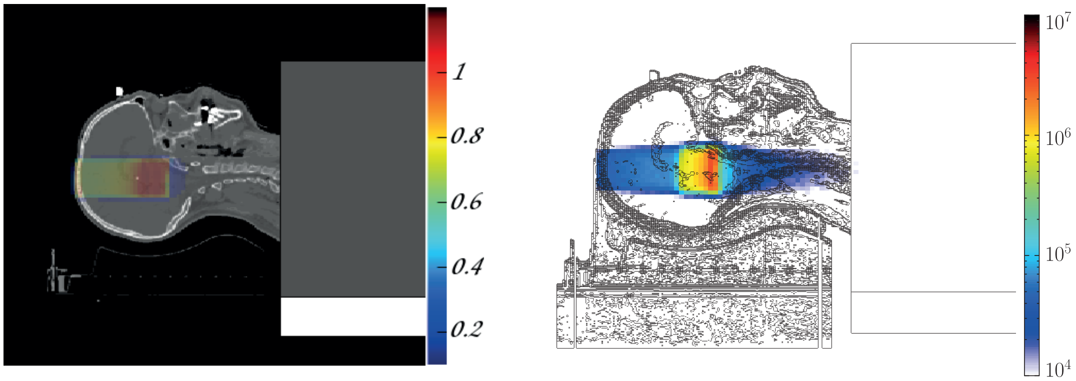

(a) (b)

Figure 5.8: *1 Gy SOBPs in the anthropomorphic head* VOXEL *for* ^{15}O*: (a) The dose distribution can be seen in a* CT*-like view environment, in Gy; (b) The annihilation events at rest result, integrated over time, is shown in a geometry mesh centered and integrated over the SOBP lateral dimensions.*

The dose deposited by the different ion beams studied, in range, as well as the annihilation events at rest map, integrated over time through the phantom, can be assessed in figure 5.9.

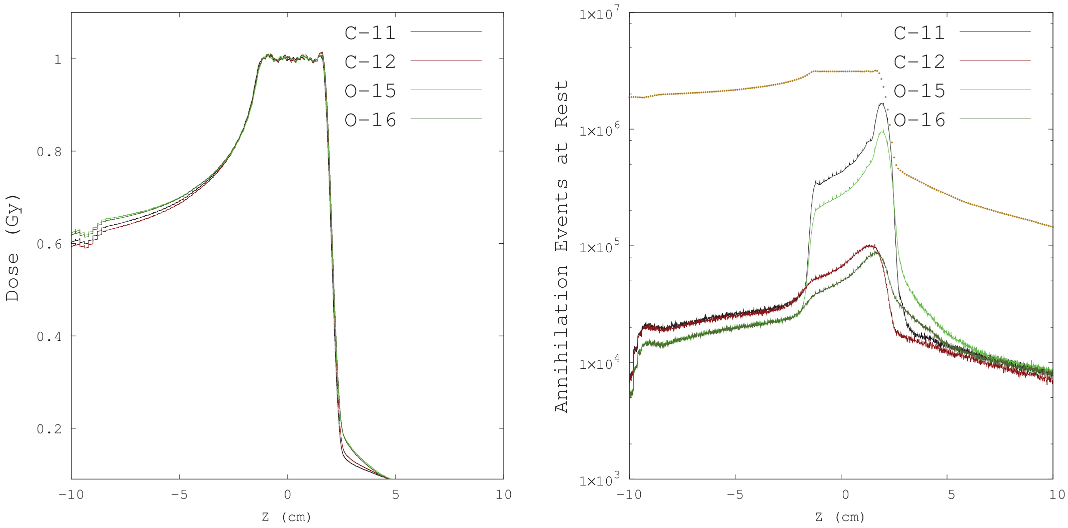

(a) (b)

Figure 5.9: *1 Gy SOBPs of different ion beams resulting from an optimized intensity modulation, in the anthropomorphic head* VOXEL *geometry (a). The annihilation events at rest can be seen in (b) with the* SOBP *golden dotted dose profile superimposed.*

The resulting Annihilation events at rest obtained during each PET acquisition time's modality can be seen in figure 5.10

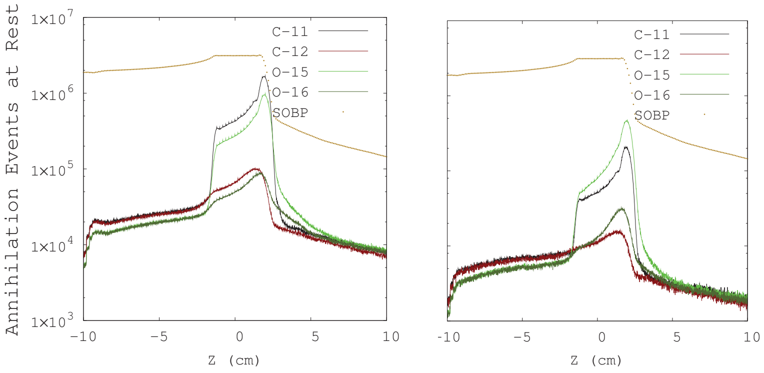

(a) *Time integrated*

(b) *In room*

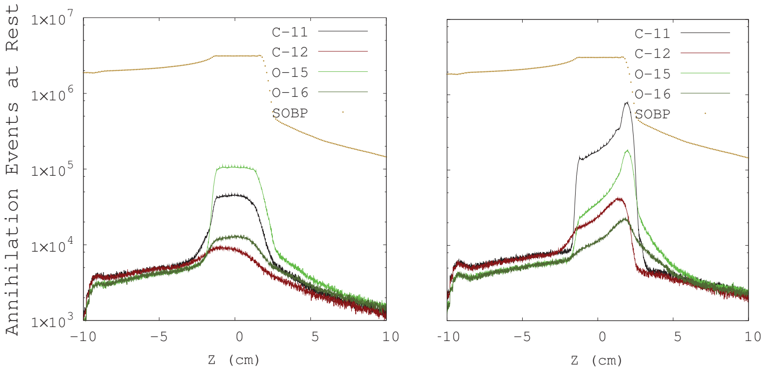

(c) *Online*

(d) *Offline*

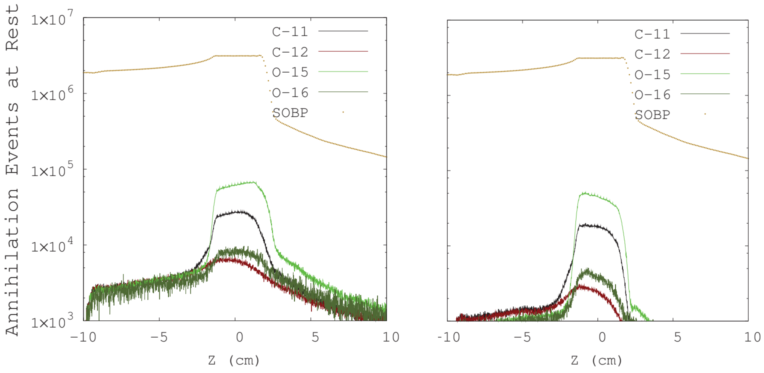

(e) *In–spill*

(f) *Inter–spill*

Figure 5.10: *Annihilation Events at Rest obtained only during the considered acquisition scenarios. The SOBP dose profile is superimposed in the plot as golden points.*

For the four SOBPs studied, while using the *PET Biograph mCT in silico* model and an HIT–based approximated beam line, the reconstructed PET images were obtained throughout the various acquisition modalities, and can be seen throughout figures 5.11–5.16. The beam time structures were kept consistent with those stated in table 4.3, while the number of ions delivered followed table's 5.3 parameters.

Moreover, the number of decays observed and the subsequent coincidences detected are consistent, in proportion, with previous studies reported in the literature for ^{12}C for head irradiations at HIT[PBH08]. Namely, an availability of physical decays for imaging estimated at $\sim 3 \times 10^6$ during spill ($\sim 7 \times 10^6$ in this work), a similar value in between spills and $\sim 1.2 \times 10^7$ offline ($\sim 2 \times 10^7$ in this work). The irradiation schemes and acquisition times naturally differed from those followed in the current work and hence a direct comparison is not possible but, nevertheless, it is relevant to mention that this work's simulation yields are not entirely detached from reported calculations.

The *offline PET* acquisition is the current procedure adopted at HIT, and the sole acquisition modality among those studied in this work which could be compared with operational data. However, the signal will be affected by the *biological washout* and therefore a direct comparison was impossible. In addition, one must consider that the scanner in HIT is in a different room, thus being less subject to activation and noise disruption, whereas in the present scenario the scanner and beam line system is integrated as in an *in beam PET* scenario, even for the *offline*, and *in room PET* acquisitions. Still, in this work the only noise background levels arise from the 130 seconds irradiation (without accounting for the LSO radioactivity), whereas a non–negligible background would be certain to occur after several irradiations and consequent activation of some beam line elements. Possibly the configuration hereby employed could eventually become ineffective as the LSO crystals become activated, lowering the true coincidences' acquisition count rates.

Ion beam therapy PET acquisitions have lower true counts with respect to typical nuclear medicine imaging, the amount of coincidence counts obtained in the current work is in line with the offline ^{12}C irradiation number of registered coincidences reported in other works[Sha11] ($\sim 10^{5-6}$). Moreover, it is found generally within the typical limits of advanced image reconstruction methods' applicability (80 000), reported in previous a work[Kur13].

In view of the prompt generated noise and typical low true count rates, which could decrease the quality of the images beyond acceptable levels, the reconstructions were obtained using two distinct methods:

- A version of the MLEM method, implemented in the FLUKA PET TOOLS as a standard by Y. Toufique, reading directly from the coincidence list file[Tou16].
- *Biograph mCT* FOV–optimized MLEM method with *Fourier rebinning* and intra–reconstruction smoothing, devised by C. Gianoli *et al.* and employed to the *sinogram* file[Gia16, Gia14].

The latter method would ensure that reconstructions were done with a more appropriate methodology considered, since the former was missing any noise reduction–techniques options and was not optimized for the PET scanner model.

Both images were seen to be somewhat equivalent in contrast, differing only in generation time and quality depending on the iteration number, as well as other parameters (*e.g.* corrective methods applied such as ToF). The contrast recovery is performed in steps, converging iteratively to the stable value. However, the noise will increase consistently with each iteration.

In the following figures 5.11–5.16, one can appreciate the results of both reconstruction methods employed for the total coincidence events, in list mode and *sinograms*, respectively. In the standard mode the contrast is presented with a relative scale, to highlight the overall distribution of signal emitters in all beam irradiations. On the other hand, in the optimized mode an absolute scale is provided for each scenario to assess the difference between $RI\beta^+$ and stable ion beams resulting contrast.

On the top left of the figures 5.11–5.16, the number of ions employed in the irradiation for each beam species are presented in blue. For the time comprising each acquisition, it is also shown the number of photons effectively hitting the scanner (violet) and the actual coincidence events detected (red), in order to understand the scale of events involved in the reconstructions for each beam specie and acquisition time. Regarding *in–spill* and *inter–spill PET* acquisitions, in figure 5.15 and 5.16 the number of ions employed in each spill is provided as taller bars while the information on the photons hitting the scanner will be given in smaller bars. The top right panel of figures 5.11–5.16 provides the number of coincidence events for each ion beam species in the acquisition time considered, as well as the proportion of true, scatter and random events among the total value.

For oxygen ion beams, the highest amount of coincidence events is acquired online, attaining $\sim 10^6$ with an ^{15}O beam, of which two thirds are true coincidences, most definitely due to the contribution of short lived ^{15}O as main source of β^+ emitters. For the same acquisition mode, but irradiating with ^{16}O, the coincidence events decrease to 60%, of which only slightly more than half are trues. In the acquisitions after EOB one observes a steadily decrease in true coincidence events compared with online using stable oxygen ion beams already in an *in–room PET* acquisition, with a decrease of almost a factor 2 of the online "trues" count. On the other hand, the same number of events is observed offline, albeit with a longer acquisition time. The ^{15}O beam, on the contrary, maintains the same level of true coincidence events during the *in room PET* acquisition time compared to the online, but in the offline acquisition it halves.

Regarding carbon ion beams, the maximum number of coincidence events is acquired offline with the ^{11}C beam in view of the high levels of ^{11}C produced, with slightly over 10^6 true coincidence events. Using ^{12}C beams, the number of coincidences observed decreases by sevenfold in the same acquisition period. In an *in room PET* acquisition modality the difference is only a factor four, favouring the radioactive ion beam, whose overall coincidence events decrease to about a third of what observed during the *offline PET* acquisition. In the online acquisition modality, the performance of stable ion beams is comparable in terms of true coincidence events ($\sim 3 \times 10^5$) while for radioactive ion beams, ^{11}C underperforms comparing to ^{15}O by $\sim 25\%$.

When analyzing the online acquisition submodalities, namely *inter–spill* and *in–spill*, it is observed that the amount of coincidence events in the latter is generally much higher than in the former. In acquisitions during spill, the total coincidence event count varies from $\sim 5 \times 10^5$ for ^{16}O ions to almost $\sim 8 \times 10^5$ for the radioactive oxygen ion beam, with the proportion of true coincidence events varying from half to two thirds, respectively. As for carbon ion irradiations, the amount of true coincidences obtained by using the radioactive ion beam ($\sim 3.6 \times 10^5$) is only about 20% higher with respect to its stable counterpart.

While the non true coincidence events in offline modalities were only scatters, during spill the random coincidences dominate, particularly for the stable ion irradiations were they account for almost half of the total value.

In between spills, the difference between radioactive and stable ion irradiations is more considerable. Using ^{15}O ions, the true count increases by a factor 6, from $\sim 1.9 \times 10^4$ to 1.3×10^5. For carbon ion irradiations, this difference is slightly less than a factor 4. Moreover, the true coincidence counts acquired with radioactive oxygen ion beams are more than twice those observed in ^{11}C irradiations.

Time integrated acquisition

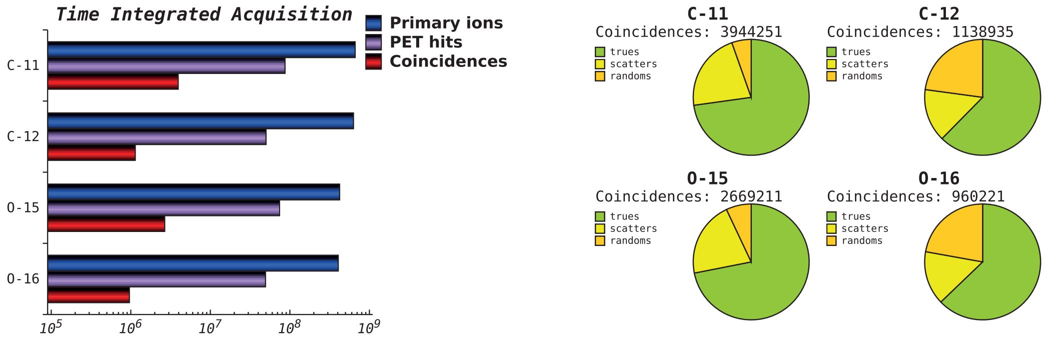

Standard FLUKA PET tools MLEM

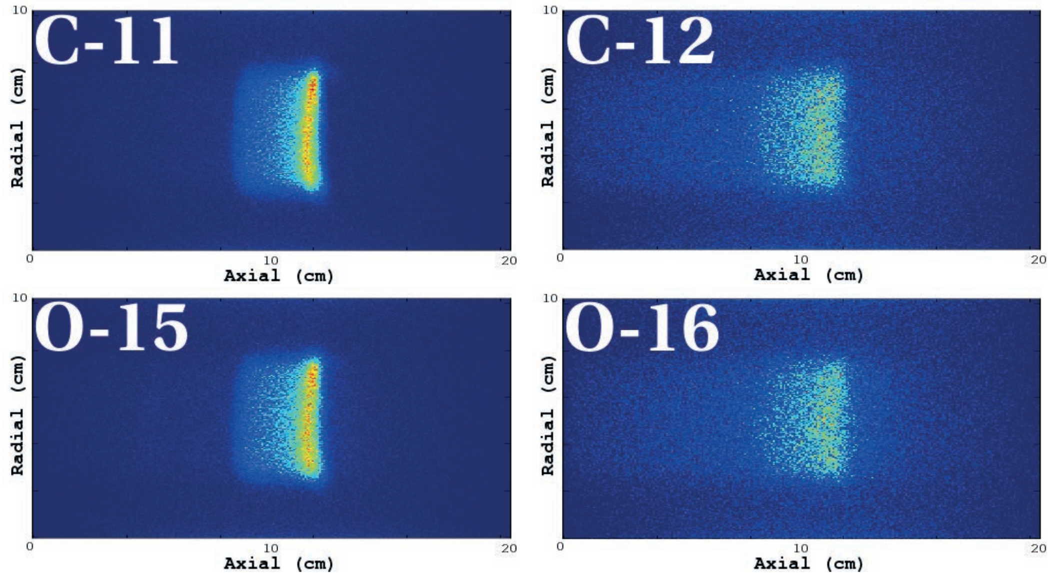

Optimized MLEM reconstruction

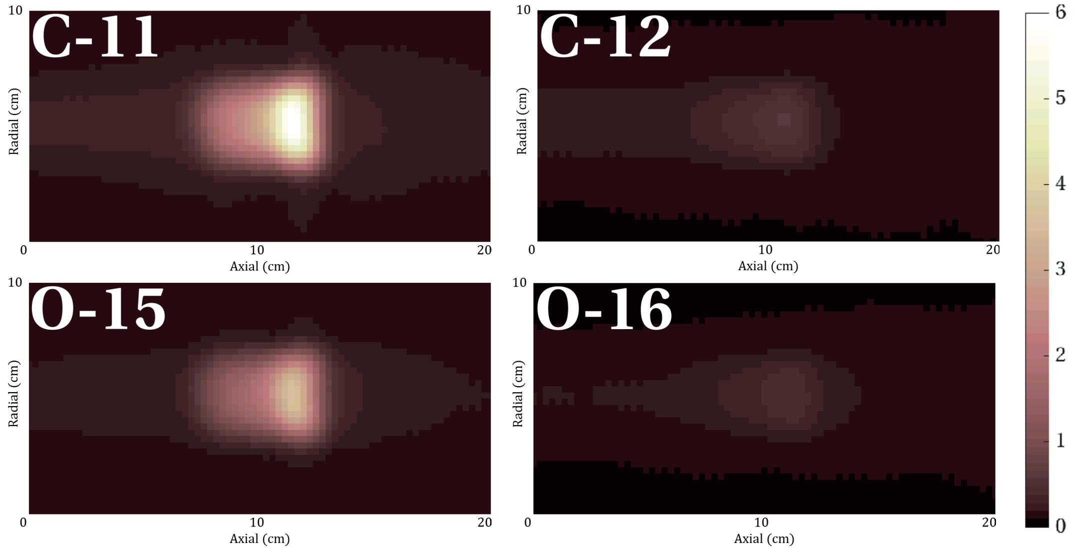

Figure 5.11: *Top panel: acquisition data on the PET scanner (left) with respective coincidence analysis (right). Standard – Reconstructed SOBPs (90 iterations), seen longitudinally, using FLUKA PET tools' standard MLEM method. Optimized – Reconstructed SOBPs (10 iterations), seen longitudinally with an optimized MLEM method.*

Offline acquisition (5 – 30 m EOB)

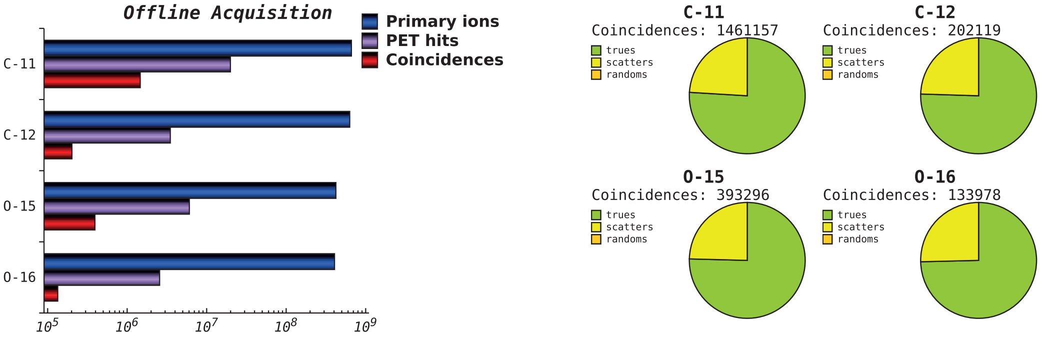

Standard FLUKA PET tools MLEM

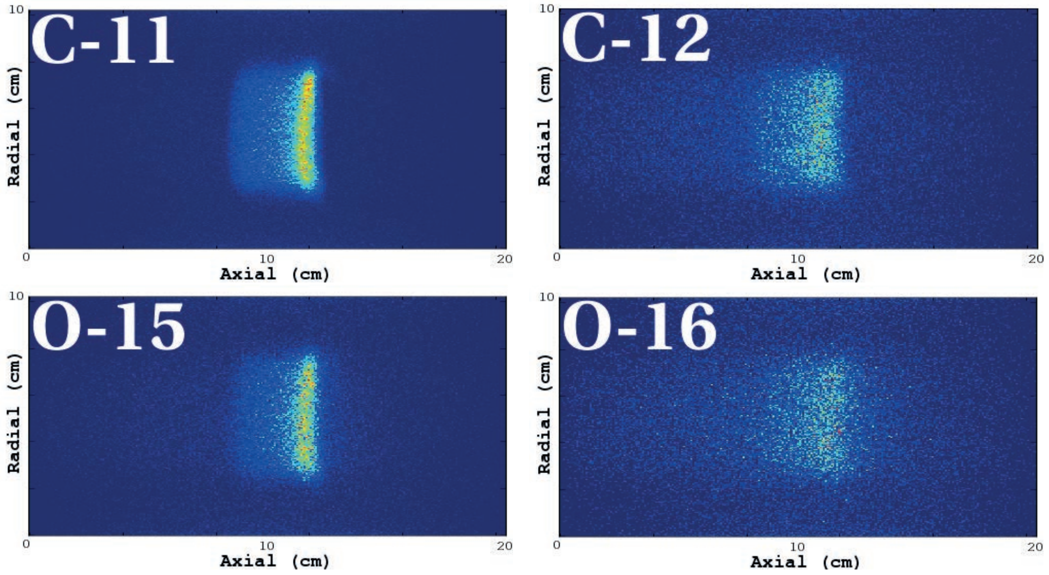

Optimized MLEM reconstruction

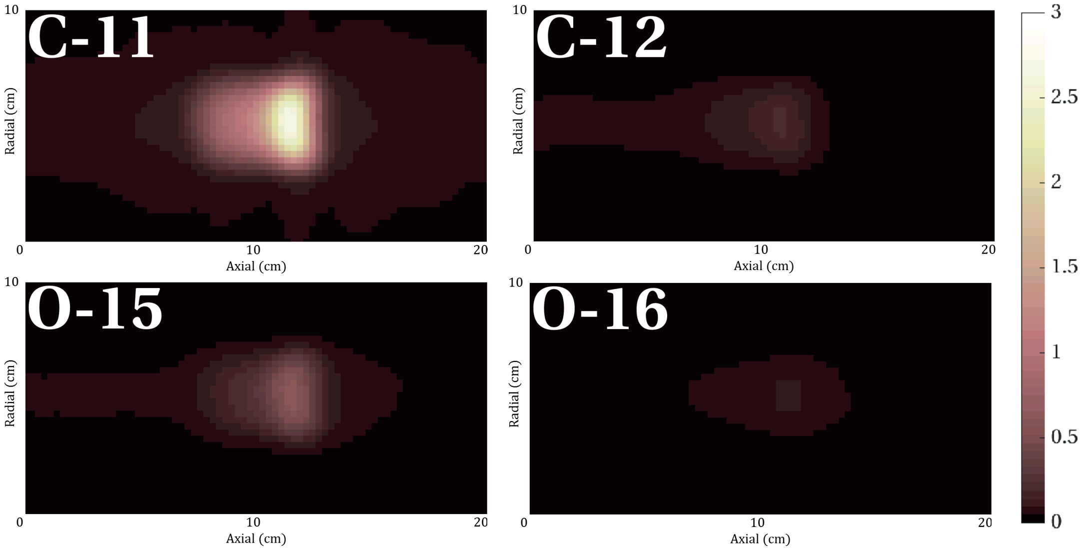

Figure 5.12: *Top panel: offline acquisition data from 5 to 30 m (*EOB*) on the PET scanner (left) with respective coincidence analysis (right). Standard – Reconstructed SOBPs (90 iterations), seen longitudinally, using FLUKA PET tools' standard MLEM method. Optimized – Reconstructed SOBPs (10 iterations), seen longitudinally but using an optimized MLEM method.*

In–room acquisition (1 – 5 m EOB)

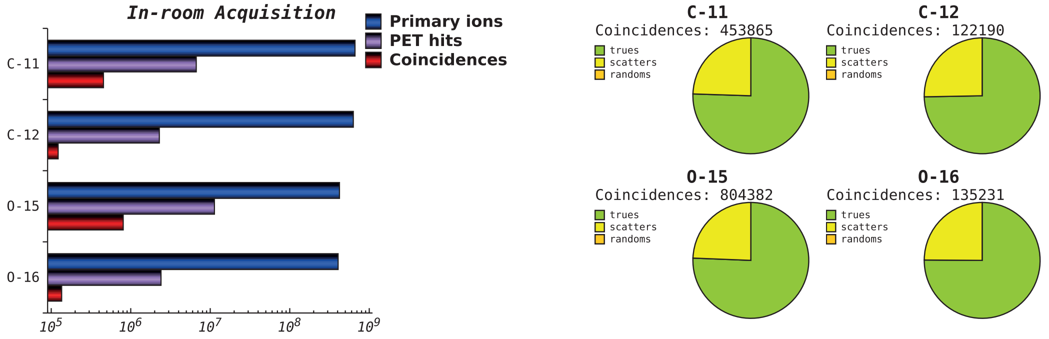

Standard FLUKA PET tools MLEM

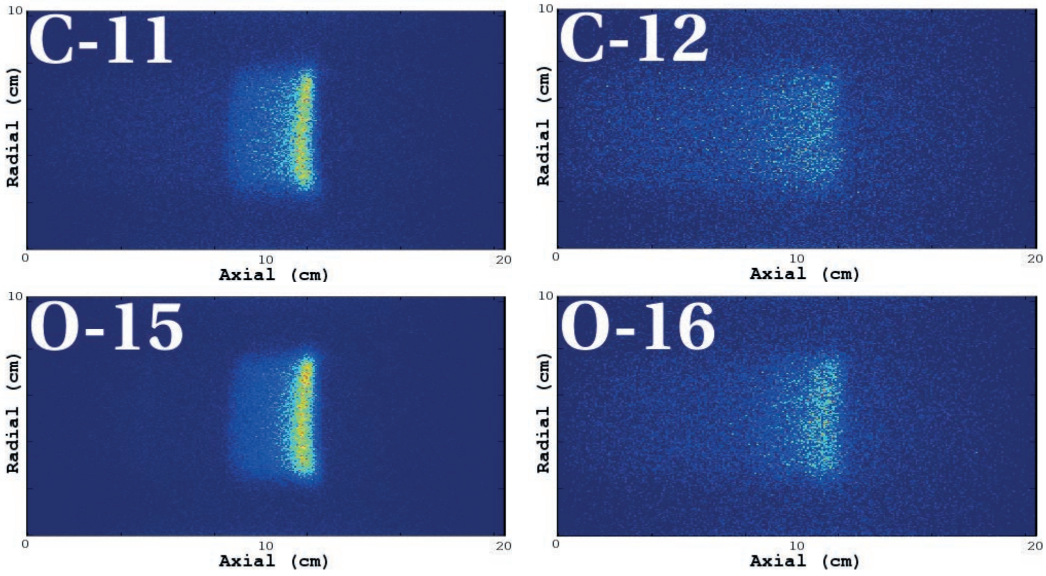

Optimized MLEM reconstruction

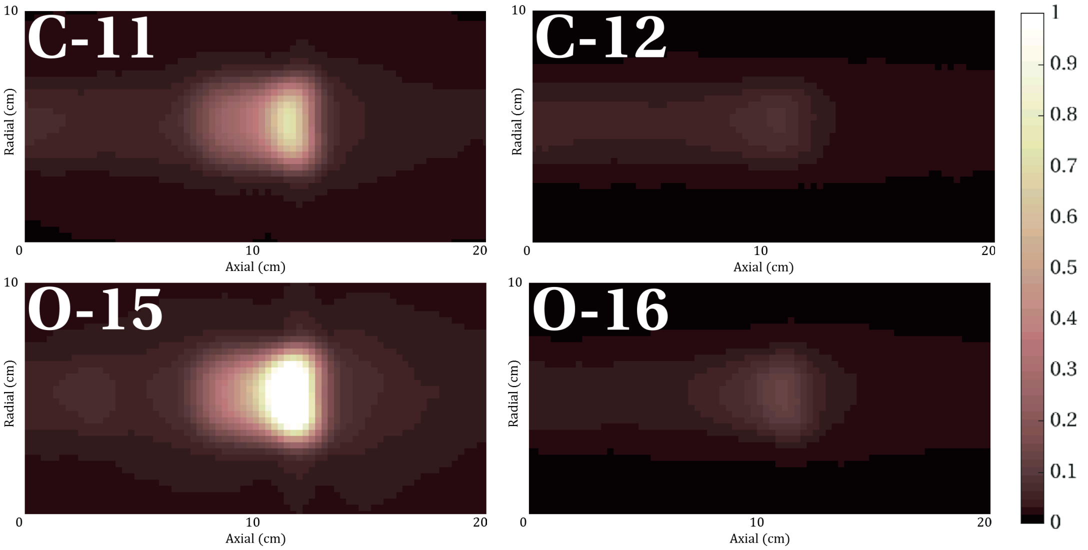

Figure 5.13: *Top panel: in–room acquisition data from 1 to 5 m (EOB) on the PET scanner (left) with respective coincidence analysis (right). Standard – Reconstructed SOBPs (90 iterations), seen longitudinally, using FLUKA PET tools' standard MLEM method. Optimized – Reconstructed SOBPs (10 iterations), seen longitudinally with an optimized MLEM method.*

Online acquisition (130 s)

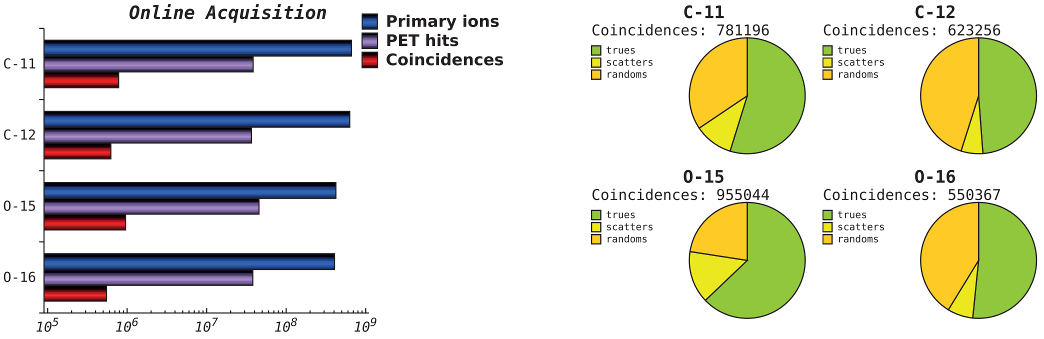

Standard FLUKA PET tools MLEM

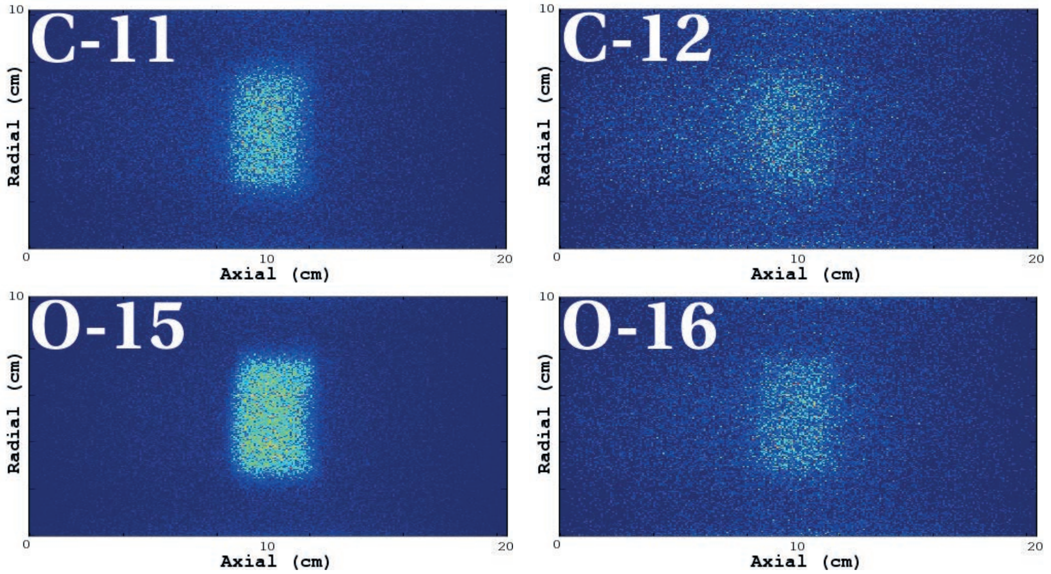

Optimized MLEM reconstruction

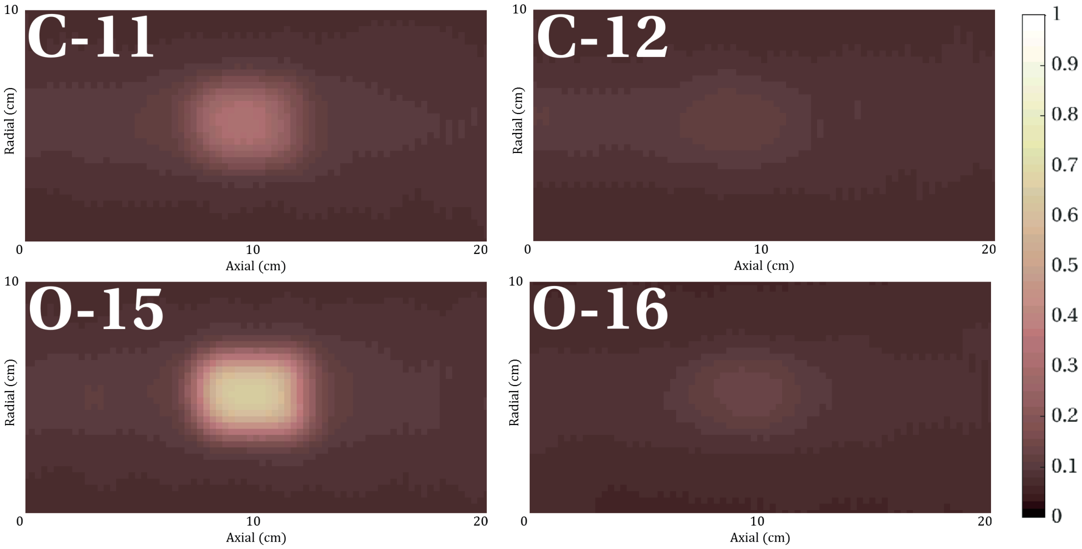

Figure 5.14: *Top panel: online acquisition data (130 s) on the PET scanner (left) with respective coincidence analysis (right). Standard – Reconstructed SOBPs (90 iterations), seen longitudinally, using FLUKA PET tools' standard MLEM method. Optimized – Longitudinally reconstructed SOBPs (10 iterations), with an optimized MLEM method.*

In–spill acquisition (during spill time only)

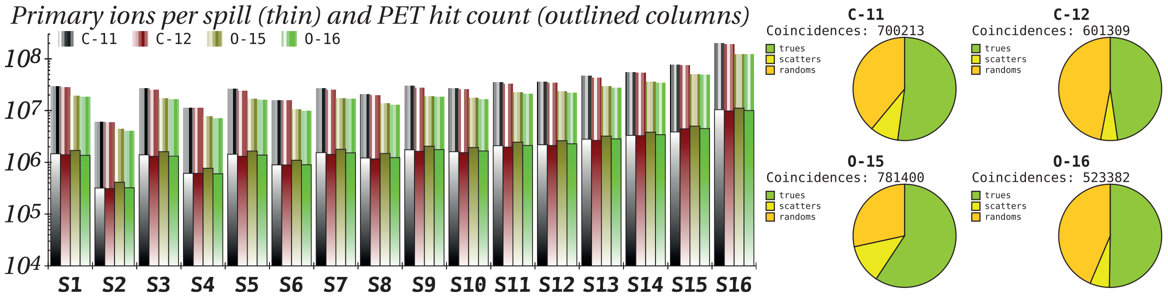

Standard FLUKA PET tools MLEM

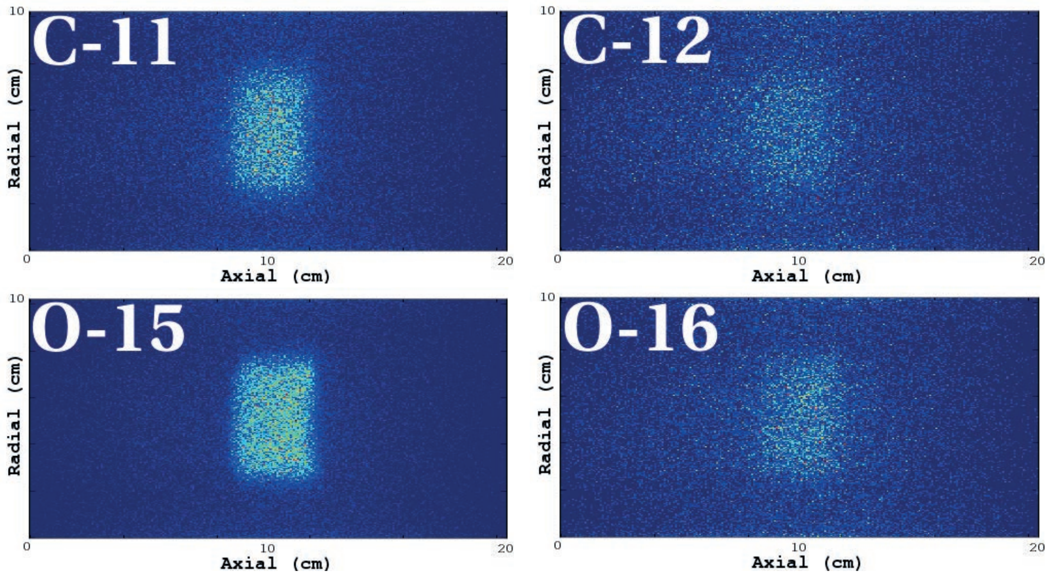

Optimized MLEM reconstruction

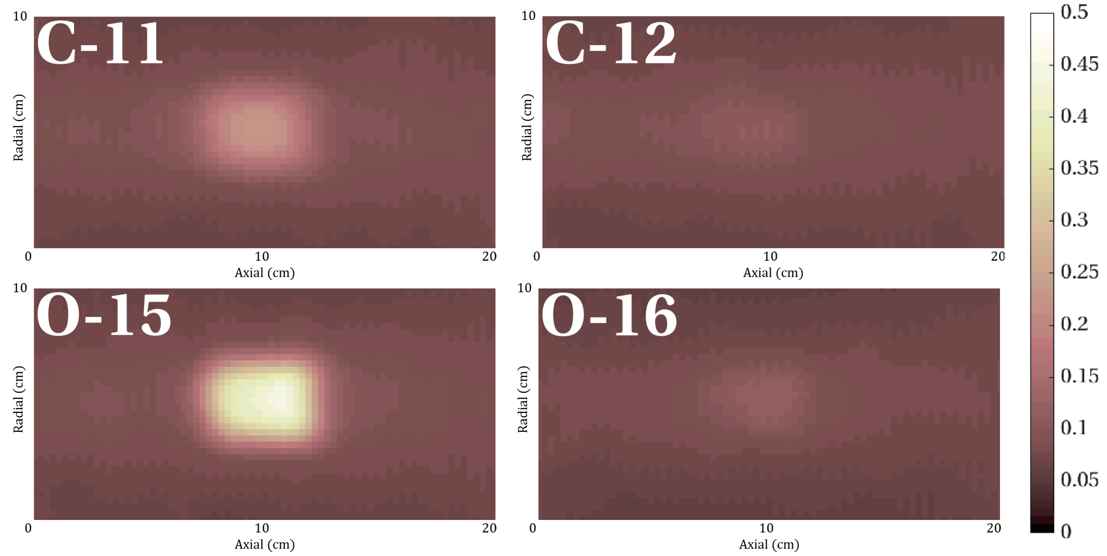

Figure 5.15: *Top panel: in–spill ions/spill (thinner columns) and acquired hits (larger columns) by the PET-scanner (left) with respective coincidence analysis (right). Standard – Reconstructed SOBPs (90 iterations), seen longitudinally, using FLUKA PET tools' standard MLEM method. Optimized – Reconstructed SOBPs (10 iterations), seen longitudinally with an optimized MLEM method.*

Inter–spill acquisition (during spill intervals only)

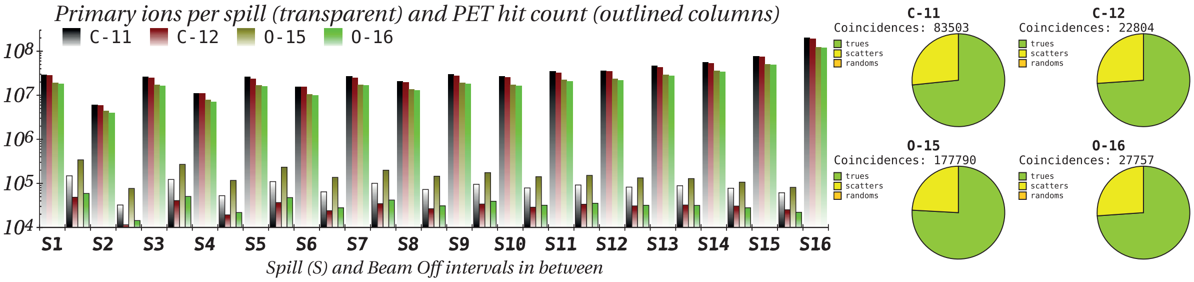

Standard FLUKA PET tools MLEM

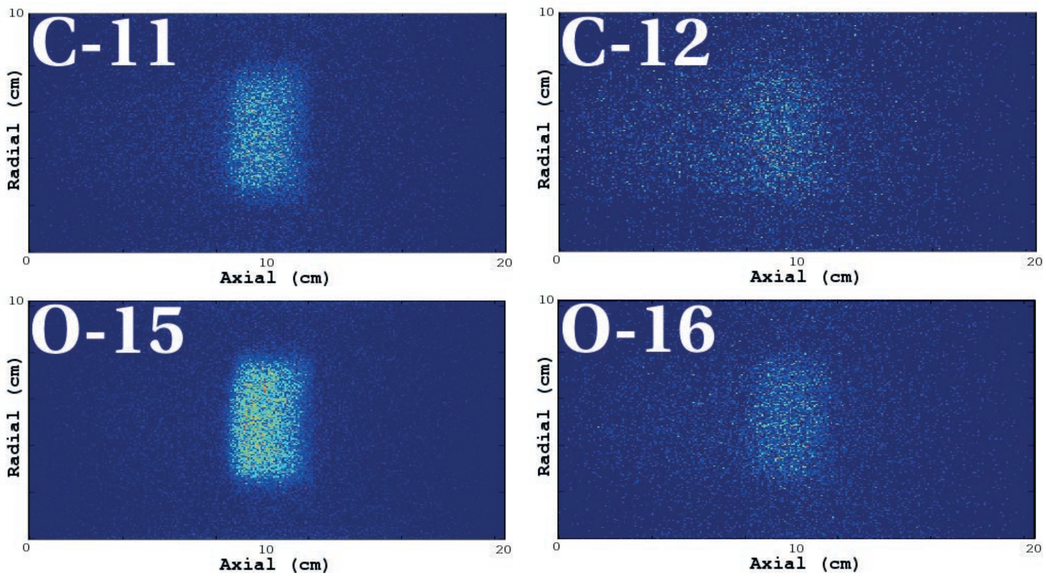

Optimized MLEM reconstruction

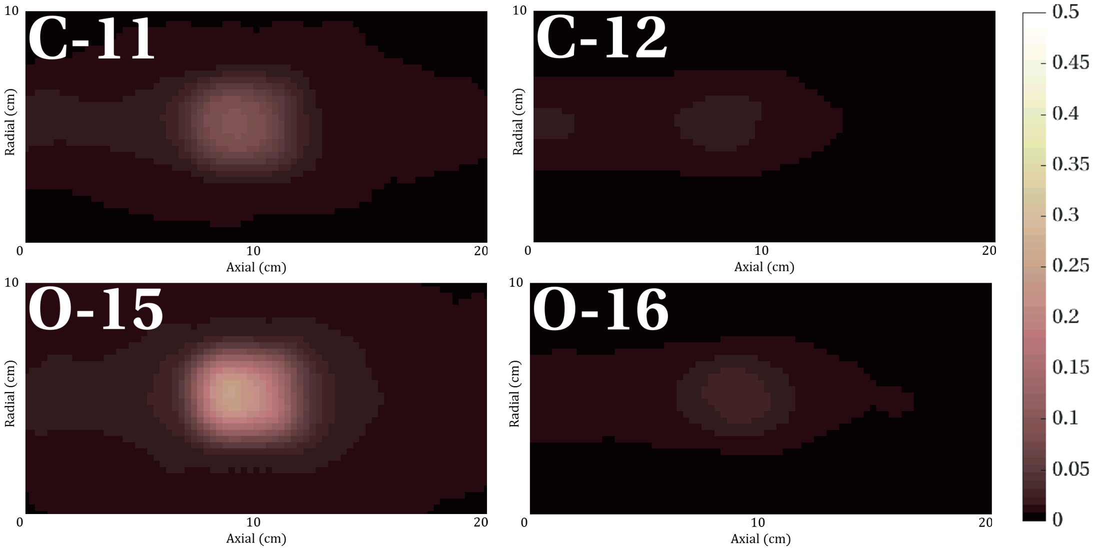

Figure 5.16: *Top panel: inter–spill acquisition data on the PET–scanner (left) with respective coincidence analysis (right). Standard – Reconstructed SOBPs (90 iterations), seen longitudinally, with FLUKA PET tools' standard MLEM method. Optimized – Longitudinally reconstructed SOBPs (10 iterations), with an optimized MLEM method.*

Therefore, there is clearly a positive impact in using radioactive ion beams, in all acquisitions, as summarized in table 5.4.

Table 5.4: *Ratio between true coincidence events acquired using radioactive and stable ion beams.*

Species compared	Offline	in room	online	in–spill	inter–spill
^{11}C/^{12}C	*7.27*	*3.77*	*1.41*	*1.27*	*3.64*
^{15}O/^{16}O	*2.97*	*5.99*	*2.11*	*1.76*	*6.58*

For the irradiations studied, the total coincidence count evolution in time, and their parent isotopes are depicted in figure 5.17 and table 5.5, respectively.

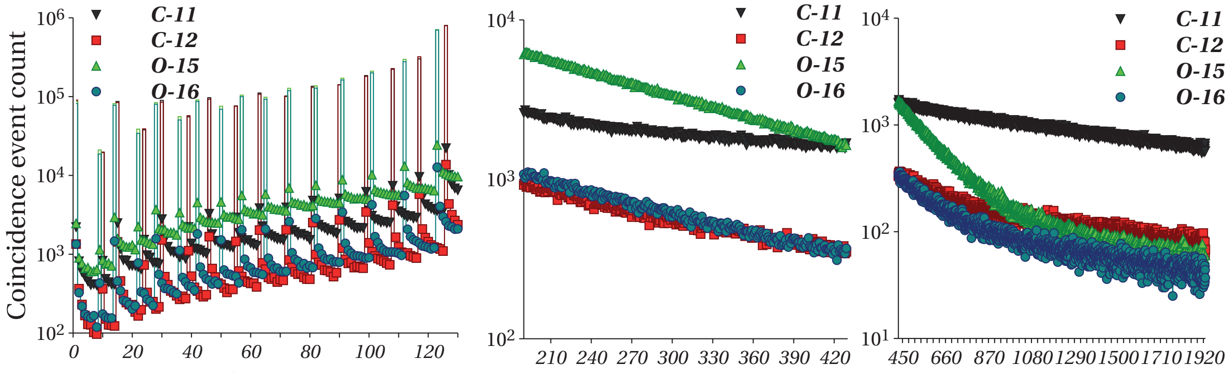

(a) Online (b) In room (c) Offline

Figure 5.17: *Total coincidence event counts throughout the acquisition time considered with the different beam species, the points denote the counts without neutron background.*

Table 5.5: *Coincidence events filtered by parent isotope in the various acquisition modalities.*

Acquisition	Ion beam	^{8}B	^{9}C	^{10}C	^{11}C	^{12}N	^{13}N	^{13}O	^{14}O	^{15}O
Online	^{11}C	34297	8408	102906	75156	3210	1008	485	1629	34199
	^{12}C	19785	3293	16989	7937	4223	970	378	1480	31741
	^{15}O	22308	5851	22956	4856	8327	4473	2860	20748	424736
	^{16}O	15898	2917	13475	4362	3895	1599	743	3061	54472
In room	^{11}C	0	0	8678	360777	0	5238	0	1982	81881
	^{12}C	0	0	1511	42413	0	4916	0	1922	76948
	^{15}O	0	0	1462	23025	0	17865	0	21374	747125
	^{16}O	0	0	856	20925	0	6716	0	3443	108563
Offline	^{11}C	0	0	2	1420043	0	12904	0	225	28399
	^{12}C	0	0	0	166794	0	12364	0	227	26260
	^{15}O	0	0	1	91584	0	46198	0	2206	257537
	^{16}O	0	0	1	82399	0	17332	0	352	37564

However, besides the qualitative enhancements in imaging and the quantified higher level of coincidence events observed for radioactive ion beams, one must assess how these coincidences reflect a better definition of the *Bragg Peak* for range monitoring. This problem is addressed in table 5.6 and continued in table 5.7:

Table 5.6: *Characterization of annihilation events at rest, coincidence event counts and the SOBP dose profile in different acquisition scenarios for all beams considered.*

Dataset	Characteristic	^{11}C	^{12}C	^{15}O	^{16}O
Dose SOBP	Ions delivered	6.93×10^8	6.61×10^8	4.44×10^8	4.31×10^8
	Proximal edge [cm]	8.71 ± 0.1	8.72 ± 0.1	8.70 ± 0.1	8.80 ± 0.1
	Distal edge [cm]	11.63 ± 0.1	11.63 ± 0.1	11.64 ± 0.1	11.63 ± 0.1
Online					
Annihilation events at rest	max. value	47220	9487	111200	13600
	max. position [cm]	9.99 ± 0.01	9.60 ± 0.01	9.19 ± 0.01	9.99 ± 0.01
	ΔW90% [cm]	1.67 ± 0.01	0.84 ± 0.01	2.14 ± 0.01	0.72 ± 0.01
	ΔW50% [cm]	3.07 ± 0.01	5.49 ± 0.01	3.17 ± 0.01	3.87 ± 0.01
	Distal fall–off [mm]	10.4 ± 0.1	45.9 ± 0.1	8.2 ± 0.1	39.4 ± 0.1
Coincidence event counts (PET)	max. value	20407	$16301^\dagger$	26823	$14492^\dagger$
	max. position [cm]	10.3 ± 0.1	$20.7 \pm 0.1^\dagger$	10.3 ± 0.1	$20.7 \pm 0.1^\dagger$
	ΔW90% [cm]	2.3 ± 0.1	—	2.3 ± 0.1	—
	ΔW50% [cm]	16.3 ± 0.1	—	4.1 ± 0.1	—
	Distal fall–off [mm]	97 ± 1	—	91 ± 1	—
In–spill					
Annihilation events at rest	max. value	28250	6991	67330	9707
	max. position [cm]	10.19 ± 0.01	9.99 ± 0.01	11.19 ± 0.01	10.59 ± 0.01
	ΔW90% [cm]	1.34 ± 0.01	0.03 ± 0.01	1.31 ± 0.1	0.04 ± 0.01
	ΔW50% [cm]	3.24 ± 0.01	5.80 ± 0.01	3.32 ± 0.1	3.48 ± 0.01
	Distal fall–off [mm]	12.1 ± 0.1	45.8 ± 0.1	8.8 ± 0.1	38.2 ± 0.1
Coincidence event counts (PET)	max. value	17786	$16271^\dagger$	21136	$14460^\dagger$
	max. position [cm]	10.3 ± 0.1	$20.7 \pm 0.1^\dagger$	11.4 ± 0.1	$20.7 \pm 0.1^\dagger$
	ΔW90% [cm]	0.9 ± 0.1	—	0.8 ± 0.1	—
	ΔW50% [cm]	18.3 ± 0.1	—	5.0 ± 0.1	—
	Distal fall–off [mm]	92 ± 1	—	87 ± 1	—
Inter–spill					
Annihilation events at rest	max. value	20090	3088	51460	5152
	max. position [cm]	9.19 ± 0.01	8.77 ± 0.01	9.19 ± 0.01	9.34 ± 0.01
	ΔW90% [cm]	0.39 ± 0.01	0.12 ± 0.01	0.71 ± 0.01	0.05 ± 0.01
	ΔW50% [cm]	2.82 ± 0.01	3.66 ± 0.01	2.89 ± 0.01	2.42 ± 0.01
	Distal fall–off [mm]	10.9 ± 0.1	29.6 ± 0.1	13.4 ± 0.1	23.3 ± 0.1
Coincidence event counts (PET)	max. value	2754	433	6424	644
	max. position [cm]	9.8 ± 0.1	8.7 ± 0.1	9.5 ± 0.1	9.6 ± 0.1
	ΔW90% [cm]	1.5 ± 0.1	0.4 ± 0.1	1.5 ± 0.1	1.2 ± 0.1
	ΔW50% [cm]	2.8 ± 0.1	3.9 ± 0.1	2.9 ± 0.1	3.3 ± 0.1
	Distal fall–off [mm]	10 ± 1	40 ± 1	13 ± 1	19 ± 1

† Inconclusive due to the high background level.

Table 5.7: *(Continuation of the previous table).*

Dataset	Characteristic	^{11}C	^{12}C	^{15}O	^{16}O
In room					
Annihilation events at rest	max. value	209100	16260	481600	32470
	max. position [cm]	11.89 ± 0.01	11.32 ± 0.01	11.99 ± 0.01	11.58 ± 0.01
	ΔW90% [cm]	0.30 ± 0.01	0.25 ± 0.01	0.27 ± 0.1	0.38 ± 0.01
	ΔW50% [cm]	0.81 ± 0.01	4.04 ± 0.01	0.84 ± 0.01	1.57 ± 0.01
	Distal fall–off [mm]	3.3 ± 0.1	19.6 ± 0.1	3.5 ± 0.1	6.9 ± 0.1
Coincidence event counts (PET)	max. value	22831	2045	49269	3612
	max. position [cm]	11.6 ± 0.1	10.8 ± 0.1	11.7 ± 0.1	11.2 ± 0.1
	ΔW90% [cm]	0.4 ± 0.1	1.1 ± 0.1	0.4 ± 0.1	0.6 ± 0.1
	ΔW50% [cm]	1.1 ± 0.1	4.2 ± 0.1	1.1 ± 0.1	2.2 ± 0.01
	Distal fall–off [mm]	4 ± 1	28 ± 1	3 ± 1	10 ± 1
Offline					
Annihilation events at rest	max. value	786600	42680	184100	22900
	max. position [cm]	11.93 ± 0.01	11.34 ± 0.01	11.99 ± 0.01	11.84 ± 0.01
	ΔW90% [cm]	0.29 ± 0.01	0.60 ± 0.01	0.32 ± 0.01	0.44 ± 0.01
	ΔW50% [cm]	0.79 ± 0.01	2.30 ± 0.01	0.91 ± 0.1	2.49 ± 0.01
	Distal fall–off [mm]	3.3 ± 0.1	5.5 ± 0.1	4.1 ± 0.1	24.6 ± 0.1
Coincidence event counts (PET)	max. value	87274	5127	19163	2588
	max. position [cm]	11.7 ± 0.1	11.0 ± 0.1	11.7 ± 0.1	11.4 ± 0.1
	ΔW90% [cm]	0.4 ± 0.1	1.0 ± 0.1	0.5 ± 0.1	1.0 ± 0.1
	ΔW50% [cm]	1.1 ± 0.1	2.8 ± 0.1	1.1 ± 0.1	3.4 ± 0.1
	Distal fall–off [mm]	4 ± 1	6 ± 1	5 ± 1	27 ± 1

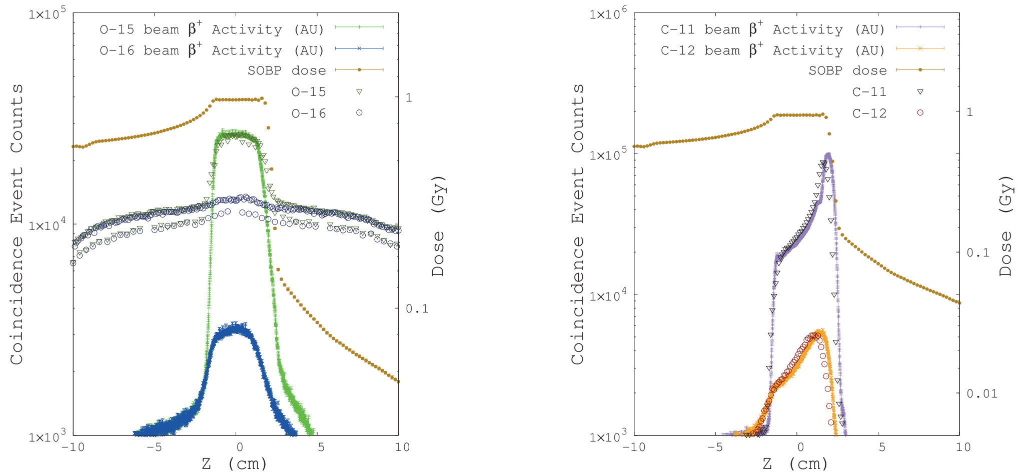

(a) Online (oxygen ion beams only)   (b) Offline (carbon ion beams only)

Figure 5.18: *Points: coincidence event counts obtained with PET tools in depth, with the SOBP dose profile superimposed, in golden points (Gy). The total annihilation events at rest simulated are shown in arbitrary units.*

The results from table 5.4 quantify the relative increase in true coincidence events, observed in the figures 5.11–5.16 and attained by using ^{15}O and ^{11}C. In particular, it is observed a gain of over a factor 7 in *offline* acquisition using ^{11}C, while the greatest gain employing ^{15}O is verified at *inter–spill*, with over a factor 6, and *in–room* with almost a factor 6.

As for tables 5.6 and 5.7, they include the SOBP region limits in depth, along with an evaluation of both the annihilations events and the PET coincidence counts profile, also in depth. The distal fall–off corresponds here to the longitudinal distance required to have the distributions' curve descending from 80% to 20% of its maximum value, in mm. The ΔW% values denote the longitudinal distance in between the proximal rise and distal fall–offs at 90% and 50% of the maximum value. These quantities are meant to illustrate the favourable correlation between coincidence counts and annihilation events distributions with respect to the distal edge of the SOBP dose profile. In the simulation results presented, this advantage is only evident for the offline modalities. The reason for this lies in the beam delivery time structure, for it goes from the lowest to the highest energy layer. Consequently, during the 130 s of online acquisition, the contribution from the higher energy layers, and particularly the last which alone amounts to $\sim$ 30% of all particles delivered to the SOBP (see table 4.3) is not fully accounted for. Should the beam delivery sequence be reverted, the online acquisition would be improved, as demonstrated in the appendix C with the coincidence event counts distributions resulting in sharper peaks for ^{11}C and particularly ^{15}O, with maxima within 1 mm of the SOBP distal edge. Conversely, the offline acquisition modalities benefit from both the extended acquisition time (240 s for in–room, 25 minutes for offline) and the fact that the last layer delivered corresponds to the distal edge of the SOBP. An online and offline acquisition is illustrated in figure 5.18. In the offline acquisition modalities, in table 5.7, more coincidence counts are verified for $RI\beta^+$ with respect to the stable ions, by a factor of 8–9, this increase is also corroborated by the annihilation events at rest results. Contrarily to the stable ion beams, the $RI\beta^+$ coincidence/annihilation peaks are better defined in shape and their peak position tends to be nearer to the distal peak of the SOBP.

As for the inter–spill acquisition modality, in table 5.6, one can appreciate a more notable difference between the signal gain from ^{11}C and ^{15}O beams, with respect to their stable counterparts, of a factor $\sim$ 7 and almost 10, respectively. This is due to the shorter half life of the ^{15}O ions contributing to the signal acquisition, during a relatively short time. The correlation with the distal edge of the SOBP is not as advantageous as in the other offline modalities in table 5.7, because of the lack of the contribution from the last spill (the last acquisition interval in inter–spill is between the 15th and the 16th spills) and its relevance to the overall amount of ions delivered. Concerning in–spill acquisitions in table 5.6, the (mostly) neutron and prompt gamma background has a great impact on the quality of the coincidence event signal obtained, preventing treatment of data from stable ion beams. Moreover, it affects the gain observed with $RI\beta^+$ compared to stable ion beams. This gain is a factor $\sim$ 4 for carbon and $\sim$ 7 for oxygens ions if annihilation events at rest are considered, but almost inexistent for the coincidence event counts due to the noise. The background effect can be better understood in figure 5.18–a. Nevertheless, one can observe a stronger signal ($\sim$ 20%) with ^{15}O rather than ^{11}C, due to the interplay between the effects of ^{14}O and ^{15}O of oxygen ion beams with respect to ^{10}C and ^{11}C from carbon ion beams (see table 5.5).

The correlation between the position of annihilation and coincidence event distributions with the SOBP dose profile is, for the reasons already discussed, very difficult to disentangle from the online data acquisition simulated with the present work's methodology, unless the SOBP is reversed. However, it is very satisfactory in the offline acquisition modalities simulated. Overall, $RI\beta^+$ attain a consistently better performance with respect to stable ion beams.

5.2 Radioactive ion beam results from HIMAC

The experimental data presented in the following was acquired at HIMAC with the NIRS's *Physics Imaging Team*, for comparison with FLUKA simulations[Au18b]. It consisted essentially of two parts:

1. *Bragg peak* curves data acquired for ^{11}C, ^{12}C, ^{15}O and ^{16}O ions in water.
2. *In beam* PET data, with the above mentioned beam species, but using a PMMA target and an OPENPET prototype[Yam17]. The β^+ annihilation signals were collected and reconstructed afterwards.

Experimental activities at NIRS take place using the two secondary beam lines `SB1` and `SB2` (bending magnet radius of 5 m) detailed in figure 5.19, attaining a maximum magnetic rigidity of 8.13 [Tm][Kou98].

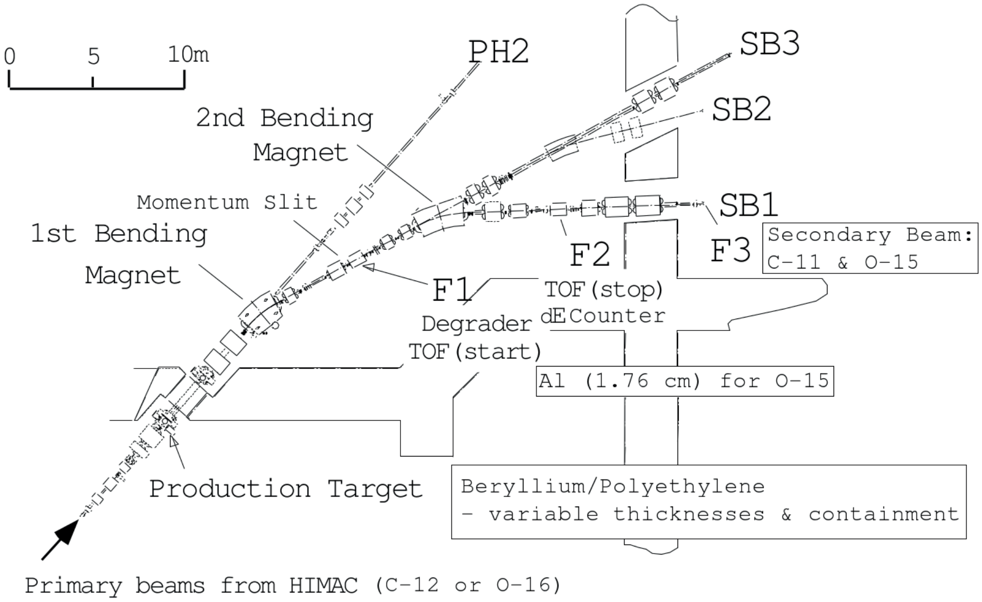

Figure 5.19: *Adapted schematic of HIMAC secondary beam line elements*[Kan98].

`SB1` is entirely dedicated to medical experiments whereas `SB2` has a more physics driven purpose. Thus, `SB1` dwells mostly with beam range quality assessment (*e.g.* positron cameras) and RIB investigation, using a fixed beam line and range verification medical setup. On the other hand, `SB2` is more spacious, allowing larger equipment to be put into place for scientific experiments.

Production of RIB is achieved with a projectile–fragmentation method, by singling out and extracting a single isotope from the fragments produced through the primary beam interaction on pre–defined targets[Hir14].

The online isotope separation takes place using two dipole magnets and three slits[Kan02]. The beam angular acceptance is limited by the first slit just following the production target depicted in figure 5.19. An isotope beam is separated according to the fragments momentum and magnetic rigidity (*i.e.* employing the first bending magnet and first horizontal slit), resulting in fragment production according to its z/A ratio.

Behind the slit, an achromatic wedge shaped energy degrader may be applied to reduce the fragments' energy and energy spread, an holder moves within 20 cm vertically to select among four possible degraders (figure 5.19). Applying the energy loss difference, an horizontal, second slit at `F2` selects the particles and the final beam (figure 5.19). Using a second bending magnet before `F2`, the fragmented beam can still be further charge separated since fragment charge and energy loss in the degrader are correlated.

The purity of the extracted beam will vary according to the slit width parameters. In fact, low–purities and intensities are considered the major factors limiting RIB clinical usage. Therefore, the contaminant species should be well identified (*e.g.* ^{11}C beams are known to be prone to have contamination of ^{12}C and ^{7}Be, ^{10}B)[Kan98, Tom03]. An attempt to characterize impurities is included in the appendix D, via the magnetic rigidity in the scenarios simulated. However, it can only be applied if the relevant inter–target geometry is known, which was not the case.

Contaminant particle identification is performed using a system consisting of a ToF counter and a silicon semiconductor detector ΔE–ToF counter at the third slit. The ToF measurement is performed exploiting the 10.466 m long flight–path between `F1` and `F2`, which are equipped with start & stop counters, and 0.5–mm–thick plastic scintillators at `F2` (energy degrader and third slit in figure 5.19)[Kou98, Tom03]. MWPCs at `F1`, `F2`, and `F3` are used to assess the positions and sizes of the beam with cross monitors. Hence, with the ToF and ΔE information, the particles can be identified and the purity of the selected particle in the separator is found[Kan04]. Production yields are then extracted from the ratio between the number of identified particles and the primary beam intensity, calibrated with a secondary emission monitor within a 10% error margin.

Below, two examples of a production scheme applied for both ^{11}C and ^{15}O, are given. Further below, the general characteristics of primary/secondary beams experimentally obtained are shown in table 5.8.

$$^{12}\text{C}\ \ [290\ \text{MeV/u}] + \text{Be}\ \ [4.2\ \text{cm}] \longrightarrow\ ^{11}\text{C}\ \ [210\ \text{MeV/u}] + \text{fragments}$$

$$^{16}\text{O}\ \ [430\ \text{MeV/u}] + \text{Be}\ \ [6.0\ \text{cm} + \text{Al}] \longrightarrow\ ^{15}\text{O}\ \ [254.4\ \text{MeV/u}] + \text{fragments}$$

At NIRS, the primary beam kinetic energy can attain a maximum of 430 MeV/u, yielding ranges of 30 and 22 cm with ^{12}C and ^{16}O beams in water, respectively[Nod11]. As the energies of the secondary beams will be lower, their ranges will be therefore lower as well.

Table 5.8: *General irradiation experimental parameters*[Kan98, Moh16].

Beam	^{11}C	^{12}C	^{15}O	^{16}O
Energy (MeV/u)	210.0	290.0	254.4	430.0
Momentum acceptance (FWHM)	±2.5%	±0.1%	±2.5%	±0.1%
Angular acceptance (mrad)	26	26	26	26
Production rate	$\sim 0.4\%$	—	$\sim 0.45\%$	—
Purity	$90 \pm 5\%$	—	$97 \pm 5\%$	—
FWHM (mm)	19.5	9.0	19.5	9.0

The intermediate target material is chiefly selected according to its physical properties (*e.g.* cross section), and thus fragment–of–interest production as an outcome of nuclear reactions. Its shape is then evaluated with MC codes, in order to maximize the secondary beam production and quality out of the various fragments produced[Moh16].

Secondary beams exhibit a wide energy spread due to interaction with the primary target, as the projectile's energy is divided among fragments. The energy of the secondary particles will vary according to the reaction point in the target and subsequent energy loss, thus being greatly affected by the type and thickness of the target[Tom03]. Besides being responsible for beam quality reduction, the target also affects the precision of beam delivery due to the less sharp energy distribution/large momentum spread.

Rates of production will then vary depending on target thickness and degrader effect, larger thicknesses may increase probability of production of secondary beams but also increase their attenuation, thus an optimization should be sought between purity and yield[Ura01]. Note that even though production rates are relatively small, it results in spills of adequate intensity for experimental PET activities[Kit06, Yos12, Hir14].

5.2.1 Radioactive and stable ion *Bragg Peaks*

Experiment. For the *Bragg peak* position and fragmentation tail dose measurements in water, the setup was placed as indicated in figure 5.20. A movable cross ionization chamber was used, in water, to measure relative dose at different depths during beam delivery with respect to an ionizing chamber located at the exit of the beam line.

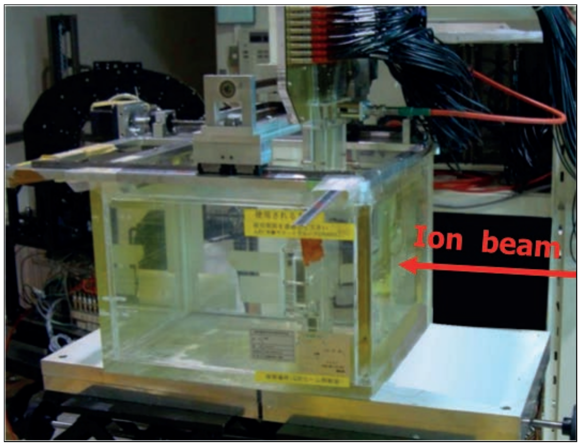

Figure 5.20: *Water tank with cross ionization chamber positioned perpendicular to the ion beam direction*[Moh16].

The information on the ionization magnitude at different depths is, in turn, directly proportional to energy deposition and hence physical absorbed dose. To characterize the profile of *Bragg Peak* curves more precisely, the readings were concentrated in between the peak rising and the fragmentation zones, focusing into the distal fall–off region. Moreover, in order to prevent accounting for intensity fluctuations, the ionization measured in water was normalized to the ionization at the entrance with an additional monitor.

Simulations. The simulated water compound was attributed a density $\rho = 0.9982$ [g cm^{-3}], since it was at about 20 °C degrees. As for the ionization potential, it was kept to 76.8 eV, for consistentcy with the optimal values observed earlier in this chapter.

The movable cross ionization chamber, equipped with 64 ionization chambers spaced by 2 mm horizontally and vertically, was used to get the data for the *Bragg Peak* curves at depth intervals with a minimum stepsize of 0.5 mm. The simulated detectors were created in FLUKA with the appropriate dimensions and binning size/intervals of 2 mm. This measurement binning was reproduced in the scoring by means of both vertical and horizontal sections of an `USRBIN` card, having 2 mm along `x,y` directions, and 0.1 mm in depth (`z`) in water as illustrated in figure 5.21.

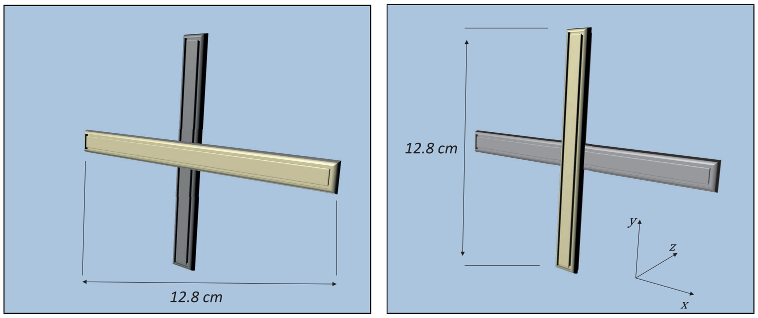

(a) `X scoring` (b) `Y scoring`

Figure 5.21: *Cross sections of the scoring volume schematic, as applied in* `FLUKA`*, highlighted in golden.*

FLUKA results were first compared with the data acquired from the cross ionization chamber, in water. In order to compare more straightforwardly the simulated and measured datasets, the 64 elements of the cross ionization chamber in `x` were summed up. The same procedure was also applied in `y`, rendering two unique curve datasets for both the simulated and measured values. Each simulated curve was then normalized to the first data point in range, to be consistent with the methodology adopted at NIRS, and they are presented in figure 5.22.

Momentum acceptance intervals were rather broad (see table 5.8 and figure 5.22) for radioactive ion beams, with ±2.5%, still within the maximum momentum acceptance value at HIMAC of ±3%. Consequently, the *Bragg Peak* curves could vary greatly within the FLUKA simulations, the momentum spread values ($\Delta p/p$) of ^{11}C and ^{15}O were ±1.5 and ±1.25%, respectively. As for stable beams, the momentum spread used in the simulation was of ±0.05%. In both cases, these values were obtained via a trial and error approach.

The *Bragg Peak* curves characteristics of the experimentally acquired and simulated data are compared in table 5.9. The peak–to–entrance ratio (PER) is obtained comparing the first data entry in depth with the maximum measured value, the same procedure was applied for the simulations. Please note that the depth of the first entry measured varied between the experimental acquisitions, this was accounted for when comparing with the simulations. The *Penumbra* values are defined as the longitudinal distance where the descending curve decreases from 80 to 20% of the peak value (90 to 10% distance was evaluated as well). The *Range* corresponded to the longitudinal distance measure up to the point at which the *Bragg Peak* curve descends to 80% of its maximum value. As for the ΔW50% value, it consists of the longitudinal width between the 50% of the peak value in the proximal rise zone and the 50% of the distal fall–off.

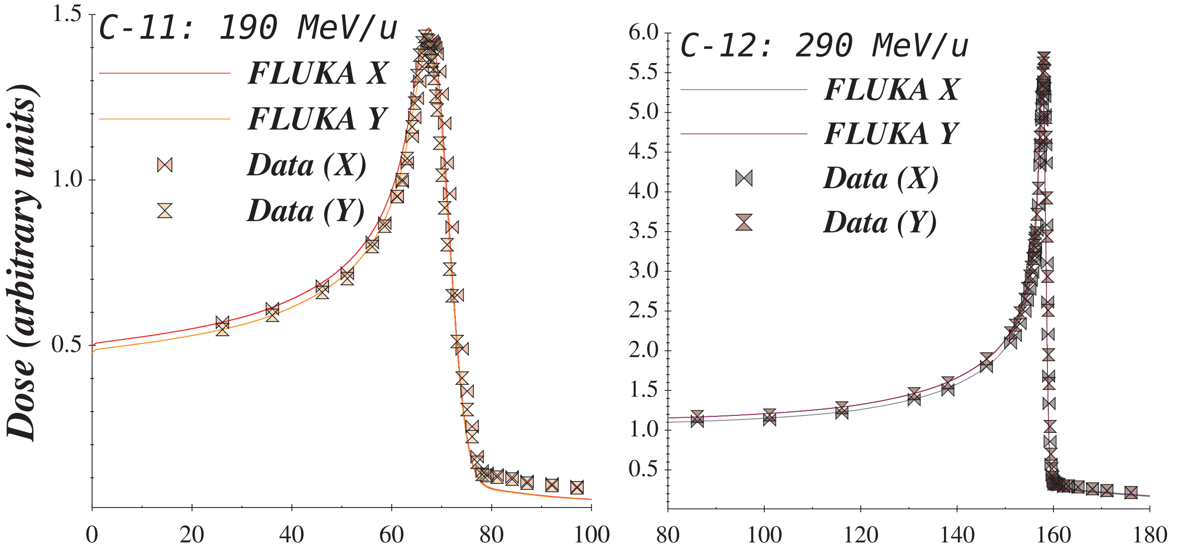

(a) ^{11}C (190 MeV/u) with $\frac{\Delta p}{p} = \pm 1.5\%$.

(b) ^{12}C (290 MeV/u), with $\frac{\Delta p}{p} = \pm 0.05\%$ and degrader*.

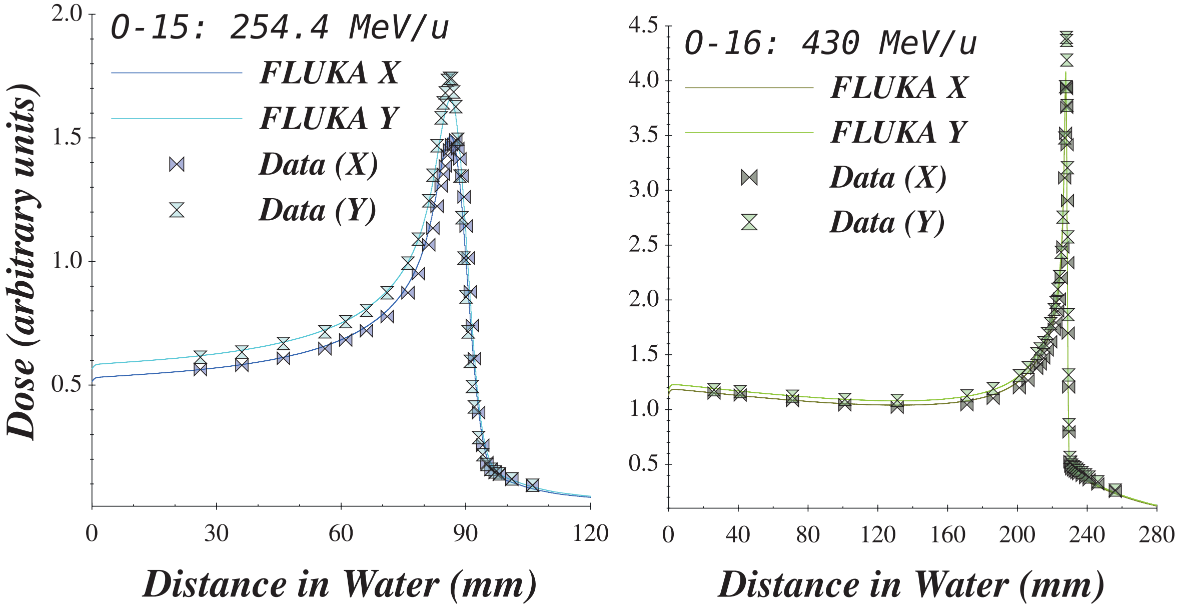

(c) ^{15}O (254.5 MeV/u), obtained using $\frac{\Delta p}{p} = \pm 1.25\%$.

(d) ^{16}O (430 MeV/u), with $\frac{\Delta p}{p} = \pm 0.05\%$.

Figure 5.22: *Comparison between simulation and experimentally acquired absorbed dose profiles in water for the various beams.*

* *A paper–like degrader was present in the experimental acquisition and therefore, to account for its effect, a 1.5 mm thick paper* $(C_6H_{10}O_5)_n$ *sheet, placed at beam line exit, was simulated with* $\rho = 1.2$ *[g cm^{-3}].*

Table 5.9: *Beam profile analysis for the Bragg Peaks simulated. The data pertaining to measurements is found enclosed in parentheses.*

Dataset	Beam	PER	*Penumbra* 90–10% [mm]	*Penumbra* 80–20% [mm]	Peak [mm]	*Range* [mm]	ΔW50% [mm]
X	^{11}C	2.56 (2.49)	6.8 (9.0)	4.3 (4.8)	67.4 (68.1)	70.2 (71.1)	22.4 (24.0)
	^{12}C	4.96 (5.04)	1.2 (1.3)	0.7 (0.7)	157.7 (158.0)	158.3 (158.6)	4.1 (3.9)
	^{15}O	2.68 (2.65)	8.5 (7.3)	4.7 (3.8)	86.5 (87.6)	89.2 (90.1)	23.5 (22.8)
	^{16}O	3.42 (3.43)	6.2 (9.7)	1.0 (1.3)	227.7 (228.1)	228.4 (228.7)	6.1 (5.4)
Y	^{11}C	2.56 (2.62)	6.9 (7.8)	4.3 (6.3)	67.4 (66.6)	69.5 (69.6)	20.3 (18.3)
	^{12}C	4.97 (5.06)	1.2 (1.3)	0.7 (0.6)	157.7 (158.1)	158.3 (158.6)	4.4 (4.0)
	^{15}O	2.68 (2.84)	8.3 (7.8)	4.7 (4.3)	86.3 (86.1)	89.2 (88.6)	23.6 (21.3)
	^{16}O	3.42 (3.72)	6.3 (7.7)	1.0 (0.9)	227.9 (228.1)	228.4 (228.7)	6.0 (5.4)

Regarding the dose results, it was observed that the fragmentation dose tail of ^{11}C was slightly underestimated by FLUKA, as visible in figure 5.22, which could be at least partially ascribed to the beam impurities. This discrepancy between the data and simulation occurs chiefly beyond the 10% distal fall–off (see table 5.9) and could have an impact not only in ^{11}C therapeutic performance with respect to ^{12}C, but also highlights a possible discrepancy in the fragmentation channel modeling in FLUKA. Regarding ^{15}O, the code's predictions matched well the experimental data, which could indicate that the discrepancy observed for ^{11}C could be attributed to its higher impurity level (table 5.8), with respect to ^{15}O. In order to assess the contribution from the fragmentation in the *Bragg Peak* one would need to characterize the beams' impurity content, so as to include this information in the simulated framework and then proceed with the re–calculation, afterwards checking if a better agreement with the data is verified. However, since such information was difficult to integrate and validate via simulation, this course of action was not pursued in this work.

Concerning ^{15}O, when applying the normalization the experimental data evidenced an offset in the horizontal part of the cross ionization chamber while the vertical data subset appears to be in line with the predictions, this could be caused by a small misalignment of the phantom or the beam before the irradiation, as the setup is fully symmetric.

Also, the simulation results put into evidence a disagreement between the simulated and measured ^{16}O peak value for the vertical dataset acquisiton. A small vertical misalignment seems to be the most plausible explanation, given that the PER value in table 5.9's horizontal dataset is confirmed by the data.

Overall, there was a good agreement of the simulation values with the experimental data in most of the range indicators of table 5.9. In fact, for the *Range* values the agreement was verified to be within 0.3 mm for stable and up to 1 mm for radioactive ion beams. Peak positions differed slightly more, but still less than 0.4 mm for stable and up to 1.1 mm for radioactive ion beams. It was also possible to notice deviations in the ΔW50% values especially for *RIβ*$^{+}$, with discrepancies up to 0.7 mm for stable beams and 2.3 mm for radioactive ion beams. These effects are also reflected in the *Penumbra* $(90 - 10\%)$ values, which can differ by up to 3.5 mm.

Some of those variations can be attributed to the reproduction of the secondary beam port in the simulation, since not all its settings are known. The momentum acceptance of *RIβ*$^{+}$ shown in table 5.8, ±2.5% was relatively high. Even though the optimal momentum spread values used in the simulations (±1.5 and ±1.25%, for ^{11}C and ^{15}O, respectively) were found to be within the margins defined in table 5.8, the resulting *Bragg Peak* curves are more difficult to analyze than those of stable beams.

5.2.2 Fragmentation and imaging results

Experiment. As dose profiles in depth are mainly due to atomic physics processes, whereas β^+ production and target activation depend on nuclear physics processes, the latter evaluation requires imaging analysis. With the same ion beam parameters described in table 5.8, a PMMA sample was placed into the FOV center of a single ring openPET prototype. Data acquisition ensued, as depicted in figure 5.23.

The PMMA block was characterized by a density of 1.186 [g cm^{-3}] and a volume of 3 000 cm^3 (dimensions 30 × 10 × 10 cm). As for the openPET scanner, it consisted of four detector rings assembled in a single unit, axially shifted, with 66 cm diameter. Its crystal type was GSOZ, with smallest volume of 2.8 × 2.8 × 7.5 mm^3. The geometrical efficiency attained 27.8%[Yam17].

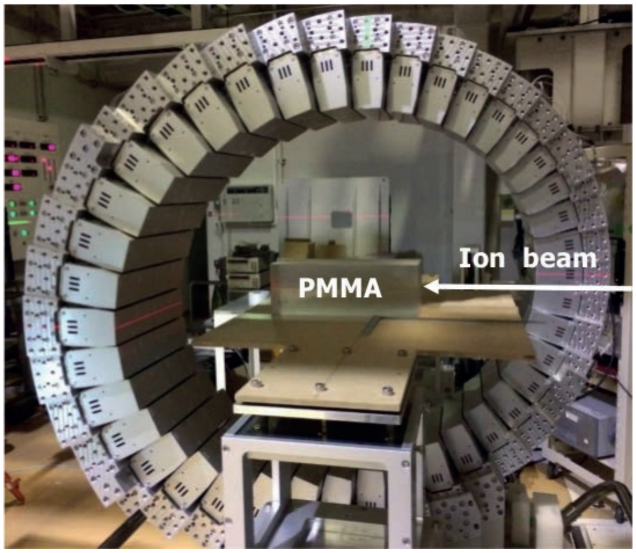

Figure 5.23: *In beam PET imaging setup, with Bragg Peak position centered at* openPET*'s FOV*[*Moh16*].

The pencil-beam of lateral Gaussian shape was delivered in spills lasting 1.9 s and, in the ^{11}C irradiation case, intensities of $\sim 9.5 \times 10^6$ particles per second [pps] were reached, accounting for a total of about $1.8{\times}10^7$ ions per spill. The interval between spills was 1.4 s, as depicted below in an example for a three spill event.

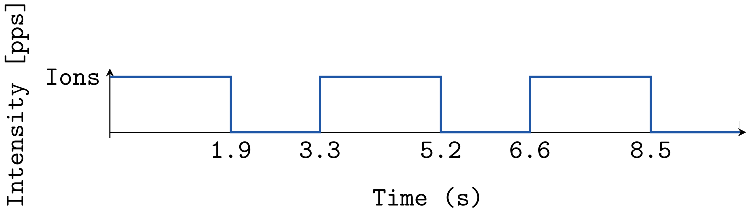

The full extent of the irradiation and acquisition information is given in table 5.10.

Table 5.10: *Carbon and oxygen ion irradiation details.*

Beam	Inter–target	*Bragg Peak* [cm]	Spills	t_{scan} [s]	Energy [MeV/u]
^{11}C	`Be` [5.1 cm]	5.7	3	1380	190
^{12}C	—	13.6	5	1380	290
^{15}O	`Al+Be` [6.0 cm]	7.6	2	780	254.4
^{16}O	—	19.7	5	1380	430

Inter–target corresponds to intermediate targets, simple blocks of variable shape, thickness and material, used to obtain secondary beams with the desired characteristics[Moh16]. As for t_{scan} it refers to the scanning time.

Multiple range–shifters can be applied to achieve the selected secondary beam range, as it is generally more practical than modifying the primary beam energy. The range–shifter thickness is decided *a priori* according to calculated factors for water and PMMA stopping powers. For the acquisitions in table 5.10, no range shifters were employed.

Simulation. Having previously characterized the beam range and momentum spread in water against experimental data, these results were extended to PMMA, as this was the target material used for imaging acquisition. For the PMMA blocks inclusion in the simulation, a density value of 1.186 [g cm^{-3}] was recommended by NIRS *Imaging Physics Team.* Using tables 5.10 data as range reference, I_{PMMA} value in FLUKA was set at 74.0 eV, as it was found that it matched the *Bragg Peak* position predicted by the NIRS colleagues (this value was also used in other validation work[Rob13]), leading to the following results reported in figure 5.24.

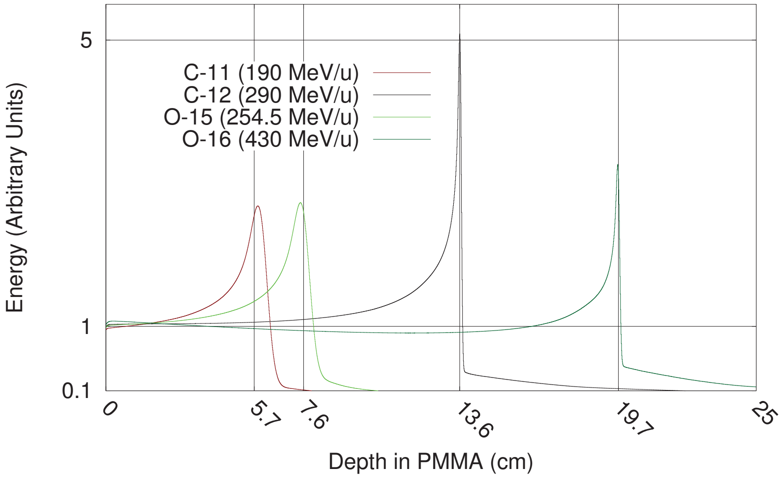

Figure 5.24: *Simulated results in* PMMA*, for all the beams previously benchmarked in water, with the scanner FOV center marked on the plot with vertical dashed lines.*

A small shift in the *Bragg Peak* position in depth was observed for the RIB only, and will be later quantified in table 5.13. Nonetheless, by using a stopping power ratio between PMMA and water of *circa* 1.160–1.165[KKO13], one can verify that the simulated results lie within the expected depth interval.

Fragmentation simulations. Among the many fragments relevant to this study, and before discriminating between different light ions species, it was important to observe how the primary beam attenuation and fragment production (see figure 5.25) evolves in depth in PMMA for the irradiations considered.

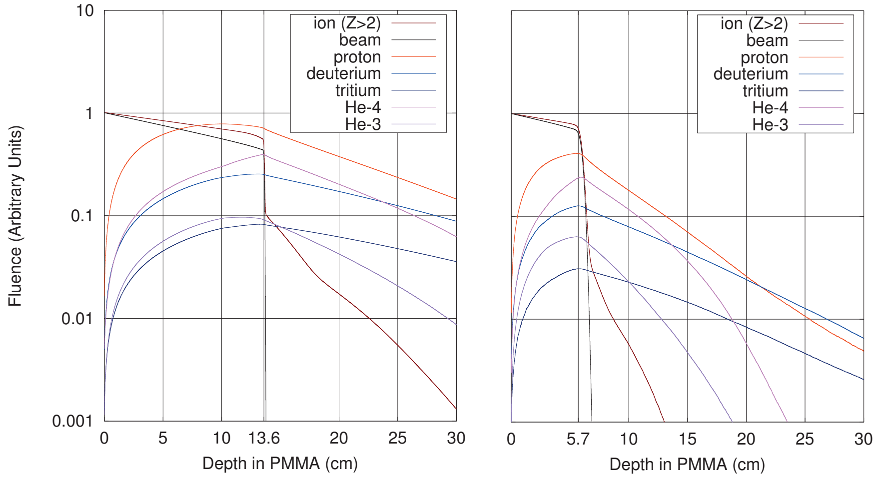

(a) ^{12}C (290.0 MeV/u) (b) ^{11}C (190.0 MeV/u)

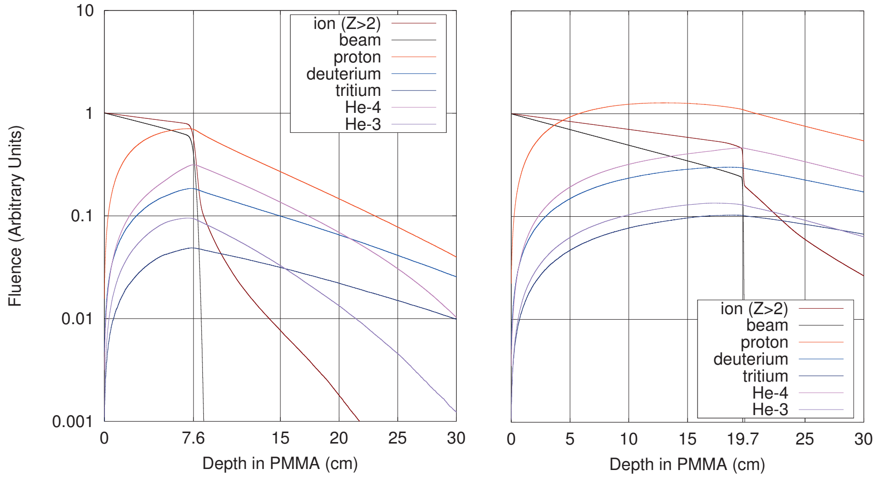

(c) ^{15}O (254.5 MeV/u) (d) ^{16}O (430.0 MeV/u)

Figure 5.25: *Relative fluence of different particles in the* PMMA *block, normalized with respect to the maximum (initial) fluence of the primary beam.*

Regarding the energy deposition results, but discerning among ions with Z > 2 (figure 5.26), for an easier evaluation of their contribution to the overall energy deposition, one obtains the plots of figure 5.26:

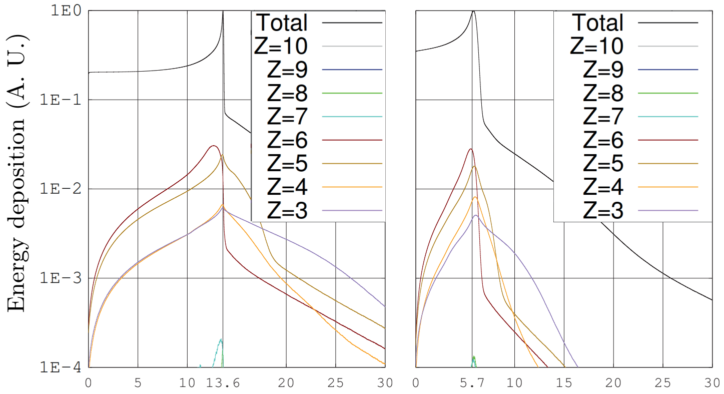

(a) ^{12}C (290 MeV/u) (b) ^{11}C (190 MeV/u)

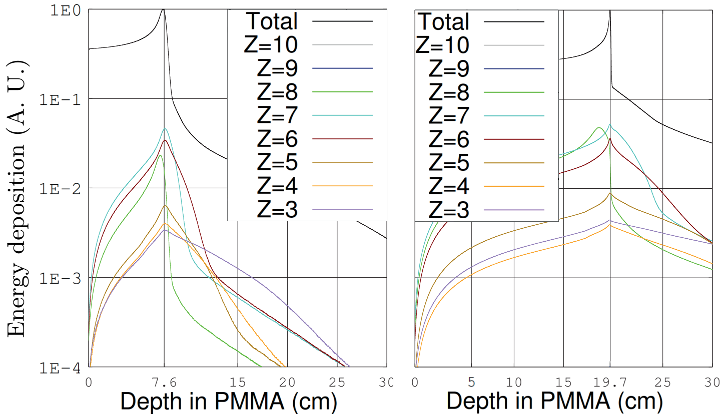

(c) ^{15}O (254.5 MeV/u) (d) ^{16}O (430 MeV/u)

Figure 5.26: *Relative energy deposition of different ions (from* $2 \leq Z \leq 10$*) in the* `PMMA` *block, normalized to the maximum peak energy. The total energy deposition is also plotted in black.*

The results depicted in figures 5.25 and 5.26, are solely qualitative and are meant to provide the reader some visual guidance on a few relevant effects, namely: the fragmentation dose tail which, as seen in chapter 4, is formed essentially by projectile fragments travelling farther than the *Bragg Peak* position; the position at which some ions come at rest can have a considerable shift (∼ 1 cm for Z=6 and Z=8 in figures 5.26-a and –d, respectively) with respect to the *Bragg Peak*; for $RI\beta^+$ this shift is not as pronounced and thus the β^+ emitting fragments position, and thence their signal, will more accurately coincide with the *Bragg Peak*.

This simulated data cannot be properly benchmarked since there was no fragment identification in the experiment. However, these results can support some of the following conclusions via imaging.

Imaging simulations. Following the characterization of the major ion species' behavior at the *Bragg Peak* depth in the PMMA block, the study of the annihilation events at rest produced by the different isotopes ensued. These isotopes will be the source of signal detected by the openPET scanner apparatus.

In figure 5.27, dose distribution and the total annihilation events at rest can be seen, in depth and integrated over time. In addition to the total yield of annihilation events at rest, the contributions according to the isotope (β^+ emitters) of origin were also distinguished.

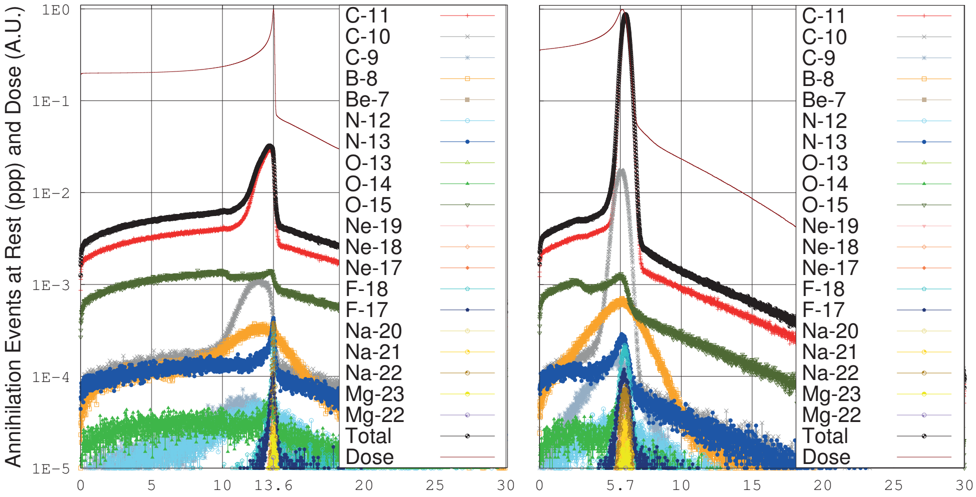

(a) ^{12}C (290 MeV/u) (b) ^{11}C (190 MeV/u)

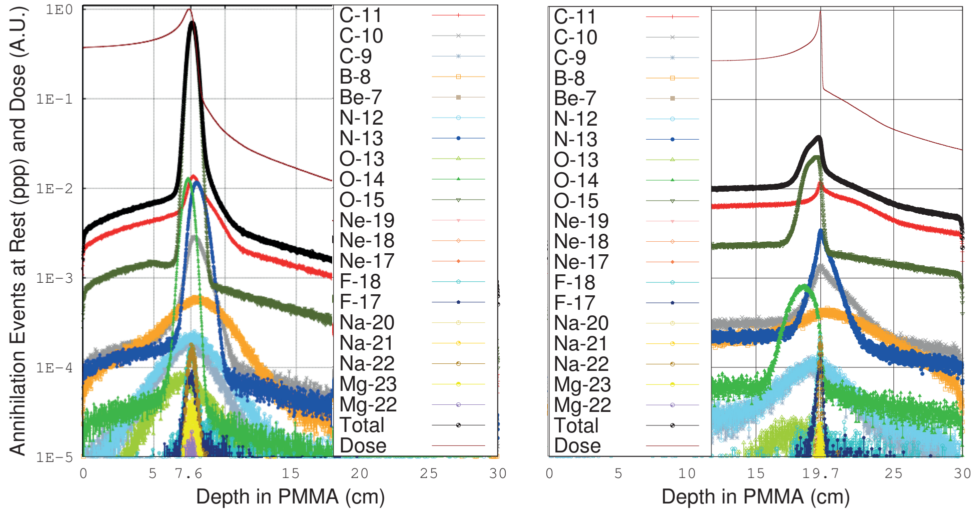

(c) ^{15}O (254.5 MeV/u) (d) ^{16}O (430 MeV/u)

Figure 5.27: *Total annihilation events at rest, per single primary particle, according to isotope of origin. The result is scored in the* PMMA *block, with the dose distribution shown in arbitrary units.*

From figure 5.27, one can observe that $RI\beta^+$ yield of annihilation events at rest, integrated in time and per primary particle, is more than one order of magnitude above that of the stable beams, at its maximum. Moreover, it is possible to observe, qualitatively, that the distributions of the annihilation events at rest resulting from ^{11}C and ^{15}O irradiations are much better correlated with the distal fall–off of the respective *Bragg Peaks*. The main isotope contributing to the ^{12}C irradiation's total annihilation events at rest distribution, at the maximum, is essentially ^{11}C (albeit ^{10}C and ^{15}O distort its peaked shape). For ^{16}O irradiations, ^{11}C and ^{15}O broaden the *Bragg Peak* shape in depth. Concerning $RI\beta^+$ annihilation event at rest distributions, for ^{11}C irradiations the peak is mostly formed by ^{11}C ions, with only $\sim 2\%$ of ^{10}C at the peak. As for ^{15}O, the annihilation event at rest peak is also mostly formed by the beam particle, with contributions from ^{14}O, ^{11}C and ^{13}N amounting to a few per cent each.

Despite providing general information on the relative amount of annihilation events at rest, their location and provenience, the simulation results discussed in this section so far lack time information. Since the different isotopes decay contribution is dynamic in time, according to each specie's half–life, the signal time acquisition interval and the beam time structure need also to be accounted for.

Considering the time structure depicted below in the schematic in figure 5.28 and in table 5.11, for stable and $RI\beta^+$, the annihilation events were estimated at any point of the OPENPET acquisition time up to the end of the scanning time.

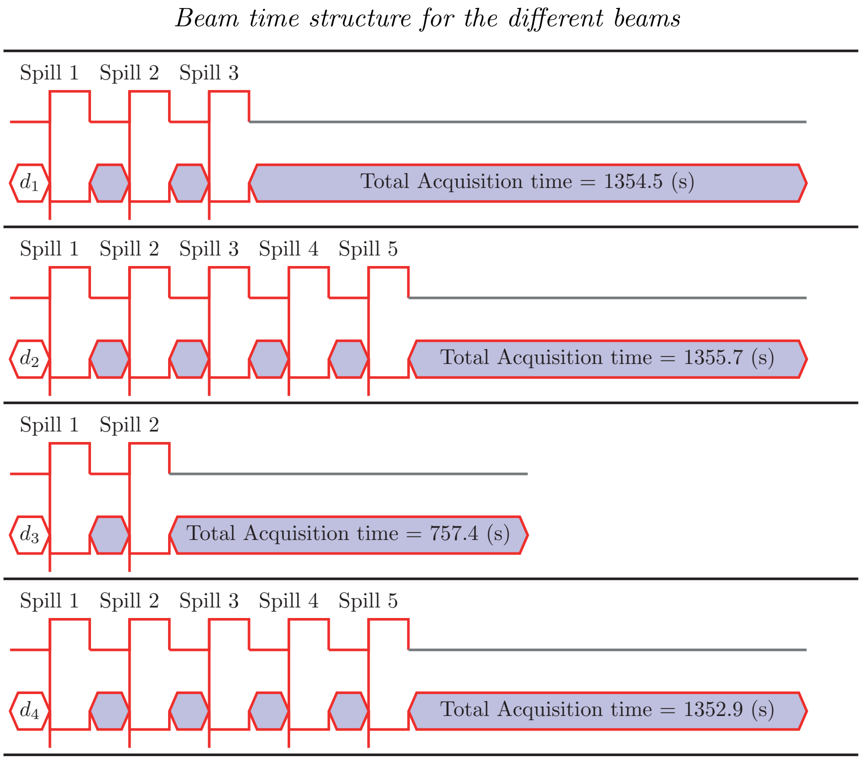

Figure 5.28: OPENPET *beam time structure details, for the* DELAY TIME *(d) please refer to table 5.11.*

For all the beams evaluated, the openPET measurement time accounted for 1380 s, except ^{15}O which lasted only 780 s. Essentially, the openPET scanning time consisted of three major stages: Delay time (d), Beam On and acquisition time, with the latter taking place not only after the last spill, but also in between spills (lilac colored in the schematic). The Beam On periods are represented by the upward rectangular function, where no acquisition occurs. The Delay time corresponded to a variable time in each scan before the 1st spill.

To complement the beam time structure data, the number of particles delivered was also included, these values are provided in table 5.11 and were used to normalize the simulation results.

Table 5.11: *In beam PET irradiation data.*

Beam	Ions per spill [10^6 ions spill^{-1}]	Intensity [10^6 ions s^{-1}]	Total ions delivered [10^6 ions]	Delay time [s]
^{11}C (190 MeV/u)	18.0	9.5	54.0	19.8
^{12}C (290 MeV/u)	18.0	9.5	90.0	14.8
^{15}O (254.5 MeV/u)	12.2	6.4	24.4	18.8
^{16}O (430 MeV/u)	11.6	6.1	58.0	17.6

This way, it would be possible to reproduce all the beam interactions and quantify the annihilation events at rest at any point in time, both during and after irradiation. An example of the annihilation events at rest rates [events s^{-1}] evolution in time, scored in the PMMA phantom, is provided in table 5.12. These values take into account the different irradiation profiles depicted in the schematic in figure 5.28, as well as the values in table 5.11.

Table 5.12: *Annihilation events at rest rate [Events s^{-1}] calculated in the PMMA phantom with FLUKA at different scanning times: EOB – End of Beam; 5 minutes after EOB and at the end of the PET scanning time.*

Beam	EOB	5 minutes EOB	At scan's end
^{11}C	109 822	19 303	10 253
^{12}C	103 261	9 801	3 579
^{15}O	147 139	16 820	3 833
^{16}O	131 722	12 758	3 517

The annihilation event at rest results were then integrated in time, but over the specific acquisition intervals only. This was done in an attempt to correlate the results with the image acquired by the scanner, since ultimately the annihilations would be the chief source of signal detected by the openPET scanner. These results can be seen plotted in figure 5.29, for a qualitative comparison. In the referred figure, the simulation results were normalized to the number of beam particles delivered. However, please note that the reconstructed results did not correspond quantitatively to β^+ activity and therefore, since the quantities compared are different, the simulation and the experimental data do not match under the same color scale. Subsequently, figure's 5.24 simulated *Bragg Peak* position, along with the FOV center values, were respectively compared with the annihilation events at rest peak position and the peak position of the experimental data counts from figure 5.29.

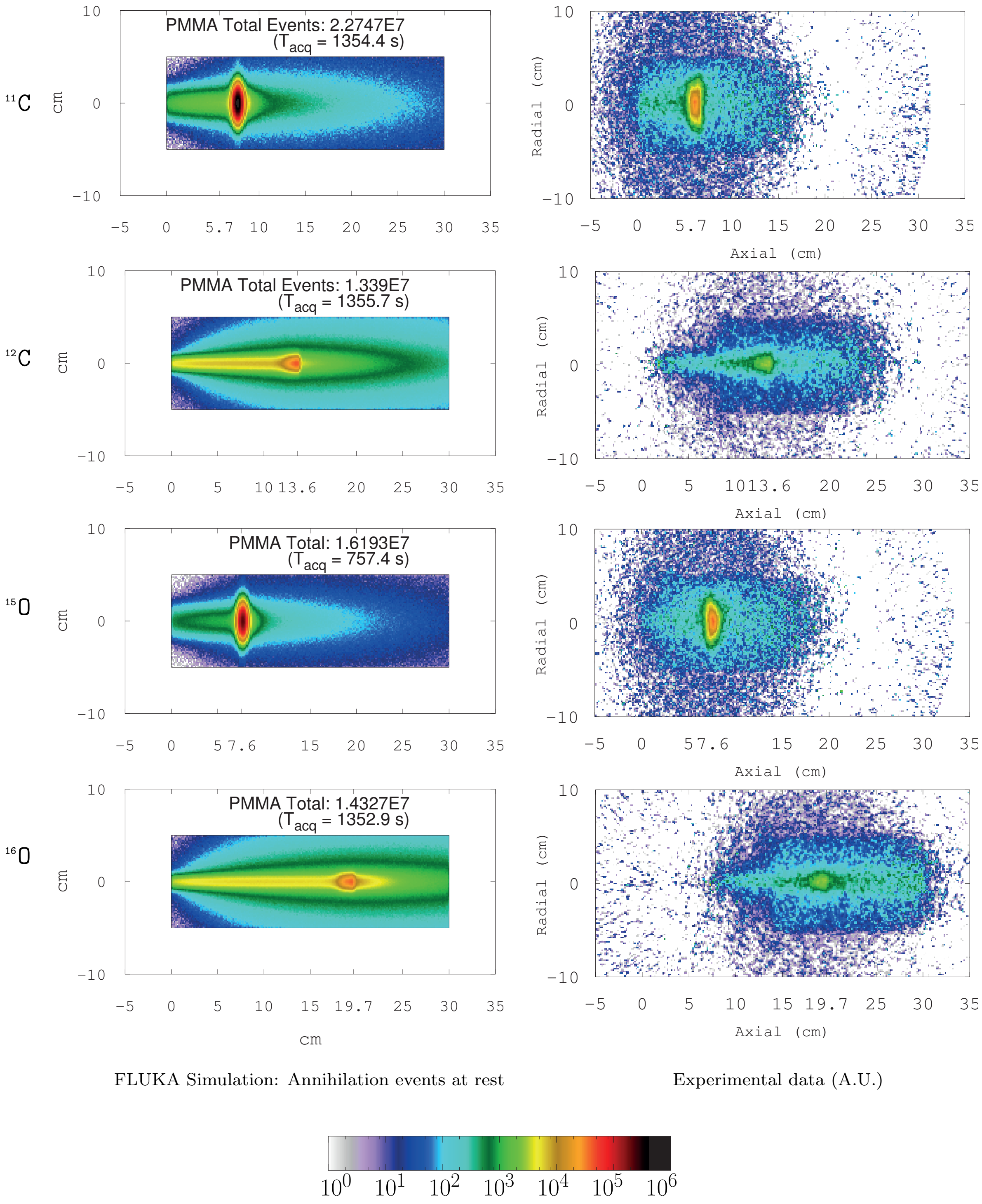

Figure 5.29: *Annihilation events at rest simulated in PMMA throughout the acquisition time (left column) and* openPET *signal reconstruction experimentally acquired in relative counts (right column, in arbitrary units).*

This comparison was performed in depth, with the lateral components integrated, to investigate the agreement between simulated and measured data. These results are presented in table 5.13, with annihilation events at rest being abbreviated as Æverest.

Table 5.13: *Comparison between simulated Bragg Peak position and position of the maximum of both simulated annihilation events ($\mathcal{S}$) and experimental ($\mathcal{E}$) signal acquired. The values $\Delta\mathcal{S}$ and $\Delta\mathcal{E}$ correspond to $|\mathcal{S}_2 - \mathcal{S}_1|$ and $|\mathcal{E}_2 - \mathcal{E}_1|$, respectively.*

Beam	*Bragg Peak* ($\mathcal{S}_1$) position [mm]	FOV center† ($\mathcal{E}_1$) position [mm]	Æverest peak ($\mathcal{S}_2$) position [mm]	Experimental data ($\mathcal{E}_2$) max position [mm]	$\Delta\mathcal{S}$ [mm] ($\Delta\mathcal{E}$) [mm]
^{11}C	58.5	57	61.5	60.0	3.0 (3.0)
^{12}C	136.1	136	136.5	135.0	0.4 (1.0)
^{15}O	74.8	76	78.0	75.0	3.2 (1.0)
^{16}O	196.8	197	195.0	196.3	1.8 (0.7)

† *OpenPET's FOV position along the axis, corresponding to the expected Bragg Peak position.*

The acquired signal depicted on the right side column of figure 5.29 was reconstructed using an in–house implementation of an OSEM algorithm (8 subsets and 10 iterations), with a normalization and scattering correction being performed for 3D image reconstruction[Moh16]. This method is similar to MLEM, but handles instead the data into subsets of projections throughout the volume for faster convergence[Zan04]. However, no detector calibration has been performed, thus the result reconstructed can be regarded as "relative counts", instead of absolute ones. Regarding the dataset volume, it consisted of a 340 × 340 × 500 voxelized matrix, being each VOXEL a cube of 1.5 mm length. For the FLUKA simulation (left side column of figure 5.29), the binning size was selected so as to coincide with the data pixel size, allowing for a straightforward comparison.

`ImageJ` software was employed to extract the reconstructed data and plot it into a 2D matrix form, integrating laterally over the phantom geometry, for comparison with the FLUKA simulation plot. Subsequently, it was plotted using only an arbitrary normalization factor, matching the FLUKA result, which was directly given per primary particle. Following this procedure, both results were then equally normalized by the number of beam particles delivered.

Since the experimental data are not calibrated for obtaining activity, they do not compare directly with the simulated annihilation events at rest distribution, quantitatively. As a consequence, no normalization factor could be employed to extrapolate quantitative parameters (*e.g.* scanner efficiency factor) and the comparison with simulated data was performed by evaluating the distributions' relative profiles, as well as their shape and position.

Taking the integrated result in the vicinity of the *Bragg peak* zones the results obtained for the different beams are compared in more detail in figure 5.30, with a substantially reduced volume mesh of $6 \times 6 \times 6$ cm^3. This volume will be, from now onwards, denominated as the region of interest (ROI). In order to obtain a more meaningful comparison between simulation and experimental data, background reduction techniques were applied. These techniques consisted of the subtraction of a constant value in the ROI voxels of each of the experimental data sets provided which was found to correspond to the background.

One–dimensional profile plots (figure 5.31) were created integrating both the simulation and experimental data in either their radial or axial components throughout the ROI. This allowed for a clearer assessment of the comparison performed, particularly nearer the *Bragg Peak* zone.

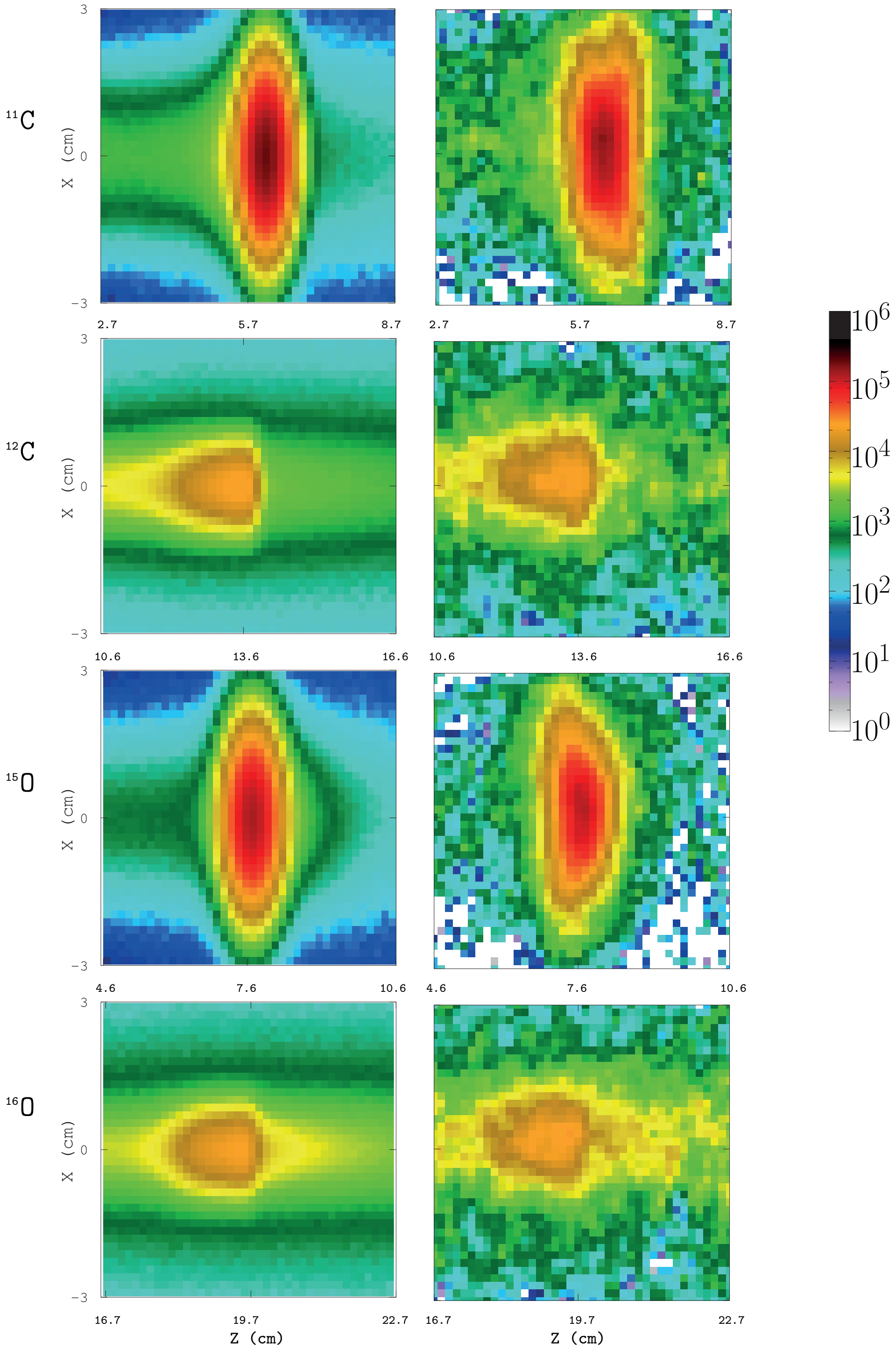

Figure 5.30: *Detail of the distribution of annihilation events at rest in PMMA, for the different irradiations obtained with FLUKA throughout the acquisition time, in the ROI (left). Detail over the same region, but plotting the* OPENPET *signal reconstructions (right) experimentally acquired and treated with background reduction techniques. The experimental data, given in relative counts, were normalized to the simulation's results integrated in the ROI for a more direct comparison of both distributions.*

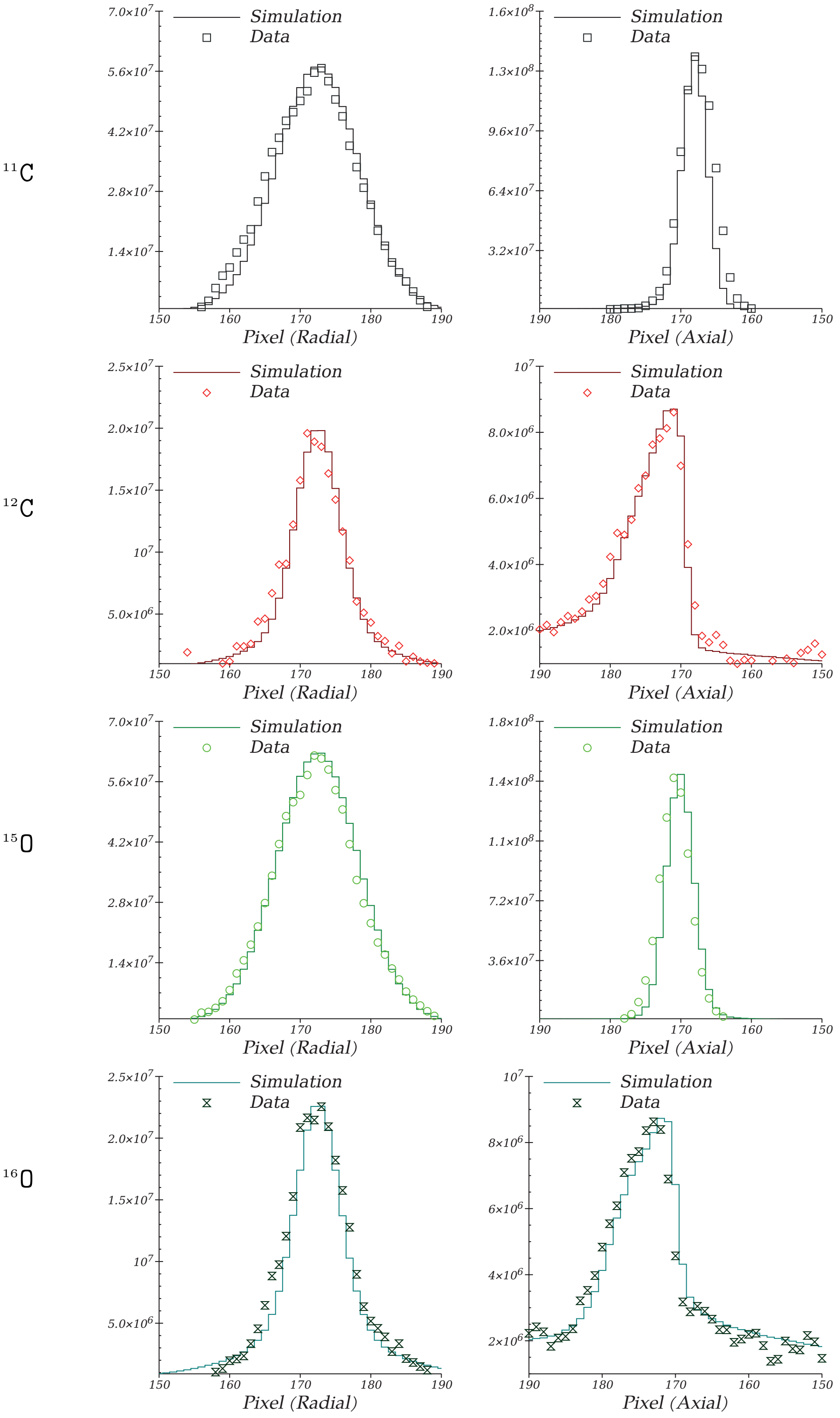

Figure 5.31: *Radial (left) and axial (right) comparison between integrated annihilation events at rest simulated and the reconstructed data acquired in PMMA. The reconstructed results were treated with background reduction and normalized to the respective simulations' maxima, for visualization purposes.*

For the data acquisition with OPENPET and the following reconstruction in table 5.13, the *Bragg Peak* positions obtained with FLUKA were found to differ slightly from the OPENPET scanner FOV centered position (figure 5.24) in the situations pertaining to $RI\beta^+$ irradiation only, by 1.5 mm for ^{11}C and 1.2 mm for ^{15}O.

An evaluation of the shape and relative annihilation events at rest peak magnitude was then performed for the different distributions, its results are detailed in tables 5.14 and 5.15.

Table 5.14: *Comparison between the distribution shape and profile resulting from different irradiations for both simulated and experimental data (the latter is presented in parentheses).*

Beam	FWHM [mm]	ΔW50% [mm]	ROI value [%] of total	Maximum value [%] of ROI	Peak section [%] of ROI
^{11}C	21.0 (22.5)	7.5 (9.0)	95.4 (79.1)	1.45 (1.20)	21.18 (15.95)
^{12}C	12.0 (12.0)	13.5 (16.5)	41.1 (42.7)	0.90 (0.83)	7.37 (7.21)
^{15}O	21.0 (19.5)	7.5 (7.5)	94.7 (79.0)	1.35 (1.30)	19.49 (17.07)
^{16}O	12.0 (15.0)	15.0 (16.5)	36.9 (39.3)	0.74 (0.66)	6.24 (6.12)

In order to characterize the shape, the lateral distribution's FWHM was obtained for both the simulated and experimental results, the latter enclosed in parentheses. Regarding the longitudinal shape, it was characterized using the previously defined ΔW50% parameter. In addition to that, the figure of merit of $RI\beta^+$ usage was estimated by evaluating the percentage of events obtained in the ROI with respect to the total. This allows for a more representative comparison between the annihilation events at rest simulated and signal actually reconstructed by the apparatus, since for ^{11}C and ^{15}O, the vast majority of signal is contained in the ROI (see table 5.14)

Moreover, it was calculated (1) the maximum value in a single voxel unit (1.5–mm–length cube) and (2) the "peak section", which is here defined as the laterally integrated volume at the range corresponding to the aforementioned VOXEL unit (*i.e.* 1.5 mm in longitudinal length and the lateral dimensions coinciding with that of the ROI). Both the values (1) and (2) were presented in table 5.14 as percentage of the integrated signal at the ROI, for a more direct assessment of the higher density of localized events at the respective peak position.

Regarding the evaluation of the relative signal magnitude in table 5.15, the distributions resulting from the different beam irradiations were again compared using both the ROI value, the maximum value in a voxel unit and the peak section. However, instead of presenting the results as percentage of the ROI total it was decided, for the sake of clarity, to compare it directly with the ^{12}C value instead. In table 5.15, the simulated values of annihilation events at rest were compared directly to the ^{12}C value, considering also their yield per primary beam particle, at the ROI, maximal voxel unit value and peak section.

On the other hand, the relationship between experimental data β^+ emitter signal maximum position in depth observed was seen to be rather in line with the peak of FLUKA's annihilation events at rest calculated (table 5.13), except for ^{15}O, where the variation was slightly higher (2.2 mm). Some of these deviations could be attributed to experimental calibration factors. Nevertheless, both the range and shape of β^+ emitters signal experimentally obtained were considered to be in fairly good agreement with the simulated distribution of annihilation events at rest throughout the acquisition time, as displayed in figure 5.29 and, more in detail, in figures 5.30 and finally 5.31.

Table 5.15: *Different distributions' values relative magnitude for both simulated and experimental (exp.) data, with respect to ^{12}C, which is normalized to the unity ($^{12}C \equiv 1$).*

Beam	Æverest max. value	Æverest peak section	Æverest ROI volume	Exp. data max. value	Exp. data peak section	Exp. data ROI volume
^{11}C	12.53	22.27	5.24	12.08	16.75	6.41
^{12}C	1	1	1	1	1	1
^{15}O	18.27	32.07	6.20	13.16	17.83	6.22
^{16}O	1.45	1.49	1.20	1.02	1.00	1.14

Although the peaks of annihilation events at rest simulated for $RI\beta^+$ are characterized by a better correlation with the *Bragg Peak* position (figure 5.28), this was not verified experimentally as the beam properties of $RI\beta^+$ differed greatly from the stable ion beams used, particularly in momentum spread, as verified in the FWHM comparison (table 5.14). A more direct evaluation would ideally require equivalent beam properties to be more accurate. In spite of that, one can appreciate a major gain in both *Bragg Peak* and annihilation events at rest localization by comparing table 5.14's ΔW50% values, for $RI\beta^+$ (FLUKA's annihilation events at rest, corroborated by experimental data). Namely, it reports approximately a factor 2 decrease in ΔW50%, for $RI\beta^+$, despite the fact that their dose ΔW50% (table 5.9) was almost 4–5 times higher than for stable beams, due to the aforementioned differences in momentum spread values. These findings are clear indicators of steeper signal peaks in range (also visible in figure 5.31).

In fact, the higher concentration of signal resulting from $RI\beta^+$ irradiations, in the ROI and more particularly at its maximum values and peak section, is a characteristic observed visually in figure 5.29 and (quantitatively) corroborated by table 5.14 data. However, one should note that the use of a ROI does not avoid all possible imaging artifacts, since the reconstructed shapes have some irregularity while the simulations are symmetric and therefore the comparisons tend to worsen for smaller partitions of the ROI (table 5.15). It was also verified via FLUKA simulations that the rate of annihilation events at rest immediately after the irradiation's end was rather comparable in between the carbon and oxygen beams species (see table 5.12). This despite the much higher amount of particles delivered in the stable ion irradiations (table 5.11, almost a factor 2) which is in line with the observations for *inter–spill PET* acquisitions in the previous section of this chapter.

Besides the aforementioned $RI\beta^+$'s advantage in localizing the *Bragg Peak* in range, with respect to stable beams, one also observes a much higher overall signal magnitude. This latter property is observed in figure 5.30, for the ROI, and using the same scale for the annihilation events at rest calculated with FLUKA (its distribution compared with relative counts), and confirmed by table 5.15 data. Using $RI\beta^+$ and per comparison to their stable counterparts, it was reported in the aforementioned table at least an order of magnitude in signal increase in some zones of interest of the ROI, and a factor of ~ 6 in the ROI itself.

Chapter 6

Conclusions

6.1 General Discussion

The FLUKA simulations performed in chapter 4 supported the feasibility of using radioactive ion beams in hadrontherapy, as the dose distributions obtained were found to be either comparable in terms of peak–to–entrance ratios or even beneficial as in the case of ^{11}C ions fragmentation dose tail, evidencing a $\sim$ 20% lower dose. Other ion species simulated, such as ^{10}C ions, also evidenced a promising fragmentation dose tail behavior, but a further analysis was not pursued in view of their lack of clinical relevance. As for ^{15}O, the simulations did not report any dosimetric disadvantage with respect to ^{16}O. The investigations with FLUKA have characterized the different nuclear fragments contributing to the dose distribution up to, and beyond the *Bragg Peak*, with the fragmentation dose tail formation.

The radioactive ion beams decay products were verified to have a considerably small impact, circa three orders of magnitude lower in fact, on the overall dose delivered. Therefore, $RI\beta^+$ enhanced decay products and thence imaging signal do not significantly impact treatment effectiveness.

In general, the simulation work benefited from the development and benchmarking of models involved in fragment production at therapeutic energies, as well as the models for charged particle transport and positron emission. Although the application of the FLUKA code with stable ion beams in the hadrontherapy context is well established, the present work details its first systematic application to radioactive ion beams. It was verified that the transition between the models governing fragmentation, and particularly at the frontier between rQMD and BME modules ($\sim$ 125 MeV/u), was smooth and artifact free (see chapter 4 for more details). Moreover, the peak position trends for the different fragmented species were seen to be in line with the A/z^2 ratio and their nature as either projectile or target fragments.

The use of water equivalent thickness degraders as approximations for the beam line elements from HIT, a realistic RiFi model and the FLUKA recalculations of SOBP treatment plans based on the methodology described in chapter 3 allowed for the systematic creation of customized SOBPs for both stable and $RI\beta^+$, in a synchrotron–like irradiation scenario. Although a systematic shift in number of ions was verified in the comparisons, this has been attributed to the intrinsic differences between the research TPS versions, which led to dose values of 0.95 Gy at the SOBP region instead of 1 Gy. Also, when FLUKA recalculations were compared with the newer version of the research

TPS employed at HIT, without RiFi, the results were adequate and deemed consistent for the subsequent imaging potential assessment in between the different SOBPs of 1 Gy in water.

Regarding imaging evaluation, it was estimated based on annihilation events at rest induced by the irradiation and FLUKA PET TOOLS image reconstruction, both features currently under development in FLUKA. The latter allowed for the extraction of elements of interest for *a posteriori* physical analysis, besides the image reconstruction result from the signals collected in a simulated treatment with an *in silico* version of the same PET scanner model used at HIT. It consisted of the first use of these tools in *in beam PET* scenarios and its description can be found in chapter 3.

Annihilation events at rest simulated for the various 1 Gy SOBPs were found in chapter 4 to lead to about one order of magnitude higher number of annihilation events, for ^{11}C and ^{15}O, over their respective stable counterparts. This effect is even higher (25 and 15, respectively) considering the gain at the distal edge of the SOBPs, which is the last isoenergetic layer delivered in range, and by far the one with the highest number of ions for the considered flat SOBPs. Overall, it was found that the annihilation events' distributions maximum for the $RI\beta^+$ coincided within 1.5 mm with the distal dose peak, whereas the annihilation event at rest distribution resulting from stable ion irradiations has a much less prominent peak, and deviated in range from the distal edge of the SOBP by more than 1 cm in some cases. When analyzing the evolution in time of the annihilation events rate, considering SOBPs of 1 Gy in water delivered in spills in a synchrotron–like manner, it was found that ^{11}C ion irradiations had an higher imaging potential than ^{15}O starting from 5 minutes after EOB, therefore being more suitable for *offline PET* acquisitions. Before that period, which is often associated with *online* and *in–room PET* acquisitions, ^{15}O is indeed more advantageous. This is due to the latter shorter half–life and the role of the primary ions as main contributors to the annihilation event rate after EOB.

Coupling to the previously defined HIT beam line elements approximations integrating an anthropomorphic phantom and virtual *Siemens Biograph mCT PET* scanner, and employing FLUKA PET TOOLS in various acquisition modalities, the 1 Gy SOBPs irradiations with ^{11}C, ^{12}C, ^{15}O and ^{16}O were followed by image reconstructions and quantitative assessment of the signals collected in *in beam PET* scenarios in chapter 5. In order to obtain more realistic results, the simulations were fully integrated, so that the PET response will reflect also the effect of secondary particles produced. The previous estimates with annihilation events at rest were essentially confirmed, now in the form of true coincidence events, for the *offline PET* acquisition modalities. However, given the neutron generated background, the quality of the imaging acquisitions during spill time were seen to suffer from a considerable distortion. With ^{11}C, the *offline PET* acquisition gain in true coincidence counts was estimated a factor 7 over that of ^{12}C. For ^{15}O the gain was ~ 6 for *in room* and *inter–spill PET* acquisitions. During spill, the true coincidence events acquired with $RI\beta^+$ did not surpass by a factor 2 those of stable ions, mostly due to the background effect. However, the reconstructed signal distribution was more favorable, peaking closer to the distal edge of the SOBP distribution (especially ^{15}O), and the proximal to distal region almost coincides with that of the SOBP. Furthermore, it can be concluded that $RI\beta^+$ can be an asset for range monitoring in circumstances where background hinders stable ion beams usage, this was verified to be particularly true in the alternate scenario annexed in which a reverted SOBP is employed. Nonetheless, it must be noted that the acquisitions exempting spill time signal were able to highlight the distal peak more effectively than the *in spill PET* scenarios, with proximal to distal regions consistently better defined than those of stable beams. In addition to that, the distal fall–off coincided almost exactly with the distal edge of the SOBP, which confirmed the remarkable potential of $RI\beta^+$ in treatment verification and range monitoring.

Regarding the results obtained at HIMAC and detailed in chapter 5, the experimental *Bragg Peak* curves obtained in water were seen to be within ~ 1 mm agreement in range with the FLUKA simulated results. The *Bragg Peak* distributions were broader for the radioactive ion beams due to their production via the projectile fragmentation method. Possibly, the effect of impurities and the high momentum spread of the secondary beams, which had to be estimated for the simulations, further deteriorated the comparison consistency particularly by altering the descending trend of the curves after the *Bragg Peak*. On the other hand, some of the dosimetric deviations in water can also be attributed to experimental misalignments, as in the case of ^{15}O, in which the readings from the horizontal and vertical sections of the cross ionization chambers were not symmetric. A discrepancy of almost 10% in the peak–to–entrance ratio is also seen for the vertical reading of the cross ion chamber for ^{16}O irradiation, but this was not confirmed by the horizontal data. Clearly, there was a systematically lower value in the simulation with respect to experimental data for the fragmentation dose tail of ^{11}C, which could be explained by a FLUKA underestimation of the fragments produced in ^{11}C interactions with PMMA or the presence of impurities. However, without reproducing the impurity content of HIMAC's ^{11}C beam, none of the aforementioned possibilities can be confirmed.

The OPENPET image reconstructions confirmed that ^{15}O and ^{11}C outperform stable ions in the magnitude of signal acquired in all *in beam PET* scenarios evaluated (by a factor of ~ 13 and ~ 12 at the peak, respectively), even with a factor of two lower amount of ions delivered. Unfortunately, it was not possible to compare directly the imaging results with the simulations of annihilation events at rest, as the data provided was not corrected for quantitative activity, comprising only "raw data" in relative counts. Thus, all comparisons with these distributions were performed in a relative form and by analyzing their shape, and not quantitatively, as ideally envisaged. Also, it was not possible to verify in HIMAC's results the agreement previously observed in chapter 4, while correlating the positions of FLUKA simulated *Bragg Peak* with annihilation events at rest maxima positions. The signal reconstruction maximum did not correlate favorably with the predicted *Bragg Peak* position for radioactive ion beams, which could be ascribed to the influence of many factors such as impurities' effect, large momentum spread of $RI\beta^+$ and the fact that the *Bragg Peaks* of different ion beams were being evaluated at different ranges.

Nevertheless, in the imaging reconstructions of HIMAC's results in chapter 5, it was possible to identify that both the lateral shape and the region between proximal and distal edges of the acquired distributions were considerably better defined for $RI\beta^+$. This is because the beam shape FWHM is initially more than a factor of two higher for $RI\beta^+$, whereas in the reconstructed distribution the FWHM is instead lower than a factor of two, and becomes almost comparable for oxygen ions in the experimental data. Regarding the β^+ signal longitudinal peak sharpness, those originating from $RI\beta^+$ are halved, hence leading to more well defined distributions. As for the dose peak sharpness verified in water, these were a factor of 4–5 higher for $RI\beta^+$. Therefore, even though with a fairly less optimal initial beam shape, the signal obtained with $RI\beta^+$ clearly outperforms stable ions signal in range verification scenarios. Moreover, this trend was also verified by the FLUKA simulations as well, despite the fact that only the annihilation events at rest obtained in the PMMA were being considered. Both experimental and simulation data reported at least a factor of ~ 6 increase in signal with $RI\beta^+$, compared to their stable counterparts, and this effect surpassed one order of magnitude in some localized estimators of the ROI.

Overall, one can conclude that $RI\beta^+$ can enhance the imaging signal output available for beam range verification and treatment monitoring with respect to stable ion beams in hadrontherapy, while maintaining comparable dose performance.

6.2 Future Work

In view of the promising results obtained, future work will include:

I Full validation of FLUKA PET TOOLS using *National Electrical Manufacturers Association* (NEMA) protocols. To this end, some elements described in this work will become standardized in the workflow of *in beam PET* simulations with FLUKA PET TOOLS. Currently, attenuation and scattering corrections are still missing in order to proceed with further validation;

II Inclusion of a biological dose assessment (via *i.e.* RBE estimations based on available biological models) to investigate whether the performance levels reported with physical dose will still be valid attending to the $RI\beta^+$ different fragments' biological impact;

III Better assessment of the background effects (*e.g.* in routine clinical application activation should not be neglected) along with the use a more realistic *in beam PET* geometry setup (*i.e.* either opened/shifted). If possible, effects of *biological washout* should be modeled in the reconstructions, and the effects of alternative sequence orders in the formation of the SOBP should be more thoroughly assessed. All these factors will allow for the reproduction of imaging reconstruction artifacts in *in beam PET* scenarios and lead to an improvement of the image quality;

IV Attempt to compare a real patient case scenario with ^{12}C against a simulated ^{11}C treatment. Thereafter, the present work methodology would be applied to simulate an equivalent treatment with ^{11}C, so as to obtain subsequently PET reconstructed images for a more realistic comparison with a clinical scenario per contrast with the here presented evaluation for an anthropomorphic phantom. This course of action can only be followed once I-III are addressed;

V Improvement of the comparison using results from HIMAC, overcoming the limitation of this work to an indirect comparison between simulation and experiment. This problem could be approached in the future with either an activity calibrated result of the reconstructed experimental data, to be provided for the comparison against FLUKA calculated β^+ activity or instead, the replication of the OPENPET scanner in FLUKA PET TOOLS for a complete simulation and fully–equivalent comparison (this latter, more complex option could not be followed in this work due to lack of time);

VI Study of the momentum spread unknown parameters and impurities for the accessible beams at HIMAC. This way, their effect could be inserted in the FLUKA simulation so as to obtain a directly equivalent beam exiting the beam–line as in HIMAC. This would allow for a more accurate reproduction of the $RI\beta^+$ impurities' effect on the β^+ activity reconstruction, as well as a more reliable distribution shape.

Finally, given the expected upcoming availability of facilities able to directly acceleration of radioactive beams, the results of this work and its envisioned continuation should enable a more thorough assessment of $RI\beta^+$ for potential future use in medical applications.

Appendix A

FLUKA routines

`comscw.f` and `stuprf.f` — Excerpts:

```
*-------------Comscw-------------*
*FOR ENERGY DEPOSITION
      IF (ISCRNG.EQ.1) THEN
*SELECT USRBIN#1
         IF (JSCRNG.EQ.1) THEN
*PROMPT SCORING, AND OTHERWISE NOTHING
            IF (IPRODC.EQ.1) THEN
               COMSCW = ONEONE
               ELSE
               COMSCW = ZERZER
               LSCZER = .TRUE.
            ENDIF
*SELECT USRBIN#2
         ELSE IF (JSCRNG.EQ.2) THEN
*DECAY SCORING, AND OTHERWISE NOTHING
            IF (IPRODC.EQ.2) THEN
               COMSCW = ONEONE
               ELSE
               COMSCW = ZERZER
               LSCZER = .TRUE.
            ENDIF
*SELECT USRBIN#3
         ELSE IF (JSCRNG.EQ.3) THEN
*SCORE TOTAL ENERGY DEPOSITION
            COMSCW = ONEONE
            ELSE
            COMSCW = ZERZER
            LSCZER = .TRUE.
         ENDIF
*OTHERWISE, AND TERMINATION...
      ELSE
         LSCZER = .TRUE.
      ENDIF
      RETURN
 *===  End of function Comscw ===*
      END
```

```
*-------------Stuprf-------------*
*(...)
*
       INCLUDE '(EVTFLG)'
       INCLUDE '(FLKSTK)'
       INCLUDE '(TRACKR)'
       INCLUDE '(GENSTK)'
       INCLUDE '(PAPROP)' !properties of secondaries
            created in a hadronic event
       INCLUDE '(FHEAVY)' !intrinsic particle properties
            (mass, charge, half live...)
       INCLUDE '(EVTFLG)' !special stack for nuclear
            fragments
*(...)

*     FLAGS FOR IDENTIFYING INTERACTION
         IF (LELEVT) THEN        !Elastic interaction
            ISPARK(1,NPFLKA) = 1
         ELSE IF (LINEVT) THEN   !Inelastic interaction
            ISPARK(1,NPFLKA) = 2
         ELSE IF (LDECAY) THEN   !Particle decay
            ISPARK(1,NPFLKA) = 3
         ELSE IF (LDLTRY) THEN   !Delta ray production
            ISPARK(1,NPFLKA) = 4
         ELSE IF (LPAIRP) THEN   !Pair production
            ISPARK(1,NPFLKA) = 5
*(...)

         IF (LDECAY) THEN
            WRITE(61,*)
                 XX,YY,ZZ,IJ,KPART(NPSECN),ISPARK(1,NPFLKA)
         ENDIF
      ENDIF
      RETURN
 *===  End of function Stuprf ===*
      END
```

The `comscw.f` user routine is employed to weight the energy distribution obtained via the `USRBIN` card, and it was modified to filter energy contributions from different origins using “decay”, “prompt” and “total” flags. As for the `stuprf.f` user–routine, it is employed to provide additional details on the decay elements scored (*e.g.* type, position).

Source — Beam geometry parameters are fixed *a priori* for every field, thus being embedded in `source.f` directly. Changeable parameters are either passed by the input (*e.g.* beam type) or read from an external file with 625 entries corresponding to the raster scan beam spots for an isoenergetic layer.

```
*-----------Source---------------*
      PARAMETER(NLINES = 625)
      DIMENSION XBP (NLINES), XSB (NLINES), YBP (NLINES), YSB (NLINES),
     &EGY (NLINES)
      SAVE LFIRST, KOUNT
      DATA LFIRST / .TRUE. /
*(...)
* User initialization
         WRITE(LUNOUT,*)'Modified source.f for Hitlike beams'
         OPEN(UNIT=88,
     &   FILE=''/path1''
     &   ,STATUS=''OLD'')
         OPEN(UNIT=89,
     &   FILE=''/path2''
     &   ,STATUS=''UNKNOWN'')
         DO I = 1, NLINES
            READ(88,*) EGY (I), XBP (I), YBP (I), XSB (I), YSB (I)
         END DO
         KOUNT = 0
     ENDIF
* 88 is the external data file, 89 is a test sample
*Sample creation with 50 entries:
     KOUNT = KOUNT+1
     XI = FLRNDM(DUMMY)
     LINE = INT(XI * DBLE(NLINES)) + 1
     IF(KOUNT .LE. 50) THEN
        WRITE(89,*) LINE, EGY (LINE), XBP (LINE), YBP (LINE),
    &   XSB (LINE), YSB(LINE)
     ENDIF
*(...)
*Kinetic energy of the particle in GeV
     TKEFLK (NPFLKA) = EGY (LINE)
* Translating kinetic energy into momentum
     PMOFLK (NPFLKA) = SQRT (TKEFLK (NPFLKA)*(TKEFLK (NPFLKA)
    &                       + TWOTWO * AM (IONID) ) )
* Polarization cosines:
     TXPOL (NPFLKA) = -TWOTWO
     TYPOL (NPFLKA) = +ZERZER
     TZPOL (NPFLKA) = +ZERZER
* Particle coordinates, Z origin
     XFLK (NPFLKA) = XBP (LINE)
     YFLK (NPFLKA) = YBP (LINE)
     ZFLK (NPFLKA) = -575.D3
*----------------Momentum Spread Implementation---------------*
*  Getting energies as kinetic energy
      TKEFLK (NPFLKA) = EGY (LINE)
*  Translate kinetic energy into momentum
      PMOFLK(NPFLKA) = SQRT ( TKEFLK (NPFLKA)*(TKEFLK (NPFLKA)
     &      + TWOTWO*AM (IONID)))
*  Apply momentum spread (TT suggestion)
      CALL FLNRRN (RGAUS0)
      PMOFLK(NPFLKA)=PMOFLK(NPFLKA)+1.5E-3*PMOFLK(NPFLKA)*
     &     RGAUS0/S2FWHM
*  Give each beam the appropriate FWHM (2.5 mm according to data)
      CALL FLNRR2 (RGAUS1,RGAUS2)
      XFLK(NPFLKA) = RGAUS1*0.1062D0
      YFLK(NPFLKA) = RGAUS2*0.1062D0
```

Fragmentation. The modified excerpts of `comscw.f` and `stuprf.f` routines to study fragmentation are shown below, `LTRACK` (Generation Number) and `JTRACK` (Particle Identity) are associated explicitly to the inelastic nuclear reaction flags. The identification of the models responsible for fragment transport, namely the BME or rQMD, is done according to the energy deposition boundary condition using `stuprf.f`. As for `comscw.f`, it passes the filtered information into `USRBIN` estimators.

```
*——————————————Comscw——————————————*
*ENERGY DEPOSITION
         IF (ISCRNG.EQ.1) THEN
*Carbon example
*SELECT USRBIN#21
            ELSE IF (JSCRNG .EQ. 21) THEN
*ENFORCING CONDITIONS (C & BME)
               IF (ISPUSR(3) .EQ. 11 .AND.
                    ISPUSR(2) .EQ. 2) THEN
                  COMSCW = ONEONE
               ELSE
                  COMSCW = ZERZER
                  LSCZER = .TRUE.
               ENDIF
*SELECT USRBIN#22
            ELSE IF (JSCRNG .EQ. 22) THEN
*ENFORCING CONDITIONS (C & RQMD)
               IF (ISPUSR(3) .EQ. 11 .AND.
                    ISPUSR(2) .EQ. 1) THEN
                  COMSCW = ONEONE
               ELSE
                  COMSCW = ZERZER
                  LSCZER = .TRUE.
               ENDIF
```

`comscw.f` — Filtering annihilation events at rest of ^{11}C ions:

```
*——————————Condition enforcement——————*
*Aniquilacao
         IF (ISCRNG.EQ.9) THEN
*1 segundo
*Seleccionar USRBIN#1
            IF (JSCRNG.EQ.1) THEN
*Aplicar aos seguintes isotopos (C—11)
               IF (IAZTRK .EQ. 6011) THEN
                  COMSCW = ONEONE
               ELSE
                  COMSCW = ZERZER
                  LSCZER = .TRUE.
               ENDIF
```

```
*——————————————Stuprf——————————————*
*Particle ID (secondary)
!Individual flags
IF(LINEVT .AND. JTRACK .EQ. —2 .AND. LTRACK
     .EQ. 1) THEN ! Inelastic nuclear reaction
   IF (ILOFLK(NPFLKA) .EQ. 1) THEN
      ISPARK(3,NPFLKA) = 1 ! Proton flag
   ELSE IF (ILOFLK(NPFLKA) .EQ. —6) THEN
      ISPARK(3,NPFLKA) = 2 ! Alfa flag
*(...)
!Group flags I
   ELSE IF (ILOFLK(NPFLKA) .EQ. —2) THEN
*carbon example — part 1
      IF (ICHRGE(—2) .EQ. 6) THEN
         ISPARK(3,NPFLKA) = 11 !C flag
      ENDIF
!Group flags II
      ELSE IF ((ABS(ILOFLK(NPFLKA))) >=
           10000) THEN
            IZ = (ABS(ILOFLK(NPFLKA))/100000)
*carbon example — part 2
            ELSE IF (IZ .EQ. 6) THEN
            ISPARK(3,NPFLKA) = 11 !C flag
            ENDIF
!Group flags III
      ELSE IF (((ILOFLK(NPFLKA)) .LT. —6)
           .AND.
   &     ((ILOFLK(NPFLKA)) .GT. —10000)) THEN
*carbon example — part 3
         ELSE IF (ICHEAV(—ILOFLK(NPFLKA))
              .EQ. 6) THEN
         ISPARK(3,NPFLKA) = 11 !C flag
         ENDIF
*(...)
*—Energy boundary RQMD/BME*
   IF ((ETRACK—AM(—2))/DBLE(IBARCH(—2))>=
        0.125D+00) THEN
      ISPARCK(2,NPFLKA) = 1
   ELSE IF ((ETRACK—AM(—2))/DBLE(IBARCH(—2))<
        0.125D+00) THEN
      ISPARCK(2,NPFLKA) = 2
   ENDIF
ENDIF
*(...)
```

A more detailed view of fragments contribution (by Z) to the *Bragg Peak* is shown below in figure A, for carbon ions only. It already includes the summed up fractions from both BME and rQMD.

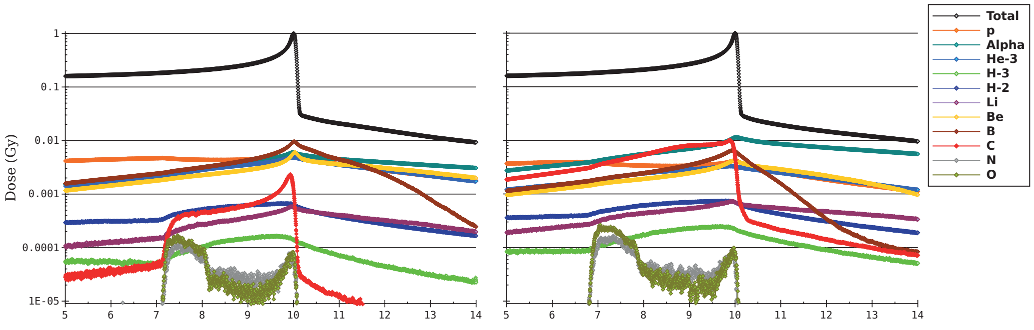

(a) ^{9}C (`BME+RQMD`) (b) ^{10}C (`BME+RQMD`)

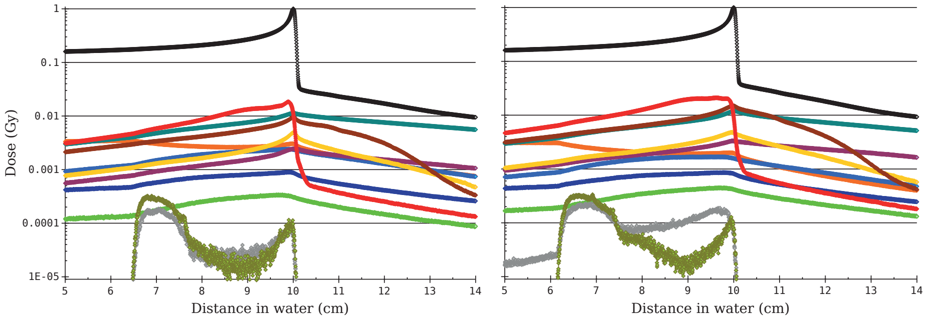

(c) ^{11}C (`BME+RQMD`) (d) ^{12}C (`BME+RQMD`)

Figure A: *Carbon irradiations and respective Z–filtered dose contribution, for an 1 Gy Bragg Peak at 10 cm depth.*

Auxilliary programs

`bpgen.cpp`: database with energy and *Bragg Peak* positions to produce SOBP

```
//Bragg Peak's E vs Pz code, version 3.0 (Jul2016)
#include<stdio.h>
#include<stdlib.h>
#include<math.h>
#include<iostream>
#include<iomanip>
#include<string>
#include<fstream>
using namespace std;
int main(){
  std::ofstream outfile;
  outfile.open("Energy.dat", std::ios_base::app);
  int a,y,i,n;
  char sce,ion;
  double x,z,p,p2,p3,p4,E,p5,p6;
    cout << "RSA-Jul2016_3.0-SOBPgen\n" << endl;
  cout << "Choose the letter corresponding to the desired irradiation environment;"<< endl;
    cout << "Basic - FLUKA Calculations with Beam on Water Phantom (B)"<< endl;
    cout << "HIT - Incremented according to Heidelberg's setup (H)"<< endl;
    cout << "VOXEL - Voxel instead of water phantom with Heidelberg's setup (V)"<< endl;
    cout << "Customized - For personalized geometries (P)"<< endl;
    cin >> sce;
    // Previous fit data applies here
    if(sce=='B'){
    cout << "Please introduce the Atomic Mass (8<A<17) of the ion: "<< endl;
    cin >> a;
    //Flag for ions not yet implemented
    if(a<8 or a>17){cout << "Patience is a virtue" << endl;return 0;}
    cout << "Define the plateau length (cm): " << endl;
    cin >> x;
    cout << "Centered at which depth? (cm): " << endl;
    cin >> z;
    cout << "Total number of peaks to be generated: " << endl;
    cin >> y;
    cout << "\n\n" << endl;
    //Generating table
    if(a==8){ion='B';}
    if(a==9){ion='C';}
    if(a==10){ion='C';}
    if(a==11){ion='C';}
    if(a==12){ion='C';}
    if(a==13){ion='N';}
    if(a==14){ion='O';}
    if(a==15){ion='O';}
    if(a==16){ion='O';}
    if(a==17){ion='F';}
      cout << " ______________________"<<ion<<"-"<<a<<"___________________________ " << endl;
      cout << "|__Field___|_____Energy_(MeV/u)___|___Peak_Z_(cm)___|" << endl;
    //Mighty powers used in our fit
    for(i=0;i<=y-1;i++){p = z - (x/2) +i*(x/(y-1));
    p2 = p*p;
    p3 = p*p*p;
    p4 = p*p*p*p;
    p5 = p*p*p*p*p;
    p6 = p*p*p*p*p*p;
    //Database of August 2016
    if(a==8){
    E = -0.0000008657*p6 + 0.0000986864*p5 -0.0046372990*p4 + 0.1178606612*p3 -1.8451014685*p2 +
        28.7175754188*p + 38.8987935615;
      cout << "|   ("<< setprecision(10) <<i<<")     |      "<<E<<"      |       "<< p <<"       |" << endl;
      outfile << setprecision(12) << E << endl;}
    else if(a==9){
    E = -0.0000018268*p6 + 0.0001813354*p5 -0.0074918738*p4 + 0.1692761372*p3 -2.3847886850*p2 +
        34.2141873721*p + 42.6552189447;
      cout << "|   ("<< setprecision(10) <<i<<")     |      "<<E<<"      |       "<< p <<"       |" << endl;
      outfile << setprecision(12) << E << endl;}
    else if(a==10){
    E = -0.0000012791*p6 + 0.0001366633*p5 -0.0060407346*p4 + 0.1449100813*p3 -2.1470493289*p2 +
        31.8644522456*p + 40.7708279408;
      cout << "|   ("<< setprecision(10) <<i<<")     |      "<<E<<"      |       "<< p <<"       |" << endl;
      outfile << setprecision(12) << E << endl;}
    else if(a==11){
    E = -0.0000007885*p6 + 0.0000912957*p5 -0.0043704710*p4 + 0.1134971616*p3 -1.8199914643*p2 +
        29.1918996333*p + 40.4020030546;
    cout << "|   ("<< setprecision(10) <<i<<")     |      "<<E<<"      |       "<< p <<"       |" << endl;
    outfile << setprecision(12) << E << endl;}
    else if(a==12){
    E = -0.0000007794*p6 + 0.0000905893*p5 -0.0043396583*p4 + 0.1122961392*p3 -1.7851777584*p2 +
        28.0422709316*p + 38.0560267087;
      cout << "|   ("<< setprecision(10) <<i<<")     |      "<<E<<"      |       "<< p <<"       |" << endl;
      outfile << setprecision(12) << E << endl;}
    else if(a==13){
    E = -0.0000013527*p6 + 0.0001416543*p5 -0.0061657168*p4 + 0.1465320143*p3 -2.1669027062*p2 +
        32.5225003906*p + 42.2542439773;
      cout << "|   ("<< setprecision(10) <<i<<")     |      "<<E<<"      |       "<< p <<"       |" << endl;
      outfile << setprecision(12) << E << endl;}
```

```
      //Dismissing A=14...
    else if(a==14){
      cout << "Train your mind to see the positive in every situation"<< endl;}
    else if(a==15){
    E = -0.0000026397*p6 + 0.0002455236*p5 -0.0095149104*p4 + 0.2020229257*p3 -2.6810657257*p2 + 36.3976655724*p + 42.9209091957;
    cout << "|   ("<< setprecision(10) <<i<<")    |      "<<E<<"     |       "<< p <<"      |" << endl;
    outfile << setprecision(12) << E << endl;}
    else if(a==16){
    E = -0.0000021728*p6 + 0.0002086695*p5 -0.0083289183*p4 + 0.1817978994*p3 -2.4797973045*p2 + 34.6060088414*p + 42.2527126903;
    cout << "|   ("<< setprecision(10) <<i<<")    |      "<<E<<"     |       "<< p <<"      |" << endl;
    outfile << setprecision(12) << E << endl;}
    else if(a==17){
    E = -0.0000044294*p6 + 0.0003755346*p5 -0.0132836210*p4 + 0.2581423299*p3 -3.1516142483*p2 + 39.8534582220*p + 44.1860760712;
    cout << "|   ("<< setprecision(10) <<i<<")    |      "<<E<<"     |       "<< p <<"      |" << endl;
    outfile << setprecision(12) << E << endl;}
  else{cout << "The sky above the port was the color of a Television, tuned to a death channel..."<< endl;
      return 0;}}
    cout << " ---------------------------------------------------" << endl;}
    //Heidelberg scenario
  else if(sce=='H'){
    cout << "Please introduce the Atomic Mass (8<A<17) of the ion: "<< endl;
    cin >> a;
    //Flag for cases not yet implemented
    if(a<8 or a>17){cout << "Patience is a virtue" << endl;return 0;}
    cout << "Define the plateau length (cm): " << endl;
    cin >> x;
    cout << "Centered at which depth? (cm): " << endl;
    cin >> z;
    cout << "Total number of peaks to be generated: " << endl;
    cin >> y;
    cout << "\n\n" << endl;
    //Generating table
    if(a==8){ion='B';}
    if(a==9){ion='C';}
    if(a==10){ion='C';}
    if(a==11){ion='C';}
    if(a==12){ion='C';}
    if(a==13){ion='N';}
    if(a==14){ion='O';}
    if(a==15){ion='O';}
    if(a==16){ion='O';}
    if(a==17){ion='F';}
    cout << " ____________________"<<ion<<"-"<<a<<"__________________________ " << endl;
    cout << "|__Field___|_____Energy_(MeV/u)___|___Peak_Z_(cm)___|" << endl;
    //Implementing the new fit data retrieved from FLUKA simulations
    for(i=0;i<=y-1;i++){p = z - (x/2) +i*(x/(y-1));
    p2 = p*p;
    p3 = p*p*p;
    p4 = p*p*p*p;
    if(a==8){
    E = -0.000539868*p4 + 0.0371249*p3 - 1.03167*p2 + 24.6565*p + 63.8477;
    cout << "|   ("<< setprecision(10) <<i<<")    |      "<<E<<"     |       "<< p <<"      |" << endl;
    outfile << setprecision(12) << E << endl;}
    else if(a==9){
    E = -0.000539868*p4 + 0.0371249*p3 - 1.03167*p2 + 24.6565*p + 63.8477;
    cout << "|   ("<< setprecision(10) <<i<<")    |      "<<E<<"     |       "<< p <<"      |" << endl;
    outfile << setprecision(12) << E << endl;}
    else if(a==10){
    E = -0.000539868*p4 + 0.0371249*p3 - 1.03167*p2 + 24.6565*p + 63.8477;
    cout << "|   ("<< setprecision(10) <<i<<")    |      "<<E<<"     |       "<< p <<"      |" << endl;
    outfile << setprecision(12) << E << endl;}
    else if(a==11){
    E = -0.000539868*p4 + 0.0371249*p3 - 1.03167*p2 + 24.6565*p + 63.8477;
    cout << "|   ("<< setprecision(10) <<i<<")    |      "<<E<<"     |       "<< p <<"      |" << endl;
    outfile << setprecision(12) << E << endl;}
    else if(a==12){
    E = -0.000215611*p4 + 0.0166102*p3 - 0.57039*p2 + 19.6732*p + 72.444;
      cout << "|   ("<< setprecision(10) <<i<<")    |      "<<E<<"     |       "<< p <<"      |" << endl;
      outfile << setprecision(12) << E << endl;}
     else if(a==13){
    E = -0.000215611*p4 + 0.0166102*p3 - 0.57039*p2 + 19.6732*p + 72.444;
      cout << "|   ("<< setprecision(10) <<i<<")    |      "<<E<<"     |       "<< p <<"      |" << endl;
      outfile << setprecision(12) << E << endl;}
     else if(a==14){
      cout << "Maybe one day."<<  endl;}
    else if(a==15){
    E = -0.000460215*p4 + 0.0357108*p3 - 1.09586*p2 + 28.5532*p + 73.4068;
    cout << "|   ("<< setprecision(10) <<i<<")    |      "<<E<<"     |       "<< p <<"      |" << endl;
    outfile << setprecision(12) << E << endl;}
    else if(a==16){
    E = -0.000202313*p4 + 0.0169548*p3 - 0.623042*p2 + 23.1456*p + 84.8733;
    cout << "|   ("<< setprecision(10) <<i<<")    |      "<<E<<"     |       "<< p <<"      |" << endl;
    outfile << setprecision(12) << E << endl;}
      //Dismissing A=13 and A=14...
  else{cout << "The sky above the port was the color of a Television, tunned to a death channel..."<< endl;
      return 0;}}
    cout << " ---------------------------------------------------" << endl;}
```

```
    //VOXEL scenario
  else if(sce=='V'){
    cout << "Please introduce the Atomic Mass (8<A<17) of the ion: "<< endl;
    cin >> a;
    //Flag for cases not yet implemented
    if(a<8 or a>17){cout << "Patience is a virtue" << endl;return 0;}
    cout << "Define the plateau length (cm): " << endl;
    cin >> x;
    cout << "Centered at which depth? (cm): " << endl;
    cin >> z;
    cout << "Total number of peaks to be generated: " << endl;
    cin >> y;
    cout << "\n\n" << endl;
    //Generating table
    if(a==8){ion='B';}
    if(a==9){ion='C';}
    if(a==10){ion='C';}
    if(a==11){ion='C';}
    if(a==12){ion='C';}
    if(a==13){ion='N';}
    if(a==14){ion='O';}
    if(a==15){ion='O';}
    if(a==16){ion='O';}
    if(a==17){ion='F';}
    cout << " ____________________"<<ion<<"-"<<a<<"________________________ " << endl;
    cout << "|__Field___|_____Energy_(MeV/u)___|___Peak_Z_(cm)___|" << endl;
    //Implementing the new fit data retrieved from FLUKA simulations
    for(i=0;i<=y-1;i++){p = z - (x/2) +i*(x/(y-1));
    p2 = p*p;
    p3 = p*p*p;
    p4 = p*p*p*p;
    if(a==8){
    E = -0.000539868*p4 + 0.0371249*p3 - 1.03167*p2 + 24.6565*p + 63.8477;
    cout << "|   ("<< setprecision(10) <<i<<")     |       "<<E<<"      |        "<< p <<"       |" << endl;
    outfile << setprecision(12) << E << endl;}
    else if(a==9){
    E = -0.000539868*p4 + 0.0371249*p3 - 1.03167*p2 + 24.6565*p + 63.8477;
    cout << "|   ("<< setprecision(10) <<i<<")     |       "<<E<<"      |        "<< p <<"       |" << endl;
    outfile << setprecision(12) << E << endl;}
    else if(a==10){
    E = -0.000539868*p4 + 0.0371249*p3 - 1.03167*p2 + 24.6565*p + 63.8477;
    cout << "|   ("<< setprecision(10) <<i<<")     |       "<<E<<"      |        "<< p <<"       |" << endl;
    outfile << setprecision(12) << E << endl;}
    else if(a==11){
    E = -0.000539868*p4 + 0.0371249*p3 - 1.03167*p2 + 24.6565*p + 63.8477;
    cout << "|   ("<< setprecision(10) <<i<<")     |       "<<E<<"      |        "<< p <<"       |" << endl;
    outfile << setprecision(12) << E << endl;}
    else if(a==12){
    E = -0.000215611*p4 + 0.0166102*p3 - 0.57039*p2 + 19.6732*p + 72.444;
      cout << "|   ("<< setprecision(10) <<i<<")     |       "<<E<<"      |        "<< p <<"       |" << endl;
      outfile << setprecision(12) << E << endl;}
     else if(a==13){
    E = -0.000215611*p4 + 0.0166102*p3 - 0.57039*p2 + 19.6732*p + 72.444;
      cout << "|   ("<< setprecision(10) <<i<<")     |       "<<E<<"      |        "<< p <<"       |" << endl;
      outfile << setprecision(12) << E << endl;}
     else if(a==14){
      cout << "Maybe one day."<<  endl;}
    else if(a==15){
    E = -0.000460215*p4 + 0.0357108*p3 - 1.09586*p2 + 28.5532*p + 73.4068;
    cout << "|   ("<< setprecision(10) <<i<<")     |       "<<E<<"      |        "<< p <<"       |" << endl;
    outfile << setprecision(12) << E << endl;}
    else if(a==16){
    E = -0.000202313*p4 + 0.0169548*p3 - 0.623042*p2 + 23.1456*p + 84.8733;
    cout << "|   ("<< setprecision(10) <<i<<")     |       "<<E<<"      |        "<< p <<"       |" << endl;
    outfile << setprecision(12) << E << endl;}
      //Dismissing A=13 and A=14...
  else{cout << "The sky above the port was the color of a Television, tunned to a death channel..."<<
       endl;
      return 0;}}
    cout << " ------------------------------------------------------" << endl;}
  //Customized scenario
  else if(sce=='P'){
    cout << "Introduce the Atomic Mass of the Projectile: "<< endl;
    cin >> a;
    cout << "And the atomic number: "<< endl;
    cin >> n;
    cout << "Define the plateau length (cm): " << endl;
    cin >> x;
    cout << "Centered at which depth? (cm): " << endl;
    cin >> z;
    cout << "Total number of peaks to be generated: " << endl;
    cin >> y;
    cout << "\n\n" << endl;
    //Generating table
    cout << " __________________Z="<<n<<",A="<<a<<"______________________ " << endl;
    cout << "|__Field___|_____Energy_(MeV/u)___|___Peak_Z_(cm)___|" << endl;
    //Implementing the new fit data retrieved from FLUKA simulations
    for(i=0;i<=y-1;i++){p = z - (x/2) +i*(x/(y-1));
    p2 = p*p;
    p3 = p*p*p;
    p4 = p*p*p*p;
    p5 = p*p*p*p*p;
```

```
    p6 = p*p*p*p*p*p;
    if(a>0){
//E = (primus6)*p6 + (primus5)*p5 + (primus4)*p4 + (primus3)*p3 + (primus2)*p2 + (primus1)*p + (primus0);
    cout << "|    ("<< setprecision(10) <<i<<")     |       "<<E<<"      |        "<< p <<"       |" << endl;
    outfile << setprecision(12) << E << endl;}
  else{cout << "The sky above the port was the color of a Television, tunned to a death channel..."<<
      endl;
      return 0;}}
    cout << " -------------------------------------------------------" << endl;}
    else{cout << "HAL 9000: Are you sure you're making the right decision? I think we should stop."<<
        endl;}
      return 0;
      return 0;}
```

`supra.cpp`: code providing the list of commands to produce SOBPs.

```
#include<stdio.h>
#include<stdlib.h>
#include<math.h>
#include<iostream>
#include<iomanip>
#include<string>
#include<fstream>
#define _USE_MATH_DEFINES
using namespace std;
int main(int argc, char *argv[]){int a,i,x,y,z,w;char plot[50];
  cout << "RSA-May2015-Suprascript" << endl;
  cout << "Total number of Simulations/beam/dat files:" << endl;
  cin >> a;
  cout << "File name: " << endl;
  cin >> plot;
  cout << "\n" << endl;
  //Send the results of all files to a single dat file
  cout << "paste ";
    x = 1;
    y = 2;
    for(i=1;i<=a;i++){cout << plot << setfill('0') << setw(2) << i <<".dat ";}
  cout << " | awk \'{print ";
  cout << "$" << x << ", $" << y;
     for(i=1;i<a;i++){z = 4*i - 1;
      cout <<", $" << z;}
        w= 4*a - 1;
        //Take out the first line and the bin information
     cout << ", $" << w << "}\' > bigdat.txt \n\n" << "tail -n+2 bigdat.txt > big.dat \n\ncut -d \" \"
          -f 3- big.dat > nobin.dat \n\n";
     //Retrieve the lines containing the maximum values
     for(i=1;i<a;i++){cout << "awk \'$"<< i <<"> max { max = $"<< i <<"; output = $0 } END { print
          output }\' nobin.dat >> quad.dat && \n";}
     cout <<"awk \'$"<<a<<" > max { max = $"<< a <<"; output = $0 } END { print output }\' nobin.dat >>
          quad.dat\n\n";
 float r;
 double norm;
  cout << "Define the usrbin plot radius\n" << endl;
  cin >> r;
  setprecision(10);
  norm = 1.0/(M_PI*r*r*1.602176462E-7);
  cout<<fixed<< "\nThe normalization factor is: " << norm << endl;
  //Creating the vector for the normalization
  ofstream fout;
  fout.open("vector.dat");
   for (int i=0; i<a; i++){fout<<fixed<<norm<< endl;};
  string slash,dat;
  //Use "\t"
  cout << "\nSeparator type (in quotes) \n" << endl;
  cin >> slash;
  cout << "\nName of the output dat file is ival.dat by default\n" << endl;
  //R input
  cout<<"\nA <- as.matrix(read.table(\"quad.dat\"))\nV <- as.matrix(read.table(\"vector.dat\"))\nx <-
       solve(A) %*% V\nwrite.table(x,file=\"ival.dat\",sep="<< slash <<",col.names = F, row.names =
       F)"<< endl;
  string u,v,col,tit;
  char log;
  char eps[20];
  //Gnuplot input
  cout << "\nGnuplot\n\nHorizontal limits separated by :\n" << endl;
    cin >> u;
  cout << "\nVertical limits separated by :\n" << endl;
    cin >> v;
  cout << "\nChoose the name of the eps file plot\n" << endl;
    cin >> eps;
  cout << "\nPlease select the gnuplot color, wisely...\n" << endl;
    cin >> col;
  cout << "\n...and the inplot title (in quotes)\n" << endl;
    cin >> tit;
```

```cpp
  cout << "\nLog scale y? (y or n)\n" << endl;
    cin >> log;
    cout<<"\n\nset terminal postscript eps enhanced color size 4, 3 font 'Helvetica,16' solid lw
        3"<<"\nset output \""<<eps<<"\"\nset grid"<<"\nset yrange["<<v<<"]"<<"\nset
        xrange["<<u<<"]\nset xlabel 'Depth in water (cm)'\nset ylabel 'Dose (Gy)'";
    if(log=='y'){cout<<"\nset log y\n";}
    else cout<<"\n";
    cout<<"plot 'big.dat' us 1:("<<M_PI<<"*1.602176462E-7*(";
        for (int i=3; i<2+a; i++){
        cout<<"($"<<i<<")*";
        const int LINE_TO_FIND = i-2;
        string line;
        ifstream f( "ival.dat" );
        for (int k=0; k<LINE_TO_FIND;k++){getline(f,line);}
        cout<< line<<"+";};
        int q = a + 2;
        cout<<"($"<<q<<")*";
        const int LINE_TO_FIND = a;
        string line;
        ifstream f( "ival.dat" );
        for (int k=0; k<LINE_TO_FIND;k++){getline(f,line);}
        cout<< line <<")) w steps lw 1 lc rgb '"<< col <<"' title " << tit << endl;
        cout<<"\nepstopdf "<<eps<<endl;
return 0;}
```

The data for the FLUKA simulations' input is obtained using the energies retrieved with the `SOBPGen.cpp` code, and respective fit. The `supra.cpp` program is then applied to obtain the SOBP.

This procedure still requires the user to apply the data output as input, sequentially in `bash`, `R` and `gnuplot` scripts. For simplicity, a single code was created, in the form sequential bash shell script to manipulate the data and plot the final result. The script used two programs: `infra1.cpp` and `infra2.cpp`).

Script `infra.sh`:

```bash
#!/bin/bash
#infrascript

g++ infra1.cpp -o infra1 &&
make infra1 &&
./infra1 &&
chmod +x supra.sh &&
./supra.sh &&
Rscript script.r &&
g++ infra2.cpp -o infra2 &&
make infra2 &&
./infra2
gnuplot gnuscript.gp &&
```

Directory environment example:

```
[rdossant@krazny-cern-ch local]\$ ls -1 | sort -r
infra.sh
infra2.cpp
infra1.cpp
Carbonized_plot30.dat
Carbonized_plot29.dat
Carbonized_plot28.dat
Carbonized_plot27.dat
Carbonized_plot26.dat
Carbonized_plot25.dat
Carbonized_plot24.dat
Carbonized_plot23.dat
Carbonized_plot22.dat
Carbonized_plot21.dat
Carbonized_plot20.dat
Carbonized_plot19.dat
Carbonized_plot18.dat
Carbonized_plot17.dat
```

Filling in correctly the parameters asked, a plot will be automatically generated.

`infra1.cpp`. First stage:

```
#include<stdio.h>
#include<stdlib.h>
#include<math.h>
#include<iostream>
#include<iomanip>
#include<string>
#include<fstream>
#define _USE_MATH_DEFINES
 using namespace std;
 int main(int argc, char *argv[]){int a,i,x,y,z,w;char plot[50];
  cout << "RSA-Jun2015-Infra.cpp (1/2)" << endl;
  cout << "Total number of field dat files:" << endl;
  cin >> a;
  cout << "File name: " << endl;
  cin >> plot;
  //Send the results of all fields to a single dat file (future quad.dat)
  ofstream fout;
  fout.open("supra.sh");
    fout << "#!/bin/bash\n"<<"# suprascript\n\n"<<"paste ";
    x = 1;
    y = 2;
    for(i=1;i<=a;i++){fout << plot << setfill('0') << setw(2) << i <<".dat ";}
  fout << " | awk \'{print ";
  fout << "$" << x << ", $" << y;
     for(i=1;i<a;i++){z = 4*i - 1;
      fout <<", $" << z;}
        w= 4*a - 1;
        //Take out the first line and the bin information
     fout << ", $" << w << "}\' > bigdat.txt \n\n" << "tail -n+2 bigdat.txt > big.dat \n\ncut -d \" \" -f 3- big.dat > nobin.dat \n\n";
     //Retrieve the lines containing the maximum values
     for(i=1;i<a;i++){fout << "awk \'$"<< i <<"> max { max = $"<< i <<"; output = $0 } END { print output }\' nobin.dat >> quad.dat && \n";}
     fout <<"awk \'$"<<a<<" > max { max = $"<< a <<"; output = $0 } END { print output }\' nobin.dat >> quad.dat\n\n";
  fout.close();
  //Now focus in vec.dat
 float l,r,s;
 double norm;
  cout << "\nDefine the length of the usrbin-1D window (squared)..." << endl;
  cin >> l;
  cout << "...the material density (g/cm3)..." << endl;
  cin >> r;
  cout << "...and the SOBP's DAP value (Gy.cm2)" << endl;
  cin >> s;
  setprecision(10);
  norm = (1.0*s*r)/(l*l*1.602176462E-7);
  cout<<fixed<< "\nThe normalization factor is: " << norm << endl;
  //Creating the vector for the normalization
  fout.open("vector.dat");
   for (int i=0; i<a; i++){fout<<fixed<<norm<< endl;};
   fout.close ();
   string slash,dat;
  //Use "\t"
  cout << "\nSeparator type is tab (use quotes)" << endl;
  cin >> slash;
  fout.open("script.r");
  //R input
  fout<<"#!/usr/bin/Rscript\nA <- as.matrix(read.table(\"quad.dat\"))\nV <- as.matrix(read.table(\"vector.dat\"))\nx <- solve(A) %*% V\nwrite.table(x,file=\"ival.dat\",sep="<< slash <<",col.names = F, row.names = F)"<< endl;
  fout.close ();
  return 0;}
```

`infra2.cpp`. Second stage:

```cpp
#include<stdio.h>
#include<stdlib.h>
#include<math.h>
#include<iostream>
#include<iomanip>
#include<string>
#include<fstream>
#define _USE_MATH_DEFINES
 using namespace std;
 int main(int argc, char *argv[]){int a;string u,v,col,tit;char log;float l, r;char eps[20];
    //Gnuplot input
  cout << "\n RSA-Jun2015-Infra.cpp (2/2) \n Gnuplot \n Number of fields:" << endl;
    cin >> a;
  cout << "Field window limit l (Area=lxl):" << endl;
    cin >> l;
    cout << "Material density:" << endl;
    cin >> r;
    cout << "Horizontal limits separated by:" << endl;
    cin >> u;
  cout << "Vertical limits separated by:" << endl;
    cin >> v;
  cout << "Choose the name of the eps file plot" << endl;
    cin >> eps;
  cout << "Please select the gnuplot color, wisely..." << endl;
    cin >> col;
  cout << "...and the inplot title (in quotes)" << endl;
    cin >> tit;
  cout << "Log scale y? (y or n)" << endl;
    cin >> log;
    ofstream fout;
    fout.open("gnuscript.gp", std::ios::app);
    fout <<"#!/usr/bin/gnuplot"<<endl;
    fout<<"set terminal postscript eps enhanced color size 4, 4 font 'Helvetica,16' solid lw 1"<<"\nset output \""<<eps<<".eps\"\nset grid"<<"\nset yrange["<<v<<"]"<<"\nset xrange["<<u<<"]\nset xlabel 'Depth in water (cm)'\nset ylabel 'DAP (Gy.cm^2)'";
    if(log=='y'){fout<<"\nset log y\n";}
    else fout<<"\n";
    fout<<"plot 'big.dat' us 1:(("<<l<<"/"<<r<<")*"<<l<<"*1.602176462E-7*(";
        for (int i=3; i<2+a; i++){fout<<"($"<<i<<")*";
        const int LINE_TO_FIND = i-2;
        string line;
        ifstream f( "ival.dat" );
        for (int k=0; k<LINE_TO_FIND;k++){getline(f,line);}
        fout<< line<<"+";};
        int q = a + 2;
        fout<<"($"<<q<<")*";
        const int LINE_TO_FIND = a;
        string line;
        ifstream f( "ival.dat" );
        for (int k=0; k<LINE_TO_FIND;k++){getline(f,line);}
        fout<< line <<")) w steps lw 1 lc rgb '"<< col <<"' title " << tit << endl;
    fout.close ();
  fout.open("infra.sh", std::ios::app);
  fout <<"epstopdf "<<eps<<".eps &&"<<endl;
  fout <<"gnome-open "<<eps<<".pdf &&"<<endl;
  //  fout <<"rm -rf big.dat ival.dat quad.dat bigdat.txt nobin.dat gnuscript.gp script.r "<<eps<<".eps vector.dat *.o &&"<<endl;
  fout <<"sed -n '1,13p' infra.sh > infra.sh.tmp &&"<<endl;
  fout <<"cp infra.sh.tmp infra.sh &&"<<endl;
  fout <<"rm -rf infra.sh.tmp"<<endl;
  fout.close ();
 return 0;}
```

Script$_0$

```

#!/bin/bash
#Script0
#Define beam type and input name
printf ’\n%s\n\n’ ’Generate and simulate various inputs with
     50<E<450 MeV/u’
echo —n "Z: "
read Z
echo —n "A: "
read A &&
echo "Input name: "
read I &&
sed —i "s/HI—PROPE          6.       12./HI—PROPE
     $Z.       $A./g" $I.inp &&
#Multiply inputs
cp $I.inp $I—1_aa.inp;
#Abbreviated
cp $I.inp $I—1_dw.inp &&
#Generate energies in 50—450 MeV/n steps
sed —i ’s/keywordE/   0.50 /g’ $I—1_aa.inp;
#Abbreviated
sed —i ’s/keywordE/  0.450 /g’ $I—1_dw.inp &&
#Running inputs in short queue
SHORTY=/soft/flair/utils/qshort.sh
RUN=/soft/flukadev/flutil/rfluka
CARRASCO=$PWD/carrasco &&
echo "short queue: " $SHORTY
echo "full ldpmqmd executable location: " $CARRASCO
echo "Input name: " $I—1_i+
printf ’\n%s\n\n’ ’Just to verify last one...’
{
$SHORTY $RUN —e $CARRASCO —N0 —M10 $I—1_aa &&
#Abbreviated
$SHORTY $RUN —e $CARRASCO —N0 —M10 $I—1_dv &&
} &> /dev/null
$SHORTY $RUN —e $CARRASCO —N0 —M10 $I—1_dw
$
```

Description

Requisites: a valid (`HEAVYION`) `FLUKA` input.

The script will then automatically create 100 copies of such input, with:

1. User–defined A and Z to identify the primary particle.
2. Different energy for each copy — 100 steps of 4 MeV/u within a 50 and 450 MeV/u interval.

Following the simulations’ end, each of the 100 binning detectors must be plotted, creating 100 `.dat` files to be employed as input for the next script.

Out of these 100 `.dat` files, some energy and ion type combinations can lead to ranges surpassing the length of the phantom (30 cm), creating artifacts. Only the valid cases out of 100 peaks were picked up, the validity was ensured by plotting each individual `.dat` file in *flair* and verifying the result.

The next script collects the 100 `.dat` files’ *Bragg Peak* positions and evaluates their position against the corresponding beam energy as shown in figure B. This results in a polynomial fit, whose parameters are promptly optimized with `gnuplot` to a 6$^{\text{th}}$ order polynomial which was verified to correspond to a high fit quality.

Script$_1$

```bash
#!/bin/bash
#Script1 -- Identify the dat plots
printf '\n%s\n\n' 'Data processing, fit and plot generation'
echo "Input name: "
read I &&
#Take data from dat files
awk 'BEGIN{x=0;while(x<=9){print "sort -grk3 '$I'_plot0"x".dat | tail -n +1 |head -1
     >> adamantium.dat" >> "tempo.sh";x++}}' OFMT='%.15f' &&
awk 'BEGIN{x=10;while(x<=99){print "sort -grk3 '$I'_plot"x".dat | tail -n +1 |head -1
     >> adamantium.dat" >> "tempo.sh";x++}}' OFMT='%.15f' &&
sh tempo.sh &&
cat adamantium.dat
rm -rf tempo.sh &&
#Process data and add energy info
awk 'BEGIN {x=0; while(++x<=101){print 2*(x*2+23)}; exit}' >> "adamantine.dat" &&
awk '{getline f1 <"adamantine.dat" ; print f1,($1+$2)/2.0}' OFMT='%.15f' <
     adamantium.dat > adamant.dat &&
rm -rf adamantium.dat; rm -rf adamantine.dat &&
cat adamant.dat
#Creating gnuplot script
echo "Type of beam: "
read N &&
printf '%s\n%s\n%s\n%s\n%s\n%s\n%s\n%s\n%s\n%s\n%s\n%s\n%s\n%s\n%s\n%s\n' 'set
     terminal postscript eps enhanced color size 6, 6 font "Helvetica,24" solid lw 1'
     'set title "Fitting plot for '$N'"' 'set grid' 'set size ratio 0.5' 'set xrange
     [0:30]' 'set yrange [0:500]' 'set xlabel "Depth (cm)"' 'set ylabel "Initial
     kinetic Energy (MeV/u)"' 'set key top left font "Helvetica,16" Left ' 'g(x) = h +
     i*x + j*x**2 + k*x**3 + l*x**4 + m*x**5 + n*x**6' 'fit [3:30] g(x) "adamant.dat"
     u 2:1 via h,i,j,k,l,m,n' 'ti =
     sprintf("%.10f+%.10fx+\n%.10fx^{2}+%.10fx^{3}+\n%.10fx^{4}+%.10fx^{5}+\n%.10fx^{6}",
     h, i, j, k, l, m, n)' 'set output "gnufit.eps"' 'plot "adamant.dat" us 2:1 w p pt
     12 ps 1 lc rgb "dark-red" title "Bragg Peak location", g(x) w lines lw 2 lc rgb
     "purple" t ti' 'show variables' 'set print "tmp.dat"' 'print h,i,j,k,l,m,n' >>
     gnuscript.gp &&
#Now fitting with gnuplot...
gnuplot gnuscript.gp &&
epstopdf gnufit.eps &&
evince gnufit.pdf &&
rm -rf gnufit.eps; rm -rf adamant.dat; rm -rf gnuscript.gp; rm -rf gnufit.gp
```

Terminal and graphic output

```
Data processing, fit and plot generation
Input name:
bare
  0.71  0.72  2.16617918  0.0645973906
#Abbreviated, this is the original data in dat files
  29.66  29.67  0.140467152  0.940728366
...
50 0.715000000000000
#Abbreviated, energy and Bragg Peak position
430 29.664999999999999
Type of beam:
B−8
#Convergence handled by gnuplot:
 Iteration 0
#Abbreviated
 Iteration 12
 WSSR        : 0.343896          delta(WSSR)/WSSR   : −3.81237e−06
 delta(WSSR) : −1.31106e−06      limit for stopping : 1e−05
 lambda    : 6.98552e−05
After 12 iterations the fit converged.
final sum of squares of residuals : 0.343896
rel. change during last iteration : −3.81237e−06
degrees of freedom    (FIT_NDF)                        : 73
rms of residuals      (FIT_STDFIT) = sqrt(WSSR/ndf)    : 0.068636
variance of residuals (reduced chisquare) = WSSR/ndf   : 0.0047109
Final set of parameters            Asymptotic Standard Error
=======================            ==========================
h               = 38.8988          +/− 0.4093       (1.052%)
i               = 28.7176          +/− 0.2314       (0.8057%)
j               = −1.8451          +/− 0.04847      (2.627%)
k               = 0.117861         +/− 0.004902     (4.159%)
l               = −0.0046373       +/− 0.0002566    (5.532%)
m               = 9.86864e−05      +/− 6.679e−06    (6.768%)
n               = −8.65719e−07     +/− 6.833e−08    (7.893%)
#Abbreviated
  ti = "38.8987935615+28.7175754188x+\n−1.8451014685x^{2}
+0.1178606612x^{3}+\n−0.0046372990x^{4}+0.0000986864x^{5}+\n−0.0000008657x^{6}"
```

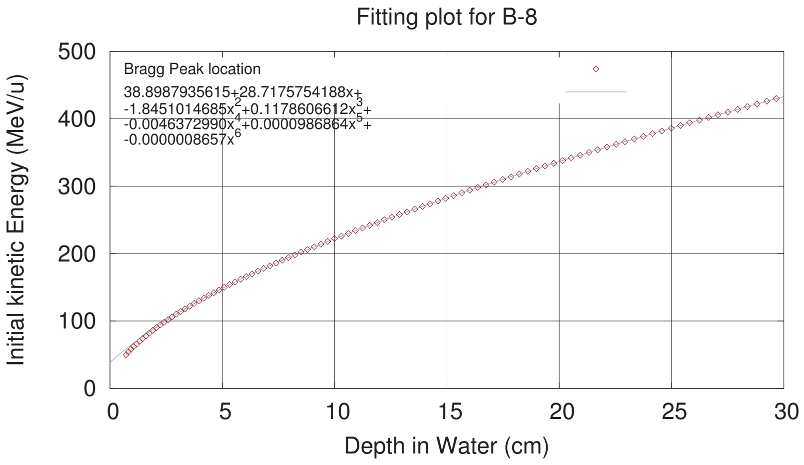

Figure B: *Automatically generated fit plot, with parameters.*

Below 75 MeV/u, the fit diverges. Despite that, the SOBPs that will be generated in this work are all beyond the 2.5 cm ranges in water, where the fit is adequate.

To pass the converged fit parameters to the *Bragg Peak* generator code, another code is required:

Script$_2$

```bash
#!/bin/bash
#Script2
#Write fit parameters to bpgen
cp —r bgen.cpp bpgenx.cpp &&
printf ’\n%s\n’ ’Unlock and apply customization:’
sed —i ’s/\/\/E/    E/g’ bpgenx.cpp &&
p6="$(cut —d’ ’ —f7 < tmp.dat)" &&
echo "${p6}" &&
sed —i ’s/primus6/’${p6}’/g’ bpgenx.cpp &&
p5="$(cut —d’ ’ —f6 < tmp.dat)" &&
echo "${p5}" &&
sed —i ’s/primus5/’${p5}’/g’ bpgenx.cpp &&
p4="$(cut —d’ ’ —f5 < tmp.dat)" &&
echo "${p4}"  &&
sed —i ’s/primus4/’${p4}’/g’ bpgenx.cpp &&
p3="$(cut —d’ ’ —f4 < tmp.dat)"  &&
echo "${p3}"  &&
sed —i ’s/primus3/’${p3}’/g’ bpgenx.cpp &&
p2="$(cut —d’ ’ —f3 < tmp.dat)" &&
echo "${p2}"  &&
sed —i ’s/primus2/’${p2}’/g’ bpgenx.cpp &&
p1="$(cut —d’ ’ —f2 < tmp.dat)"  &&
echo "${p1}"  &&
sed —i ’s/primus1/’${p1}’/g’ bpgenx.cpp &&
p0="$(cut —d’ ’ —f1 < tmp.dat)"  &&
echo "${p0}" &&
sed —i ’s/primus0/’${p0}’/g’ bpgenx.cpp &&
#execute bpgen
g++ bpgenx.cpp —o bpgenx &&
rm —rf tmp.dat &&
make bpgenx &&
./bpgenx
```

Output

```
Append fitting factors to Bragg Peak generator
make: ‘bpgenx’ is up to date.
RSA—Jul2016_3.0—SOBPgen
Choose the letter corresponding to the desired
     irradiation environment;
Basic — FLUKA Calculations with Beam on Water Phantom
     (B)
HIT — Incremented according to Heildelberg’s setup (H)
VOXEL — Voxel instead of water phantom with
     Heildelberg’s setup (V)
Customized — For personalized geometries (P)
P
Introduce the Atomic Mass of the Projectile:
8
And the atomic number:
5
Define the plateau length (cm):
3
Centered at which depth? (cm):
10
Total number of peaks to be generated:
9
  ___________________Z=5,A=8_______________________
|__Field___|_____Energy_(MeV/u)___|___Peak_Z_(cm)___|
|   (0)    |      201.916055      |       8.5       |
|   (1)    |      207.0673879     |       8.875     |
|   (2)    |      212.1372985     |       9.25      |
|   (3)    |      217.131463      |       9.625     |
|   (4)    |      222.0549953     |       10        |
|   (5)    |      226.9124914     |       10.375    |
|   (6)    |      231.7080716     |       10.75     |
|   (7)    |      236.445421      |       11.125    |
|   (8)    |      241.1278292     |       11.5      |
 ____________________________________________________
```

Which results in the database bpgen.cpp. Its output, in text format, contains the energies required for each *Bragg Peak*. These values are then appended to the `source.f`, for HIT–like simulations, in the following manner:

Description

An `executable` hosting folder (`exe`) with three type–files is needed:

1. **Source.f** – `Fortran` routine
2. **Phasespace** – File to be called by `source.f`, containing the phasespace/energy beam parameters.
3. **Makefile** – Typical script to create the executable from the `Fortran` file (using `ldpm3qmd`).

The script$_3$, on the right side, will then multiply the `exe` folders, and:

- Convert the kinetic energies, originally in MeV/u, into GeV for each phasespace file.
- Create different `source.f` routines, from the type–set, with an automatically defined path.
- Fill each phasespace model file, with energies calculated from `bpgen.cpp`
- Compile and create executables.

Script$_3$

```
#!/bin/bash
#Script3
#Introduce Energy values in source.f
printf '\n%s\n\n' 'Set Source.f Energy Parameters'
#Create a file for each energy (at HIT only 16 are used)
cp —r exe exe1; cp —r exe exe2; cp —r exe exe3; cp —r exe
     exe4; cp —r exe exe5; cp —r exe exe6; cp —r exe exe7;
     cp —r exe exe8; cp —r exe exe9; cp —r exe exe10;  cp
     —r exe exe11;  cp —r exe exe12;  cp —r exe exe13;  cp
     —r exe exe14;  cp —r exe exe15 &&
#Convert the energy values from MeV/u to GeV
echo —n "A: "
read A &&
awk '{print ($1*'$A'/1000),$2}' OFMT='%.8E' Energy.dat >
     energy.dat &&
cd exe; sed —i "s@keyword1@$(pwd)@" source.f; cd ..
#Abbreviated
cd exe15; sed —i "s@keyword1@$(pwd)@" source.f; cd ..
s1="$(awk 'NR==1' energy.dat)"; echo "${s1}"; cd exe; sed
     —i "s@keyword2@${s1}@" s4fluka.txt; cd ..
#Abbreviated
s16="$(awk 'NR==16' energy.dat)"; echo "${s16}"; cd exe15;
     sed —i "s@keyword2@${s16}@" s4fluka.txt; cd ..
# Executable makers
cd exe; make clean all; cd ..
#Abbreviated
cd exe15; make clean all; cd ..
```

With the executables created, the inputs can be set with the adequate energies for simulation in a specific geometry, analogous to script$_0$.

Script$_4$

```
#!/bin/bash
#Script4
#Define beam type and identify input
printf '\n%s\n\n' 'Generate and simulate 16 inputs (or other
     number of peaks) with a proper energy/phase space'
echo "Input name: "
read I &&
sed —i "s/HI—PROPE          6.       12./HI—PROPE          $Z.
          $A./g" $I.inp &&
#Deactivate BEAMPOS, use a limit energy and activate source card
sed —i "s/BEAMPOS/SOURCE\n*BEAMPOS/g" $I.inp &&
sed —i "s/keywordE/1000.0  /g" $I.inp &&
sed —i "s/START            1E5/START            1E6/g" $I.inp &&
#Multiply for 16 inputs (unique energies)
cp $I.inp $I—1_aa.inp; cp $I.inp $I—1_ab.inp;
#Abbreviated and run procedure
$NORMAN $RUN —e $CARRASCO/exe/carb1 —N0 —M10 $I—1_aa &&
#Abbreviated } &> /dev/null
$NORMAN $RUN —e $CARRASCO/exe15/carb1 —N0 —M10 $I—1_ap
```

Description

Requisites: An (`HEAVYION`) `FLUKA` input, equivalent* to the one used before.

1. Create the right amount of edited inputs, preparing them to be used with `source.f`.
2. Single input → Unique Energy → One Peak.
3. Run each input coupled with the corresponding executables.

The transport, physics, and geometry parameters should remain identical to those used in the last steps. Otherwise the simulation could lack consistence. The scoring, on the other hand, may be adapted, according to the user needs.

After the simulation, the results for `ENERGY` (or `DOSE`) deposition per primary particle are retrieved at the correct positions of the isoenergetic layer and lie in the base of the SOBP generation.

The last step is the definition of the particle intensity value for each peak, for attaining the right dose magnitude in the SOBP. This is accomplished with:

Script$_5$

Produce an output (`ival.dat`) containing the values of intensity for achieving a SOBP, with a defined dose, and generate 1D plots.

```
#!/bin/bash
#infrascript
g++ infra1.cpp —o infra1 &&
make infra1 &&
./infra1 &&
chmod +x supra.sh &&
./supra.sh &&
Rscript script.r &&
g++ infra2.cpp —o infra2 &&
make infra2 &&
./infra2
gnuplot gnuscript.gp &
```

Script$_6$

Uses the `ival.dat` to produce 1D plots or 2D maps, for different quantities besides Energy Deposition (*e.g.* Annihilation Events at Rest).

```
#!/bin/bash
#ultrascript
g++ ultra.cpp —o ultra &&
make ultra &&
./ultra &&
chmod +x altra.sh &&
./altra.sh &&
gnuplot gnusrbinx.gp &
```

Applying these programs, a plot of the corresponding output is obtained, as well as the number of particles $\mathcal{I}_S$ calculated to achieve the envisaged dose level in the SOBP. The $\mathcal{I}_S$ values are appended to the "`ival.dat`" file.

Provided the correct approximations were used for the beam line elements, the spots initial kinetic energy, *Bragg Peak* positions and number of ions calculated should match those of the research TPS data. An example of that agreement can be appreciated looking into table 5.2. As for the $RI\beta^+$, these could not be compared with the research TPS data but the isoenergetic layers kinetic energy values and number of ions calculated can be seen in table A.

Finally, for a PET simulation, "`ival.dat`" content must be included directly in `START`, for the reconstruction requires every particle history to be included so that the coincidences can be properly recorded. In fact, it requires not only the appropriate number of histories, these also need to be independent which hinders the use of biasing techniques. Such constraint, result in a big `CPU` burden and prevents the routine application of this method in clinical workflow.

`ultra.cpp.` Program to plot the SOBP data from the `USRBIN`.

```
#include<stdio.h>
#include<stdlib.h>
#include<math.h>
#include<iostream>
#include<iomanip>
#include<string>
#include<fstream>
#define _USE_MATH_DEFINES
using namespace std;
int main(int argc, char *argv[]){int a,i,x,y,w,z;string u,v,col,tit;char log;char dim;char nome[50];
    cout << "\nRSA−Aug2015−ultra.cpp\n"<< endl;
    cout << "SOBP Annihillation Map USRBIN plot generator"<< endl;
    cout << "Choose 1 for an 1D USRBIN or 2 for a 2D USRBIN"<< endl;
```

```
    cin >> dim;
    if(dim=='2'){
  cout << "\nNumber of Pristine Peaks in the SOBP:" << endl;
    cin >> a;
    cout << "Common file name: " << endl;
    cin >> nome;
    ofstream fout;
    fout.open("altra.sh", std::ios::app);
      fout << "#!/bin/bash\n"<<"# altrascript\n\n"<<"paste ";
    x = 1;
    y = 2;
      for(i=1;i<=a;i++){fout << nome << setfill('0') << setw(2) << i <<".dat ";}
    fout << " | awk \'{print ";
    fout << "$" << x << ", $" << y;
     for(i=1;i<a;i++){z = 4*i - 1;
      fout <<", $" << z;}
        w= 4*a - 1;
     fout << ", $" << w << "}\' > totalbin.dat \n\n";
    fout.close ();
    float l, h;
    char eps[20];
    cout << "Minimum value in color scale:" << endl;
    cin >> l;
    cout << "Maximum value in color scale:" << endl;
    cin >> h;
    cout << "Name of the output file:" << endl;
    cin >> eps;
    fout.open("gnusrbinx.gp", std::ios::app);
    fout <<"#!/usr/bin/gnuplot"<<endl;
    fout <<"set terminal postscript eps enhanced color\nset output \""<<eps<<".eps\"\nset title
         ''\nunset grid\nset xlabel 'Z (cm)'\nset xtics\nset ylabel 'X (cm)'\nset ytics\nset cblabel
         ''\nset cbtics\nunset logscale x\nunset logscale y\nunset logscale z\nset logscale cb\nset
         cbrange ["<<l<<":"<<h<<"]\nunset logscale x2\nunset logscale y2\nset size ratio 1\nset key
         default\nset style line 1 lt -1 lw 1\nset cbrange ["<<l<<":"<<h<<"]\nset colorbox vertical\nset
         pm3d map explicit corners2color c1\nset palette defined (0  0.0 0.0 0.5,1  0.0 0.0 1.0,2  0.0
         0.5 1.0,3  0.0 1.0 1.0,4  0.5 1.0 0.5,5  1.0 1.0 0.0,6  1.0 0.5 0.0,7  1.0 0.0 0.0,8  0.5 0.0
         0.0 )\nset palette maxcolors 200\nset logscale cb"<< endl;
    fout <<"splot 'totalbin.dat' us 1:2:(";
        for (int i=3; i<2+a; i++){
        fout<<"($"<<i<<")*";
        const int LINE_TO_FIND = i-2;
        string line;
        ifstream f( "ival.dat" );
        for (int k=0; k<LINE_TO_FIND;k++){
        getline(f,line);}
        fout<< line<<"+";};
        int q = a + 2;
        fout<<"($"<<q<<")*";
        const int LINE_TO_FIND = a;
        string line;
        ifstream f( "ival.dat" );
        for (int k=0; k<LINE_TO_FIND;k++){
        getline(f,line);}
        fout<< line <<") w image notitle " << endl;
    fout.close ();
    fout.open("ultra.sh", std::ios::app);
    fout <<"epstopdf "<<eps<<".eps &&"<<endl;
    fout <<"gnome-open "<<eps<<".pdf &&"<<endl;
    fout <<"sed -n '1,9p' ultra.sh > ultra.sh.tmp &&"<<endl;
    fout <<"cp ultra.sh.tmp ultra.sh &&"<<endl;
    fout <<"rm -rf ultra.sh.tmp"<<endl;
    fout.close ();}
    else if(dim=='1'){cout << "\nNumber of Pristine Peaks in the SOBP:" << endl;
    cin >> a;
    cout << "Common file name: " << endl;
    cin >> nome;
    ofstream fout;
    fout.open("altra.sh", std::ios::app);
      fout << "#!/bin/bash\n"<<"# altrascript\n\n"<<"paste ";
    x = 1;
    y = 2;
      for(i=1;i<=a;i++){fout << nome << setfill('0') << setw(2) << i <<".dat ";}
    fout << " | awk \'{print ";
    fout << "$" << x << ", $" << y;
     for(i=1;i<a;i++){z = 4*i - 1;
      fout <<", $" << z;}
        w= 4*a - 1;
     fout << ", $" << w << "}\' > totalbin.dat \n\n" << "tail -n+2 totalbin.dat > bin.dat \n\n";;
    fout.close ();
    char eps[20];
    cout << "Horizontal limits separated by:" << endl;
    cin >> u;
  cout << "Vertical limits separated by:" << endl;
    cin >> v;
  cout << "Please select the gnuplot color, wisely..." << endl;
    cin >> col;
  cout << "...and the inplot title (in quotes)" << endl;
    cin >> tit;
  cout << "Log scale y? (y or n)" << endl;
    cin >> log;
    cout << "Name of the output file:" << endl;
    cin >> eps;
```

```
    fout.open("gnusrbinx.gp", std::ios::app);
    fout <<"#!/usr/bin/gnuplot"<<endl;
    fout<<"set terminal postscript eps enhanced color size 4, 4 font 'Helvetica,16' solid lw 1"<<"\nset
         output \""<<eps<<".eps\"\nset grid"<<"\nset yrange["<<v<<"]"<<"\nset xrange["<<u<<"]\nset
         xlabel 'Depth in water (cm)'\nset ylabel 'DAP (Gy.cm^2)'";
    if(log=='y'){fout<<"\nset log y\n";}
    else fout<<"\n";
    fout <<"plot 'bin.dat' us 1:(";
        for (int i=3; i<2+a; i++){fout<<"($"<<i<<")*";
        const int LINE_TO_FIND = i-2;
        string line;
        ifstream f( "ival.dat" );
        for (int k=0; k<LINE_TO_FIND;k++){getline(f,line);}
        fout<< line<<"+";};
        int q = a + 2;
        fout<<"($"<<q<<")*";
        const int LINE_TO_FIND = a;
        string line;
        ifstream f( "ival.dat" );
        for (int k=0; k<LINE_TO_FIND;k++){getline(f,line);}
        fout<< line <<") w steps lw 1 lc rgb '"<< col <<"' title " << tit << endl;
      fout.close ();
    fout.open("ultra.sh", std::ios::app);
    fout <<"epstopdf "<<eps<<".eps &&"<<endl;
    fout <<"gnome-open "<<eps<<".pdf &&"<<endl;
    fout <<"sed -n '1,9p' ultra.sh > ultra.sh.tmp &&"<<endl;
    fout <<"cp ultra.sh.tmp ultra.sh &&"<<endl;
    fout <<"rm -rf ultra.sh.tmp"<<endl;
    fout.close ();}
 else{cout << "HAL 9000: Are you sure you're making the right decision? I think we should stop."<< endl;}
return 0;}
```

For the three geometries analyzed in the present work, and nine ion species, the program `bpgen.cpp` generates energy values to create SOBPs based on FLUKA simulations with different characteristics. Also, for a customized geometry, and provided enough simulated results (within the desired energy range) are provided, the code can deliver fitted data to create the SOBP. An example of the calculated polynomial expressions can be appreciated in the next page, while a visual representation is provided in figure C.

As mentioned already in chapter 3, if the phantom is very heterogeneous over the lateral integration limits the number of ions calculated will not converge correctly and other approaches should be used, such as the evolutionary algorithms refered to in chapter 5.

Example of the list of polynomial fit expressions (E vs z) for the basic scenario without beam line elements, as applied in `bpgen.cpp`, with the respective curves plotted below in figure C.

$$
\begin{aligned}
\mathrm{E}_{\text{B-8}} &= -8.657 \times 10^{-7} z^6 + 9.869 \times 10^{-5} z^5 - 4.637 \times 10^{-3} z^4 + 0.1178606612 z^3 - 1.8451014685 z^2 + 28.7175754188 z + 38.8987935615 \\
\mathrm{E}_{\text{C-9}} &= -1.827 \times 10^{-6} z^6 + 1.813 \times 10^{-4} z^5 - 7.492 \times 10^{-3} z^4 + 0.1692761372 z^3 - 2.3847886850 z^2 + 34.2141873721 z + 42.6552189447 \\
\mathrm{E}_{\text{C-10}} &= -1.279 \times 10^{-6} z^6 + 1.367 \times 10^{-4} z^5 - 6.041 \times 10^{-3} z^4 + 0.1449100813 z^3 - 2.1470493289 z^2 + 31.8644522456 z + 40.7708279408 \\
\mathrm{E}_{\text{C-11}} &= -7.885 \times 10^{-7} z^6 + 9.130 \times 10^{-5} z^5 - 4.371 \times 10^{-3} z^4 + 0.1134971616 z^3 - 1.8199914643 z^2 + 29.1918996333 z + 40.4020030546 \\
\mathrm{E}_{\text{C-12}} &= -7.794 \times 10^{-7} z^6 + 9.059 \times 10^{-5} z^5 - 4.340 \times 10^{-3} z^4 + 0.1122961392 z^3 - 1.7851777584 z^2 + 28.0422709316 z + 38.0560267087 \\
\mathrm{E}_{\text{N-13}} &= -1.353 \times 10^{-6} z^6 + 1.417 \times 10^{-4} z^5 - 6.166 \times 10^{-3} z^4 + 0.1465320143 z^3 - 2.1669027062 z^2 + 32.5225003906 z + 42.2542439773 \\
\mathrm{E}_{\text{O-15}} &= -2.640 \times 10^{-6} z^6 + 2.455 \times 10^{-4} z^5 - 9.515 \times 10^{-3} z^4 + 0.2020229257 z^3 - 2.6810657257 z^2 + 36.3976655724 z + 42.9209091957 \\
\mathrm{E}_{\text{O-16}} &= -2.173 \times 10^{-6} z^6 + 2.087 \times 10^{-4} z^5 - 8.329 \times 10^{-3} z^4 + 0.1817978994 z^3 - 2.4797973045 z^2 + 34.6060088414 z + 42.2527126903 \\
\mathrm{E}_{\text{F-17}} &= -4.429 \times 10^{-6} z^6 + 3.755 \times 10^{-4} z^5 - 1.328 \times 10^{-2} z^4 + 0.2581423299 z^3 - 3.1516142483 z^2 + 39.8534582220 z + 44.1860760712
\end{aligned}
$$

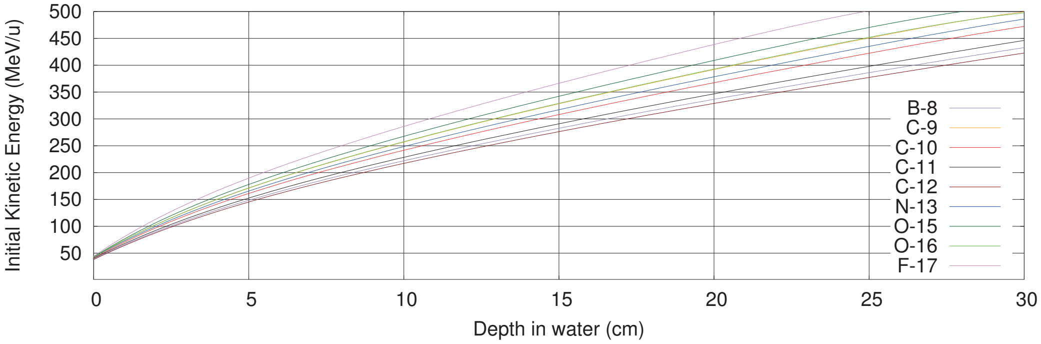

Figure C: *Polynomial expressions plotted for the different ions, without beam line elements.*

Table A: *SOBP data simulated with approximated HIT beam line elements, using RIβ^+ only:*
E – Energy [MeV/u]; $\mathcal{I}_S$ – Number of ions delivered per energy layer [$\times 10^6$ ions].

Layer	^{8}B		^{9}C		^{10}C		^{11}C		^{13}N		^{15}O		^{17}F	
#	E	$\mathcal{I}_S$	E	$\mathcal{I}_S$	E	$\mathcal{I}_S$	E	$\mathcal{I}_S$	E	$\mathcal{I}_S$	E	$\mathcal{I}_S$	E	$\mathcal{I}_S$
1	209.78	38.578	242.60	29.949	228.26	28.454	215.89	27.423	234.77	21.883	252.76	18.111	270.08	15.443
2	212.46	9.926	245.75	7.862	231.20	7.319	218.66	7.065	237.80	5.739	256.05	4.648	273.61	3.806
3	215.12	34.490	248.86	26.769	234.12	25.377	221.40	24.360	240.81	19.246	259.31	16.123	277.12	13.704
4	217.76	17.954	251.96	14.174	237.01	13.070	224.13	12.473	243.79	10.254	262.55	8.120	280.61	6.701
5	220.38	33.858	255.03	25.853	239.88	24.792	226.83	23.646	246.76	18.557	265.77	15.474	284.07	13.289
6	222.98	24.483	258.09	19.496	242.74	17.918	229.52	17.299	249.70	13.779	268.96	11.085	287.51	9.266
7	225.57	35.790	261.12	27.229	245.57	26.040	232.18	24.617	252.62	19.319	272.14	16.178	290.93	13.862
8	228.13	31.227	264.13	24.964	248.38	22.978	234.83	21.855	255.52	17.476	275.29	14.181	294.32	11.817
9	230.68	40.204	267.12	30.593	251.18	29.028	237.46	27.651	258.40	21.486	278.42	17.929	297.70	15.568
10	233.21	39.413	270.10	31.302	253.96	28.986	240.07	27.046	261.26	21.806	281.54	17.813	301.05	15.068
11	235.72	47.797	273.05	37.114	256.72	35.181	242.66	33.294	264.11	25.891	284.63	21.384	304.38	18.622
12	238.22	52.332	275.99	40.790	259.46	38.273	245.24	36.034	266.94	28.472	287.71	23.324	307.70	19.830
13	240.70	63.301	278.91	49.637	262.19	47.133	247.81	44.539	269.75	34.892	290.76	28.493	310.99	24.812
14	243.17	77.221	281.81	60.623	264.90	57.401	250.35	54.556	272.54	42.637	293.80	35.058	314.27	29.781
15	245.63	102.85	284.70	83.152	267.59	80.218	252.89	77.768	275.32	61.010	296.83	49.456	317.52	41.133
16	248.07	270.85	287.57	204.55	270.27	200.58	255.41	190.83	278.08	145.65	299.83	118.86	320.76	99.193
Total		920.27		714.06		682.75		650.46		508.10		416.24		351.90
1	271.76	44.890	315.47	35.599	296.31	32.182	279.87	31.240	304.95	26.040	329.04	21.613	352.26	18.775
2	274.06	11.769	318.18	8.887	298.85	9.455	282.25	8.378	307.56	6.297	331.88	5.629	355.33	5.080
3	276.36	40.815	320.88	31.101	301.37	28.399	284.62	27.761	310.17	23.135	334.71	19.136	358.38	16.434
4	278.64	19.782	323.57	16.625	303.88	15.934	286.98	14.458	312.76	11.245	337.53	9.766	361.42	8.660
5	280.91	40.452	326.25	30.390	306.38	28.225	289.32	27.200	315.34	22.180	340.33	18.440	364.45	15.809
6	283.18	27.793	328.92	22.578	308.87	20.753	291.66	19.213	317.91	15.386	343.12	13.228	367.46	11.435
7	285.43	42.201	331.57	32.620	311.35	29.796	293.99	28.675	320.47	23.017	345.90	18.840	370.46	16.531
8	287.67	35.560	334.22	28.144	313.82	26.893	296.31	24.717	323.02	19.641	348.67	16.642	373.45	14.378
9	289.90	47.374	336.85	36.783	316.27	33.556	298.61	31.637	325.56	25.555	351.43	21.043	376.43	18.218
10	292.13	45.748	339.47	35.968	318.72	33.906	300.91	31.599	328.09	24.721	354.18	20.535	379.40	18.218
11	294.34	56.002	342.08	43.476	321.16	41.007	303.20	38.564	330.60	30.526	356.91	24.986	382.35	22.085
12	296.55	60.853	344.68	47.466	323.58	44.620	305.48	42.250	333.11	32.952	359.64	27.161	385.29	24.003
13	298.74	73.120	347.27	57.413	326.00	55.745	307.74	52.018	335.61	40.982	362.35	33.642	388.22	29.137
14	300.93	91.038	349.85	70.209	328.40	67.633	310.00	64.594	338.10	49.513	365.05	41.095	391.15	35.959
15	303.11	110.10	352.42	89.136	330.80	89.479	312.25	84.758	340.57	68.826	367.75	55.143	394.06	48.509
16	305.27	339.03	354.98	258.47	333.19	250.31	314.50	243.15	343.04	182.58	370.43	150.76	396.96	122.29
Total		1086.5		844.87		807.89		770.21		602.60		497.66		425.52
1	326.51	54.927	380.10	43.043	356.58	39.194	336.45	36.004	367.23	30.802	396.81	25.403	425.43	23.103
2	328.59	9.723	382.57	8.351	358.87	8.557	338.60	9.515	369.61	7.187	399.40	7.283	428.23	6.449
3	330.67	51.703	385.03	39.661	361.16	34.855	340.74	32.227	371.97	27.307	401.99	22.146	431.01	20.073
4	332.73	20.301	387.48	16.484	363.44	16.457	342.88	15.777	374.33	12.730	404.57	12.291	433.79	10.674
5	334.79	50.277	389.93	38.542	365.71	33.517	345.01	31.670	376.68	26.092	407.14	21.267	436.56	19.388
6	336.85	29.638	392.37	23.779	367.98	23.755	347.13	21.715	379.02	17.506	409.71	16.356	439.31	14.003
7	338.89	52.739	394.80	40.431	370.23	34.962	349.25	33.503	381.36	27.148	412.27	22.086	442.06	20.615
8	340.93	39.367	397.23	31.743	372.49	30.731	351.36	28.472	383.69	22.287	414.82	19.587	444.79	17.382
9	342.97	57.490	399.64	44.701	374.73	40.463	353.46	37.865	386.01	30.071	417.36	24.702	447.51	22.790
10	345.00	51.792	402.06	40.564	376.97	38.602	355.56	36.602	388.33	29.475	419.90	24.527	450.22	21.783
11	347.02	67.342	404.46	52.995	379.20	49.965	357.64	45.489	390.63	35.761	422.43	31.218	452.92	26.914
12	349.03	69.502	406.86	55.085	381.42	51.158	359.73	50.268	392.93	39.659	424.95	31.379	455.60	28.402
13	351.04	87.284	409.26	68.216	383.64	65.300	361.80	60.996	395.23	47.457	427.46	41.573	458.27	35.240
14	353.05	105.28	411.65	83.007	385.86	81.268	363.88	77.867	397.52	59.177	429.97	48.988	460.92	42.168
15	355.05	115.54	414.03	97.405	388.06	96.104	365.94	95.806	399.80	74.171	432.46	65.198	463.55	55.758
16	357.04	424.78	416.40	321.80	390.27	317.35	368.00	301.83	402.08	232.87	434.95	187.53	466.17	152.44
Total		1287.7		1005.8		962.24		915.61		719.70		601.53		517.18

Appendix B

PET implementation description

The *Siemens Biograph* mCT PET/CT is a CE-labelled model regarded as having a high sensitivity, making use of thick LSO crystals and an extended axial FOV. The scanner parameters are described below in table B.

Table B: *Siemens Biograph mCT PET device general parameters*[Jak11, STP08].

Patented PET Detector Assembly	Biograph (`TrueV`)
Detector Material	LSO
Crystal Dimensions	0.4×0.4×2 (cm)
Crystals per detector block	169 (1×13×13)
Number of detector blocks	192 (48×4)
Photomultiplier tubes	4 per block
Detector ring radius	42.1 cm
Detectors per ring	624 (48×13)
Number of detector rings	52 (4×13)
Total number of detectors	32448 (1×13×13×48×4)
Transaxial `FOV`	60.5 cm
Axial `FOV`	21.6 cm
Number of image planes	109 (52 crystals + 3 artificial)×2–1
Plane spacing	2 mm
PET Data Acquisition/Processing	Biograph (`TrueV`)
Coincidence time resolution	500 ps
Coincidence window	4.5 ns

Its scintillator material is characterized by a relatively high light output, effective Z, and density. In spite of that, LSO crystals are a (known) additional source of background, affecting the quality of reconstructed images, an effect mitigated by both the increased counts and corrective factors in reconstruction algorithms. In validation studies, to certify the models' performance, a source of noise could be applied (*e.g.* simulating a ^{176}Lu source) to model the background[Poo15]. This approach was not followed, as it was not deemed necessary for the goal of this work which focused in the comparison among the signals induced by different ion species.

The PET scanner structural elements, in the different stages of the construction process, are illustrated in the next page as seen in *flair*. The unitary element is the scintillation crystal detector, which is the pixel of the scanner. An array of whose makes up a block, which in turn can be grouped into a module. The latter being the basic blocks of a scanner ring. The spacing between elements can be defined by the user, and additional layers of crystals can be placed radially as well. All these elements are inserted in a cylindrical geometry R, Z, θ, radial, transaxial and axial, simplifying the construction procedure.

Manipulating these values an user can create different PET models, whose function can then be replicated in FLUKA. The scanner can also be shifted/rotated and even "opened" ($0° < \theta_{\texttt{open}} < 180°$). This latter procedure can also be accomplished by the user manually, removing the modules accordingly, leaving the ring incomplete. Additional elements (*e.g.* shielding) can then be placed manually as well[Ort13, Ort14].

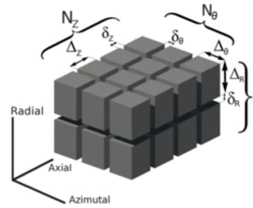

Number of Crystals per block [N$_{(R,Z,\theta)}$] - 1, 13, 13 (52)

Crystal dimension in cm [$\Delta_{(R,Z,\theta)}$] - 2, 0.4, 0.4

Crystal separation in cm [$\delta_{(R,Z,\theta)}$] - 0, 0.01666, 0.01666

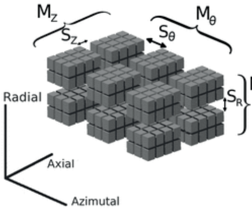

Number of radial crystal blocks [M$_{(R,Z,\theta)}$] - 1, 4 (1), 1

Radial separation between crystal blocks [S$_{(R,Z,\theta)}$] - 0, 0, 0

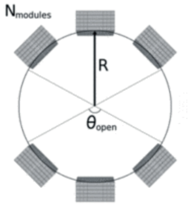

Number of Modules - 48

Ring radius (in cm) - 42.1

After collecting the data, special reconstruction algorithms must be applied to extract the data in an image, the original data can be in a 2D or 3D form, the latter typically formed by 2D grouped projections as a *Michelogram* representation mentioned in chapter 3. A 3D *sinogram* can be characterized by sets of bins corresponding to unique segments and axial position. Without axial compression, it would simply come as LORs either for a detector ring (direct) or different rings (oblique). In a scanner of n detector rings there will be a total $n \times n$ *sinograms*, n direct and $(n \times n) - n$ oblique[Fah02].

The ring difference (axial direction) will describe the distance between two rings associated to a *sinogram.* A sinogram binning will then consist of LORs binned into a block matrix with index dimensions in R, Z, θ directions. In the following nomenclature in post processing, these will be referred as x, y, z or radial, transaxial and axial. The postprocessing parameters can be seen throughout table C.

Table C: *Siemens Biograph mCT PET device post–processing parameters*[Jak11]

Feature (dimensions in cm, time in ns)	Value
Number of ring steps (segments of the ring)	48
Number of blocks per ring step (block line in y, z)	1, 1
Ring radius & field of view	42.1, 21.6
Number of crystals per block in x,y,z directions	1, 13, 55 (*de facto* 52)
Crystal dimension inside the block (z-axial, y-transaxial, x-radial)	y = 0.4, z = 0.4
Separation between adjacent crystals, in x, y, z directions	y = 0.005, z = 0.005
Arc correction	On
Maximum ring difference	109 (includes artificial)
Number of segments	9
Axial span number	11
Angular sinogram mashing	Off
Time coincidence window for coincidence pairs	4.1
Coincidence dead time	500

Postprocessing parameters

```
*# Parameters for BIO
*# Number of ring steps (segments of the ring)
     NMODUL = 48
*# Number of blocks per ring step (block line in y,z)
     NYBLOC = 1
     NZBLOC = 1
*# Radio and field of view of the ring
     RADFOV = 42.10000
     ZZZFOV = 21.6
*# Number of crystals per block in x,y,z directions
     NXCRYS = 1
     NYCRYS = 13
     NZCRYS = 52
*# Dimensions of cristals inside the block (z = axial, y =
      transaxial, x = radial) in cm
     YYYCRY = 0.400000
     ZZZCRY = 0.400000
*# Separation between adjacent crystals in x,y,z directions in
      cm
     YSEPCR = 0.005000
     ZSEPCR = 0.005000
*# Arc correction (on = 1, off = 0)
     NUMARC = 1
*# Maximum Ring Difference (Default = rings—1)
     MAXRDF = 109
*# Number of segments (Default = 2*rings—1)
     NSEGMN = 9
*# Axial span number (Default = 1 (off))
     NMSPAN = 11
*# Angular sinogram mashing (Default = 0 (off))
     NMMASH = 0
*# Output file unit number (positive ascii, negative binary)
     LUNPET = 41
*# Time coincidence window for coincidence pairs [ns]
     TCWPET = 4.5
*# Coincidence dead—time [ns] (don't confuse with the singles
      dead—time)
*    If > 0 : Non—paralyzable dead time
*             The new dead—time period is the one of the old hit
*    If < 0 : Paralyzable dead time
*             The dead—time is restarted, the new one is the
*             old hit DT plus the DT of the new hit
     DTMPET = 100.0
```

Required FLUKA input cards

**...+....1....+....2....+....3....+....4....+....5....+....6....+....7....+....*

Initialization card for PET parameters:
#1 : Minimum region number of PET crystals
#2 : Minimum lattice number of PET crystals
#3 : Number of modules per ring
#4 : Number of crystals per module in `X` direction
#5 : Number of crystals per module in `Y` direction
#6 : Number of crystals per module in `Z` direction

```
 USRICALL    PET00000    1.    48.      1.    13.  52.
DIMEN
```

Initialization card for PET parameters:
#1: Output unit (negative for binary, positive for `ASCII`)
#2: E_{window} (set as E_{0-dw}, E_{0+dw} with E_0=511 keV) [GeV]
#3: E_{window} (set as E_{0-dw}, E_{0+dw} with E_0=511 keV) [GeV]
#4: Minimum acquisition time [s]
#5: Maximum acquisition time [s]
#6: Time resolution of the detector [ns]

```
 USRICALL    41.      4.35E-04   6.5E-04    0.    1E+99
.14 SCORE
```

1: Pulse time of the detector [ns]
2: Dead time of the detector [ns] (positive: Non-paralyzable, negative: paralyzable, 0: not considered[default])

```
 USRICALL    50.      500.             SCORE2
```

Call user routine `mgdraw.f` to dump info about energy deposition and time

```
 USERDUMP    100.      40.    0.0    1.            hits
```

Arc correction can be applied to account for the effect of the shape of the scanner to the radial bin size. *Maximum ring difference* describes the range of rings that will participate in the generation of

LORs. *Span* and *Mashing factor* refer to the reduction of axial and angular sampling, respectively. *Segment number* option will affect the number of segments *de facto* used in the 3D reconstruction.

Additionally, in the post processing folder of the PET routines, the *Michelogram* dimensions in `(IFLHDR)` must be tuned according to the PET scanner model employed. For the PET *Biograph mCT*, the optimal parameters considered were:

- `MAXSGM: 9`
- `MAXRNG: 109`
- `MAXCRI: 416`

Where `MAXSEG`, `MAXRNG` and `MAXCRI` are the maximum number of segments, rings and crystals to be taken into account in the *Michelogram*, respectively.

USERDUMP. Processing script for beam–time structure and PET acquisition time (modified)

```bash
#!/bin/bash
#Code was cutted for USERDUMP1 only...for presentation reasons
#Cutting header
tail -n+3 *aa001_fort.41 > filtaay &&
#Printing the time and Parent isotope data
awk '{print $1 " " $12 " " $17}' filtaay > filtaaw &&
#Controlled Random Number generation...
awk '{print $1}' filtaaw > tmp1 &&
#Preserve random number correlation with ID
awk '{ tempo=$1/('$(awk 'END{print}' tmp1)'+'$(awk 'NR==1' tmp1)') ; printf"%0.1E\n",
    tempo }' tmp1 > rand1 &&
#Take out the garbage
rm -rf tmp* &&
#Join Random numbers and Times in the same file , for the subsequent operation
cut -f2 filtaaw >> tmp &&
cut -f1 rand1 | paste tmp - >> filtaax &&
rm -rf tmp rand1 &&
#take out the garbage
rm -rf filta*w &&
#Apply Beam time Structure...Note to self...carbon =/= oxygen
awk '{printf("%i %1.19E %1.19E \n",$1,$2,$3)}' filtaax > filtaaz &&
#Join the correct times to the main data list
paste filtaay filtaaz > filtaav &&
#Take garbage out
rm -rf filta*z &&
rm -rf filta*y &&
rm -rf filta*x &&
#Create data sets in original format with correct beam time structures
awk '{printf("%13s%13s%13s%13s%8s%8s%8s%8s%32s%32s%32s%32s%32s%32s%32s%32s%32s%32s%32s
%10s%10s\n",$1,$2,$3,$4,$5,$6,$7,$8,$9,$10,$11,$23,$13,$14,$15,$16,$24,
$18,$19,$20,$21)}'filtaav>filtaau &&
#Create new single file for the filtering by PET acquisition times
sed -n '1,2p' Carbonized-1_aa001_fort.41 > Carbonized-1_aa001_fort.42 &&
awk '$12 >= 4.3E11 { print $0 }' filtaau > tmp &&
awk '$12 <= 1.93E12 { print $0 }' tmp >> Carbonized-1_aa001_fort.42 &&
rm -rf tmp &&
#Take garbage out
rm -rf filta*v &&
rm -rf filta*u
```

Appendix C

Effect of reversing SOBP layers

The layer delivery sequence from the lowest to the highest energy penalizes online PET acquisitions since the most energetic isoenergetic layers compose the vast majority of the total beam particles delivered ($\sim 30\%$ of which in the last layer). Consequently, the signal acquired from β^+ emitters generated within the online PET acquisition time could be in theory improved if the beam delivery sequence is inverted, since the effect of *biological washout* is not being accounted for in this work. In this way, the contribution from the signal induced by the more relevant isoenergetic layers will be taken into account for the reconstruction.

In order to evaluate the effect that a reverted sequence would have in the online PET signal acquisition the total event output previously obtained was reprocessed using the scripts developed in this work, but with an inverse SOBP order, the resulting plot can be seen in figure D. The total PET acquisition time was kept as 130 s and the intensity value of each isoenergetic layer was also preserved.

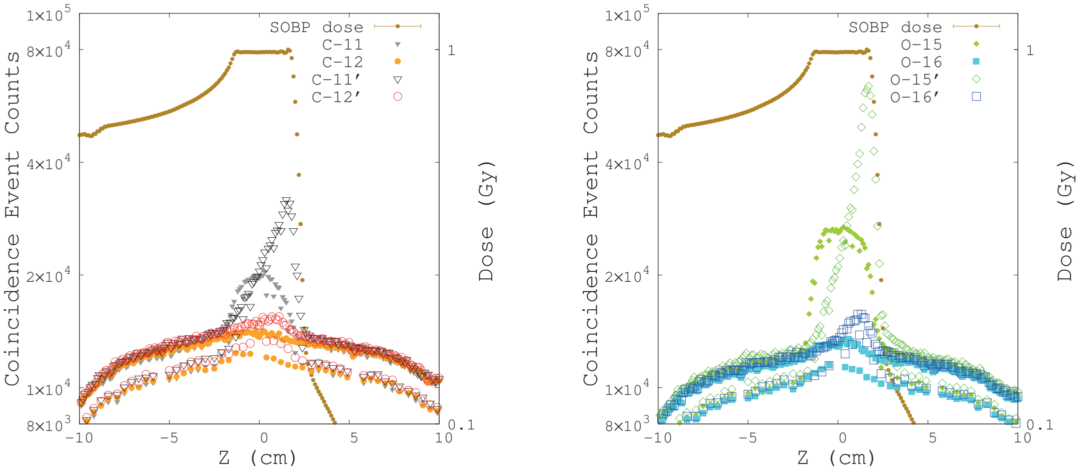

(a) carbon ions

(b) oxygens ions

Figure D: *Comparison between online PET signal acquisition obtained from SOBPs with a reverted and "standard" energy layer delivery order. The counts pertaining the reverted SOBPs correspond to open symbols and appear primed in the legend.*

The improvement verified with $RI\beta^+$ can be ascribed to an increase in acquired signal from additional isotope decays, namely ^{15}O in the case of ^{15}O ion beam and ^{11}C and ^{10}C in the case of ^{11}C ion irradiation, as shown in table D.

Table D: *Coincidence events filtered by parent isotope in the online PET acquisition with a reverted SOBP, and respective variation with respect to the values previously reported in table 5.5 (in italics).*

Acquisition	Ion beam	^{8}B	^{9}C	^{10}C	^{11}C	^{12}N	^{13}N	^{13}O	^{14}O	^{15}O
Online	^{11}C	34403	8413	158484	148409	3212	2450	485	3368	77123
	^{12}C	19840	3297	27202	18341	4225	2326	376	3037	72412
	^{15}O	22285	5854	31293	9498	8345	8163	2863	34019	670745
	^{16}O	15888	2917	18619	8682	3903	3028	743	5414	99769
Variation	^{11}C	*+106*	*+5*	*+55578*	*+73253*	*+2*	*+1442*	*0*	*+1739*	*+42924*
	^{12}C	*+55*	*+4*	*+10213*	*+10404*	*+2*	*+1356*	*-2*	*+1115*	*+40671*
	^{15}O	*-23*	*+3*	*+8337*	*+4642*	*+18*	*+3690*	*+3*	*+13271*	*+246009*
	^{16}O	*-10*	*+54*	*+5144*	*+4320*	*+8*	*+1429*	*0*	*+2353*	*+45297*

Applying the same methodology used in table 5.6, one can observe a substantial improvement in online range verification when the SOBP order is reverted, as displayed in table E. In fact, while the stable ion beams results are still affected by the background noise, the $RI\beta^+$ maximum lies within ∼ 1 mm of the distal edge of the SOBP. Particularly, ^{15}O $\Delta W50\%$ and distal fall off values are comparable to the *offline PET* coincidence event counts results observed in table 5.6, but with a fraction of the acquisition time only.

Table E: *Characterization of coincidence event counts and the SOBP dose profile in an online PET acquisition scenario with a standard and a reversed SOBP.*

Dataset	Characteristic	^{11}C	^{12}C	^{15}O	^{16}O
Dose SOBP	Ions delivered	6.93×10^{8}	6.61×10^{8}	4.44×10^{8}	4.31×10^{8}
	Proximal edge [cm]	8.71 ± 0.1	8.72 ± 0.1	8.70 ± 0.1	8.80 ± 0.1
	Distal edge [cm]	11.63 ± 0.1	11.63 ± 0.1	11.64 ± 0.1	11.63 ± 0.1
Online (standard)					
Coincidence event counts (PET)	max. value	20407	16301†	26823	14492†
	max. position [cm]	10.3 ± 0.1	$20.7 \pm 0.1^{\dagger}$	10.3 ± 0.1	$20.7 \pm 0.1^{\dagger}$
	ΔW90% [cm]	2.3 ± 0.1	—	2.3 ± 0.1	—
	ΔW50% [cm]	16.3 ± 0.1	—	4.1 ± 0.1	—
	Distal fall–off [mm]	97 ± 1	—	91 ± 1	—
Online (reversed)					
Coincidence event counts (PET)	max. value	31795	16444†	63880	15704
	max. position [cm]	11.5 ± 0.1	$20.7 \pm 0.1^{\dagger}$	11.7 ± 0.1	11.1 ± 0.1
	ΔW90% [cm]	0.7 ± 0.1	—	0.5 ± 0.1	—
	ΔW50% [cm]	3.2 ± 0.1	—	1.7 ± 0.1	—
	Distal fall–off [mm]	88 ± 1	—	10 ± 1	—

† Inconclusive due to the high background level.

Appendix D

Magnetic Rigidity

A secondary beam, such as in HIMAC, is subject to contamination with different fragments upon extraction. These follow the same curvature of the deflected beam, as the magnetic field acts on the ions, an effect that is characterized by a unique value of the magnetic Rigidity (maximum of 8.13 [Tm] for the secondary beam line),

$$B\rho = \frac{p}{q} \quad [\mathrm{Tm}] \tag{1}$$

Where B is the magnetic field, p the momentum [kg m s^{-1}], q the charge [C], and ρ the gyroradius [m]. Different combinations of ion energy, mass and charge may then result in similar magnetic rigidities, ultimately leading to the presence of "impurities" in the extracted beam.

Even though the overall experimental impurity levels are very low for both ^{11}C and ^{15}O beams, their impact on the "fragmentation tail dose" after the *Bragg Peak*, could still be of relevance, hence the need to characterize these fragments.

Firstly, to identify these fragments the combinations of mass, charge and energy that lead to equivalent gyroradius value must be found, as the magnetic field is constant. However, it should be noted that, at hadrontherapy energies, relativistic effects need to be accounted for. Thus, defining the kinetic Energy (T) as

$$E = T + m_0c^2 = \sqrt{p^2c^2 + m_p^2c^4}, \tag{2}$$

where m_0 is the rest mass and m_p the mass of the projectile. Since p is related to E by

$$E^2 = p^2c^2 + (m_0c^2)^2 \Leftrightarrow p = \sqrt{\frac{E^2 - (m_0c^2)^2}{c^2}}.$$

Inserting E from equation 2, in the above expression, it follows that

$$p = \sqrt{\frac{(T + m_0c^2)^2 - (m_0c^2)^2}{c^2}} \Leftrightarrow p = \frac{1}{c}\sqrt{T^2 + 2Tm_0c^2}$$

Substituting in equation 1, it leads to

$$B\rho = \frac{1}{qc}\sqrt{T^2 + 2Tm_0c^2}. \tag{3}$$

As $B\rho$ will be used as a constant term, the following manipulation can be applied:

$$(B\rho)^2 = \frac{T^2 + 2Tm_0c^2}{q^2c^2}.$$

Simplifying using; [p] ≡ [MeV/c] [T] ≡ [MeV/u] [m] ≡ [MeV/c^2].

In order to compute more easily the above mentioned equation, the atomic mass number (A), charge number (Z) will be singled out to identify different impurities.

Assuming that the total rest mass can be expressed approximately as $\mathrm{m}_0 \approx 931.4940954 \times A$ [MeV/c^2], disregarding the minor effects of binding energy, the following relation is valid:

$$(B\rho)^2 \sim \frac{A^2T^2 + 2TAm_0}{Z^2} \sim \frac{TA(TA + 2 \times 931.4940954 \times A)}{Z^2}.$$

Comparing two different ion species of equal $B\rho$, their relationship is

$$\frac{A^2}{Z^2}T(T + 2 \times 931.4940954) = \frac{A'^2}{Z'^2}T'(T' + 2 \times 931.4940954),$$

Where the primed values are impurity ions attributes. Therefore, solving for T' becomes simply a quadratic polynomial problem, implemented in the following code. The code produces a matrix of "possible" impurity kinetic energies for Z and A up to 10 and 20, respectively. This can be used to map their variation depending on the principal extracted ion characteristics, and reproduce possible "contaminant" beams in future simulations for a better agreement with experimental data.

riggy.cpp. Rigidity code.

```cpp
#include <stdio.h>
#include <math.h>
#include <iostream>
#include <stdlib.h>
#include <iomanip>
#include <string>
#include <fstream>
 using namespace std;
 int main(){std::ofstream outfile;outfile.open("lol.dat", std::ios_base::app);int A1, A2,
    Z1, Z2;double T1, a, b, c, d, g, T2;
    printf("Enter Kinetic Energy of the principal ion: ");
    scanf("%lf",&T1);
    printf("Enter Atomic Mass of the principal ion: ");
    scanf("%i",&A1);
    printf("Enter Atomic Number of the principal ion: ");
    scanf("%i",&Z1);
    g = -T1*A1*(T1*A1+2*931.4940954*A1)/(Z1*Z1);
 for(A2=1;A2<=20;A2++){a=A2*A2;b=2*A2*931.4940954*A2;
 for(Z2=1;Z2<=10;Z2++){c = Z2*Z2*g;d=b*b-4*a*c;T2 =(-b+sqrt(d))/(2*a);
    if (Z2 > A2){T2=0;}
  cout<< setprecision(5) <<T2<<" ";
  outfile << setprecision(5) << T2<< " ";}
  outfile << endl;
  cout<<"\n";}
    return 0;}
```

Four examples of these maps are plotted in figure E, for the $RI\beta^+$ extracted during the experiment. Some of the "possible" beam contaminants with CSDA ranges higher than the stable primary beam are identified in table F.

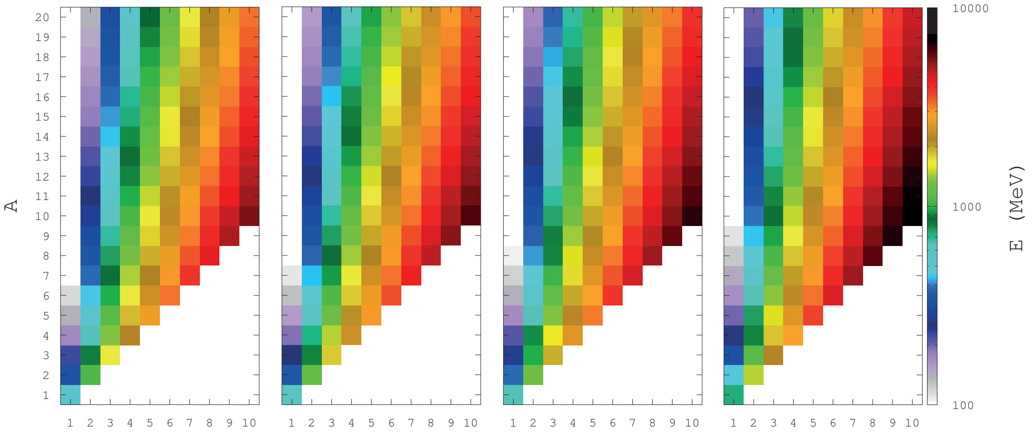

(a) ^{11}C (190 MeV/u) (b) ^{11}C (210 MeV/u) (c) ^{15}O (219 MeV/u) (d) ^{15}O (254.5 MeV/u)

Figure E: *Kinetic energy values of possible impurities with equivalent magnetic rigidity as the extracted beam.*

Table F: *Possible beam contaminants in ^{11}C ($\sim$ 7%) and ^{15}O ($\sim$ 3%), according to their energy and CSDA depth values, obtained from* `efltst.f` *FLUKA routine. The species shadowed in lilac color have CSDA depth values beyond that of the primary beam.*

	^{11}C (190 MeV/u)		^{15}O (254.5 MeV/u)	
Species	E (MeV/u)	CSDA (cm)	E (MeV/u)	CSDA (cm)
^{2}H	161.9	36.0385	226.7	64.3124
^{3}H	75.2	13.9305	106.9	26.0914
^{3}He	272.8	33.0046	376.0	55.9278
^{4}He	161.9	18.1098	226.7	32.2585
^{6}Li	161.9	12.0327	226.7	21.4607
^{7}Li	121.4	8.47837	171.1	15.4650
^{7}Be	206.9	12.0486	287.7	21.0140
^{9}Be	130.0	6.92581	182.9	12.5485
^{8}B	243.1	11.5843	336.5	19.8769
^{10}B	161.9	7.22605	226.7	12.8800
^{11}B	135.6	5.83192	190.6	10.5433
^{12}B	115.1	4.76924	162.4	8.71964
^{9}C	272.8	10.970	376.1	18.5893
^{10}C	225.9	8.88616	313.4	15.3604
^{11}C	190.0	7.27772	264.9	12.7887
^{12}C	161.8	6.02273	226.7	10.7369
^{12}N	—	—	298.3	12.4748
^{13}N	—	—	258.9	10.6824
^{13}O	—	—	327.5	12.0633
^{14}O	—	—	287.6	10.4968
^{15}O	—	—	254.5	9.17193
^{16}O	—	—	226.7	8.05248

Introducing this information in the simulation could allow the estimation of the production of these fragments from the primary beam interaction with the inter–target material.

Bibliography

[AB11] U. Amaldi & S. Braccini, *Eur. Phys. J. Plus* **126**:70, 2011.

[Ago03] S. Agostinelli *et al.*, *Nucl. Inst. Meth. Phys. Res. A* **506** 250–303, 2003.

[Ag12a] C. Agodi *et al.*, *JINST* **7** P03001, 2012.

[Ag12b] C. Agodi *et al.*, *Phys. Med. Biol.* **57** 5667–78, 2012.

[Aig05] H. Aiginger *et al.*, *Adv. Space Res.* **35** 214–22, 2005.

[AK05] U. Amaldi & G. Kraft, *Rep. Prog. Phys.* **68** 1861–82, 2005.

[Alo96] J. R. Alonso, *Proc. Part. Accel. Conf.* **1** 58–62, 1996.

[Alo00] J. R. Alonso, *Proc. Eur. Part. Accel. Conf.*, 235–9, Vienna, 2000.

[An12] S. J. An *et al.*, *Nucl. Instr. Meth. Phys. Res. A* **698** 37–43, 2013.

[And04] V. Andersen *et al.*, *Adv. Space Res.* **34**(6) 1302–10, 2004.

[AOS15] A. S. Ahmad, N. Ormiston-Smith and P. D. Sasieni, *British Journal of Cancer* **112** 943–7, 2015.

[Ash72] J. C. Ashley, R. H. Ritchie and W. Brandt, *Phys. Rev. B* **5** 2393–7, 1972.

[Att09] F. Attanasi *et al.*, *Phys. Med. Biol.* **54** N29–N35 2009.

[Aug16] R. S. Augusto *et al.*, *Nucl. Instr. Meth. Phys. Res. B*, **376** 374–8, 2016.

[Au18a] R. S. Augusto *et al.*, *Physica Medica* (submitted, under review).

[Au18b] R. S. Augusto *et al.*, *Phys. Med. Biol.* (submitted).

[AWK] A. V. Aho, B. Kernighan and P. Weinberger, "The AWK Programming Language." Addison–Wesley, Reading, 1988.

[Bai05] D. L. Bailey *et al.* (ed.), "Positron Emission Tomography: Basic Sciences", Springer-Verlag London, 2005.

[Bal05] F. Ballarini *et al.*, *AIP Conference Proceedings* **769**, 1197–202, 2005.

[Bal06] F. Ballarini *et al.*, *Advances in Space Research* **37** 1791–7, 2006.

[Bal07] F. Ballarini *et al.*,*Advances in Space Research* **40** 1339–49, 2007.

[Bat03] Battistoni *et al.*, *Braz J. Phys.* **34** 897–900, 2004.

[Bat05] G. Battistoni *et al.*, *J. Phys. Conf. Ser.* **41** 151–60, **SLAC-PUB-11549**, 2006

[Bat15] G. Battistoni *et al.*, *Annals of Nuclear Energy* **82** 10–8, 2015.

[Bat16] G Battistoni *et al.*, *Frontiers in Oncology*, **6** 116, 2016.

[Bau13] J. Bauer *et al.*, *Radiother. Oncol.*, **107**(2) 218–26, 2013.

[Bau14] J. Bauer *et al.*, *Phys. Med. Biol.* **59** 4635–59, 2014.

[BBS56] W. H. Barkas, W. Birnbaum and F. M. Smith *Phys. Rev.* **101** 778–95, 1956.

[BDH63] W. H. Barkas, J. N. Dyer, H. H. Heckman, *Phys. Rev. Lett.* **11** 26–8, 1963.

[Bass14] N. Bassler *et al.*, *J. Phys.: Conf. Ser.* **489** 012004, 2014.

[Ber74] H. W. Bertini *et al.*, Oak Ridge: **ORNL-TM-4134**, 1974.

[Ber09] C. A. Bertulani, "Nuclear reactions", *Wiley Encyclopedia of Physics*, Wiley-VCH, Berlin, 2009.

[Bet30] H. A. Bethe, *Ann. Physik* **5** 325–400, 1930.

[Bet32] H. A. Bethe, *Z. Phys.* **76** 293–9, 1932.

[Bet53] H. Bethe, *Phys. Rev.* **89** 1256–66, 1953.

[Bey00] T. Beyer *et al.*, *J. Nucl. Med.* **41**(8) 1369–79, 2000.

[Bey04] T. Beyer *et al.*, *J. Nucl. Med.* **45**(1) 25S–35S, 2004.

[BH34] H. A. Bethe & W. Heitler, *Proc. Roy. Soc.* **A146** 83–112, 1934.

[BH80] J. P. Biersack & L. G. Haggmark, *Nucl. Instr. Meth.* **174** 257–69, 1980.

[Bia99] M. Biaggi *et al.*, *Nucl. Instr. Meth. B* **159** 89–100, 1999.

[Bic92] H. Bichsel, *Phys. Rev. A* **46**(9), 1992.

[Bie] A. F. Bielajew, "Fundamentals of the Monte Carlo method for neutral and charged particle transport", Department of Nuclear Engineering and Radiological Sciences, `http://www-personal.umich.edu/~bielajew/MCBook/book.pdf`

[Bis17] M. G. Bisogni *et al.*, *Journal of Medical Imaging* **4**(1) 011005, 2017.

[BMM16] G. Battistoni, I. Mattei and S. Muraro, *Advances in Physics: X* **1**(4) 661–86, 2016.

[BK04] W. H. Bragg & R. Kleeman, *Philos. Mag.* **S6** 726–38, 1904.

[BK05] W. H. Bragg & R. Kleeman, *Philos. Mag.* **10** 318–40, 1905.

[Bla83] M. Blann, *Phys. Rev.* **C**28 1648–62, 1983.

[Blo33a] F. Bloch, *Ann. Phys.* **16** 287, 1933.

[Blo33b] F. Bloch, *Z. Phys.* **81** 363–76, 1933.

[Boh15] N. Bohr, *Philos. Mag.* **30** 581–612, 1915.

[Böh10] T. T. Böhlen *et al.*, *Phys. Med. Biol.* **55** 5833–47, 2010.

[Böh12] T. T. Böhlen *et al.*, *JINST* **7** p07018, 2012.

[Böh14] T. T. Böhlen *et al.*, *Nuclear Data Sheets* **120** 211–4, 2014.

[Bor97] T. Bortfeld, *Med. Phys.*, **24**(12) 2024–33, 1997.

[Bou08] F. Bourhaleb *et al. J. Phys.: Conf. Ser.* **102** 012002, 2008.

[Boy15] A. Yu. Boytsov *et al.*, *Rev. Sci. Instr.* **86** 083308, 2015.

[BP82] H. Bichsel & L. E. Porter, *Phys. Rev. A* **25**(5) 2499–510, 1982.

[Bra09] S. Braccini, 11th *ICATPP Conference, Como, Italy* 2009.

[Bra14] H. H. Braun *et al.*, *Phys. Rev. Special Topics - Accelerators and Beams* **17**(2) 021006, 2014.

[BRT90] B. Borderie, M. F. Rivet and L. Tassan-Got, *Ann. Phys.* **15**(4) 287–390, 1990.

[Bry00] "PIMMS: Proton-ion medical machine study", P. J. Bryant (ed.) **CERN-2000-006**, Geneva, CERN, 2000.

[Cas80] J. R. Castro *et al.*, *Cancer* **46** 633–41, 1980.

[Cas82] J. R. Castro *et al.*, *Int. J. Rad. Oncol.*, **8**(12) 2191–8, 1982.

[Cav98] M. Cavinato *et al.*, *Nucl. Phys. A* **643** 15–29, 1998.

[Cav01] M. Cavinato *et al.*, *Nucl. Phys. A* **679** 753–64, 2001.

[CCG05] F. Cerutti, A. Clivio and E. Gadioli, *Eur. Phys. J. A*, **25**(3) 413–8, 2005.

[CD06] S. R. Cherry & M. Dahlbom "PET: Physics, Instrumentation, and Scanners", M. E. Phelps (ed.) Springer–Verlag New York, 2006.

[Cer06] F. Cerutti *et al.*, *Proc.* 11^{th} *Int. Conf. Nucl. Reaction Mechanisms*, Varenna, Italy, 2006.

[Cer92] I. Cervesato *et al.*, *Phys. Rev. C* **45**(5) 2369–78 ,1992.

[CE16] M. Conti & L. Eriksson, *EJNMMI Physics* **3**:8 2016.

[Com12] S. E. Combs *et al.*, *BMC Cancer* **12** 133 2012.

[CTL76] A. Chatterjee, C. A. Tobias and J. T. Lyman, "Nuclear fragmentation in therapeutic and diagnostic studies with heavy ions", B. S. P. Shen & M. Merker (ed.) "Spallation nuclear reactions and their applications", *Astrophysics and Space Science Library*, **59**, 169–91 D. Reidel, 1976.

[Cha81] A. Chatterjee *et al.*, *Int. J. Radiat. Oncol. Biol. Phys.* **7** 503–7, 1981.

[CSE06] P. Crespo, G. Shakirin and W. Enghardt, *Phys. Med. Biol.* **51** 2143–63, 2006.

[Cur34] I. Curie & F. Joliot–Curie, Nature **133** 201, 1934.

[Def97] M. Defrise *et al.*, *IEEE Transactions on Medical Imaging* **16**(2) 145–58, 1997.

[Der79] S. E. Derenzo, **LBL–9169**, 1979.

[Dre62] L. Dresner, *Oak Ridge National Laboratory report* **ORNL–TM–196**, 1962.

[Eck87] R. Eckhardt, "Stan Ulam, John Von Neumann, and the Monte Carlo Method", *Los Alamos Science*, 1987.

[EWA11] H. Eickhoff, U. Weinrich and J. Alonso, "Chapter 20: Design Criteria for Medical Accelerators", U. Linz (ed.) "Ion Beam Therapy" *Biological and Medical Physics, Biomedical Engineering*, **320**, 325–43, 2012.

[EK16] D. K. Ebner & T. Kamada, *Front. Oncol.* **6** 140, 2016.

[Eng92] W. Enghardt *et al.*, *Phys. Med. Biol.* **37**(11) 2127–31, 1992.

[Eng99] W. Enghardt *et al.*, *Nucl. Phys. A* **654** 1047–50, 1999.

[En04a] W. Enghardt *et al.*, *Radiother. Oncol.* **73**(2) S96–8, 2004.

[En04b] W. Enghardt *et al.*, *Nucl. Instrum. Methods Phys. Res.* **525** 284–8, 2004.

[ENLIGHT] ENLIGHT – The European Network for Light Ion Hadron Therapy.

[ENVISION] European NoVel Imaging Systems for ION therapy

[EUR] *Eurostat Newsrelease*, 179/2014 – 25 November 2014, Causes of death in the EU28 in 2011.

[Fah02] F. H. Fahey, *J Nucl. Med. Technol.* **30** 39–49, 2002.

[Fan54] U. Fano, *Phys. Rev.* **93** 117–20 1954.

[Fas97a] A. Fassò *et al.* *Proc.* 2^{nd} *Workshop on Simulating Accelerator Radiation Environments (SARE 2)*, CERN, Geneva, Switzerland 9–11 1995. Ed. G. R. Stevenson, CERN Report TIS–RP/97–05, 1997.

[Fas97b] A. Fassò *et al.*, *Proc.* 3^{rd} *Workshop on Simulating Accelerator Radiation Environments (SARE 3)*, KEK, Tsukuba, Japan, 1997. H. Hirayama (ed.), KEK Proceedings 97–5, 1997.

[Fas01] A. Fassò *et al.*, "FLUKA: Status and Prospects for Hadronic Applications". A. Kling, F.J.C. Barão, M. Nakagawa, L. Távora , P. Vaz (ed.) "Advanced Monte Carlo for Radiation Physics, Particle Transport Simulation and Applications", Springer, Berlin, Heidelberg 2000.

[Fas03] A. Fassò *et al.*,*Computing in High Energy and Nuclear Physics*, La Jolla, California, US, 2003.

[Fas11] A. Fassò *et al.*, *Prog. Nucl. Sci. Tech.*, **2** 769–75, 2011.

[Fer50] E. Fermi, *Prog. Theor. Phys.*, **5**(1) 570–83, 1950.

[Fer92] A. Ferrari *et al.*, *Nucl. Instr. Meth.* **B71** 412–26, 1992.

[Fer05] A. Ferrari *et al.* **CERN 2005-10**, **INFN/TC_05/11**, **SLAC-R-773**, 2005.

[Fer06] A. Ferrari *et al.*, *Computing in High-Energy and Nuclear Physics*, Mumbai, India, 2006.

[Fer13] J. Ferlay *et al.*, *European Journal of Cancer* **49** 1374–403, 2013.

[INSIDE] V. Ferrero *et al.*, 14^{th} *Topical Seminar on Innovative Particle and Radiation Detectors*, Siena, 2016.

[Fer17] V. Ferrero *et al.*, *J. Phys.: Conf. Ser.* **841** 012011, 2017.

[FFS11] A. Fassò, A. Ferrari, P. R. Sala, "Chapter 4: Principles of Monte Carlo Calculation and Codes", M. C. Cantone & C. Hoeschen (ed.) "Radiation Physics for Nuclear Medicine" *Springer–Verlag Berlin Heidelberg*, 2011.

[Fie06] Fiedler *et al.*, *IEEE Trans. Nucl. Sci.* **53** 2252–9, 2006.

[Fie10] F. Fiedler *et al.*, *Phys. Med. Biol.* **55** 1989–98, 2010.

[Fie11] F. Fiedler *et al.*, "Chapter 31: Online Irradiation Control by Means of PET", U. Linz (ed.) "Ion Beam Therapy." *Biological and Medical Physics, Biomedical Engineering*, **320**, 527–544, 2012.

[FS97] A. Ferrari & P. R. Sala, *International Conference on Nuclear Data for Science and Technology*, NDST–97.

[FS96] A. Ferrari & P. R. Sala, *Proc. Workshop on Nuclear Reaction Data, Nuclear Reactors Physics, Design, and Safety* Trieste, 1996.

[Gad03] E. Gadioli *et al.*, *Eur. Phys. J. A* **17** 195–212, 2003.

[Gar07] M. V. Garzelli *et al.*, *Adv. Space Res.* **40** 1350–6, 2007.

[Gei06] O. Geithner *et al.*, *Phys. Med. Biol.* **51** 2279–92, 2006.

[Gia14] C. Gianoli *et al.*, *Comp. Med. Imag.* **38**(5) 358–68, 2014.

[Gia16] C. Gianoli *et al.*, *Phys. Med. Biol.* **61**(11) 4141–55, 2016

[Gre12] M. L. Grevillot, "Monte Carlo simulation of active scanning proton therapy system with Gate/Geant4: Towards a better patient dose quality assurance", *PhD thesis*, 2011.

[Hab93] T. Haberer *et al.*, *Nucl. Instr. Meth. Phys. Res. A*, **330**(1–2), 296–305 1993.

[Han17] J. Handrack *et al.*, *Acta Oncol.* **56**(11) 1451–8, 2017.

[Har17] B. Hartmann *et al.*, *Int J Particle Ther* **3**(4) 439–49, 2017.

[Hig75] V. L. Highland, *Nucl. Instr. Meth.* **129** 497–9, 1975.

[Hir14] Y. Hirano *et al.*, *Phys. Med. Biol.* **59** 1623–40, 2014.

[Hir16] Y. Hirano *et al.*,*Phys. Med. Biol.* **61** 4870–89, 2016.

[HIS06] E. Haettner, H. Iwase and D. Schardt, *Rad. Prot. Dos.*, **122**(1–4) 485–7, 2006.

[HIT] Heidelberg Ion Therapy Center, HIT Bildergalerie

[Hir90] Y. Hirao *et al.*, *EPAC* 112, 1990.

[HL15] P. He & Q. Li, *Int. J. Part. Ther.* **1**(4) 884, 2015.

[HBG89] F. Hubert, R. Bimbot and H. Gauvin, *Nucl. Instr. Meth. Phys. Res. B* **36** 357–363, 1989.

[IAEA–NDS] IAEA - Nuclear Data Section – Live Chart of Nuclides (Oct. 2017).

[IAEA–TCS–42] IAEA, "Radiation Biology: A Handbook for Teachers and Students", **IAEA–TCS–42**, 2010.

[IAEA–TECDOC–1560] IAEA, "Dose Reporting in Ion Beam Therapy", **IAEA–TECDOC–1560**, 2006.

[IAEA–TRS–398] IAEA, "Absorbed Dose Determination in External Beam Radiotherapy: An International Code of Practice for Dosimetry Based on Standards of Absorbed Dose to Water", **IAEA–TRS–398**, 2000.

[IAEA–TRS–461] IAEA, "Relative Biological Effectiveness In Ion Beam Therapy", **IAEA–TRS–461**, 2008.

[IAEA–HHR–3] IAEA, "Inequity in Cancer Care: A Global Perspective", **IAEA–HHR–3**, 2011.

[IAEA–HHS–31] IAEA, "Accuracy Requirements and Uncertainties in Radiotherapy", **IAEA–HHS–31** 2016.

[Ian15] G. Iancu *et al.*, *Int. J. Particle Ther.* **2**(2) 415–25, 2015.

[ICRP–103] ICRP, "The 2007 Recommendations of the International Commission on Radiological Protection", ICRP–103 **37**(2-4), 2007.

[ICRU–49] M. J. Berger *et al.*, ICRU, "Stopping Power and Ranges for Protons and Alpha Particles", **ICRU Report 49**, Bethesda, MD, 1993.

[ICRU–37] M. J. Berger *et al.*, ICRU, "Stopping powers for electrons and positrons", **ICRU Report 37**, Bethesda, MD, 1984.

[Ina05] T. Inaniwa *et al.*, *Phys. Med. Biol.* **50** 1131–45, 2005.

[Ina08] T. Inaniwa *et al.*, *Phys. Med. Biol.* **53** 529–42, 2008.

[Ina17] T. Inaniwa *et al.*, *Phys. Med. Biol.* **62** 5180–97, 2017.

[Ise04] Y. Iseki *et al.*, *Phys. Med. Biol.* **49** 3179–95, 2004.

[Iwa12] Y. Iwata *et al.*, *Phys. Rev. Special Topics - Accelerators and Beams* **15** 044701, 2012.

[Jak11] B. W. Jakoby *et al.*, *Phys. Med. Biol.* **56** 2375–89, 2011.

[Jam90] F. James, *Comp. Phys. Comm.* **60** 329–44, 1990.

[Jan82] J. F. Janni, *Atomic Data and Nuclear Data Tables*, **27**(2–5) 147–339, 1982.

[JKE09] I. Jun, W. Kim and R. Evans, *IEEE Trans. Nucl. Sci.* **56**(6) 3229–35, 2009.

[JP04] H. Jiang & H. Paganetti, *Med. Phys.* **31** 2811–8, 2004.

[KKO13] N. Kanematsu, Y. Koba and R. Ogata, *Med. Phys.* **40**(4) 041724, 2013.

[Kam15] T. Kamada *et al.*, *Lancet Oncol.* **16** e93–e100, 2015.

[Kan99] T. Kanai *et al.*, *Int. J. Rad. Onc. Biol. Phys.* **44**(1) 201–10, 1999.

[Kan98] M. Kanazawa *et al.*, *EPAC98*, 2357–9, 1998.

[Kan02] M. Kanazawa *et al.*, *Nucl. Phys. A* **701** 244–52, 2002.

[Kan04] M. Kanazawa *et al.*, *Nucl. Phys. A* **746** 393–6, 2004.

[Kar75] P. J. Karol, *Phys. Rev. C*, **11**(4), 1203–9, 1975.

[Kat13] K. Katagiri *et al.*, *Rev. Sci. Instrum.* **85** 02C305, 2014.

[Kat15] K. Katagiri *et al*, *Rev. Sci. Instrum.* **86** 123303, 2015.

[Kat16] K. Katagiri *et al.*, *Rev. Sci. Instrum.* **87** 02B509 2016.

[Kim86] L. Kim *et al.*, *Phys. Rev. A* **33**, 3002–9, 1986.

[Kit06] A. Kitagawa *et al.*, *Rev. Sci. Instr.* **77** 03C105, 2006.

[Kit08] A. Kitagawa *et al.*, *J. Korean Phys. Soc.*, **53**(6) 3709–13, 2008.

[Kit10] A. Kitagawa *et al.*, *Rev. Sci. Instr.* **81** 02B909, 2010.

[Kit16] A. Kitagawa *et al.*, *Rev. Sci. Instr.* **87** 02C107, 2016.

[Kno10] G. F. Knoll, "Radiation Detection and Measurement", Wiley & Sons, fourth edition, 2010.

[Kou98] S. Kouda *et al.*, *Proc. Part. Accel. Conf.*, **3** 3822–4, Vancouver, Canada, 1997.

[Kr14a] A. C. Kraan *et al.*, *JINST* **10** C01010, 2014.

[Kr14b] A. C. Kraan *et al.*, *Physica Medica* **30** 559–69, 2014.

[Kr15a] A. C. Kraan *et al.*, *Nucl. Instr. Meth. Phys. Res. A*, **786** 120–6 2015.

[Kr15b] A. C. Kraan, *Frontiers in Oncology*, **5** 150, 2015.

[Krä00] M. Krämer *et al.*, *Phys. Med. Biol.* **45** 3299–317, 2000.

[KS00] M. Krämer & M. Scholz, *Phys. Med. Biol.* **45** 3319–30, 2000.

[Kra08] M. Krämer, "Swift ions in radiotherapy: Treatment planning with TRiP98". *The Seventh International Symposium on Swift Heavy Ions in Matter*, Lyon, France, 2008.

[KMP12] C. Kurz, A Mairani and K. Parodi, *Phys. Med. Biol.* **57** 5017–34, 2012.

[Kur13] C. Kurz *et al.*, *IEEE NSS MIC* 1–3, 2013.

[Kur14] C. Kurz, "4D offline PET-based treatment verification in ion beam therapy: experimental and clinical evaluation", *PhD thesis*, 2014.

[KV17] W. S. Kozłowska & V. Vlachoudis, to be published, 2018.

[Lan08] J. Langner, "Event–Driven Motion Compensation in Positron Emission Tomography: Development of a Clinically Applicable Method", *PhD thesis*, 2008

[LBL77] Division of Biology and Medicine LBL–UCB, California "Biological and Medical Research with Accelerated Heavy Ions at the Bevalac 1974–1977", Sheryl Elam (ed.), *Biomedical Division and Technical Information Department Staff*, **LBL-5610**, 1977.

[LBL80] M. C. Pirruccello & C. A. Tobias, "Biological and Medical Research with Accelerated Heavy Ions at the Bevalac, 1977–1980", University of California (ed.), **LBL-11220** UC-48, 1980.

[LD91] G. R. Lynch & O. I. Dahl, *Nucl. Instr. Meth. B* **58** 6–10 1991.

[Leo94] W. R. Leo, "Techniques for Nuclear and Particle Physics Experiments: A How-to Approach", Springer, 1994.

[LFO13] A. Lomax, L. K. Folkes and P. O'Neill, *Clinical Oncology*, **25** 578–85, 2013.

[LIK10] A. Lechner, V. N. Ivanchenko and J. Knobloch, *Nucl. Instr. Meth. Phys. Res. B* **268** 2343–54, 2010.

[Lla79] J. Llacer *et al.*, *IEEE Trans. Nucl. Sci.* **26**(1) 634–47, 1979.

[Lla84] J. Llacer *et al.*, *IEEE Trans. Med. Imag.* **3**(2) 80–90, 1984.

[Lom09] A. J. Lomax, *Cancer J.* **15**(4) 285–91, 2009.

[Lop16] P. Cambraia Lopes *et al.*, *Phys. Med. Biol.* **61** 6203–30, 2016.

[LQZ95] T. Lijian, H. Qing and L. Zhengming, *Radiat. Phys. Chem.* **45**(2) 235–45, 1995.

[Lui13] R. F. Luís, "Radiological Protection and Nuclear Engineering Studies in Multi–MW Target Systems", *PhD Thesis*, 2013.

[Mac69] H. D. Maccabee, U. Madhvanath and M. R. Raju, *Phys. Med. Biol.* **14** 213–24, 1969.

[Mag17] G. Magro *et al.*, *Phys. Med. Biol.* **62** 3814–27, 2017.

[Mai07] A. Mairani, "Nucleus–Nucleus Interaction Modelling and Applications in Ion Therapy Treatment Planning", *PhD Thesis*, 2007.

[Mai10] A. Mairani *et al.*, *Phys. Med. Biol.* **55** 4273–89, 2010.

[Mai13] A. Mairani *et al.*, *Phys. Med. Biol.* **58** 2471–90, 2013.

[Man15] C. M. Terracciano, "Analysis and interpretation of Carbon ion fragmentation in the Bragg peak energy range", *PhD Thesis*, 2014.

[Mar11] M. Martišíková *et al.*, *JINST* **6** C11014, 2011.

[Mas11] S. G. Mashnik, **LA-UR-11-00083**, 2011.

[Mat05] N. Matsufuji *et al.*, *Phys. Med. Biol.* **50** 3393–403, 2005.

[MAT14] T. Mendonça, R. Augusto and T. Stora, **CERN-ACC-NOTE-2014-0028**, 2014.

[Met87] N. Metropolis, "The beginning of the Monte Carlo Method", *Los Alamos Science*, 1987.

[MGH] T. Bortfelt, "Treatment with Protons (and heavier particles)", `gray.mgh.harvard.edu`.

[Min13] C. H. Min *et al.*, *Int. J. Radiat. Oncol. Biol. Phys.* **86**(1) 183–9, 2013.

[Miz11] K. Mizushima *et al.*, *IPAC2011*, San Sebastián, Spain, 2011.

[Moh16] A. Mohammadi *et al.*,*Nucl. Instr. Meth. Phys. Res. A* **849** 76–82, 2017.

[Moh17] O. Mohamad *et al.*, *Cancers* **9**:66, 2017.

[Mol48] G. Z. Molière, *Z. Naturforsch.* **3a** 78–97, 1948.

[Mol55] G. Z. Molière, *Z. Naturforsch.* **10a**, 177–211, 1955.

[Mot29] N. F. Mott, *Proc. R. Soc. Lond. A* **124** 425–42, 1929.

[MT04] G. Marsaglia & W. W. Tsang, *Statistics & Probability Letters* **66** 183–7, 2004.

[NCI] *National Cancer Institute.*

[Nis06] T. Nishio *et al.*, *Med. Phys.* **33** 4190, 2006.

[Nod11] K. Noda *et al.*, *Nucl. Instr. Meth. Phys. Res. B* **269** 2924–7, 2011.

[Nod14] K. Noda *et al.*, *Nucl. Instr. Meth. Phys. Res. B* **331** 6–9, 2014.

[Nod17] K. Noda *et al.*, *Nucl. Instr. Meth. Phys. Res. B* **406** 374–8, 2017.

[Ohn13] T. Ohno *et al.*, *The EPMA Journal* **4**:9 2013.

[OLA96] U. Oelfke, G. K. Y. Lam and M. S. Atkins, *Phys. Med. Biol.* **41** 177–96, 1996.

[PDG14] K. A. Olive *et al.* (PDG), *Chin. Phys.* **C38**, 090001 2014, `http://pdg.lbl.gov`.

[Ort13] P. G. Ortega *et al.*, *IEEE NSS*, 1–7, 2013.

[Ort14] P. G. Ortega *et al*, *Radiotherapy and Oncology* **110**(1) S37, 2014.

[Ort15] P. G. Ortega *et al*, *FLUKA Collaboration Meeting* May 2015.

[Pag12] H. Paganetti, *Phys. Med. Biol.* **57** R99–R117, 2012.

[Par04] K. Parodi, "On the feasibility of dose quantification with in-beam PET data in radiotherapy with ^{12}C and proton beams", *PhD thesis*, 2004.

[Pa07a] K. Parodi *et al.*, *Int. J. Radiat. Oncol. Biol. Phys.* **68** 920–34, 2007.

[Pa07b] K. Parodi *et al.*, *Phys. Med. Biol.* **52** 3369–87, 2007.

[Pa07c] K. Parodi *et al.*, *Proc. 12th Int. Conf. Nucl. Reaction Mechanisms* Varenna, Italy, 2009.

[Par10] K. Parodi *et al.*, *Phys. Med. Biol.* **55** 5169–87, 2010.

[Pa12a] K Parodi, *Nucl. Med. Rev.* **15** C37–C42, 2012.

[Pa12b] K. Parodi *et al.*, *Phys. Med. Biol.* **57** 3759–84, 2012.

[Par14] K. Parodi, *Phys. Med.* **30** 539–43, 2014.

[Paw96] J. Pawelke *et al.*, *Phys. Med. Biol.* **41** 279–96, 1996.

[PBH08] K. Parodi, T. Bortfeld and T. Haberer, *Int. J. Radiat. Oncol. Biol. Phys.* **71** 945–56, 2008

[PCF01] L. Pinsky, F. Carminati and A. Ferrari, *Rad. Meas.* **33** 335–9, 2001.

[PE00] K. Parodi & W. Enghardt, *Phys. Med. Biol.* **45** N151–N156, 2000.

[Ped95] E. Pedroni *et al.*, *Med. Phys.* **22** 37–53, 1995.

[PEH2a] K. Parodi, W. Enghardt and T. Haberer, *IEEE Conf. Proc. NSS* **2** 1193–6, 2002.

[PEH2b] K. Parodi, W. Enghardt and T. Haberer, *Phys. Med. Biol.* **47** 21–36, 2002.

[PEL03] F. Pönisch, W. Enghardt and K. Lauckner, *Phys. Med. Biol.* **48** 2419–36, 2003.

[Phe75] M. E. Phelps *et al.*, *J. Nucl. Med.* **16** 210–24 1975.

[PMS13] K. Parodi, A. Mairani and F. Sommerer, *Journal of Radiation Research* **54** i91–i96, 2013.

[Pol14] J. C. Polf *et al.*, *Phys. Med. Biol.* **59**(9) 2325–40, 2014.

[PPE05] K. Parodi, F. Pönisch and W. Enghardt, *IEEE Trans. Nucl. Sci.* **52** 778, 2005.

[Pin14] M. Pinto, "Modelling and simulation of physics processes for in–beam imaging in hadrontherapy", *PhD thesis*, 2014.

[Pit95] J. M. Pitarke, R. H. Ritchie and P. M. Echenique, *Phys. Rev.* **B**52 13883, 1995.

[Pön04] F. Pönisch *et al.*, *Phys. Med. Biol.* **49** 5217–32, 2004.

[Poo15] J. K. Poon *et al.*, *Phys. Med. Biol.* **60** N35–N45, 2015.

[Por99] L. E. Porter, *Nucl. Instr. Meth. Phys. Res. B*, **159**, 195–200, 1999.

[Pri08] M. Priegnitz *et al.*, *IEEE NSS* 2008.

[Pri12] M. Priegnitz *et al*, *IEEE Trans. Nucl. Sci.* **59**(1) 77–87, 2012.

[PTCOG] *Particle Therapy Co-Operative Group, Particle therapy facilities in operation (30 June 2017).*

[R] The R Project for Statistical Computing.

[Ran65] J. Ranft, *Nuclear Intrum. Meth.* **48** 133–40, 1967.

[RER01] S. Roesler, R. Engel and J. Ranft, "FLUKA: Status and Prospects for Hadronic Applications". A. Kling, F.J.C. Barão, M. Nakagawa, L. Távora, P. Vaz (ed.) *Advanced Monte Carlo for Radiation Physics, Particle Transport Simulation and Applications.* Springer, Berlin, Heidelberg 2000.

[Ric16] C. Richter *et al.*, *Radiot. Oncol.* **118** 232–7, 2016.

[Rin15] T. P. Ringbæk *et al.*, *Phys. Med. Biol.* **60** N59–N69, 2015.

[Rob13] C. Robert *et al.*, *Phys. Med. Biol.* **58** 2879–99, 2013.

[Sal16] S. Salvador,*Phys. Rev. C* **95** 044607, 2017.

[San12] D. Sánchez Parcerisa, "Experimental and computational investigations on the water-to-air stopping power ratio for ion chamber dosimetry in carbon ion radiotherapy", *PhD thesis* 2012.

[Sat13] T. Sato *et al.*, *J. Nucl. Sci. Tech.* **50** 9, 2013.

[SB86] S. M. Seltzer & M. J. Berger, *At. Data Nucl. Data Tab.* **35** 345–418, 1986.

[SBS00] W. Schneider, T. Bortfeld and W. Schlegel, *Phys. Med. Biol.* **45** 459–78, 2000.

[Sch96] C. Scheidenberger *et al.*, *Phys Rev Lett.* **77**(19) 3987–90, 1996.

[Sch14] C. D. Schlaff *et al.*, *Radiation Oncology* **9** 88, 2014.

[Ser47] R. Serber *Phys. Rev.* **72** 1114–5, 1947.

[SES10] D. Schardt, T. Elsässer and D. Schulz–Ertner, *Rev. Mod. Phys.* **82**(1) 383–425, 2010.

[Sha11] G. Shakirin *et al.*, *Phys. Med. Biol.* **56** 1281–98, 2011.

[SF02] J. K. Shultis & R. E. Faw, "Fundamentals of Nuclear Science and Engineering", Taylor & Francis, 2002.

[Smi16] C. R. Smittenaar *et al.*, *British Journal of Cancer* **115** 1147–55, 2016.

[Som06] F. Sommerer *et al.*, *Phys. Med. Biol.* **51** 4385–98, 2006.

[Som07] F. Sommerer, "Experiments and FLUKA simulations of ^{12}C and ^{16}O beams for therapy monitoring by means of in–beam Positron Emission Tomography", *PhD thesis*, 2007.

[Som09] F. Sommerer *et al.*, *Phys. Med. Biol.* **54** 3979–96, 2009.

[Sor95] H. Sorge, *Phys. Rev. C* **52** 3291–314, 1995.

[SSG89] H. Sorge, H. Stöcker and W. Greiner, *Annals of Physics* **192** 266–306, 1989.

[Ste84] R. M. Sternheimer, M. J. Berger and S. M. Seltzer, *At. Data Nucl. Data Tab.* **30** 261–71, 1984.

[STP08] Inside Biograph TruePoint PET·CT – *System Specifications*, Siemens AG, 2008.

[Sud00] M. Suda *et al.*, *EPAC*, Vienna, Austria, 2000.

[Sui10] H. Suit *et al.*, *Radiot. Oncol.* **95** 3–22, 2010.

[Suz00] M. Suzuki *et al.*, *Int. J. Radiat. Oncol. Biol. Phys.* **48** 241–50, 2000.

[Tak00] E. Takada *et al.*, *Proc. 13th SAST Osaka, 2001* 187–9, 2001.

[Tas12] H. Tashima *et al.*, *Phys. Med. Biol.* **57**(14), 4705–18, 2012.

[Tav10] S. Tavernier, "Experimental Techniques in Nuclear and Particle Physics", Springer-Verlag, Berlin, Heidelberg 2010.

[TCS71] C. A. Tobias, A. Chatterjee and A. R. Smith, *Phys. Lett.* **37A** 119–20, 1971.

[Ter09] T. Terasawa *et al.*, *Ann. Intern. Med.* **151** 556–65, 2009.

[Tes16a] T. Tessonnier *et al.*, *Front. Oncol.* **5** 297, 2016.

[Tes16b] T. Tessonnier, private communication.

[Tes17] T. Tessonnier, "Treatment of low-grade meningiomas with protons and helium ions", *PhD Thesis*, 2017.

[TK12] H. Tsujii & T. Kamada, *Jpn. J. Clin. Oncol.* **42**(8) 670–85, 2012.

[To08a] D. W. Townsend, *Semin Ultrasound CT MR*, **29**(4) 232–5, 2008.

[To08b] D. W. Townsend, *J. Nucl. Med*, **49**(6) 938–55, 2008.

[Tob77] C. A. Tobias *et al.*, *Int. J. Rad. Oncol. Biol. Phys.* **3** 35, 1977.

[Tom03] T. Tomitani *et al.*, *Phys. Med. Biol.* **48** 875–89, 2003.

[Tou16] Y. Toufique, *Qatar Found. Annual Res. Conf. Proc.* 1, 2016.

[Tur95] J. E. Turner, "Atoms, Radiation and Radiation Protection", Wiley, New York, 1995.

[Tur11] T. G. Turkington "Chapter 2: PET Imaging Basics", P. Shreve & D. W. Townsend (ed.), "Clinical PET–CT in Radiology: Integrated Imaging in Oncology", Springer Science+Business Media, LLC 2011.

[Ura99] E. Urakabe *Jpn. J. Appl. Phys.* **38** 6145–9, 1999.

[Ura01] E. Urakabe *et al.*, *Jpn. J. Appl. Phys.* **40** 2540–8, 2001.

[VAF11] S. Verdú–Andrés, U. Amaldi and A. Faus–Golfe, *Int. J. Mod. Phys. A*, **26**(10–11) 1659–89, 2011.

[Vas17] O. N. Vassiliev, "Monte Carlo Methods for Radiation Transport: Fundamental and Advanced Topics", New York, Springer, 2017.

[Vav57] P. V. Vavilov, *Soviet Physics JETP* **5**:749, 1957.

[Vla08] V. Vlachoudis, *Proc. Int. Conf. on Mathematics, Computational Methods & Reactor Physics* (MC 2009), Saratoga Springs, New York, 2009.

[Vyn93] S. Vynckier *et al.*, *Radiother. Oncol.* **26** 275–77, 1993.

[Wei37] V. F. Weisskopf, *Phys. Rev.* **52** 295–303, 1937.

[WHO] *World Health Organization*, Cancer Factsheet (February 2017).

[WHO12] *World Health Organization* – International Agency for Research on Cancer, GLOBOCAN 2012: Estimated Cancer Incidence, Mortality and Prevalence Worldwide in 2012.

[Wil46] R. R. Wilson, *Radiology*, **47** 487–91, 1946.

[WK99] U. Weber & G. Kraft, *Phys. Med. Biol.* **44** 2765–75, 1999.

[Wolf] Wolfram Alpha "cat curve".

[Xie17] Y. Xie *et al.*, *Int. J. Radiat. Oncol. Biol. Phys.* **99**(1) 210–8, 2017.

[Yam98] S. Yamada *et al.*, *Proceedings of the Asian Particle Accelerator Conference Tsukuba*, Japan, 885–9, 1998.

[Yam08] T. Yamaya *et al.*, *Phys. Med. Biol.* **53**(3) 757–73, 2008.

[Yam11] T. Yamaya *et al.*, *Phys. Med. Biol.* **56** 1123–37, 2011.

[Yam16] T. Yamaya, "OpenPET enabling PET imaging during radiotherapy", *Int. Nucl. Phys. Conf.*, Adelaide, Australia, 2016.

[Yam17] T. Yamaya, *J Phys.: Conf. Ser.* **777** 012023, 2017.

[Yos12] E. Yoshida *et al.*, *Radiol. Phys. Technol.* **5** 92–7, 2012.

[Zan04] P. Zanzonico, *Semin. Nucl. Med.*, **34**(2) 87–111, 2004.

[Zhu11] X. Zhu *et al.*, *Phys. Med. Biol.* **56** 4041–57, 2011.

[Zie08] J. F. Ziegler, J. P. Biersack, and M. D. Ziegler, "The Stopping and Range of Ions in Matter", Ion Implantation Press, 2008.

[Zie99] J. F. Ziegler, *J. Appl. Phys/Rev. Appl. Phys.* **85** 1249–72, 1999.

Acknowledgment

Em primeiro lugar, gostaria de agradecer aos meus pais pelos sacrifícios em prol da minha educação, bem como ao resto da minha família por grande parte da motivação necessária para prosseguir os meus estudos. Em segundo lugar, gostaria de agradecer à Prof. Lídia Ferreira, sem a qual eu nunca teria seguido este caminho profissional na Física Nuclear.

Aussi, je dois remercier Prof. Stora, qui m'a donné la possibilité de travailler au CERN, m'a accueilli dans un groupe dynamique tel que EN-STI-RBS et m'a encouragé à poursuivre un doctorat.

I would like to thank my friends, in Lisbon and scattered (elastically) all around the world, for not letting our friendship decay over time. All the remarkable people I was priviledged to work or the new friends I made during the last couple of years certainly consist of the most rewarding findings of this PhD, I will always cherish the learning and shared experiences.

The present work would never have been possible without my supervisors, to whom I had the honor to work for: firstly Prof. Parodi, for her professionalism and exemplary dedication, disregarding of the distance. I feel extremely lucky for having been able to learn from her teachings and useful comments. Secondly, Prof. Ferrari, to whom I will be always grateful for the years of experience in the various groups of EN-STI, for all his patience and valuable time dedicated to teach me solving problems which I never even imagined possible to conceive before starting the PhD. Both of you made me a better physicist but, most importantly, showed me how far I still need to go (and the effort and dedication it entails). Finally, I would like to thank Francesco Cerutti, for his legendary skills as group leader as well as Vasilis Vlachoudis, for being always available to discuss simulation problems didactically.

This thesis benefited also from the direct contribution of dedicated and brilliant people such as Pablo Ortega, for his development work of PET tools and teachings, as well as to Caterina Cuccagna, with whom I shared the learning experience. I acknowledge Yassine Toufique for the embedded MLEM algorithm in the PET tools and Chiara Gianoli for the more specific reconstruction methods on the data, her teachings on image reconstruction during the days at LMU were very helpful. Furthermore, I thank Matthias Frankl for the aid translating the reconstructed data matrixes into images and english into german. During my visit at HIT Thomas Tessonnier and Julia Bauer help proved to be paramount for this thesis, namely with the research TPS data analysis and PET parameters for the simulation. Also, I acknowledge Wioletta Sandra Kozłowska for contributing with her own original (r)evolutionary method to calculate dose distributions in voxelized structures and for the office comradeship throughout the PhD, which I also extend to João Pedro Saraiva and Giulia Aricò. For the opportunity to partake in the experimental data acquisition in Japan, and meet an amazing culture and people, I will be always grateful to Prof. Yamaya and his *Imaging Physics Team* members, dômo arigatô gozaimasu! I would also like to thank particularly the support of Yoshida Eiji throughout my stay at NIRS–HIMAC and Akram Mohammadi in the data processing and subsequent discussions.

Na koniec moje najważniejsze podziękowania, dla mojej żony Barbary, za jej oddane wsparcie przez wszystkie lata mojej pracy, i dzięki której ta rozprawa wogóle mogła powstać. Dziękuję również mojej polskiej Rodzine, w szczególności moim teściom i szwagrom, za ich życzliwe i wsparcie.

This work was supported by the CERN KT–Fund.